

Diss. ETH No. 26508

NOVEL APPROACHES TO POWER SCALE ULTRAFAST THIN-DISK LASERS AT SHORT PULSE DURATIONS

A thesis submitted to attain the degree of
DOCTOR OF SCIENCES of ETH ZURICH
(Dr. sc. ETH Zurich)

presented by

IVAN JOSHUA GRAUMANN

Diplôme d'Ingénieur, Institut d'Optique Graduate School

born on 23.09.1992

citizen of France

accepted on the recommendation of

Prof. Dr. Dr. h. c. Ursula Keller, examiner
Prof. Dr. Jens Limpert, co-examiner

2020

Contents

Contents	i
List of Figures	v
List of Tables	vii
List of Symbols and Acronyms	ix
Publications	xv
Journal Papers	xv
Conference Papers	xvi
Abstract	xxi
Résumé (French)	xxv
1 Introduction	1
1.1 State of the art of high-power ultrafast laser technologies . .	2
1.2 Ultrafast thin-disk lasers	5
1.2.1 The thin-disk laser concept	5
1.2.2 Passively modelocked thin-disk laser oscillators	6
1.2.2.1 Soliton modelocking	6
1.2.2.2 Modelocking techniques	8
1.2.2.3 Modelocking stability	10
1.2.3 State of the art of ultrafast thin-disk lasers	11
1.3 Outline of this thesis	14
2 Peak-power scaling Yb:LuO thin-disk lasers	17
2.1 A promising material for high peak-power operation	17
2.2 Publication	21
2.3 Conclusion	40

3	Investigation of the short-pulsed modelocking regime via numerical simulations	43
3.1	The average power vs. pulse duration trade-off	43
3.2	Numerical model	45
3.2.1	Limitations of the linearized model	45
3.2.2	Self-consistent numerical model	46
3.2.2.1	General definitions	47
3.2.2.2	Determination of the steady-state	49
3.2.2.3	Stability of the steady-state	54
3.3	Evaluation of the modulation depth requirements for a 100-W 200-fs TDL	56
3.3.1	Design considerations	56
3.3.2	Gain reduction at 200 fs	58
3.3.3	SESAM modulation depth requirements	59
3.4	Conclusion on high-peak-power modelocking at short pulse durations	62
4	Thin-disk lasers based on Yb:CALGO	65
4.1	Properties of Yb:CALGO	65
4.2	Modelocked lasers based on Yb:CALGO	67
4.3	Investigation of thin-disk laser operation using Yb:CALGO	68
4.3.1	Visual inspection of the disks	70
4.3.2	Laser operation	72
4.4	Conclusion	74
5	SESAM with reduced two-photon absorption	75
5.1	Two-photon absorption in typical high-power SESAMs	76
5.2	SESAM with reduced two-photon absorption	81
5.3	Conclusion	84
6	Gain-matched mirrors	87
6.1	Roundtrip gain flattening by intracavity optics	87
6.2	Design of gain-matched mirrors	88
6.3	Gain-matched OC experiments	90
6.3.1	GMOC design	90
6.3.2	Modelocking experiments with Yb:LuO	92
6.3.3	Modelocking experiments with Yb:YAG	94
6.3.4	Conclusion of GMOC experiments	97
6.4	Gain-matched mirrors for Yb:YAG	98
6.4.1	GMM design	98
6.4.2	Modelocking experiments	100
6.5	Conclusion	102
7	Nonlinear-mirror modelocking	103
7.1	A promising alternative modelocking technique	103
7.2	Publication 1	106
7.3	Manuscript 2	120
7.4	Conclusion	136

8 Conclusion	139
Bibliography	145
Acknowledgements	159

List of Figures

1.1	Overview of the performance of high-power Yb-based ultrafast laser sources	4
1.2	Illustration of the thin-disk laser concept	5
1.3	Illustration of different modelocking states	10
1.4	Overview of the performance of modelocked TDL oscillators	12
2.1	Dependence of the thermal conductivity of typical host materials on the Yb-doping concentration	18
3.1	Gain cross-sections and gain reduction for Yb-doped YAG, LuO and CALGO	59
3.2	Pulse gain advantage and SESAM reflectivity for a 100-W 200-fs TDL based on Yb:YAG, Yb:LuO or Yb:CALGO	61
4.1	Illustration of the two available disk cuts and simulated gain cross-section of Yb:CALGO for the σ and π axes	66
4.2	Overview of the performance of modelocked Yb:CALGO oscillators	67
4.3	Microscope images of Yb:CALGO disks observed under different illumination conditions	71
4.4	Temperature rise in fluorescence operation and output power in cw operation with the different Yb:CALGO disks	73
5.1	Simulated nonlinear reflectivity curves of a typical high-power SESAM	76
5.2	Typical SESAM design for use in high-power TDLs	77
5.3	TPA contributions in a standard 1x3 QWs SESAM and in a 6x1 SCQWs SESAM	80
5.4	Growth and processing of the SESAM structures used in our TPA reduction study	81
5.5	Nonlinear reflectivity measurements and theoretical fits of the SESAM structures and DBRs prepared for our TPA reduction study	83
6.1	GMOC reflectivity and roundtrip gain flattening in an Yb:LuO TDL	91
6.2	Reflectivity of the produced GMOCs and simulated roundtrip gain flattening for the GMOC used in our experiments with Yb:LuO	91
6.3	Cavity layout of the TDL oscillator used for the GMOC experiments	93
6.4	GMOC reflectivity and roundtrip gain flattening in an Yb:YAG TDL	95

6.5	Diagnostics of the modelocking performance obtained with our Yb:YAG TDL oscillator operating with a standard OC and with a GMOC	96
6.6	GMM reflectivity and roundtrip gain flattening in an Yb:YAG TDL	99
6.7	Cavity layout of the Yb:YAG TDL oscillator used for the GMM experiments	100
6.8	Evolution of the output pulse duration as a function of the intracavity power in our Yb:YAG TDL oscillator without spectral filtering and with GMMs	101
7.1	Example nonlinear reflectivity curve of a nonlinear mirror based on a 1-mm-thick LBO and a 60% dichroic OC	104

List of Tables

3.1	Disk parameters for the numerical simulation of a 100-W 200-fs TDL . .	57
3.2	SESAM parameters for the numerical simulation of a 100-W 200-fs TDL	60
4.1	Properties of Yb:CALGO for an Yb-doping concentration of ≈ 5 at.% . .	66
4.2	Properties and cw laser performance of the Yb:CALGO disks tested during this thesis	69
5.1	Refractive index, bandgap energy and TPA coefficient of typical materials used in SESAM structures and topcoating layers	79
5.2	Rollover intensity I_2 estimated for a 1x3 QWs and a 6x1 SCQWs SESAM with a semiconductor or a dielectric DBR	79
5.3	Least-square fit parameters retrieved from the measured nonlinear reflectivity curves of the 1x3 QWs, 6x1 SCQWs and the DBR samples . . .	83
6.1	Nonlinear reflectivity parameters of the SESAMs used for the GMOC experiments	93
6.2	Modelocking performance of our Yb:LuO TDL oscillator with a standard OC and a GMOC	93
6.3	Modelocking performance of our Yb:YAG TDL oscillator with a standard OC and a GMOC	95
6.4	Parameters for the lorentzian reflectivity of the GMM for Yb:YAG	99

List of Symbols and Acronyms

Symbols

$\alpha_p(\beta)$	pump absorption coefficient.
B_{rt}	roundtrip B-integral.
β_{ss}	steady-state inversion level.
β_{TPA}	TPA coefficient.
D_{disk}	disk diameter.
$\Delta\Omega_g$	FWHM gain bandwidth.
ΔR_{ns}	SESAM nonsaturable losses.
ΔR	SESAM modulation depth.
$\Delta\nu_p$	FWHM bandwidth of the pump spectrum.
$\Delta\lambda_{FWHM}$	FWHM of the reflectivity dip of a gain-matched mirror.
D_{rt}	roundtrip dispersion.
E_p	pulse energy.
$E_{p,0}^{cav}$	pulse energy leading to the maximum gain advantage for pulsed operation against cw.
ϵ_n	normalized electric field in the SESAM structure.
$\eta_{enh}(\beta)$	pump enhancement factor.
η_{QML}	QML stability term.
F	fluence.
$F(r)$	radial fluence distribution on the SESAM.
F_0	fluence maximizing the SESAM reflectivity.
$F_2(\tau_p)$	SESAM rollover coefficient (fluence).

$F_{2,\text{meas}}$	measured rollover coefficient.
F_{pk}	peak fluence on the SESAM.
F_{sat}	SESAM saturation fluence.
f_{rep}	repetition rate.
G_{cw}	roundtrip power gain for a cw wave.
G_{lin}	linearized roundtrip power gain.
$G_{\nu,\text{cw}}(r, \nu)$	spectrally-dependent power gain for a cw wave.
G_{pulse}	roundtrip power gain for a soliton pulse.
$G_{r,\text{pulse}}(r)$	radially-dependent power gain for a soliton pulse.
$G_{r\nu,\text{cw}}(r, \nu)$	radially- and spectrally-dependent power gain for a cw wave.
G_{rt}	roundtrip cavity gain.
γ_{rad}	upper-state decay rate.
γ_{rt}	roundtrip SPM coefficient.
g	roundtrip power gain (saturated).
h	Planck constant.
I_2	SESAM rollover coefficient (intensity).
I^{eff}	effective intensity.
$I_{\text{SESAM}}(r)$	radial intensity profile on the SESAM.
$I_{\text{disk}}(r)$	radial intensity profile on the disk.
I_{pk}	peak intensity (on the disk).
I_{sat}	saturation intensity.
L_{cav}	roundtrip cavity losses.
l_{n}	total thickness of the SESAM.
λ	wavelength.
λ_{pump}	pump center wavelength.
λ_{pk}	center wavelength of the reflectivity dip of a gain-matched mirror.
l_{cav}	cavity length.
l_{disk}	disk thickness.
N_1, N_2	population of the ground state and upper laser level.
$N_{\text{dop,at.\%}}$	Yb-ion density, or doping concentration (in at. %).
N_{dop}	Yb-ion density, or doping concentration (in m^{-3}).
$N_1^{\text{eff}}(r)$	effective laser photon flux.
$N_{\text{p,ss}}^{\text{eff}}(\beta, r)$	effective pump photon flux in the steady state.
$N_{\text{p}}(r)$	incident pump photon flux.
n_2	nonlinear refractive index.
$n_{\text{passes,l}}$	number of laser passes on the disk per roundtrip.
ν	frequency.
ν_{cw}	frequency of the cw wave.

ν_1	center frequency of the laser pulse.
ν_p	center frequency of the pump spectrum.
n	refractive index.
P_0^{cav}	average power leading to the maximum gain advantage for pulsed operation against cw.
P_{avg}	average power.
$P_{\text{ic,ref}}$	reference intracavity power for soliton shaping.
P_{ic}	intracavity power.
P_{pk}	pulse peak power.
$P_{\text{pump,ss}}$	steady-state pump power.
P_{pump}	pump power.
$\varphi_{\text{rt,sol}}, \varphi_0$	roundtrip soliton phase.
R_{DBR}	reflectivity of the SESAM DBR.
R_{GMM}	gain-matched mirror reflectivity.
R_{GMOC}	gain-matched OC reflectivity.
$R_{\text{OC}}(\nu)$	frequency-dependent OC reflectivity.
R_{SESAM}	SESAM reflectivity.
$R_{\text{cav,lin}}$	linear cavity reflectivity.
$R_{\text{cav,opt}}$	cavity reflectivity for optimal gain flattening.
R_{cav}	roundtrip cavity reflectivity.
R_{filter}	reflectivity of an intracavity spectral filter.
R_{lin}	linear reflectivity.
R_{ns}	SESAM nonsaturatable reflectivity.
R_{pk}	reflectivity at the reflectivity dip of a gain-matched mirror.
$S_{\text{norm}}(\nu)$	normalized spectrum.
$\sigma_{\text{abs}}^{\text{eff}}$	effective absorption cross-section.
$\sigma_{\text{abs}}(\nu)$	frequency-dependent absorption cross-section.
$\sigma_{\text{em}}^{\text{eff}}$	effective emission cross-section.
$\sigma_{\text{em}}(\nu)$	frequency-dependent emission cross-section.
$\sigma_{\text{g,cw}}(r, \nu)$	radially- and spectrally-dependent gain cross-section for a cw wave.
$\sigma_{\text{g,pulse}}(r)$	radially-dependent gain cross-section for a soliton pulse.
σ_{g}	gain cross-section.
$\sigma_{\text{pump}}^{\text{eff}}(\beta)$	effective pump cross-section.
τ	soliton pulse width.
τ_{a}	absorber recovery time.
τ_{p}	FWHM pulse duration.
$\tau_{\text{p},F_2,\text{meas}}$	pulse duration at which the SESAM rollover coefficient is measured.
$\tau_{\text{p,ref}}$	reference pulse duration for soliton shaping.

w_{SESAM}	beam waist on the SESAM.
w_{disk}	beam waist on the disk.
$w(z)$	$1/e^2$ Gaussian beam radius inside the laser cavity.

Acronyms

AOI	angle of incidence.
AR	anti-reflection.
BF	bright field.
BP	Brewster plate.
CALGO	calcium gadolinium aluminum oxide CaGdAlO_4 .
CEO	carrier-envelope offset.
CPA	chirped-pulse amplification.
cw	continuous wave.
DBR	distributed Bragg reflector.
DF	dark field.
DM	dispersive mirror.
ESA	excited-state absorption.
FW	fundamental wave.
FWHM	full-width at half-maximum.
GDD	group delay dispersion.
GMM	gain-matched mirror.
GMOG	gain-matched output coupler.
GTI	Gires-Tournois interferometer.
GVM	group-velocity mismatch.
HEM	heat exchanger method.
HHG	high-order harmonic generation.
HR	high-reflection.
IBS	ion-beam sputtering.
ISA	inverse saturable absorption.
KLM	Kerr-lens modelocking.
KM	Kerr medium.
LuO	lutetium oxide Lu_2O_3 .
MBE	molecular beam epitaxy.
Nd	neodymium.
NLM	nonlinear mirror.
OC	output coupler.
OPA	optical parametric amplification.

QML	Q-switched modelocking.
QW	quantum well.
SA	soft aperture.
Sa	sapphire Al_2O_3 .
SAM	self-amplitude modulation.
SC	strain compensated.
SESAM	semiconductor saturable absorber mirror.
SH	second harmonic.
SHG	second harmonic generation.
singlemode	single-transverse mode.
SPM	self-phase modulation.
TDL	thin-disk laser.
TFP	thin-film polarizer.
Ti	titanium.
TPA	two-photon absorption.
VBG	volume Bragg grating.
XPL	cross-polarized light.
XUV	extreme ultraviolet.
YAG	yttrium aluminum garnet $\text{Y}_3\text{Al}_5\text{O}_{12}$.
Yb	ytterbium.
ZPL	zero-phonon line.

Publications

Parts of this doctoral thesis are published in the following journal papers and conference contributions.

Journal Papers

1. **I. J. Graumann**, F. Saltarelli, L. Lang, V. J. Wittwer, T. Südmeyer, C. R. Phillips, and U. Keller, "Power-scaling of nonlinear-mirror modelocked thin-disk lasers," submitted to *Opt. Express* (2019)
2. F. Saltarelli, **I. J. Graumann**, L. Lang, D. Bauer, C. R. Phillips, and U. Keller, "Power scaling of ultrafast oscillators: 350-W average-power sub-picosecond thin-disk laser," *Opt. Express* 27(22), 31465-31474 (2019).
3. F. Saltarelli, A. Diebold, **I. J. Graumann**, C. R. Phillips, and U. Keller, "Self-phase modulation cancellation in a high-power ultrafast thin-disk laser oscillator," *Optica* 5(12), 1603-1606 (2018).
4. A. Diebold*, F. Saltarelli*, **I. J. Graumann**, C. J. Saraceno, C. R. Phillips, and U. Keller, "Gas-lens effect in kW-class thin-disk lasers," *Opt. Express* 26(10), 12648-12659 (2018), *authors with equal contributions.
5. N. Modsching, C. Paradis, F. Labaye, M. Gaponenko, **I. J. Graumann**, A. Diebold, F. Emaury, V. J. Wittwer, and T. Südmeyer, "Kerr

- lens mode-locked Yb:CALGO thin-disk laser," *Opt. Lett.* **43**(4), 879-882 (2018).
6. F. Labaye, M. Gaponenko, V. J. Wittwer, A. Diebold, C. Paradis, N. Modsching, L. Merceron, F. Emaury, **I. J. Graumann**, C. R. Phillips, C. J. Saraceno, C. Kränkel, U. Keller, and T. Südmeyer, "Extreme ultraviolet light source at a megahertz repetition rate based on high-harmonic generation inside a mode-locked thin-disk laser oscillator," *Opt. Lett.* **42**(24), 5170-5173 (2017).
 7. F. Saltarelli, A. Diebold, **I. J. Graumann**, C. R. Phillips, and U. Keller, "Modelocking of a thin-disk laser with the frequency-doubling nonlinear-mirror technique," *Opt. Express* **25**(19), 23254-23266 (2017).
 8. **I. J. Graumann**, A. Diebold, C. G. E. Alfieri, F. Emaury, B. Deppe, M. Golling, D. Bauer, D. Sutter, C. Kränkel, C. J. Saraceno, C. R. Phillips, and U. Keller, "Peak-power scaling of femtosecond Yb:Lu₂O₃ thin-disk lasers," *Opt. Express* **25**(19), 22519-22536 (2017).
 9. A. Diebold, Z. Jia, **I. J. Graumann**, Y. Yin, F. Emaury, C. J. Saraceno, X. Tao, and U. Keller, "High-power Yb:GGG thin-disk laser oscillator: first demonstration and power-scaling prospects," *Opt. Express* **25**(2), 1452-1462 (2017).

Conference Papers

1. F. Saltarelli, **I. J. Graumann**, L. Lang, D. Bauer, C. R. Phillips, and U. Keller, "Soliton-Modelocked Thin-Disk Laser Oscillator with 350 W Average Power and Sub-ps Pulses," in Laser Congress 2019 (ASSL, LAC, LS&C), OSA Technical Digest (Optical Society of America, 2019), **AM4A.3**, talk.
2. F. Saltarelli, D. Koenen, L. Lang, **I. J. Graumann**, C. R. Phillips, and U. Keller, "Beam quality in high-power thin-disk lasers: influence and measurement of the radial inversion profile," in Laser Congress 2019 (ASSL, LAC, LS&C), OSA Technical Digest (Optical Society of America, 2019), **JM5A.35**, poster.

-
3. **I. J. Graumann**, F. Saltarelli, L. Lang, V. J. Wittwer, T. Südmeyer, C. R. Phillips, and U. Keller, "Power-Scaling Nonlinear-Mirror Modelocked Thin-Disk Lasers," in 2019 European Conference on Lasers and Electro-Optics and European Quantum Electronics Conference, (Optical Society of America, 2019), CF.1.6, talk.
 4. F. Saltarelli, A. Diebold, **I. J. Graumann**, C. R. Phillips, and U. Keller, "Nonlinearity Compensation and Thermal Lensing in High-Power Ultrafast Thin-Disk Laser Oscillators," in 2019 European Conference on Lasers and Electro-Optics and European Quantum Electronics Conference, (Optical Society of America, 2019), CF.1.3, talk.
 5. F. Saltarelli, **I. J. Graumann**, L. Lang, D. Bauer, C. R. Phillips, and U. Keller, "350-W Average-Power SESAM-Modelocked Ultrafast Thin-Disk Laser," in 2019 European Conference on Lasers and Electro-Optics and European Quantum Electronics Conference, (Optical Society of America, 2019), CF.1.1, talk.
 6. F. Saltarelli, A. Diebold, **I. J. Graumann**, C. R. Phillips, and U. Keller, "Self-Phase Modulation Cancellation in 210-W SESAM-Modelocked Thin-Disk Oscillator Operated in Air," in Laser Congress 2018 (ASSL), OSA Technical Digest (Optical Society of America, 2018), [AM2A.5](#), talk.
 7. F. Saltarelli, A. Diebold, **I. J. Graumann**, C. R. Phillips, and U. Keller, "Soliton-Modelocked 153-W Thin-Disk Laser Oscillator in Air Enabled by Negative Nonlinearities in a Phase-Mismatched $\chi^{(2)}$ Crystal," in Advanced Photonics 2018 (BGPP, IPR, NP, NOMA, Sensors, Networks, SPPCom, SOF), OSA Technical Digest (online) (Optical Society of America, 2018), [NpTh1C.1](#), talk.
 8. F. Labaye, M. Gaponenko, V. J. Wittwer, A. Diebold, C. Paradis, N. Modsching, L. Merceron, F. Emaury, **I. J. Graumann**, C. R. Phillips, C. J. Saraceno, C. Kränkel, U. Keller, and T. Südmeyer, "Extreme Ultraviolet Light Source by High-Harmonic Generation Inside an Ultrafast Thin-Disk Laser," in Advanced Photonics 2018 (BGPP, IPR, NP, NOMA, Sensors, Networks, SPPCom, SOF), OSA Technical Digest (online) (Optical Society of America, 2018), [NpTh1C.8](#), talk.
 9. F. Saltarelli, A. Diebold, **I. J. Graumann**, C. R. Phillips, and U. Keller, "Nonlinear-Mirror Modelocked Thin-Disk Laser Delivering 21 W

- Average Power with 324-fs Pulses,” in Laser Congress 2017 (ASSL, LAC), OSA Technical Digest (online) (Optical Society of America, 2017), [ATh1A.2](#), talk.
10. F. Labaye, M. Gaponenko, V. J. Wittwer, C. Paradis, N. Modsching, L. Merceron, A. Diebold, F. Emaury, **I. J. Graumann**, C. R. Phillips, C. J. Saraceno, C. Kränkel, U. Keller, and T. Südmeyer, “SESAM-Modelocked Thin-Disk Laser (TDL) with Intracavity High-Harmonic Generation (HHG),” in Laser Congress 2017 (ASSL, LAC), OSA Technical Digest (online) (Optical Society of America, 2017), [ATh5A.3](#), talk.
 11. N. Modsching, C. Paradis, M. Gaponenko, F. Labaye, F. Emaury, A. Diebold, **I. Graumann**, B. Deppe, C. Kränkel, V. J. Wittwer, and T. Südmeyer, “Towards Few-Cycle Ultrafast Thin-Disk Lasers,” in Laser Congress 2017 (ASSL, LAC), OSA Technical Digest (online) (Optical Society of America, 2017), [JM5A.41](#), poster.
 12. C. Paradis, N. Modsching, F. Labaye, M. Gaponenko, F. Emaury, A. Diebold, **I. Graumann**, B. Deppe, C. Kränkel, V. J. Wittwer, and T. Südmeyer, “Kerr lens mode-locked thin-disk lasers delivering 30-fs pulses from Yb:CALGO and 35-fs pulses from Yb:Lu₂O₃,” in Ultrafast Optics (UFO) XI, (Jackson Hole, Wyoming, United States, 8–13 Oct. 2017, 2017), talk.
 13. F. Labaye, M. Gaponenko, V. J. Wittwer, C. Paradis, N. Modsching, L. Merceron, A. Diebold, F. Emaury, **I. Graumann**, C. R. Phillips, C. J. Saraceno, C. Kränkel, U. Keller, and T. Südmeyer, “Compact megahertz repetition rate coherent XUV light source based on HHG inside a mode-locked thin-disk laser,” in Ultrafast Optics 2017 (UFO 2017), (Jackson Hole, WY, USA, October 8-13, 2017, 2017), talk.
 14. M. Gaponenko, F. Labaye, V. J. Wittwer, C. Paradis, N. Modsching, L. Merceron, A. Diebold, F. Emaury, **I. J. Graumann**, C. R. Phillips, C. J. Saraceno, C. Kränkel, U. Keller, and T. Südmeyer, “High Harmonic Generation (HHG) inside a Modelocked Thin-Disk Laser,” in Frontiers in Optics 2017, OSA Technical Digest (online) (Optical Society of America, 2017), [FTh2B.1](#), talk.
 15. M. Gaponenko, F. Labaye, V. J. Wittwer, C. Paradis, N. Modsching, L. Merceron, A. Diebold, F. Emaury, **I. J. Graumann**, C. R. Phillips, C. J.

-
- Saraceno, C. Kränkel, U. Keller, and T. Südmeyer, "Compact megahertz coherent XUV generation by HHG inside an ultrafast thin-disk laser," in *Nonlinear Optics*, OSA Technical Digest (online) (Optical Society of America, 2017), [NTh3A.1](#), **postdeadline talk**.
16. C. Paradis, N. Modsching, M. Gaponenko, F. Labaye, F. Emaury, A. Diebold, **I. Graumann**, B. Deppe, C. Kränkel, V. J. Wittwer, and T. Südmeyer, "Sub-50-fs Kerr Lens Mode-Locked Thin-Disk Lasers," in 2017 European Conference on Lasers and Electro-Optics and European Quantum Electronics Conference, (Optical Society of America, 2017), [PD.1.4](#), **postdeadline talk**.
 17. **I. J. Graumann**, A. Diebold, F. Emaury, B. Deppe, C. R. Phillips, M. Golling, D. Bauer, P. Heu, D. Follman, G. D. Cole, M. Aspelmeyer, D. Sutter, C. Kränkel, C. J. Saraceno, and U. Keller, "Peak-power Scaling of Femtosecond SESAM-modelocked Yb:Lu₂O₃ Thin-disk Lasers," in 2017 European Conference on Lasers and Electro-Optics and European Quantum Electronics Conference, (Optical Society of America, 2017), [CF.5.4](#), talk.
 18. A. Diebold, **I. Graumann**, F. Saltarelli, F. Emaury, C. Phillips, C. J. Saraceno, and U. Keller, "Optimized components for high-power ultrafast thin-disk lasers," in OCLA Symposium 2017 Optical Coatings for Laser Applications, Buchs, Switzerland, April 12, 2017, (2017), **invited talk**.
 19. **I. J. Graumann**, A. Diebold, F. Emaury, B. Deppe, C. Kränkel, C. J. Saraceno, and U. Keller, "High-Power Modelocked Yb:Lu₂O₃ Thin-Disk Laser with 10-MW sub-500 fs Pulses," in Lasers Congress 2016 (ASSL, LSC, LAC), OSA Technical Digest (online) (Optical Society of America, 2016), [ATu1A.3](#), talk.
 20. A. Diebold, Z. Jia, **I. J. Graumann**, Y. Yin, F. Emaury, C. J. Saraceno, X. Tao, and U. Keller, "Yb:GGG thin-disk oscillator with high power continuous wave operation," in Lasers Congress 2016 (ASSL, LSC, LAC), OSA Technical Digest (online) (Optical Society of America, 2016), [AM5A.18](#), poster, **Outstanding Student Poster Presentation Award**.
 21. **I. J. Graumann**, A. Diebold, F. Emaury, B. Deppe, C. Kränkel, C. J. Saraceno, and U. Keller, "10-MW sub-500-fs high-power SESAM-

- modelocked Yb:Lu₂O₃ thin disk laser," in 7th EPS-QEOD Europhoton Conference (Europhoton 2016), Vienna, Austria, August 21 - 26, 2016, talk.
22. C. Saraceno, F. Emaury, A. Diebold, **I. Graumann**, M. Golling, and U. Keller, "Trends in high-power ultrafast lasers," in [SPIE Defense + Security, \(SPIE, 2016\)](#), 7, **invited talk**.

Abstract

The laser has become an essential tool extensively used at different levels in today's society. Probably most commonly known in the form of a laser pointer, the laser technology is extremely diverse and versatile. Chip-scale lasers are found in everyday devices such as smartphones and computers and lasers are driving the high-speed, broadband internet. High-speed and high-precision micromachining, for example in the automotive industry, relies on ultrafast laser systems. Additionally, lasers are key components for remote-sensing and medical applications, such as laser eye surgery. Finally, the laser led to many breakthroughs in various fields of scientific research, such as chemistry, biology and physics.

A key feature of laser light is the ability to concentrate energy on a very small point both in space and time. In particular, modelocked laser generate a train of energetic pulses with a duration typically ranging from a few picoseconds (10^{-12} s) down to a few femtoseconds (10^{-15} s). These pulses can be amplified and tightly focused down to a typical size of a few tens to hundreds of micrometers (10^{-6} m), locally reaching extremely high peak intensities of order 10^{14} W/cm². This regime opens the door to highly-nonlinear processes, and notably high-harmonic generation (HHG), enabling a frequency conversion of the incident infrared (IR, ≈ 1 μ m) light to the extreme-ultraviolet (XUV, 10-100 nm). The combination of the high-intensity IR and the generated XUV light can be used to study matter on ultrashort timescales.

Within the scope of this thesis, we focused on one of the most powerful laser technologies available to generate IR pulses: thin-disk lasers (TDLs). The thin-disk technology relies on a power-scalable and efficiently cooled geometry of the laser crystal to achieve high-power laser operation. Mod-locked thin-disk laser oscillators directly provide sub-ps pulses at high-average powers >100 W with excellent beam quality and without the need for external amplification. Over the last twenty years, significant research efforts have been focused on scaling the performance of TDLs towards higher average powers, higher pulse energies and shorter pulse durations. The results of these endeavors have highlighted a clear trade-off between high average power and short pulse durations. The goal of this doctoral project was to investigate the origin of this trade-off and develop new approaches to combine high-power operation with short pulse durations in TDLs.

Using the semiconductor saturable absorber mirror (SESAM) technology, we scaled the output peak power of TDLs based on the gain material Yb:LuO. We demonstrated peak powers >10 MW for the first time in an Yb:LuO TDL, combined with pulse durations <600 fs, shorter than typical pulse durations achieved with the state-of-the-art gain material Yb:YAG. Additionally, we developed a numerical model to evaluate the effect of the limited gain bandwidth and the SESAM rollover effect on the laser performance. By comparing our numerical simulations with the experimental data, we could derive a criterion for estimating the maximum output power and pulse duration achievable in a given TDL oscillator.

Following on these first investigations, we further improved our model to carry out a study of the requirements on the SESAM parameters to support high-power modelocked operation (100 W) at short pulse durations (200 fs) depending on the used gain material for the disk. Our results show that reaching this goal is overly challenging using the current SESAM technology and Yb:YAG or Yb:LuO as gain material. However, the broadband gain material Yb:CALGO is well suited in terms of gain bandwidth. We therefore tested Yb:CALGO in thin-disk laser operation, with the aim to scale the output average power towards 100 W. We characterized and tested several disks with different crystal qualities, Yb-doping concentrations and thicknesses. Although we observed an improvement

of the crystal quality over the course of this thesis, the performance in continuous-wave (cw) operation still remained limited to 20-30 W due to the low crystal quality.

In our last set of investigations, we turned to alternative approaches to achieve short pulse durations with the high-power-compatible, but comparatively narrowband gain materials Yb:YAG and Yb:LuO. We first addressed the limitation due to the SESAM rollover effect. This effect is induced by two-photon absorption (TPA), particularly strong in the semiconductor materials used in the SESAM structure. We reduced this effect by replacing the semiconductor mirror with a dielectric mirror in the SESAM. In a second step, we addressed the limitation due to the gain bandwidth of Yb:YAG and Yb:LuO. The limited gain bandwidth acts as a filter on the pulse, narrowing its spectrum upon every pass through the disk. This effect can be compensated by introducing a spectral filter in the laser cavity with a spectral reflectivity profile mirroring the gain spectrum of the disk. We designed and tested such a filter in preliminary modelocking experiments. Finally, we investigated an alternative modelocking technique based on a nonlinear mirror (NLM). With the first implementation of the NLM technique in a TDL, we demonstrated 323 fs pulses using Yb:YAG as gain material, corresponding to a factor of two shorter pulses than with SESAM modelocking. We investigated this new modelocking regime and additionally demonstrated a combination of average powers >60 W and peak powers around 15 MW with pulse durations <450 fs, showing promising progress towards a 100-W class TDL operating at short pulse durations.

Résumé (French)

Le laser est devenu un outil essentiel, largement répandu à différents niveaux de la société actuelle. Communément connu par beaucoup sous la forme de pointeur laser, la technologie laser est particulièrement polyvalente et diversifiée. Smartphones et ordinateurs sont aujourd'hui équipés de puces laser et l'internet très haut débit est rendu possible par des lasers. Le micro-usinage rapide et de haute précision, réalisé par exemple par l'industrie automobile, nécessite des sources laser de puissance à impulsions ultra-courtes. De plus, les lasers sont des composants essentiels pour des applications de détection à distance ou des applications médicales, telle que la chirurgie réfractive. Enfin, de nombreuses avancées scientifiques, dans des domaines aussi différents que la chimie, la biologie ou la physique, ont été rendues possible par le laser.

La capacité à confiner une certaine énergie simultanément dans le temps et l'espace constitue un aspect fondamental de la lumière laser. En particulier, les lasers à verrouillage de mode produisent un train d'impulsions énergétiques avec une durée typiquement de l'ordre de quelques picosecondes (10^{-12} s) à quelques femtosecondes (10^{-15} s). Ces impulsions peuvent ensuite être amplifiées et fortement focalisées pour atteindre un diamètre de faisceau typiquement de l'ordre de quelques dizaines à quelques centaines de microns (10^{-6} m), ce qui permet d'obtenir localement des intensités extrêmement élevées, de l'ordre de 10^{14} W/cm². Ce régime donne l'accès à des processus fortement non-linéaires et notamment la génération d'harmoniques d'ordre élevé (HHG), qui permet de

convertir la fréquence de la lumière infrarouge (IR) incidente ($\approx 1 \mu\text{m}$) au domaine de l'extrême-ultraviolet (XUV, 10-100 nm). Le faisceau IR de haute intensité et le faisceau XUV généré par HHG peuvent ensuite être combinés pour étudier la matière sur des échelles de temps ultra-courtes.

Dans le cadre de cette thèse de doctorat, nous nous sommes concentrés sur l'une des technologies laser les plus puissantes pour la génération d'impulsions IR : les lasers à disque mince. La technologie laser à disque mince repose sur une géométrie du cristal laser permettant à la fois une évacuation de la chaleur et une augmentation de la puissance de manière efficace. Les oscillateurs laser à disque mince et à verrouillage de mode génèrent directement des impulsions sub-ps à un niveau de puissance moyenne $>100 \text{ W}$ avec une excellente qualité de faisceau, et sans recours à une chaîne d'amplification externe. Au cours des vingt dernières années, l'amélioration des performances des lasers à disque mince en termes de haute puissance, haute énergie et courte durée d'impulsion, a attiré l'attention de nombreux chercheurs. Le résultat de ces efforts a mis en lumière l'existence d'un compromis entre haute puissance et courte durée d'impulsion. L'objectif de ce projet de thèse était donc d'une part d'identifier et quantifier les causes de ce compromis, et d'autre part de développer de nouvelles approches pour combiner haute puissance et impulsions courtes avec les lasers à disques minces.

En utilisant la technologie du miroir absorbant saturable semi-conducteur (SESAM), nous avons augmenté la puissance crête des lasers à disques minces basés sur le matériau Yb:LuO. Nous avons obtenu des puissances crêtes $>10 \text{ MW}$ pour la première fois avec un laser Yb:LuO à disque mince, avec des durées d'impulsion $<600 \text{ fs}$, plus courtes que les durées d'impulsions généralement obtenues avec le matériau de choix habituel qu'est le Yb:YAG. Nous avons aussi développé un modèle de simulation numérique, avec pour objectif d'évaluer l'effet de la bande passante limitée du milieu amplificateur et du retournement de la réflectivité du SESAM sur la performance du laser. Par comparaison de nos résultats numériques avec les données expérimentales, nous avons pu définir un critère pour estimer la puissance maximale et la durée d'impulsion la plus courte pouvant être obtenues avec un certain oscillateur laser à disque mince.

À la suite de ces premiers travaux, nous avons continué d'améliorer notre modèle dans le but de réaliser une étude comparative des exigences en termes de paramètres du SESAM permettant d'assurer le régime impulsif à haute puissance (100 W) et courte durée d'impulsion (200 fs) pour différents milieux amplificateurs. Nos résultats ont montré que cette performance est difficilement atteignable avec les matériaux laser Yb:YAG et Yb:LuO, compte tenu de la technologie SESAM actuelle. En revanche, le matériau Yb:CALGO dispose d'une large bande passante favorable à l'obtention de ces impulsions ultra-courtes. Nous avons alors testé Yb:CALGO en opération laser dans le but d'obtenir une puissance moyenne de l'ordre de 100 W. Nous avons caractérisé et testé plusieurs disques avec différents niveaux de qualité du cristal, différentes concentrations en Yb et différentes épaisseurs. Malgré de nettes améliorations du point de vue de la qualité du cristal au cours de cette thèse, la performance laser en régime continu est restée limitée à 20-30 W en raison de la faible qualité du cristal.

Pour nos dernières recherches, nous nous sommes donc concentrés sur différentes nouvelles approches pour générer des impulsions courtes avec les matériaux Yb:YAG et Yb:LuO, compatibles pour la haute puissance mais disposant d'une bande passante relativement étroite. Nous nous sommes d'abord intéressés à la limitation introduite par le retournement de la réflectivité du SESAM. Cet effet résulte de l'absorption à deux photons particulièrement forte dans les matériaux semiconducteurs utilisés dans la structure du SESAM. Nous avons réduit cet effet néfaste en remplaçant le miroir en matériaux semiconducteurs par un miroir en matériaux diélectriques. Dans un deuxième temps, nous nous sommes penchés sur la limitation due à la bande passante des matériaux Yb:YAG et Yb:LuO. La bande passante étroite du milieu amplificateur agit comme un filtre pour l'impulsion, réduisant la largeur de spectre de l'impulsion avec chaque passage à travers le disque. Cet effet peut être compensé en introduisant un filtre spectral dans la cavité laser avec une réflectivité spectrale à l'inverse du spectre de gain du disque. Nous avons conçu et testé un tel filtre en régime impulsif de manière préliminaire. Enfin nous avons étudié une technique de verrouillage de mode alternative basée sur un miroir non-linéaire. Nous avons effectué la première mise en oeuvre

de cette technique dans un laser à disque mince utilisant Yb:YAG comme milieu amplificateur, et avons obtenu des impulsions de 323 fs, deux fois plus courtes qu'avec la technologie SESAM. Nous avons étudié ce nouveau régime impulsionnel et obtenu une puissance moyenne >60 W et une puissance crête de l'ordre de 15 MW avec des impulsions brèves <450 fs. Ce résultat prometteur contribue au développement des lasers à disque mince en vue d'une puissance moyenne de 100 W avec des impulsions brèves.

Chapter 1

Introduction

Once labelled “a solution seeking a problem” by its inventor Theodor Maiman [1], the laser has come a long way since it was first demonstrated nearly 60 years ago [2], and has proven to be a solution to a wide selection of “problems” in our daily life, industry and scientific research.

Light amplification by stimulated emission of radiation (LASER) produces electromagnetic radiation with a distinct property called coherence. Coherent light is characterized by a constant phase difference between two points in space or time, which confers unique properties to laser light. The spatial coherence of a laser means that a laser beam can be tightly confined in space (focused) or made to propagate with a fixed diameter over long distances (collimated). Similarly, the temporal coherence of laser light can be exploited to emit light continuously with a single frequency, or produce pulses with a broad spectrum and ultrashort durations. Laser light can therefore be applied to concentrate energy into a small point both in space and time, locally reaching extremely high powers, and to transmit or obtain information with utmost spatial and temporal resolution.

These unique properties of laser light have found a plethora of applications impacting our daily life such as optical telecommunications, optical disk drives or laser lighting displays. Lasers are used for high-precision cutting or welding of mechanical parts with extremely precise finishes and smooth edges, for example in the automotive industry, or for the microprocessing of functional surfaces. Lasers also find applications in

medicine, e.g. for eye surgery, and in biology for imaging living tissue or sequencing DNA. Finally, lasers have pushed the boundaries of scientific research in physics and are essential tools for frequency metrology, high-precision spectroscopy and the study of matter on ultrashort timescales.

Due to the extensive use of the laser at many different levels in society, laser research is a dynamic and expanding field. In this thesis, we present our contribution to the exciting world of ultrafast lasers with our work on novel approaches to power scale ultrafast thin-disk lasers at short pulse durations.

1.1 State of the art of high-power ultrafast laser technologies

A particularly attractive aspect of lasers is their ability to produce powerful, extremely short pulses of light. In modelocked operation, typical pulse durations are in the order of picoseconds (10^{-12} s) down to a few femtoseconds (10^{-15} s). We will refer to this regime of operation as the ultrafast regime, as opposed to the continuous wave (cw) regime.

Ultrafast laser sources delivering energetic ultrashort pulses with a good beam quality can be tightly focused in order to reach peak intensities sufficiently high to drive nonlinear processes for generating new frequencies, for example in the extreme ultraviolet (XUV) or THz spectral region [3–5]. In both of these spectral domains, there is a demand for compact, high-average-power sources of coherent radiation to push the boundaries of current experimental limitations, such as low signal-to-noise ratios due to low detection statistics or strong water absorption [6,7]. This translates into a demand for driving laser sources providing high average powers P_{avg} , i.e. energetic pulses (with an energy E_p) at an increased pulse repetition rate f_{rep} :

$$P_{\text{avg}} = E_p \cdot f_{\text{rep}} \tag{1.1}$$

The typical targeted parameters for ultrafast laser sources driving these nonlinear processes are:

- a pulse peak power of order 100 MW to a few GW,
- a pulse duration ideally <100 fs for efficient XUV generation via high-order harmonic generation (HHG), or few-cycle THz generation,
- pulse energies of order 100 μJ to reach the required peak power,
- repetition rates of order 1-10 MHz to achieve a sufficient average power.

The current trend is towards reaching kW-level average power at MHz repetition rates.

Historically, titanium (Ti)-doped sapphire Al_2O_3 (Sa) amplifier systems were the workhorse for driving XUV or THz generation experiments, due to their ultrashort pulses, typically ≈ 30 fs. However, the large quantum defect ($\approx 45\%$) and low availability of high-power pump lasers make the power scaling of Ti:Sa laser systems challenging. High-power Ti:Sa amplifiers typically operate at limited repetition rates ≤ 30 kHz, average powers < 100 W and require cryogenic cooling [8,9]. Ti:Sa laser systems are therefore increasingly being replaced by high-power ytterbium (Yb)-based laser sources operating at a wavelength around $1 \mu\text{m}$, and benefiting from a lower quantum defect ($\approx 5\text{-}10\%$) and the availability of high-power semiconductor pump diodes. Due to the narrower gain bandwidth of Yb-doped materials compared to Ti:Sa, these new high-power laser sources are often combined with nonlinear pulse compression schemes in order to reach the shortest pulse durations.

The leading Yb-based ultrafast technologies all exploit a geometry of the gain material that maximizes the surface-to-volume ratio, resulting in an efficient heat extraction. The current geometries of choice are the thin-disk, fiber and slab geometries (see figure 1.1). High-power ultrafast laser systems typically rely on the combination of a low-power, passively mode-locked oscillator and one or several amplification stages, with additional pulse shaping and compression stages if required. Such high-power ultrafast amplifiers have successfully demonstrated kW-level average powers in all three geometries, as illustrated in figure 1.1. In the thin-disk geometry, multipass amplifier schemes were scaled to an output power of 2 kW at 300 kHz, with pulses < 10 ps [10], and regenerative amplifier designs recently demonstrated 1 kW of average power at 5 kHz with 1.1-ps

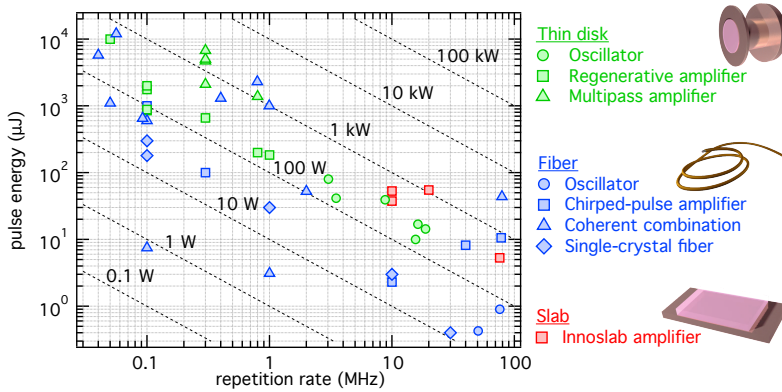


Figure 1.1 – Overview of the performance of high-power Yb-based ultrafast laser sources. The output pulse energy is shown against the repetition rate for the main high-power technologies: thin-disk, fiber and slab. References [10–48].

pulses [11]. In the fiber geometry, chirped-pulse amplification (CPA) in a single amplifier chain was used to demonstrate 830 W at a high repetition rate of 78 MHz with 640 fs pulses [12], and the coherent combination of 16 channels recently produced 1.8 kW at 800 kHz with a short pulse duration of 234 fs [13]. Finally in the slab geometry, average powers up to 1.1 kW were demonstrated at a repetition rate of 20 MHz and a pulse duration of 615 fs with the Innoslab technology [14].

An alternative approach relies on the development of high-power mod-locked oscillators, without external amplification. The leading technology for high-power ultrafast laser oscillators is the thin-disk technology, providing average powers of multi-hundred watts at MHz repetition rates (see figure 1.1, red circles). We recently demonstrated a thin-disk laser (TDL) delivering an average power of 350 W at a repetition rate of 8.9 MHz with 940-fs pulses, and further scaling to 500 W is expected in the near future [20]. Ultrafast TDLs have also demonstrated pulse energies up to 80 μJ at a repetition rate of 3.0 MHz with 1.1-ps pulses [17]. Besides a reduced footprint, these oscillators offer several advantages compared to amplifier systems, most notably a close to diffraction-limited beam quality ($M^2 < 1.1$), together with close to transform-limited, pedestal-free pulses and low-noise properties [49]. In this thesis, we focused on the develop-

ment of modelocked TDL oscillators, and particularly on the combination of high-peak powers and short pulse durations.

1.2 Ultrafast thin-disk lasers

1.2.1 The thin-disk laser concept

The thin-disk laser geometry was introduced in 1994 by Giesen et al. as a “scalable concept for diode-pumped high-power solid-state lasers” [50]. This concept relies on the use of a thin, disk-shaped gain medium with a typical thickness of $\approx 100 \mu\text{m}$, which is used in reflection as an active mirror inside the laser cavity.

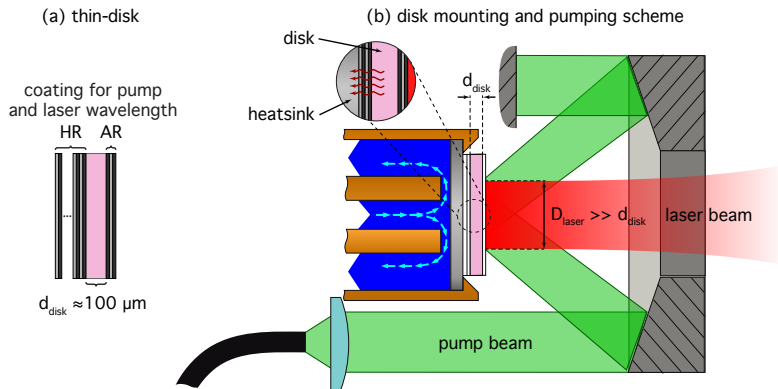


Figure 1.2 – Illustration of the thin-disk laser concept. (a) Illustration of the thin-disk-shaped gain material with high-reflection (HR) and anti-reflection (AR) coatings on the back and front face respectively. (b) Illustration of the thin-disk contacted onto a heatsink and mounted into a cooling finger. The small thickness of the disk compared to the pump and laser mode size allows for an efficient heat extraction with a quasi-one-dimensional heat flow. The multipass arrangement of the fiber-coupled pump beam is also depicted. Adapted from [51].

The back side of the disk has a high-reflection (HR) coating and is typically contacted onto a diamond heatsink, while the front side of the disk is anti-reflection (AR) coated (see figure 1.2(a)). The disk thickness ($\approx 100 \mu\text{m}$) is considerably smaller than the typical diameter of the inci-

dent pump and laser beams (few millimeters), resulting in a quasi-one-dimensional heat flow along the longitudinal direction (see figure 1.2(b)). The heat load is efficiently extracted through the back side of the disk via the water-cooled heatsink, leading to minimal thermal distortions even at high incident pump powers. Thanks to this advantageous geometry, power scaling TDLs is relatively straightforward by simultaneously increasing the pump and laser beam diameter on the disk, thus increasing the average power without changing the intensity on the gain medium. Additionally, the small interaction length between the intracavity laser beam and the gain medium is favorable for ultrafast operation, reducing the nonlinear phase accumulated in the disk.

The reduced length of the gain medium also results in a low single-pass absorption of the pump. In order to achieve an efficient pump absorption and laser operation, the disk is mounted inside a TDL head comprising a multipass arrangement for the pump beam on the disk, as illustrated in figure 1.2(b). The typical number of passes provided by commercially available TDL heads ranges from 18 to 72. Similarly, another consequence of the thin gain medium is the low single-pass gain for the laser light. In order to compensate for the reduced thickness, high Yb-doping concentrations are desirable, however a trade-off must be found with the decreasing thermal conductivity of the doped material and detrimental effects manifesting at high doping concentrations. A complementary approach consists in designing laser cavities including multiple passes of the intracavity beam on the disk in order to increase the available gain.

1.2.2 Passively modelocked thin-disk laser oscillators

1.2.2.1 Soliton modelocking

Ultrafast TDLs are typically modelocked in the soliton regime, where the pulse shaping results from the interplay of self-phase modulation (SPM) and group delay dispersion (GDD) [52, 53]. The correct balance of (positive) intracavity SPM and negative GDD leads to the formation of a *sech*²-shaped pulse with a full-width at half-maximum (FWHM) duration determined by soliton theory [54]:

$$\tau_p = 1.76 \cdot \left(-\frac{D_{rt}}{\varphi_{rt,sol}} \right)^{1/2} \quad (1.2)$$

where D_{rt} is the roundtrip GDD and $\varphi_{rt,sol}$ is the roundtrip soliton phase, i.e. the contribution of the roundtrip B-integral to the soliton pulse formation.

The roundtrip B-integral corresponds to the nonlinear phase accumulated over a roundtrip for the peak of the pulse in space and time and, assuming a Gaussian cavity mode, is calculated using:

$$B_{rt} = 2 \cdot \frac{2\pi}{\lambda} \int_0^{l_{cav}} n_2(z) \frac{P_{pk,ic}}{\frac{\pi}{2} w^2(z)} dz \quad (1.3)$$

where λ is the central wavelength of the pulse, $n_2(z)$ is the nonlinear refractive index at a position z inside the laser cavity, $P_{pk,ic}$ is the intracavity pulse peak power, $w(z)$ is the mode radius of the intracavity Gaussian beam and l_{cav} is the length of the laser cavity. The additional factor of two in equation (1.3) accounts for the linear geometry of the laser resonator.

For free-space propagation, the soliton phase is related to the B-integral via [55]:

$$\varphi_{sol,rt} = \frac{3}{4} \cdot B_{rt} = \gamma_{rt,sol} P_{pk,ic} \quad (1.4)$$

where we have introduced an effective roundtrip SPM coefficient $\gamma_{rt,sol}$ for soliton formation.

For a soliton pulse, with a *sech*² intensity profile, the pulse peak power is calculated as:

$$P_{pk} = 0.88 \cdot \frac{E_p}{\tau_p} \quad (1.5)$$

where E_p is the pulse energy and τ_p is the FWHM pulse duration.

Using equations (1.4) and (1.5), we can finally rewrite equation (1.2) as:

$$\tau_p = 1.76 \cdot \frac{2D_{rt}}{\gamma_{rt,sol} E_{p,ic}} \quad (1.6)$$

where $E_{p,ic}$ is the intracavity pulse energy.

Equation (1.6) highlights the fact that for a given configuration of a laser cavity, where the amount of intracavity nonlinearity and dispersion is fixed, the soliton pulse duration is expected to decrease inversely proportional to the intracavity pulse energy, independently of the modelocking device. The modelocking device will however play a role in the stability of the modelocked state.

In TDL oscillators, the main contributions to the roundtrip soliton phase are coming from the intracavity air and an optional Brewster plate (BP). The nonlinear phase accumulated in the disk is typically of order few milliradians and does not significantly impact the soliton shaping. The negative intracavity dispersion required for soliton shaping is usually introduced via Gires-Tournois interferometer (GTI)-type dispersive mirrors (DMs).

1.2.2.2 Modelocking techniques

Ultrafast TDLs rely on the process of soliton shaping to form a pulse in modelocked operation. However, the modelocked state has to be initiated and once it is established, stabilized against potential perturbations. This is achieved via a device or mechanism in the cavity that introduces an amplitude modulation, or loss modulation, favouring pulsed operation [56,57]. Two approaches are commonly used to achieve this in ultrafast TDLs.

Modelocking of TDL oscillators can be obtained by inserting a semiconductor saturable absorber mirror (SESAM) [58,59] in the laser cavity. As the name implies, the SESAM is a semiconductor structure consisting of a mirror and an absorber section. If the incident fluence, i.e. pulse energy per unit area, on the SESAM is sufficiently high, the absorber is saturated resulting in a higher reflectivity for an intense pulse than for cw light. This reflectivity modulation can be used to initiate and stabilize soliton modelocking [60]. The SESAM is categorized as a *slow* saturable absorber as the recovery dynamics of the reflectivity modulation is much longer than the supported pulse duration when combined with soliton pulse shaping [61]. The SESAM technology presents several key advantages:

- the saturation properties can be adjusted by the design of the absorber (semiconductor engineering),
- the SESAM can be directly inserted in the laser cavity operated close to the middle of the stability region,
- the SESAM provides self-starting modelocked operation [59], in particular at high repetition rates.

On the flip side, the SESAM offers a rather moderate loss modulation and a non-instantaneous response that can ultimately limit the minimum achievable pulse duration. The residual non-saturable losses also result in a heat load on the SESAM that needs to be evacuated in high-power operation to avoid thermal lensing effects [62]. However, the SESAM remains a very versatile and power-scalable technology used in state-of-the-art TDLs.

A second approach used to passively modelock TDLs is Kerr-lens modelocking (KLM) [63, 64], which relies on a combination of Kerr-lensing in an intracavity crystal, the Kerr medium (KM) (distinct from the gain medium in the case of TDLs), and a combination of soft and hard aperture effects induced by the resulting beam size variation on the gain medium and an intracavity hard aperture. The corresponding saturable loss modulation is used to initiate and sustain soliton modelocking [65]. KLM is categorized as a *fast* saturable absorber due to the instantaneous response of the Kerr effect [61]. In order to initiate modelocking, the laser cavity is often tuned to the edge of stability to achieve a high enough sensitivity to the Kerr lens in the KM. The KLM technique has several benefits:

- the loss modulation is large and instantaneous,
- KLM is intrinsically absorption-free, and does not result in any heat load,
- the technique can be applied to a broad wavelength range without technical restrictions.

The main drawback of KLM is the complexity of the cavity design, coupling the cavity stability to the pulse formation and stabilization. Additionally, modelocking is usually triggered by moving an intracavity mirror.

1.2.2.3 Modelocking stability

The desired regime of pulsed operation where a train of single pulses separated by the cavity roundtrip time is generated at the output of a modelocked laser is referred to as cw modelocking, or “clean” modelocking. This preferred state of operation is depicted in figure 1.3(a) and is usually achieved over a certain range of powers and pulse durations mostly depending on the characteristics of the gain and the saturable absorber.

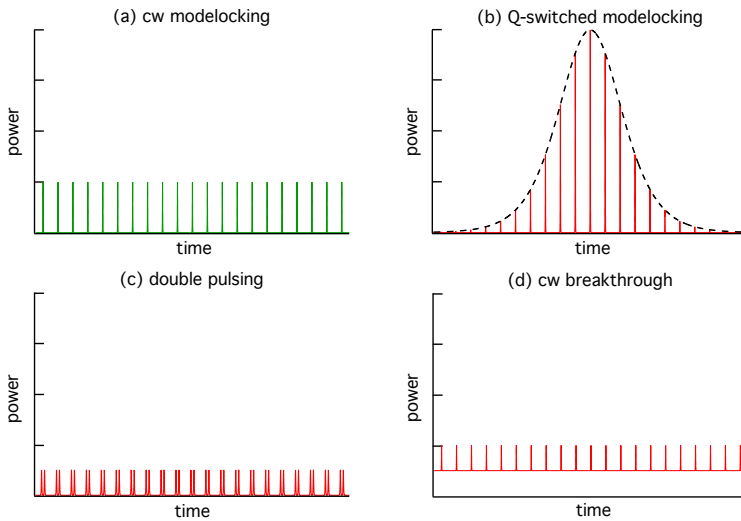


Figure 1.3 – Illustration of different modelocking states.

At the lower bound of this modelocking stability region, i.e. in the regime of low pulse energies and weak soliton shaping, the laser is likely to operate in the regime of Q-switched modelocking (QML) [66], depicted in figure 1.3(b). In this regime, the competition of gain and absorber saturation result in undamped, strong amplitude oscillations of the pulse train, typically in the kHz regime. The peak power of the modulated pulses can be significantly higher than in the cw modelocking regime and is likely to damage intracavity components. The QML regime can be mitigated by rollover effects, as for example inverse saturable absorption (ISA) [67, 68].

At the upper bound of the modelocking stability region, i.e. in the regime of strong saturation of the absorber and large soliton phase, the modelocked state can be destabilized by a break-up into multiple pulses or the build-up of a cw wave, as depicted in figure 1.3(c)-(d). Both of these effects are generally linked to an ISA effect reducing the strength of the absorber loss modulation and to the recovery dynamics of the absorber [60,67].

1.2.3 State of the art of ultrafast thin-disk lasers

The first modelocked TDL oscillator was demonstrated in the year 2000 using an Yb:yttrium aluminum garnet $\text{Y}_3\text{Al}_5\text{O}_{12}$ (YAG) disk and a SESAM as modelocking device [69]. This oscillator delivered 16.2 W of average power at a repetition rate of 34.6 MHz with 730-fs pulses and was at the time of publication already the most powerful oscillator in the sub-ps regime. Since this first demonstration, SESAM-modelocked TDLs based on Yb:YAG have constantly redefined the highest output power achievable from a laser oscillator. In our latest power scaling experiments, we demonstrated an Yb:YAG TDL delivering 350 W of average power at a repetition rate of 8.9 MHz with 940-fs pulses. Additionally, the highest pulse energy (80 μJ) and peak power (66 MW) generated by a laser oscillator were obtained with a SESAM-modelocked Yb:YAG TDL [17]. Kerr-lens modelocking of a TDL was also first demonstrated with Yb:YAG, and was successfully scaled to 270 W of average power at a repetition rate of 18.8 MHz and a pulse duration of 330 fs [18]. Most notably, a KLM Yb:YAG TDL delivered an average power of 155 W at 15.6 MHz, combined with short pulses of 140 fs and a corresponding peak power of 62 MW [19]. This remains to date one of the few TDL results combining a high-peak power with short pulse durations, as shown in our overview graphs in figure 1.4(b)-(c).

Although Yb:YAG is without a doubt the material of choice for high-power TDL oscillators, alternative gain materials providing a broader gain bandwidth have been extensively investigated in the search to combine high average powers with short pulse durations. The thin-disk technology is comparatively demanding in terms of thermo-mechanical properties

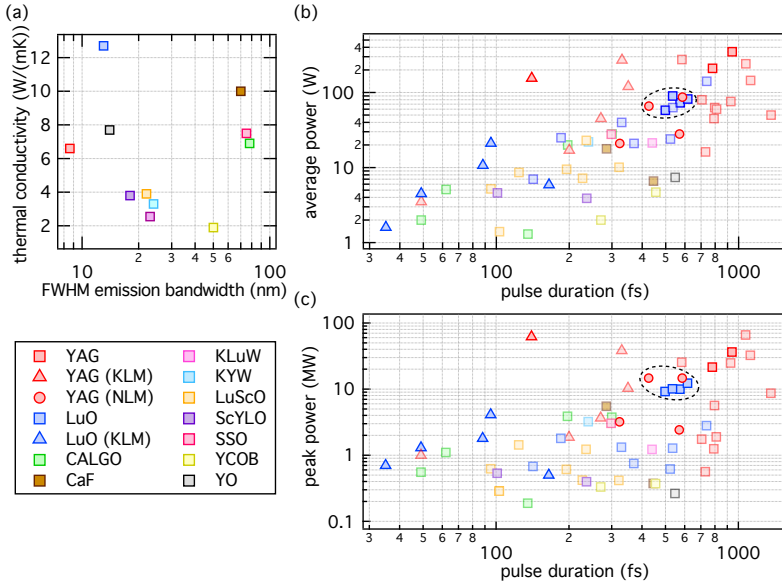


Figure 1.4 – Overview of the performance of modelocked TDL oscillators based on different gain materials and modelocking techniques. (a) Thermal conductivity and FWHM emission bandwidth of different Yb-doped materials tested in the thin-disk geometry. **(b)-(c)** Overview of the output performance of ultrafast TDLs in terms of pulse duration, average power and peak power. The marker shapes indicate the modelocking technique: SESAM modelocking (square), KLM (triangle) and NLM modelocking (circle). The points shown with a higher transparency are results demonstrated before the beginning of this thesis (September 2015). The results presented in this thesis are encircled in black. References [15–20, 69–106].

and crystal quality of the gain materials. The preparation of the disk (polishing, coating, contacting onto the heatsink) requires a certain hardness, elasticity and surface quality of the used material in order to be successful. The crystal quality must be homogeneous over a comparatively large area ($\approx 1 \text{ cm}^2$) and an isotropic crystal with a high thermal conductivity is desirable to reduce thermal effects under high pump powers. Additionally, these properties and the crystal quality should ideally be conserved at high doping concentrations. In figure 1.4(a), we show the thermal conductivity and FWHM emission bandwidth of Yb-doped materials tested in the thin-disk geometry. Promising first results have been demonstrated with many of these broadband materials and the range of pulse dura-

tion achievable with TDLs was significantly extended towards short pulses down to sub-100 fs (see figure 1.4). However the output power remained limited (≤ 30 W), as well as the output peak power (≤ 4 MW), and power scaling to the 100-W regime and beyond is restricted by a combination of unfavorable material properties and growth quality [99, 104, 107, 108].

A material standing out as particularly promising for the combination of high-average powers and short pulse durations is Yb-doped lutetium oxide Lu_2O_3 (LuO) (also called lutetia), due to its excellent thermal conductivity (almost twice that of Yb:YAG, see figure 1.4(a)) and high crystal quality combined with a FWHM emission bandwidth of 13 nm. In particular, Yb:LuO is the only material besides Yb:YAG that was modelocked at average powers exceeding 100 W [83]. Recently, KLM of Yb:LuO TDL oscillators also demonstrated promising results with an average power of 21 W in 95 fs pulses and a peak power of 4 MW [90]. We will present our results in peak-power scaling Yb:LuO TDLs to the 10 MW regime in chapter 2 of this thesis.

Finally, amongst the broadband materials investigated in the thin-disk geometry, Yb-doped calcium gadolinium aluminum oxide CaGdAlO_4 (CALGO) currently represents the best candidate for ultrashort pulse generation well below 100 fs. Using SESAM-modelocking, pulses as short as 49 fs were demonstrated at an average power of 2 W [93], and 62-fs pulses were generated at an average power of 5 W [92]. In the first successful KLM experiments with an Yb:CALGO TDL, record-short pulses of 30 fs were demonstrated, however at a very low output power of 150 mW [109] (not appearing in figure 1.4(b)-(c)).

In this thesis, we will focus on TDLs based on the three materials highlighted in this overview: Yb:YAG as the state-of-the-art gain material for high-power laser operation, Yb:LuO as an alternative to Yb:YAG with the added benefit of a broader emission bandwidth, and finally Yb:CALGO as the best candidate for ultrashort pulse generation.

1.3 Outline of this thesis

Ultrafast TDLs are attractive laser sources for driving nonlinear frequency conversion experiments to the XUV or THz spectral region. The involved nonlinear processes ideally require a combination of high peak powers and short pulse durations. The current state-of-the-art of ultrafast TDLs however shows a clear trade-off between output (peak) power and pulse duration as illustrated in figure 1.4(b)-(c).

In this thesis, we investigated the modelocking limitations when targeting high peak powers and short pulse durations, in particular in the case of SESAM modelocking, and we explored novel approaches to circumvent the identified limitations.

In **chapter 2**, we present our peak-power scaling experiments using the gain material Yb:LuO. We demonstrate peak powers in excess of 10 MW for the first time using this material, with pulse durations close to 500 fs, significantly shorter than usually achieved with Yb:YAG at these peak power levels. Additionally, we present an in-depth study of the effect of the finite gain bandwidth and SESAM rollover on the modelocking performance.

In **chapter 3**, we describe a numerical model derived from the study presented in chapter 2 and use it to investigate the loss modulation depth requirements for supporting high-peak-power modelocking at short pulse durations. In particular, we investigate the SESAM modulation depth required to modelock a 100-W, 200-fs TDL at 10 MHz depending on the gain material. We show that this goal is difficult to achieve using Yb:YAG or Yb:LuO with the current SESAM technology and that Yb:CALGO or different approaches have to be used to reach this targeted performance.

Following these conclusions, we present our work on TDL oscillators based on Yb:CALGO and discuss the associated challenges in **chapter 4**, and describe our investigations of novel approaches to improve the peak-power and pulse-duration performance of TDLs in **chapters 5 to 7**.

In **chapter 5**, we analyse the two-photon absorption contributions within typical SESAM structures. We propose a reduction of this detri-

mental effect by replacing the semiconductor mirror with a dielectric mirror and show the characterization of our first samples.

In **chapter 6**, we investigate a scheme to compensate the limited gain bandwidth by using an intracavity spectral filter. We use a mirror with a spectrally dependent reflectivity profile mirroring the gain spectrum of the disk, thus obtaining a flattened roundtrip gain spectrum. We discuss the design of such a mirror and show our first modelocking results with Yb:LuO and Yb:YAG.

In **chapter 7**, we present an alternative modelocking technique using a nonlinear mirror. This device provides a large and fast loss modulation, promising for the generation of short pulses. We apply this technique to modelock a TDL for the first time and obtain pulse durations close to 300 fs with Yb:YAG, comparable to pulse durations achieved with KLM. We further report our first power scaling of this modelocking technique to peak powers close to 15 MW and present guidelines to avoid Q-switching instabilities.

Finally, we conclude and give an outlook to future power scaling of TDLs at short pulse durations in **chapter 8**.

Parts of the results presented in **chapters 2** and **7** are given in the form of manuscripts published, or accepted for publication in peer-reviewed journals.

Peak-power scaling Yb:LuO thin-disk lasers

2.1 A promising material for high peak-power operation

As mentioned in chapter 1, nonlinear frequency conversion experiments, and in particular HHG, benefit from a combination of high peak-power and short pulse durations. High peak-powers up to 66 MW have been demonstrated in SESAM-modelocked TDLs based on the gain material Yb:YAG, however at a pulse duration >1 ps [17]. In order to generate energetic short pulses with a high peak-power, it is beneficial to use a gain material combining:

- a high thermal conductivity and crystal quality for high-power laser operation,
- a large gain bandwidth supporting short pulse durations.

The gain material Yb:LuO is one of the most promising candidates for this purpose due to its high thermal conductivity and broader emission bandwidth than Yb:YAG. Although the crystal growth of Yb:LuO is challenging due to the high melting point of lutetium oxide ($>2400^{\circ}\text{C}$), high-quality crystals with sufficiently large areas for use in thin-disk lasers can be achieved using the heat exchanger method (HEM) [110]. The availability of high-quality Yb:LuO disks however remains limited.

A key property of Yb:LuO is its high thermal conductivity of ≈ 12 W/(m·K) [111]. This value is almost twice as high as for the well-established gain material Yb:YAG (see figure 1.4(a) in chapter 1). More-

over, while most host crystals experience a decrease of their thermal conductivity with increasing doping concentrations, the thermal conductivity of Yb:LuO stays comparatively constant with Yb-concentrations up to $15 \cdot 10^{20} \text{ cm}^{-3}$ (5.3 at.%) [111], as illustrated in figure 2.1. Additionally, Yb:LuO can be pumped in the zero-phonon line (ZPL) at 976 nm using volume Bragg grating (VBG)-stabilized diodes, leading to a reduced quantum defect and heat load on the laser crystal. These two aspects make Yb:LuO particularly suited for high-power laser operation. Finally, the emission bandwidth of Yb:LuO supports sub-200 fs pulse durations (13 nm FWHM), making it a promising material for combining high-power modelocked operation with short pulse durations.

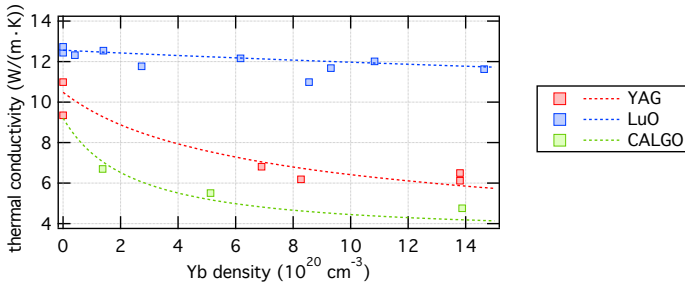


Figure 2.1 – Dependence of the thermal conductivity of typical host materials on the Yb-doping concentration. The symbols represent measured values and the dashed lines the corresponding fits for Yb densities from 0 to $15 \cdot 10^{20} \text{ cm}^{-3}$, corresponding to Yb(10.9 at.):YAG, Yb(5.3 at.):LuO and Yb(12 at.):CALGO. Adapted from [111,112].

The first TDL based on Yb:LuO was demonstrated in 2007 and delivered 20.5 W with 370 fs pulses at a repetition rate of 65 MHz [81]. With slightly longer pulses, an exceptionally high optical-to-optical efficiency of 43% was achieved, confirming the potential of Yb:LuO for further high-power modelocking experiments. The power scaling of Yb:LuO TDLs was very successful and led to a new record average power of 141 W at the time of publication in 2010 [83]. For this record performance, the pulse duration was significantly longer (738 fs) and the repetition rate remained similar to the first demonstration (60 MHz). The suitability of Yb:LuO for the generation of short pulses was later confirmed in 2012 with a TDL os-

cillator delivering 7 W of average power with 142 fs pulses at a repetition rate of 64 MHz [84]. This oscillator notably allowed for the first measurement of the carrier-envelope offset (CEO) frequency of an ultrafast TDL.

These earlier results were based on comparatively short laser resonator designs, resulting in a high repetition rate ≥ 60 MHz and consequently low peak powers < 3 MW. The oscillators were operated in ambient air and based on rather thick Yb:LuO disks (≥ 150 μm). The laser performance was partially limited by thermal effects in the disk due to a combination of suboptimal disk quality, comparatively large disk thickness and reduced heat extraction by copper heatsinks [83, 113].

For our peak-power scaling experiments, we implemented several key changes to improve the peak power compared to these earlier results:

1. we used a 110- μm thin-disk with excellent crystal quality and contacted on a diamond heatsink, resulting in minimal thermal lensing,
2. we designed our laser resonator to include two reflections of the intracavity beam on the disk in order to increase the transmission of the output coupler (OC) mirror and keep the intracavity power reasonably low,
3. we extended the cavity length by implementing telescope extensions in order to lower the repetition rate and consequently increase the pulse energy,
4. we carefully positioned the intracavity components (HR mirrors and DMs) in order to avoid potential damage due to the high peak intensities,
5. we operated the laser in a pressure-controlled environment to reduce the nonlinear phase contribution from the ambient air and the number of DMs required for soliton pulse shaping.

These improvements allowed us to demonstrate an Yb:LuO TDL generating peak powers exceeding 10 MW for the first time. In a first step, we designed the laser cavity to have a single reflection on the disk and obtained 73 W of average power with 573 fs pulses at a repetition rate of 11.2 MHz [114], reaching a peak power of 10.0 MW. In a second step, we implemented an additional reflection of the intracavity beam on the disk and obtained 82 W with 616 fs pulses at a repetition rate of 9.5 MHz [87],

resulting in a pulse energy of 8.6 μJ and a peak power of 12.3 MW. With this result we demonstrated the highest pulse energy and peak power generated from an Yb:LuO TDL to date.

Additionally, we developed a numerical model in order to investigate and quantify the influence of the limited gain bandwidth and SESAM rollover on the laser performance. By comparing the numerical results with our experimental data, we could derive a criterion for the maximum pulse energy before the onset of modelocking instabilities based on the gain advantage for pulsed operation over the cw regime.

2.2 Publication

The design and performance of our Yb:LuO TDL oscillator, together with the study of modelocking limitations, are presented in details in the following publication.

Title: "Peak-power scaling of femtosecond Yb:Lu₂O₃ thin-disk lasers", [87]

Journal: *Optics Express*

doi: 10.1364/OE.25.022519

URL: <https://doi.org/10.1364/OE.25.022519>

Published: September 7th, 2017

©2017 Optical Society of America. One print or electronic copy may be made for personal use only. Systematic reproduction and distribution, duplication of any material in this paper for a fee or for commercial purposes, or modifications of the content of this paper are prohibited.

Peak-power scaling of femtosecond Yb:Lu₂O₃ thin-disk lasers

I. J. GRAUMANN,^{*1} A. DIEBOLD,¹ C. G. E. ALFIERI,¹
 F. EMAURY,¹ B. DEPPE,^{2,3} M. GOLLING,¹ D. BAUER,⁴ D. SUTTER,⁴
 C. KRÄNKEL,^{2,5} C. J. SARACENO,¹ C. R. PHILLIPS,¹ AND U. KELLER¹

1. *Ultrafast Laser Physics, Institute for Quantum Electronics, ETH Zurich, 8093 Zurich, Switzerland*

2. *Institut für Laser-Physik, Universität Hamburg, Luruper Chaussee 149, 22761 Hamburg, Germany*

3. *The Hamburg Center for Ultrafast Imaging, Universität Hamburg, Luruper Chaussee 149, 22761 Hamburg, Germany*

4. *TRUMPF Laser GmbH, 78713 Schramberg, Germany*

5. *Center for Laser Materials, Leibniz Institute for Crystal Growth, Max-Born-Str. 2, 12489 Berlin, Germany*

**ivangr@phys.ethz.ch*

Abstract:

We present a high-peak-power SESAM-modelocked thin-disk laser (TDL) based on the gain material Yb-doped lutetia (Yb:Lu₂O₃), which exceeds a peak-power of 10 MW for the first time. We generate pulses as short as 534 fs with an average power of 90 W and a peak power of 10.1 MW, and in addition a peak power as high as 12.3 MW with 616-fs pulses and 82-W average power. The center lasing wavelength is 1033 nm and the pulse repetition rates are around 10 MHz. We discuss and explain the current limitations with numerical models, which show that the current peak power is limited in soliton modelocking by the interplay of the gain bandwidth and the induced absorption in the SESAM with subsequent thermal lensing effects. We use our numerical model which is validated by the current experimental results to discuss a possible road map to scale the peak power into the 100-MW regime and at the same time reduce the pulse duration further to sub-200 fs. We consider Yb:Lu₂O₃ as currently the most promising gain material for the combination of high peak power and short pulse duration in the thin-disk-laser geometry.

© 2017 Optical Society of America

OCIS codes: (140.3615) Lasers, ytterbium; (140.4050) Mode-locked lasers; (320.7090) Ultrafast lasers.

References and links

1. U. Keller, "Recent developments in compact ultrafast lasers," *Nature* **424**, 831-838 (2003).
2. K. Sugioka and Y. Cheng, "Ultrafast lasers - reliable tools for advanced materials processing," *Light. Sci. Appl.* **3**, e149 (2014).
3. W. Sibbett, A. A. Lagatsky, and C. T. A. Brown, "The development and application of femtosecond laser systems," *Opt. Express* **20**, 6989-7001 (2012).
4. T. Südmeyer, S. V. Marchese, S. Hashimoto, C. R. E. Baer, G. Gingras, B. Witzel, and U. Keller, "Femtosecond laser oscillators for high-field science," *Nature Photonics* **2**, 599-604 (2008).
5. J.-P. Negel, A. Loeschner, A. Voss, D. Bauer, D. Sutter, A. Killi, M. A. Ahmed, and T. Graf, "Ultrafast thin-disk multipass laser amplifier delivering 1.4 kW (4.7 mJ, 1030 nm) average power converted to 820 W at 515 nm and 234 W at 343 nm," *Opt. Express* **23**, 21064-21077 (2015).
6. M. Müller, M. Kienel, A. Klenke, T. Gottschall, E. Shestakov, M. Plötner, J. Limpert, and A. Tünnermann, "1 kW 1 mJ eight-channel ultrafast fiber laser," *Opt. Lett.* **41**, 3439-3442 (2016).
7. P. Russbüldt, T. Mans, J. Weitenberg, H. D. Hoffmann, and R. Poprawe, "Compact diode-pumped 1.1 kW Yb:YAG Innoslab femtosecond amplifier," *Opt. Lett.* **34**, 4169-4171 (2010).
8. J. Aus der Au, G. J. Spühler, T. Südmeyer, R. Paschotta, R. Hövel, M. Moser, S. Erhard, M. Karszewski, A. Giesen, and U. Keller, "16.2 W average power from a diode-pumped femtosecond Yb:YAG thin disk laser," *Opt. Lett.* **25**, 859-861 (2000).
9. C. J. Saraceno, F. Emaury, O. H. Heckl, C. R. E. Baer, M. Hoffmann, C. Schriber, M. Golling, T. Südmeyer, and U. Keller, "275 W average output power from a femtosecond thin disk oscillator operated in a vacuum environment," *Opt. Express* **20**, 23535-23541 (2012).
10. C. J. Saraceno, F. Emaury, C. Schriber, M. Hoffmann, M. Golling, T. Südmeyer, and U. Keller, "Ultrafast thin-disk laser with 80 μJ pulse energy and 242 W of average power," *Opt. Lett.* **39**, 9-12 (2014).

11. A. Giesen, H. Hügel, A. Voss, K. Wittig, U. Brauch, and H. Opower, "Scalable Concept for Diode-Pumped High-Power Solid-State Lasers," *Appl. Phys. B* **58**, 365-372 (1994).
12. U. Keller, K. J. Weingarten, F. X. Kärtner, D. Kopf, B. Braun, I. D. Jung, R. Fluck, C. Hönninger, N. Matuschek, and J. Aus der Au, "Semiconductor saturable absorber mirrors (SESAMs) for femtosecond to nanosecond pulse generation in solid-state lasers," *IEEE J. Sel. Top. Quantum Electron.* **2**, 435-453 (1996).
13. C. M. Heyl, C. L. Arnold, A. Couairon, and A. L'Huillier, "Introduction to macroscopic power scaling principles for high-order harmonic generation," *Journal of Physics B Atomic Molecular and Optical Physics* **50**(2017).
14. F. Emaury, A. Diebold, C. J. Saraceno, and U. Keller, "Compact XUV Source at Megahertz Pulse Repetition Rate with a Low-Noise Ultrafast Thin Disk Oscillator," *Optica* **23**, 980-984 (2015).
15. F. Emaury, C. J. Saraceno, B. Debord, D. Ghosh, A. Diebold, F. Gérôme, T. Südmeyer, F. Benabid, and U. Keller, "Efficient spectral broadening in the 100-W average power regime using gas-filled kagome HC-PCF and pulse compression," *Opt. Lett.* **39**, 6843-6846 (2014).
16. J. Schulte, T. Sartorius, J. Weitenberg, A. Vernaleken, and P. Russbüldt, "Nonlinear pulse compression in a multi-pass cell," *Opt. Lett.* **41**, 4511-4514 (2016).
17. S. Hädrich, M. Kienel, M. Müller, A. Klenke, J. Rothhardt, R. Klas, T. Gottschall, T. Eidam, A. Drozdy, P. Jöjárt, Z. Várallyay, E. Cormier, K. Osvay, A. Tünnermann, and J. Limpert, "Energetic sub-2-cycle laser with 216 W average power," *Opt. Lett.* **41**, 4332-4335 (2016).
18. D. E. Spence, P. N. Kean, and W. Sibbett, "60-fsec pulse generation from a self-mode-locked Ti:sapphire laser," *Opt. Lett.* **16**, 42-44 (1991).
19. J. Brons, V. Pervak, E. Fedulova, D. Bauer, D. Sutter, V. Kalashnikov, A. Apolonskiy, O. Pronin, and F. Krausz, "Energy scaling of Kerr-lens mode-locked thin-disk oscillators," *Opt. Lett.* **39**, 6442-6445 (2014).
20. J. Brons, V. Pervak, D. Bauer, D. Sutter, O. Pronin, and F. Krausz, "Powerful 100-fs-scale Kerr-lens mode-locked thin-disk oscillator," *Opt. Lett.* **41**, 3567-3570 (2016).
21. K. Beil, S. T. Fredrich-Thornton, F. Tellkamp, R. Peters, C. Kränkel, K. Petermann, and G. Huber, "Thermal and laser properties of Yb:LuAG for kW thin disk lasers," *Opt. Express* **18**, 20712-20722 (2010).
22. T. Südmeyer, C. Kränkel, C. R. E. Baer, O. H. Heckl, C. J. Saraceno, M. Golling, R. Peters, K. Petermann, G. Huber, and U. Keller, "High-power ultrafast thin disk laser oscillators and their potential for sub-100-femtosecond pulse generation," *Appl. Phys. B* **97**, 281-295 (2009).
23. F. Brunner, T. Südmeyer, E. Innerhofer, R. Paschotta, F. Morier-Genoud, J. Gao, K. Contag, A. Giesen, V. E. Kisel, V. G. Shcherbitsky, N. V. Kuleshov, and U. Keller, "240-fs pulses with 22-W average power from a mode-locked thin-disk Yb:KY(WO₄)₂ laser," *Opt. Lett.* **27**, 1162-1164 (2002).
24. O. H. Heckl, C. Kränkel, C. R. E. Baer, C. J. Saraceno, T. Südmeyer, K. Petermann, G. Huber, and U. Keller, "Continuous-wave and modelocked Yb:YCOB thin disk laser: first demonstration and future prospects," *Opt. Express* **18**, 19201-19208 (2010).
25. C. J. Saraceno, O. H. Heckl, C. R. E. Baer, C. Schriber, M. Golling, K. Beil, C. Kränkel, T. Südmeyer, G. Huber, and U. Keller, "Sub-100 femtosecond pulses from a SESAM modelocked thin disk laser," *Appl. Phys. B* **106**, 559-562 (2012).
26. C. Schriber, L. Merceron, A. Diebold, F. Emaury, M. Golling, K. Beil, C. Kränkel, C. J. Saraceno, T. Südmeyer, and U. Keller, "Pushing SESAM modelocked thin-disk lasers to shortest pulse durations," in *Advanced Solid State Lasers*, OSA Technical Digest (online) (Optical Society of America, 2014), AF1A.4.
27. C. Kränkel, "Rare-earth doped sesquioxides for diode-pumped high power lasers in the 1-, 2-, and 3- μ m spectral range," *IEEE J. Sel. Top. Quant.* **21**(2015).
28. R. Peters, C. Kränkel, S. T. Fredrich-Thornton, K. Beil, O. H. Heckl, C. R. E. Baer, C. J. Saraceno, T. Südmeyer, U. Keller, K. Petermann, and G. Huber, "Thermal analysis and efficient high power continuous-wave and mode-locked thin disk laser operation of Yb-doped sesquioxides," *Appl. Phys. B-Lasers Opt.* **102**, 509-514 (2011).
29. P. A. Loiko, K. V. Yumashev, R. Schödel, M. Peltz, C. Liebal, X. Mateos, B. Deppe, and C. Kränkel, "Thermo-optic properties of Yb:Lu₂O₃ single crystals," *Appl. Phys. B* **120**, 601-607 (2015).
30. R. Wynne, J. L. Daneu, and T. Y. Fan, "Thermal coefficients of the expansion and refractive index in YAG," *Appl. Optics* **38**, 3282-3284 (1999).
31. R. Peters, C. Kränkel, K. Petermann, and G. Huber, "Broadly tunable high-power Yb:Lu₂O₃ thin disk laser with 80% slope efficiency," *Opt. Express* **15**, 7075-7082 (2007).
32. C. R. E. Baer, C. Kränkel, C. J. Saraceno, O. H. Heckl, M. Golling, R. Peters, K. Petermann, T. Südmeyer, G. Huber, and U. Keller, "Femtosecond thin disk laser with 141 W of average power," *Opt. Lett.* **35**, 2302-2304 (2010).
33. C. J. Saraceno, S. Pekarek, O. H. Heckl, C. R. E. Baer, S. C., K. Beil, C. Kränkel, H. G., U. Keller, and T. Südmeyer, "Self-referenceable frequency comb from an ultrafast thin disk laser," *Opt. Express* **20**, 9650-9656 (2012).
34. C. J. Saraceno, C. Schriber, O. H. Heckl, C. R. E. Baer, M. Golling, K. Beil, C. Kränkel, S. T., G. Huber, and U. Keller, "25 W, 185 fs Pulses from an Yb:Lu₂O₃ Modelocked Thin Disk Laser," in *Europhoton 2012—5th EPS-QEOD Europhoton Conference*, (2012),
35. C. R. E. Baer, O. H. Heckl, C. J. Saraceno, C. Schriber, C. Kränkel, T. Südmeyer, and U. Keller, "Frontiers in passively mode-locked high-power thin disk laser oscillators," *Opt. Express* **20**, 7054-7065 (2012).

36. B. Kreipe, J. Andrade, B. Deppe, C. Kränkel, and U. Morgner, "Kerr-lens mode-locked Yb³⁺:Lu₂O₃ thin-disk laser," in *Conference on Lasers and Electro-Optics, OSA Technical Digest (2016) (Optical Society of America, 2016)*, paper SM11.4.
37. C. Paradis, N. Modsching, V. J. Wittwer, B. Deppe, C. Kränkel, and T. Südmeyer, "Generation of 35-fs pulses from a Kerr lens mode-locked Yb:Lu₂O₃ thin-disk laser," *Opt. Express* **25**, 14918-14925 (2017).
38. V. Peters, A. Bolz, K. Petermann, and G. Huber, "Growth of high-melting sesquioxides by the heat exchanger method," *J. Cryst. Growth* **237-239**, 879-883 (2002).
39. J. Neuhaus, J. Kleinbauer, A. Killi, S. Weiler, D. Sutter, and T. Dekorsy, "Passively mode-locked Yb:YAG thin-disk laser with pulse energies exceeding 13 μ J by use of an active multipass geometry," *Opt. Lett.* **33**, 726-728 (2008).
40. V. Magni, "Multielement stable resonators containing a variable lens," *J. Opt. Soc. Am. A* **4**, 1962-1969 (1987).
41. C. J. Saraceno, O. H. Heckl, C. R. E. Baer, M. Golling, T. Südmeyer, K. Beil, C. Kränkel, K. Petermann, G. Huber, and U. Keller, "High damage threshold SESAMs for high power femtosecond modelocking: 23 W, 235 fs Yb:LuScO₃ thin-disk laser," *CLEO Europe 2011* (2011).
42. C. J. Saraceno, F. Emaury, C. Schriber, A. Diebold, M. Hoffmann, M. Golling, T. Südmeyer, and U. Keller, "Toward millijoule-level high-power ultrafast thin-disk oscillators," *IEEE J. Sel. Top. Quant.* **1**, 1100318 (2015).
43. A. Diebold, F. Emaury, C. J. Saraceno, C. Schriber, M. Golling, T. Südmeyer, and U. Keller, "SESAM mode-locked Yb:CaGdAlO₄ thin disk laser with 62 fs pulse generation," *Opt. Lett.* **38**, 3842-3845 (2013).
44. R. Grange, M. Haiml, R. Paschotta, G. J. Spühler, L. Krainer, M. Golling, O. Ostinelli, and U. Keller, "New regime of inverse saturable absorption for self-stabilizing passively mode-locked lasers," *Appl. Phys. B* **80**, 151-158 (2005).
45. T. R. Schibli, E. R. Thoen, F. X. Kärtner, and E. P. Ippen, "Suppression of Q-switched mode locking and break-up into multiple pulses by inverse saturable absorption," *Appl. Phys. B* **70**, S41-S49 (2000).
46. M. Haiml, R. Grange, and U. Keller, "Optical characterization of semiconductor saturable absorbers," *Appl. Phys. B* **79**, 331-339 (2004).
47. R. Peters, "Ytterbium-dotierte Sesquioxide als hocheffiziente Lasermaterialien," PhD-Thesis (Universität Hamburg, Germany, 2009).
48. R. Paschotta, J. Aus der Au, G. J. Spühler, S. Erhard, A. Giesen, and U. Keller, "Passive mode locking of thin disk lasers: effects of spatial hole burning," *Appl. Phys. B* **72**, 267-278 (2001).
49. C. G. E. Alfieri, D. Waldburger, S. M. Link, E. Gini, M. Golling, G. Eisenstein, and U. Keller, "Optical efficiency and gain dynamics of modelocked semiconductor disk lasers," *Opt. Express* **25**, 6402-6420 (2017).
50. B. C. Stuart, M. D. Feit, A. M. Rubenchik, B. W. Shore, and M. D. Perry, "Laser-Induced Damage in Dielectrics with Nanosecond to Subpicosecond Pulses," *Phys. Rev. Lett.* **74**, 2248-2251 (1995).
51. C. G. E. Alfieri, A. Diebold, F. Emaury, E. Gini, C. J. Saraceno, and U. Keller, "Improved SESAMs for femtosecond pulse generation approaching the kW average power regime," *Opt. Express* **24**, 27587-27599 (2016).
52. A. Diebold, T. Zengerle, C. G. E. Alfieri, C. Schriber, F. Emaury, M. Mangold, M. Hoffmann, C. J. Saraceno, M. Golling, D. Follman, G. D. Cole, M. Aspelmeyer, T. Südmeyer, and U. Keller, "Optimized SESAMs for kilowatt-level ultrafast lasers " *Opt. Express* **24**, 10512-10526 (2016).

1. Introduction

Ultrafast laser sources are the workhorse of a variety of scientific and industrial applications. The diversity of available technologies and attractive performance of these table-top systems can be deployed in fundamental research experiments, new medical procedures, or high-precision micro-machining [1-3]. High-power ultrafast laser systems delivering intense infrared laser pulses are of particular interest for efficient frequency conversion up to the extreme-ultraviolet (XUV) spectral region via high-harmonic generation (HHG). The high repetition rate and high photon flux achievable through this approach can significantly reduce the acquisition time and improve the signal-to-noise ratio (SNR) of attosecond experiments [4].

The state-of-the-art of high-power ultrafast laser sources is demonstrated by amplifier systems based on the thin-disk, fiber or Innoslab technology, reaching kW-level average powers with peak powers exceeding the GW level [5-7]. However, the impressive performance of these laser amplifier systems comes at the cost of a high system complexity and, in some cases, non-diffraction-limited beam quality. Modelocked thin-disk laser oscillators are an attractive alternative to the complex amplifier systems and combine high output power and high peak power in a compact table-top MHz oscillator with excellent beam quality. Passive

modelocking of a diode-pumped thin-disk laser (TDL) was demonstrated for the first time in 2000 [8] and currently represents the state-of-the-art of sub-picosecond ultrafast oscillators, reaching average output powers up to 275 W (583 fs) [9], pulse energies up to 80 μJ (1.1 ps) [10] and peak powers up to 66 MW [10] [Fig. 1(a)]. The power scalability of the thin-disk geometry [11] and SESAM modelocking [12], combined with the continuous improvement of the thin-disk crystal quality and contacting technique, opens prospects of kW-level modelocked TDLs at picosecond pulse durations. However, shorter pulse durations are important for efficient HHG [13, 14]. Several nonlinear compression techniques have been demonstrated at high average and peak-power to shorten the pulse duration [14-17]. Nevertheless, since only limited compression factors can be achieved in these schemes, short pulses directly out of the laser oscillator are needed to reach few-cycle pulses after a single compression stage.

Reducing the pulse duration of modelocked TDLs is therefore an ongoing challenge. Kerr-lens modelocked (KLM) [18] thin-disk oscillators have approached a similar 270-W average power as SESAM-modelocked TDLs with the advantage of a shorter 330-fs pulse duration, as expected from a faster saturable absorber [19]. Even shorter pulses of 140 fs were achieved with 155 W of average power and a peak power of 62 MW [20]. However, KLM comes with a severe trade-off because the fast saturable absorber requires a strong coupling between resonator design and soliton pulse formation, and pushes the laser cavity to the edge of its stability regime. Thus, KLM lasers have had a limited impact for industrial lasers as they are highly alignment-sensitive and less flexible to operating over a wide range of output parameters than SESAM-modelocked lasers. In particular, energy scaling to $>15 \mu\text{J}$ remains to be demonstrated.

To date, the power scaling of modelocked TDLs has relied extensively on the high-quality gain material Yb:YAG, benefiting from its mature growth technology and wide availability. Yet, high-power SESAM-modelocked Yb:YAG TDLs are operating at pulse durations >500 fs mainly due to the limited gain bandwidth of Yb:YAG (8 nm full-width at half maximum (FWHM), [21]). Alternative broadband gain materials suitable for the thin-disk geometry are actively pursued in order to access the high-power sub-100-fs regime directly from the oscillator [Figs. 1(a) and 1(b)] [22]. Early investigations of short-pulsed SESAM-modelocked TDLs based on Yb-doped tungstate or borate materials demonstrated pulse durations <300 fs at power levels up to 22 W [23, 24]. First sub-100-fs modelocking was then achieved with Yb:LuScO₃, a material from the cubic sesquioxides family, with 5 W of average power and 96-fs pulses [25]. In recent years, the ultra-broadband gain material Yb:CALGO (Yb:CaGdAlO₄), allowed for even shorter pulse durations but at the expense of average output power, i.e. as short as 49 fs at 2-W average power [26].

Amongst these broadband materials, the Yb-doped sesquioxide lutetia Yb:Lu₂O₃ (Yb:LuO) is potentially an ideal candidate material to combine high average powers comparable to Yb:YAG but at significantly shorter pulse durations. This cubic material benefits from excellent thermal properties, with a thermal conductivity close to twice that of Yb:YAG at typical doping concentrations ($\kappa_{\text{LuO}} = 12 \text{ W}/(\text{m}\cdot\text{K})$ and $\kappa_{\text{YAG}} = 7 \text{ W}/(\text{m}\cdot\text{K})$ for an Yb doping density of $8 \cdot 10^{20} \text{ cm}^{-3}$ [27, 28]), and a broad emission bandwidth supporting sub-100-fs pulses [12.5 nm FWHM, [27], see Fig. 1(b)]. Furthermore, Yb:LuO has smaller thermo-optic and thermal expansion coefficients than Yb:YAG [29, 30]. These advantageous properties, together with demonstrated slope efficiencies $>80\%$ [31], make Yb:LuO an attractive candidate for high-power ultrashort-pulsed laser operation.

2. PEAK-POWER SCALING Yb:LuO THIN-DISK LASERS

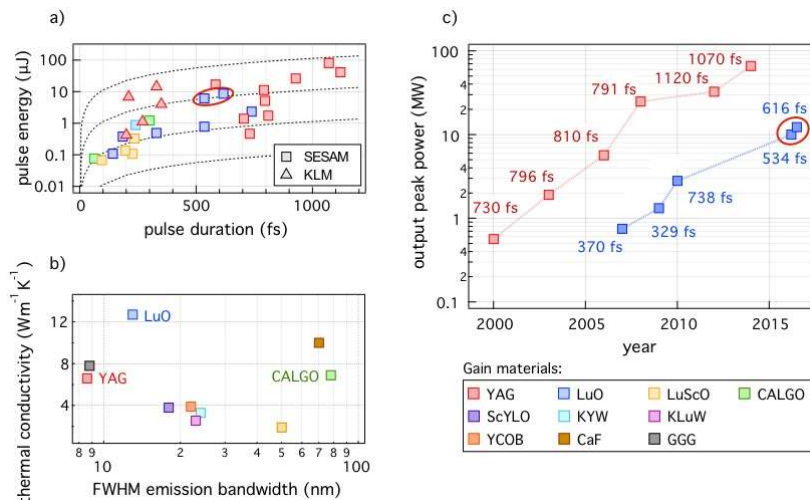


Fig. 1. a) Overview of the results demonstrated from modeled TDLs with different Yb-doped gain materials. Results presented in this paper are indicated by the red circles. b) Thermal conductivity and emission bandwidth of gain materials suitable for the thin-disk geometry. The thermal conductivity is given for a typical Yb doping density of $8 \times 10^{20} \text{ cm}^{-3}$. c) Evolution of the performance of SESAM-mode-locked Yb:YAG and Yb:LuO TDLs.

High-power modeled operation with Yb:LuO has been demonstrated in a SESAM-mode-locked TDL up to 141 W of average output power with relatively long 738-fs pulses at a repetition rate of 60 MHz [32]. Short-pulse operation was also achieved down to 140 fs at a limited power level of 7 W and a repetition rate of 64 MHz [33]. Average power scaling to 25 W was demonstrated with 185-fs pulses [34], which remains to date the highest average power achieved from a SESAM-mode-locked TDL at sub-200-fs pulse durations. These promising results, however, were all obtained at high repetition rates and consequently limited output peak powers below 3 MW. The Yb:LuO disks available at the time of these experiments were comparatively thick (150 – 250 μm) and contacted on copper-alloy heatsinks, which resulted in significant thermal lensing [32, 35]. Recently, the first Kerr-lens modelocking of an Yb:LuO TDL was demonstrated with an average power of 6 W and 165-fs pulses at a repetition rate of 60 MHz [36]. First sub-100-fs pulse generation from an Yb:LuO TDL was then achieved in a 61-MHz KLM oscillator with up to 11 W of average power and 88-fs pulses or with pulses as short as 35 fs at <2-W power level [37]. These results, however, were also limited to output peak powers below 2 MW.

Here, we present the first high peak power SESAM-mode-locked Yb:LuO TDL reaching peak powers in excess of 10 MW [see Fig. 1(c)], with average powers up to 90 W and pulse durations close to 500 fs at repetition rates below 15 MHz. To achieve these results, we designed a new set of Yb:LuO disks with reduced thickness below 150 μm , optimized crystal quality, and contacted on diamond for enhanced thermal management. These improvements allowed us to increase the cavity length compared to prior results and scale up the peak power of femtosecond Yb:LuO TDLs. After presenting the modelocking results (section 2), we identify the current challenges of high peak-power SESAM-mode-locked and present our numerical model, validated by experimental results, providing a criterion for stable modelocking (section 3). Finally, we use our model as a tool to determine the cavity and SESAM design requirements for accessing the 100-W average power, 200-fs regime, with peak-powers approaching 100 MW.

2. High-peak-power SESAM-modelocked Yb:LuO TDL

In this section, we present our high-peak-power (>10 MW) Yb:LuO modelocking results. To enable this performance, a new high-quality thin-disk was used. We chose Yb:LuO for its advantageous thermal properties and comparatively large bandwidth as discussed in the introduction. The crystal, from which the large-area (\varnothing 12 mm) 110- μm -thick Yb:LuO disk was prepared, was grown at the Institut für Laser-Physik of the Universität Hamburg by the heat exchanger method (HEM) [38]. It has a doping concentration of 3 at.% (Yb-ion density of $\approx 8.6 \times 10^{20} \text{ cm}^{-3}$). The disk was contacted onto a diamond heatsink (TRUMPF Laser GmbH) and has a cold radius of curvature (ROC) of -2.2 m, free of astigmatism. The disk was mounted within a 36-pass thin-disk laser head (TRUMPF Laser GmbH) and pumped into the zero-phonon line (ZPL) at 976 nm with a pump spot diameter of 2.5 mm. The narrow-linewidth pump diode (DILAS Diodenlaser GmbH) is wavelength-stabilized with a volume Bragg grating (VBG). The cooling water temperature for the diode stacks was adjusted to achieve optimum locking of the pump power into the VBG line at 400 W. Under these conditions, the pump absorption efficiency is above 96% for the targeted pump power range, at typical TDL inversion levels ($<20\%$). The additional thermal lensing of the disk was measured up to the highest pump intensity of 8 kW/cm² and remained below 0.06 m⁻¹ (7% of the cold disk focal power) as well as radially symmetric. This low thermal lensing of the disk, combined to operation of the oscillator within a pressure-controlled environment, allowed us to substantially increase the pulse energy and peak power compared to previous Yb:LuO results.

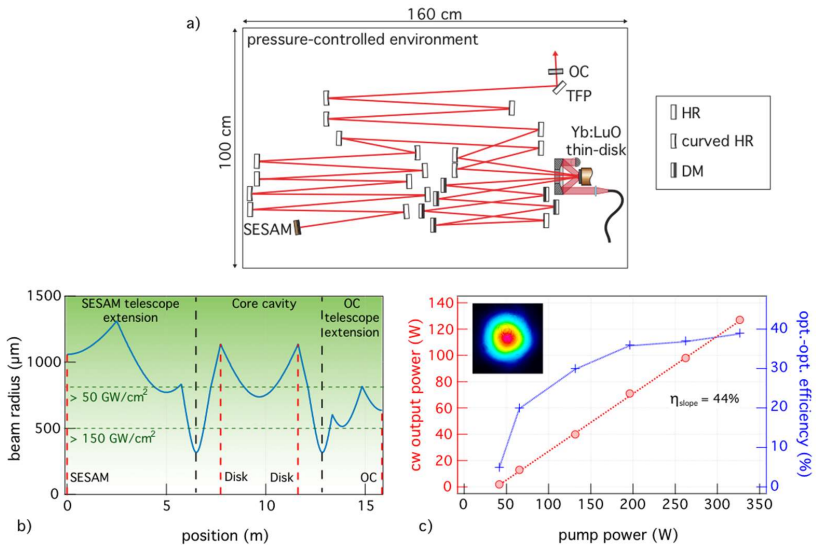


Fig. 2. a) Illustration of the full 9.5-MHz cavity layout in the pressure-controlled chamber. OC: output coupler, TFP: thin-film polarizer, HR: highly-reflective mirror, DM: dispersive mirror. b) Cavity mode radii for single transverse mode operation. The basic cavity defining the modal overlap of the laser and pump beams on the disk is extended with two 4f-telescope extensions. No optics are used within the region where peak intensities $>150 \text{ GW/cm}^2$ are expected. HR mirrors and DMs are introduced where the expected peak intensities are $<150 \text{ GW/cm}^2$ and $<50 \text{ GW/cm}^2$, respectively. c) Continuous-wave (cw) output power slope with an OC transmission of 8.4% at a pressure of 1 mbar. Inset: Measured mode profile at the maximum output power of 127 W.

The resonator design is based on a simple core cavity consisting of two flat end mirrors, the thin-disk and a concave curved mirror (CM) with a ROC of -5 m, replicated once to introduce a second double-reflection through the disk per cavity roundtrip. This 8-pass approach increases the effective gain available from the very thin disk and allows for operation at higher output coupler (OC) transmission values [39]. The core cavity is designed to have a laser mode radius that amounts to 91% of the pump mode radius on the Yb:LuO disk and to operate in the center of the stability region [40]. The cavity length is then extended by introducing telescope extensions at both ends of the cavity. An illustration of the cavity layout is given in Fig. 2(a). The cavity extensions are designed to increase the overall mode diameters in the laser resonator in order to reduce the intensity on the intracavity optics and the fluence on the SESAM in high-power operation. To avoid damaging the intracavity optics during or prior to initiating modelocking, we set conservative upper bounds for the maximum peak intensities allowed on these elements during modelocked operation. We choose upper bounds of 150 GW/cm² for the highly-reflective (HR) mirrors and 50 GW/cm² for the dispersive mirrors (DMs). Based on the expected intracavity parameters (average powers <2 kW, peak powers <500 MW), these bounds imply minimum laser spot sizes of 500 μm for the HRs and 800 μm for the DMs [Fig. 2(b)]. A thin-film polarizer (TFP) is inserted in the cavity for polarization selection and the oscillator is set up in a pressure-controlled chamber as in [9]. In this configuration and with an OC transmission of 8.4%, single transverse mode operation is achieved with >120 W of cw output power, at an optical-to-optical efficiency of 39% and a slope efficiency of 44% [Fig. 2(c)] at a pressure of 1 mbar. The measured M²-values in cw operation of M²_x = 1.01 and M²_y = 1.03 indicate close to diffraction-limited beam quality at ambient pressure, as well as at the minimum pressure of 1 mbar, limited by our vacuum pump.

For initiating and stabilizing modelocked operation, we introduce into the cavity a large-area semiconductor saturable absorber mirror (SESAM) optimized for high-damage threshold following our guidelines in [41]. The as-grown semiconductor structure is top-coated with three pairs of dielectric layers, leading to a high saturation fluence of $F_{\text{sat}} = 120 \mu\text{J}/\text{cm}^2$ and a high rollover coefficient of $F_{2, 1\text{ps}} = 5 \text{ J}/\text{cm}^2$ (measured for a 1-ps pulse), together with a moderate modulation depth of $\Delta R = 1.1\%$, low nonsaturable losses of $\Delta R_{\text{ns}} = 0.05\%$ and a recovery time of $\tau_{1e} = 6 \text{ ps}$. A measurement of the SESAM nonlinear reflectivity curve, as well as a complete description of the epitaxial structure, is given in [42]. The SESAM is contacted onto a copper substrate and mounted on a water-cooled aluminum mount equipped with a Peltier element for active temperature control. The temperature of the SESAM was set to 18 °C.

The nonlinear phase shift required for soliton pulse formation is fine-tuned by varying the residual air pressure within the chamber. Intracavity negative dispersion (D_{in}) required to balance this nonlinear phase is adjusted by introducing dispersive mirrors in the cavity. Note that a reflective TFP typically presents a non-negligible negative group-delay dispersion (GDD), in our case measured to be $\approx -500 \text{ fs}^2$. First high-peak-power modelocking was achieved with an intracavity dispersion of -4100 fs^2 per roundtrip and a residual air pressure (p_{atm}) of 15 mbar in a 14.8 MHz cavity without OC extension. Stable single-pulse modelocked operation was obtained up to 90 W of average power at a pulse duration of 534 fs. The output pulse energy was 6.1 μJ resulting in a peak power of 10.1 MW.

To further scale the output pulse energy and peak power, the OC extension was added to the cavity [see Fig. 2(b)]. The intracavity dispersion was adjusted to -7400 fs^2 per roundtrip by introducing additional dispersive mirrors and the chamber was evacuated to the minimum residual air pressure of 1 mbar. Stable single-pulse modelocked operation was achieved up to 82 W of average power at a pulse duration of 616 fs and a repetition rate of 9.5 MHz [see Fig. 3]. The pulse energy was 8.6 μJ, resulting in a peak power of 12.3 MW. These are the highest pulse energies and peak powers achieved from a modelocked TDL based on Yb:LuO. The resulting parameters are summarized in Table 1.

Table 1. Laser parameters of the presented modelocking results

$P_{pk, out}$	D_{rt}	p_{atm}	f_{rep}	P_{avg}	τ_p	$E_{p, out}$
10.1 MW	-4100 fs ²	15 mbar	14.8 MHz	90 W	534 fs	6.1 μ J
12.3 MW	-7400 fs ²	1 mbar	9.5 MHz	82 W	616 fs	8.6 μ J

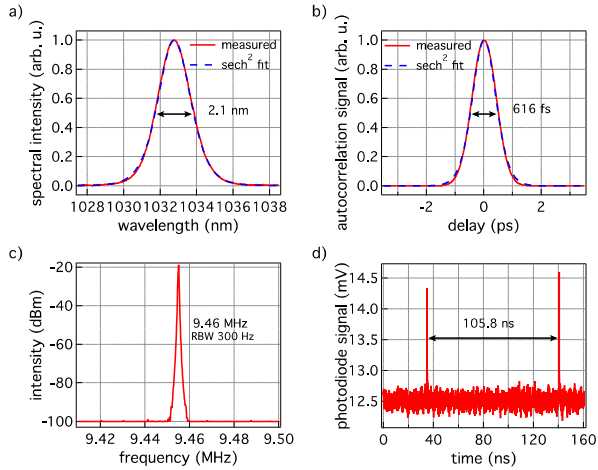


Fig. 3. SESAM-modelocked Yb:LuO TDL with the record-high 12.3-MW peak power result: a) Optical spectrum of the 616-fs pulses, with a FWHM of 2.1 nm. b) Autocorrelation trace of the nearly transform-limited 616-fs pulses (time-bandwidth product (TBP) of 0.362). The delay was scanned over a long range of 60 ps and no double-pulsing was observed. c) Microwave spectrum analyzer signal showing modelocking at a repetition rate of 9.46 MHz with a SNR >70 dB (resolution bandwidth RBW of 300 Hz over a span of 90 kHz) d) Signal acquired on a fast sampling scope from a fast photodiode (45 GHz) showing single-pulse modelocking with the corresponding roundtrip time of 105.8 ns.

In particular, these results represent the first demonstration of a high-peak-power Yb:LuO TDL reaching peak-powers in excess of 10-MW. The superior quality of the new thin-disk used for these experiments enabled the implementation of a multipass geometry as well as operation at a reduced ambient pressure. This allowed for high intracavity peak-powers up to 185 MW with reduced nonlinear phase-shifts (~ 50 mrad) for soliton pulse shaping. The resulting low amount of required negative intracavity dispersion allowed for the use of only a few DMs with low GDD values, which mitigated the thermal issues we often observe with such mirrors [42]. No damage of the SESAM was observed during our optimization of the cw-modelocking regime. However further peak-power scaling was limited by the onset of instabilities at higher powers and shorter pulse durations, such as double-pulsing and modal instabilities, which will be addressed in the next section.

3. Numerical modeling of high-peak-power SESAM-modelocked TDLs

As observed in our present peak-power scaling experiments and in prior work on short-pulsed SESAM-modelocked TDLs [25, 33, 43], modelocked operation at high pulse energies and short pulse durations is limited by the onset of modelocking instabilities or modal instabilities (i.e. beam quality degradation). These limitations can be explained by considering the combined

effect of the finite gain bandwidth (GBW) of the thin-disk material and of the reflectivity rollover happening in the SESAM at high intensities, which can be interpreted as an inverse saturable absorption (ISA) effect [44]. Within a laser cavity, these two effects lead on the one hand to a reduction of the loss modulation provided by the SESAM at the highest pulse energies and/or shortest pulse durations, which can favor double-pulsing or cw-breakthroughs, and on the other hand to increased absorption losses in the SESAM, which increase the heat load on the SESAM and introduce thermal lensing. In this section, we present a numerical model for calculating the net cavity gain of a modelocked TDL which accounts for the finite gain bandwidth and the SESAM inverse saturable absorption.

3.1 SESAM reflectivity within a modelocked laser cavity

The nonlinear reflectivity of a SESAM increases with increasing pulse fluence due to saturable absorption (SA) in the absorber layers of the epitaxial structure, in our case InGaAs quantum wells (QWs). In the absence of parasitic effects such as two photon absorption (TPA) and for sufficiently large fluences, the SESAM reflectivity would asymptotically reach a maximum, as illustrated in Fig. 4 (no TPA). However, for large pulse fluences and intensities, TPA or free-carrier absorption lead to inverse saturable absorption, i.e. a rollover of the SESAM reflectivity [44, 45] [see Fig. 4 (TPA at fixed τ_p)]. The usual model-function for the reflectivity of a SESAM is given by [46]:

$$R(F) = R_{SA}(F) \cdot R_{ISA}(F) = R_{ns} \frac{\ln[1 + R_{lin} / R_{ns} (e^{F/F_{sat}} - 1)]}{F / F_{sat}} \cdot e^{-F/F_2} \quad (1)$$

where $R_{lin} = 1 - \Delta R - \Delta R_{ns}$, is the cw nonsaturated SESAM reflectivity and $R_{ns} = 1 - \Delta R_{ns}$, is the maximum SESAM reflectivity in the absence of ISA. F , F_{sat} and F_2 are the pulse fluence, the SESAM saturation fluence and inverse saturation fluence respectively, while ΔR and ΔR_{ns} (or L_{ns}) denote the modulation depth and SESAM losses in the absence of ISA. The inverse saturation fluence F_2 characterizes the strength of the SESAM reflectivity rollover at high intensities due to ISA. Based on detailed studies [44-46], the SESAM reflectivity rollover is mainly caused by TPA in the fs-regime, taking place especially in the low-bandgap semiconductor materials (GaAs) of the SESAM structure. Therefore, the TPA-induced loss can be represented via a rollover intensity I_2 and the model-function for the SESAM reflectivity can be rewritten as a function of fluence and peak intensity:

$$R(F_p, I_p) = R_{SA}(F_p) \cdot R_{TPA}(I_p) = R_{ns} \frac{\ln[1 + R_{lin} / R_{ns} (e^{F_p/F_{sat}} - 1)]}{F_p / F_{sat}} \cdot e^{-I_p/I_2} \quad (2)$$

where $I_p = 0.88 F_p / \tau_p$ is the intensity on the SESAM and τ_p is the incident soliton pulse duration. The rollover intensity I_2 only depends on the layer structure of the SESAM. For the case considered here of TPA induced by a soliton pulse, it is related to the inverse saturation fluence F_2 , according to [44]:

$$I_2 = 0.88 \frac{F_2}{\tau_p} = \frac{1}{0.665 \int \beta_{TPA}(z) n^2(z) |\mathcal{E}(z)|^4 dz} \quad (3)$$

where $\beta_{TPA}(z)$, $n(z)$ and $\mathcal{E}(z)$ are the material-dependent TPA coefficient, the refractive index and the normalized electric field at a given position z within the SESAM structure. The distinction between the rollover fluence F_2 and the rollover intensity I_2 is particularly relevant when considering the SESAM reflectivity within a modelocked laser cavity. Due to soliton

pulse shaping, the incident pulse duration on the SESAM depends on the pulse energy according to:

$$\tau_p = 1.76 \frac{2|D_{rt}|}{\gamma_{rt} E_p} \quad (4)$$

where D_{rt} is the total intracavity negative group delay dispersion per roundtrip, $\gamma_{rt} = \phi_{NL,rt} / P_{pk}$ is the total self-phase modulation (SPM) coefficient per roundtrip, $\phi_{NL,rt}$ being the total intracavity nonlinear phase per roundtrip, and E_p is the intracavity pulse energy. Therefore, when the intracavity pulse energy is varied, the SESAM reflectivity effectively follows a curve with constant I_2 [Eq. (2)] but not with constant F_2 [Eq. (1)], as is the case during a measurement of the SESAM reflectivity. As illustrated in Fig. 4, this effectively leads to a more pronounced rollover.

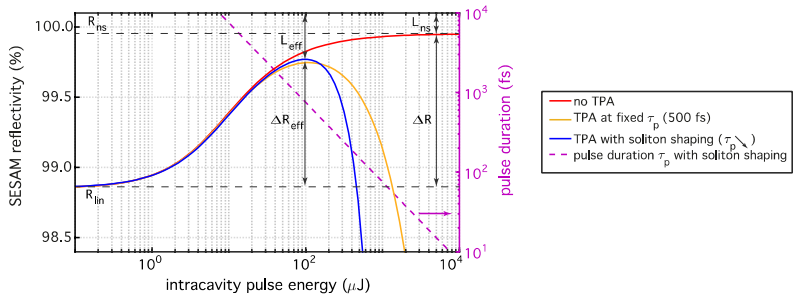


Fig. 4. Simulated nonlinear reflectivity curve of the SESAM used in the modelocking experiments for a waist $w_{SESAM} = 1.3$ mm, in different cases: without TPA effect (orange), for a fixed F_2 value corresponding to a pulse duration of 500 fs (yellow) and finally accounting for soliton shaping, for a given intracavity dispersion and nonlinearity [see Eq. (4)] (purple). The soliton pulse duration is plotted in a pink dashed line and reaches 500 fs for a pulse energy of 150 μ J. The reduced effective modulation depth and increased losses compared to the specified ΔR and ΔR_{ns} are indicated at the rollover point.

The SESAM reflectivity rollover induced by TPA at high peak intensities leads to the loss modulation provided by the SESAM reaching a maximum value for a given peak intensity. The corresponding intracavity pulse energy is denoted as $E_{p,0}^{SESAM}$. After this rollover point, the SESAM reflectivity decreases rapidly. In the presence of soliton shaping (purple line in Fig. 4), the effective available modulation depth ΔR_{eff} is always smaller and the effective the losses L_{eff} are always larger than the SESAM fit parameters ΔR and ΔR_{ns} , respectively. Thus, for shorter pulses, TPA induces higher SESAM losses, decreases the effective available modulation depth, and shifts the rollover point $E_{p,0}^{SESAM}$ to lower pulse energies. The increased SESAM losses result in a higher thermal load on the SESAM and consequently stronger thermal lensing, which can destabilize the laser cavity. Additionally, the reduced effective modulation depth sets a limit to the minimum achievable pulse duration, as discussed in the next section. To mitigate these effects, it is therefore of high interest to use SESAM structures with reflectivity rollovers shifted to the highest possible peak intensities.

3.2 Finite gain bandwidth: gain reduction at short pulse durations

An important aspect of peak power scaling modelocked oscillators is the ability to use a large fraction of the available gain bandwidth in order to reach the shortest pulse durations with a

given gain material. However, as the pulse bandwidth samples a larger fraction of the gain spectrum, the resulting effective gain for the pulse decreases compared to the gain for a cw wave. This gain reduction can be calculated numerically for a given inversion level β . The gain cross-section σ_g reads:

$$\sigma_g(\nu) = \beta \cdot \sigma_{em}(\nu) - (1 - \beta) \cdot \sigma_{abs}(\nu) \quad (7)$$

and the intensity gain G is given by:

$$G(\nu) = N_{dop} n_{passes} \sigma_g(\nu) d_{disk} \quad (8)$$

where $\beta = N_2 / N_{dop}$ is the inversion level, N_2 the inversion population, N_{dop} the Yb-ion density of the disk, σ_{em} and σ_{abs} the emission and absorption cross-sections [47], n_{passes} the number of laser passes in the gain medium per cavity roundtrip, and d_{disk} the thickness of the disk.

In cw operation, we assume a single frequency ν_{cw} lasing at the maximum of the gain spectrum. For a soliton pulse with a spectral bandwidth $\Delta\nu$, the gain is then calculated as:

$$G_p(\Delta\nu) = \int G(\nu) \cdot S\left(\frac{\nu - \nu_{cw}}{\Delta\nu}\right) \cdot d\nu \quad (9)$$

with $S((\nu - \nu_{cw}) / \Delta\nu)$ the normalized sech²-shaped intensity spectrum of a soliton pulse with a center frequency ν_{cw} and a spectral bandwidth $\Delta\nu$, related to the pulse duration via the time-bandwidth product $\Delta\nu \tau_p = 0.3148$. We verified that spatial hole burning effects have a negligible impact on the gain for the targeted short pulse durations, and therefore neglect them for simplicity [48].

In Fig. 5, we show relevant characteristics for the gain in an Yb:LuO disk with 110 μm thickness, as used in our experiments. Fig. 5(a) shows the gain cross section at 19% inversion. This inversion level is estimated based on the OC transmission and nonsaturated SESAM losses in our experiment. As the pulse duration is reduced, the increase in bandwidth means that gain for the pulse is reduced relative to cw light, as shown in Fig. 5(b). This normalized reduction is largely inversion-independent. Fig. 5(c) shows the absolute difference in gain for several values of inversion in our Yb:LuO disk. Since a lower value for the OC transmission is constrained by the need to avoid excessive intracavity powers, this absolute difference in gain values is important and can be compared to the available modulation depth of the SESAM: a modulation depth at least as large is required to favor pulsed operation.

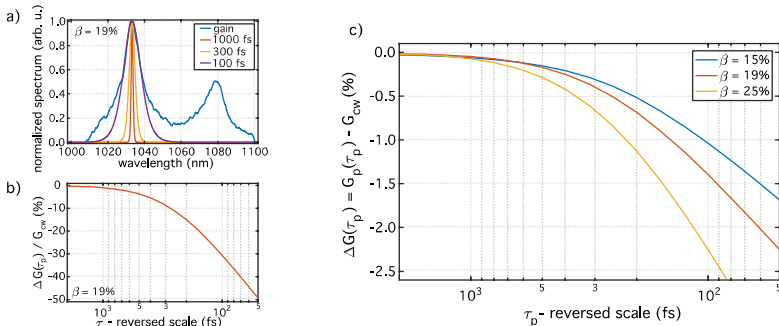


Fig. 5. Simulated reduction of the gain in pulsed operation compared to cw operation for an Yb:LuO TDL. The disk thickness is set to 110 μm and the doping concentration to 3 at.%, as in our experiments. The number of passes of the laser beam through the gain medium is set to 4 per cavity roundtrip, corresponding to a standard V-shaped cavity with a single double-reflection

of the laser beam through the disk per roundtrip. Spatial hole burning (SHB) effects, that lead to a reduction of the available gain for long pulse durations [48], were neglected in this calculation. a) Normalized gain spectrum and pulse spectra showing how shorter pulses sample more of the gain cross-section, leading to the reduction in gain. b) Normalized gain reduction for pulsed operation compared to cw operation. c) Absolute gain reduction for pulsed operation compared to cw operation, plotted for increasing inversion levels, corresponding to increasing OC rates.

3.3 Modelocking stability at high peak-powers: validation of our numerical model on peak-power scaling experiments

In order to find the conditions required to achieve stable modelocking at high peak powers, i.e. high pulse energies and short pulse durations, we now study the combined effect of the SESAM rollover and finite gain bandwidth in experimental results obtained during our peak-power scaling experiments. Our analysis is based on a set of over 30 modelocking results achieved using the same Yb:LuO disk in various cavity configurations and with different SESAMs. Here, we focus in particular on the two following results:

- high peak-power modelocking with 82 W, 616 fs, 9.5 MHz (detailed in section 2)
- lower power modelocking at shorter pulse duration with 16 W, 268 fs, 47.2 MHz

These results are both at the limit of stable modelocking, i.e. the pulse energy could not be increased further in the experiment without leading to double-pulsing or modal instabilities.

Each laser configuration is defined by a thin disk (in this case, the same Yb:LuO disk), a cavity design including nonlinearity, dispersion and a given OC, and a SESAM. As recently demonstrated for modelocked semiconductor disk lasers [49], the quantity $G - L$, defined as the net roundtrip cavity gain, represents a useful tool to investigate the possible modelocking points and the limits of stable modelocked operation in a given laser configuration. We therefore calculate the net cavity gain as a function of the intracavity pulse energy for several different cases, as shown in Fig. 6. Our numerical model calculates as follows:

First, the cw losses are set by the OC transmission and the nonsaturated SESAM losses. The rate equations are then solved for steady-state, single frequency cw operation and the corresponding inversion level β is calculated. The same inversion level is used for all of the curves on the figure. Given this value, we then calculate $G - L$ with respect to cw operation for the following cases, see Fig. 6:

- cw operation (labeled ‘cw’): the cw gain G_{cw} is given by Eqs. (7)–(8), and equals the cw losses.
- Pulsed operation, assuming no rollover effects (labeled ‘no TPA’): the losses are set by the OC transmission and the saturated SESAM losses, assuming no rollover due to TPA (infinite I_2). The pulsed gain equals the cw gain, i.e. assuming infinite gain bandwidth.
- Pulsed operation, assuming infinite gain bandwidth and fixed rollover fluence F_2 (labeled ‘TPA, fixed τ_p ’): the losses are set by the OC transmission and the saturated SESAM losses for a fixed rollover fluence F_2 [Eq. (1)], calculated for the pulse duration at the considered modelocking point. The pulsed gain equals the cw gain as in the previous case.
- Pulsed operation, assuming infinite gain bandwidth but including soliton pulse formation for the SESAM response (labeled ‘TPA, soliton shaping’): the losses are set by the OC transmission and the saturated SESAM losses, now considering the soliton pulse circulating within the cavity with a duration following Eq. (4). The SESAM reflectivity is now a function of incoming fluence and peak intensity as in Eq. (2). The pulsed gain also equals the cw gain in this case.

- Pulsed operation, considering both soliton pulse formation and the finite gain bandwidth (GBW) (labeled ‘TPA, sol. shap. + GBW’): the losses are set by the OC transmission and the saturated SESAM losses, considering soliton pulse formation. The gain is calculated according to Eq. (9), i.e. accounting for the finite gain bandwidth.

We checked that the losses introduced by reflection of the laser beam on the numerous intracavity optics have a negligible impact on the net cavity gain and therefore neglect them. In all cases, a transverse Gaussian beam shape is accounted for numerically in the SESAM losses calculations, and the inversion level is assumed constant in order to show the influence of the different effects given a realistic inversion level for lasing operation. The SESAM is also considered sufficiently fast (recovery time of a few ps), such that a cw wave potentially growing over a roundtrip time experiences the cw losses and double-pulsing is the first limitation expected to set in.

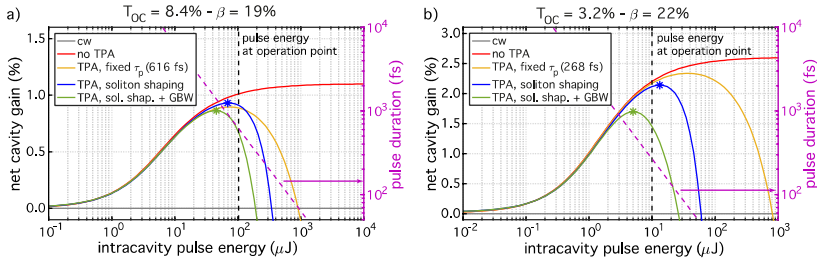


Fig. 6. Net cavity gain for a soliton pulse as a function of the intracavity pulse energy for two different laser configurations: a) high peak-power modelocking (82 W, 616 fs, 9.5 MHz) and b) low power modelocking at shorter pulse duration (16 W, 268 fs, 47.2 MHz). The different cases are listed in the text. The maximum experimental operation point before the onset of instabilities is indicated by the black dashed line. The maximum of the green curve ($E_{p,0}^{\text{cav}}$) and the purple curve ($E_{p,0}^{\text{SESAM}}$) are indicated by a marker.

In the 616-fs configuration [Fig. 6(a)], the modelocked operation point is only slightly into the rollover of the SESAM reflectivity assuming only soliton pulse shaping (purple line), however the limited gain bandwidth adds an additional rollover contribution and shifts the operation point further into the overall cavity rollover (green line). The contribution of the gain bandwidth rollover is even more pronounced for the 268-fs configuration [Fig. 6(b)]: in this case, the modelocked operation point would actually be close to the optimum operation point for the SESAM reflectivity if only soliton pulse shaping was considered (purple line). In order to explain the limitations and optimize modelocking in this short-pulse regime, it is thus crucial to consider the effect of the finite gain bandwidth in addition to the SESAM rollover, while accounting for soliton shaping to determine the pulse duration.

The optimum operation point maximizing the gain advantage for pulsed operation is located at the maximum of the overall net cavity gain curve (i.e. accounting for soliton pulse shaping and the finite gain bandwidth, green lines). The corresponding pulse energy is denoted as $E_{p,0}^{\text{cav}}$. As can be seen from comparing Figs. 6(a) and 6(b), as the targeted pulse duration gets shorter, and therefore the gain bandwidth rollover gets stronger, this point $E_{p,0}^{\text{cav}}$ is shifted to lower energies, away from the optimum operation point for the SESAM $E_{p,0}^{\text{SESAM}}$, leading to additional SESAM losses. It is therefore of interest to study how far within the overall cavity rollover stable modelocked operation can be achieved, in order to operate with minimum saturated SESAM losses.

In Fig. 7(a), the experimental operation points of over 30 different laser configurations realized during our peak-power scaling experiments are compared to the simulated optimum $E_{p,0}^{\text{cav}}$ in each case. The results show that with reasonable accuracy, the maximum operation

point leading to stable modelocking is $\approx 2 E_{p,0}^{\text{cav}}$. This is consistent with the experimentally observed appearance of double-pulsing, since in these conditions two pulses with half the energy of the soliton pulse would experience a higher gain due to the cavity rollover.

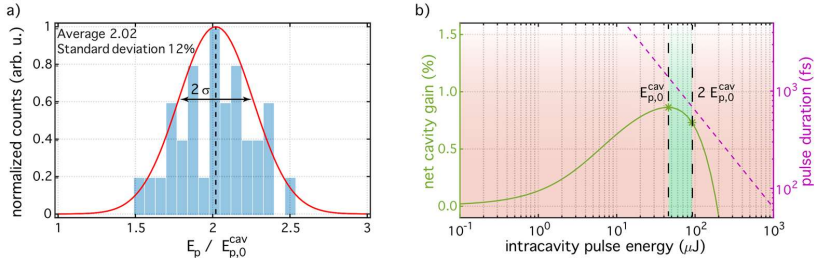


Fig. 7. a) Comparison of the maximum operation point achieved before modelocking instabilities occur, in different laser configurations based on the same Yb:LuO disk. The maximum achievable pulse energy appears to be about twice the pulse energy $E_{p,0}^{\text{cav}}$ corresponding to the optimum cavity net gain. b) Illustration of the optimum stable modelocking region. For a given laser configuration, the net cavity gain is calculated accounting for soliton pulse shaping and the finite gain bandwidth. Stable modelocking within the overall cavity rollover is possible, and even desirable to minimize the SESAM saturated losses, at pulse energies up to $2 E_{p,0}^{\text{cav}}$.

Consequently, optimizing the modelocking operation point at short pulse durations is a trade-off between operating close to the maximum of the overall net cavity gain curve, with maximum robustness to modelocking instabilities, and operating close to the maximum of the SESAM reflectivity, with minimum saturated SESAM losses. According to our study, operation within the overall cavity rollover is possible up to a pulse energy $E_{p,\text{max}} \approx 2 E_{p,0}^{\text{cav}}$ before modelocking instabilities occur.

To summarize, the optimum region for stable modelocking is determined by calculating the net cavity gain for pulsed operation, accounting for soliton pulse shaping and the finite gain bandwidth, and retrieving the pulse energy $E_{p,0}^{\text{cav}}$ corresponding to its maximum. Stable modelocked operation is possible up to a pulse energy twice higher than this optimum point, as illustrated in Fig. 7(b). As the operation point is shifted into the overall cavity rollover, the pulse energy increases and the pulse duration decreases, maximizing the achieved peak power. Additionally, the SESAM saturation increases, reducing the effective SESAM losses and thermal lensing.

4. Design guidelines for >100-W, 200-fs Yb:LuO SESAM-modelocked TDLs

We now illustrate an example of how the cavity design and the SESAM parameters can be adjusted to achieve the targeted 200-fs pulse durations at $>10 \mu\text{J}$ output pulse energies, and consequently output peak powers $>20 \text{ MW}$. This pulse duration, $\tau_p = 200 \text{ fs}$, corresponds to a spectral bandwidth that amounts to $\approx 45\%$ of the FWHM emission bandwidth of Yb:LuO. For this pulse duration, the effect of the finite gain bandwidth is already significant, as shown in Fig. 5. The targeted intracavity pulse energy is chosen to reflect our criterion for the maximum allowed peak intensity on intracavity optics discussed in section 2.1: for a maximum peak intensity of 150 GW/cm^2 on a spot with a minimum radius of $500 \mu\text{m}$, the peak power is limited to $\approx 590 \text{ MW}$ and the corresponding intracavity pulse energy to $\approx 130 \mu\text{J}$. We therefore consider a laser cavity with a target modelocking point at $120 \mu\text{J}$ (intracavity), 200 fs with a repetition rate of 10 MHz, leading to an intracavity average power of 1.2 kW. Note that these limits could be relaxed if our damage-threshold estimate is found to be overly conservative, or if a different stable cavity design with larger modes is found. Therefore, these limits are useful for

developing a design target in this paper, but substantially higher intracavity peak powers may ultimately be possible.

Given the available intracavity power and a targeted output power >100 W, we can immediately specify an output coupling rate. We choose this to be 12.5%, yielding 150 W output power. In order to maintain reasonable laser efficiency, the inversion level should not be too high, and so we target a design having $<20\%$ inversion level, as in our experiments. Consequently, additional passes of the laser on the disk are needed, in order to have enough gain to support the higher OC rate. The number of passes is therefore set to $n_{\text{passes}} = 32$.

Another effect of the higher OC rate is a larger difference in gain between cw and pulsed operation compared to Fig. 5. However, simply choosing the SESAM fit parameter ΔR equal to this difference is not enough, for two reasons: (1) The available modulation depth will be reduced due to TPA. (2) Because we target short pulses, there is a pronounced influence of the gain bandwidth on the net cavity rollover, as in Fig. 6(b); to counter-act this effect, and operate close to the net cavity rollover, we need to operate at pulse energies substantially below the SESAM rollover point $E_{p,0}^{\text{SESAM}}$. In this way, the effects of increasing SESAM reflectivity and decreasing gain (with respect to pulse energy in the soliton modelocked laser) can balance each other and support stable operation.

To illustrate these points, we show in Fig. 8 the trends for the net cavity gain curve when the SESAM and cavity design parameters are varied. As a starting point for the design procedure, we choose a similar cavity design and the same SESAM as in our high peak-power modelocking experiments presented in section 2 (see table 1). We then seek to optimize the modelocked operation point according to our criterion $E_{p,\text{max}} \approx 2 E_{p,0}^{\text{cav}}$. The varied and constant parameters for each plot are listed in table 2.

The initial net cavity gain curve is shown in Fig. 8(a) (blue curve). In Fig. 8(a), we show the influence of increasing ΔR . We observe that the cavity rollover occurs below $30 \mu\text{J}$ of intracavity pulse energy and there is no net gain for pulsed operation at the desired operation point. With an increased SESAM modulation depth and reduced OC rate, the net cavity gain at the desired operation point increases and exceeds the minimum required to favor pulsed operation over cw operation. At the same time the cavity rollover is shifted to higher pulse energies, shifting the stable modelocked operation region towards the desired operation point. Note that the OC transmission is adjusted in Fig. 8(a) to keep the inversion level constant while increasing ΔR . However, it is not desirable to only increase the modulation depth until the operation point is well within the stable modelocking region, since this would lead to a high laser threshold. Moreover, a higher modulation depth is achieved by increasing the number of quantum wells in the SESAM structure, which also results in increased SESAM losses.

Therefore, we next set the modulation depth to 10% (and the OC rate to 12.5%) and seek to shift the stability region to higher pulse energies by varying the laser mode radius on the SESAM, as shown in Fig. 8(b). As the laser mode size on the SESAM increases, TPA is reduced and the stability region shifts to higher pulse energies. However, the SESAM is also less saturated and this leads to an overall reduction of the SESAM reflectivity, with consequences on the net cavity gain. This also introduces higher losses, since the SESAM is not operated at the maximum of its reflectivity curve. As can be seen from Fig. 8(b), for laser mode radii >2.6 mm, the operation point is well within the stable modelocking region: we subsequently set the mode radius to 2.6 mm. In this configuration, the operation point is already within the stable modelocking region.

For completeness, we also consider the effect of the other SESAM parameters: saturation fluence F_{sat} and rollover fluence F_2 . As illustrated in Fig. 8(c), for increasing saturation fluences, the stable modelocking region is slightly shifted to higher pulse energies. However, the quantum wells being less saturated, the overall net cavity gain decreases and the SESAM losses increase. For our targeted operation point, a saturation fluence of $120 \mu\text{J}/\text{cm}^2$ is best suited.

Finally, we study the influence of the F_2 parameter on the cavity net gain curve: as shown in Fig. 8(d), this parameter has very little influence on the cavity net gain, as the finite gain bandwidth is the main limiting effect for the targeted pulse parameters.

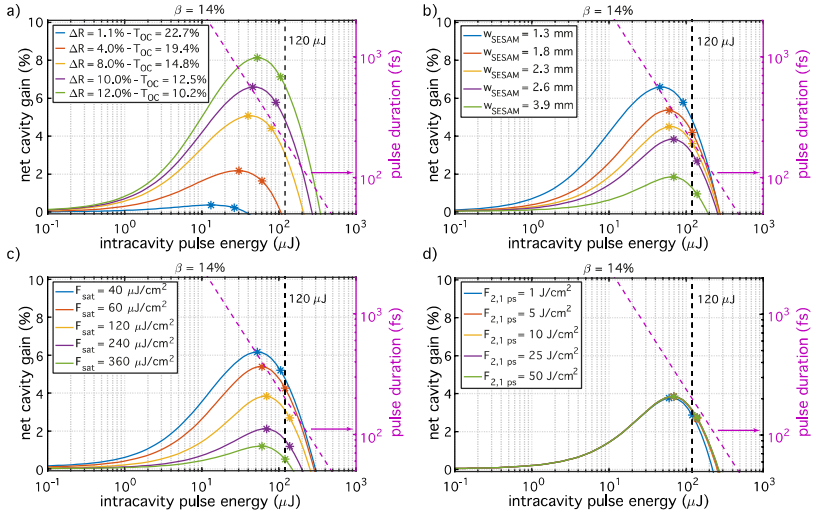


Fig. 8. Net cavity gain as a function of intracavity pulse energy and optimization of the cavity and SESAM parameters for stable modelocking at 120 μJ and 200 fs. Black dashed line: desired intracavity pulse energy, purple line: soliton pulse duration. a) Variation of the SESAM modulation depth. The OC transmission is adjusted to keep the total losses constant. b) Scaling of the laser mode radius on the SESAM. c) Scaling of the SESAM saturation fluence. d) Scaling of the SESAM reference F_2 coefficient for a pulse duration of 1 ps. The stable modelocking region is indicated by the two markers on each curve.

Table 2. Constant and varied parameters used in each step of the modelocking optimization procedure. In bold: adapted parameters in each step.

	SESAM parameters				Cavity design		OC
	F_{sat}	ΔR	ΔR_{ns}	$F_{2,1 \text{ ps}}$	W_{SESAM}	n_{passes}	
Initial	120 $\mu\text{J}/\text{cm}^2$	1.1%	0.05%	5 J/cm^2	1.3 mm	32	22.7%
Fig. 8(a) ^a	120 $\mu\text{J}/\text{cm}^2$	1.1–12.0%	0.05–0.60%	5 J/cm^2	1.3 mm	32	22.7–10.2%
Fig. 8(b)	120 $\mu\text{J}/\text{cm}^2$	10.0%	0.50%	5 J/cm^2	1.3–3.9 mm	32	12.5%
Fig. 8(c)	40–360 $\mu\text{J}/\text{cm}^2$	10.0%	0.50%	5 J/cm^2	2.6 mm	32	12.5%
Fig. 8(d)	120 $\mu\text{J}/\text{cm}^2$	10.0%	0.50%	1–10 J/cm^2	2.6 mm	32	12.5%

^aIn the first step [Fig. 8(a)], the modulation depth ΔR is the parameter of interest. Since the modulation depth and the nonsaturable losses are both determined by the number of QWs of the SESAM structure, ΔR_{ns} is varied accordingly (5% of ΔR). Additionally, in order to keep the inversion level constant, the OC transmission is also changed.

The optimized laser configuration is summarized in table 3. With an OC transmission of 12.5%, this configuration corresponds to an output peak power of 66 MW. Concerning further power scaling, note that for a given cavity design, the achievable output peak power is constrained by the tolerable intracavity peak power. However, our maximum intensity constraint was already conservative for operating at 600 fs, and the damage threshold will increase for 200-fs pulses [50]. If the peak power constraint can be relaxed by a factor of 4 via optimized optics and cavity design, then the number of passes on the disk, OC rate, and SESAM

modulation depth ΔR can all be reduced by a corresponding factor for the same output power. This alternative configuration would significantly simplify the SESAM and cavity design.

Table 3. Summary of the cavity and SESAM parameters optimization for stable modelocked operation at an intracavity pulse energy of 120 μJ and a pulse duration of 200 fs, with an OC transmission of 12.5% and 32 passes through the thin disk.

	SESAM parameters				Cavity design		OC	Expected output performance			
	F_{sat}	ΔR	ΔR_{ns}	$F_{2,1 \text{ ps}}$	w_{SESAM}	n_{passes}	T_{OC}	P_{avg}	τ_{p}	E_{p}	P_{pk}
Optimized laser configuration	120	10	0.50	5	2.6	32	12.5	150	200	15	66
	$\mu\text{J}/\text{cm}^2$	%	%	J/cm^2	mm		%	W	fs	μJ	MW

The presented optimized laser configuration allowing for high peak-power modelocking at short pulse durations require adjusting both the SESAM parameters and the cavity design. These requirements have consequences on the SESAM design, surface flatness and thermal properties. Operating with large spot sizes on the SESAM ($w_{\text{SESAM}} > 1.2 \text{ mm}$) calls for large-area SESAMs with a high surface flatness and low thermal lensing in order to avoid modal instabilities. Moreover, the required large saturation fluence and modulation depth can be achieved by increasing of the number of QWs of the SESAM structure, which requires additional strain-compensating layers in order to keep the crucial high surface quality. Recently, we have successfully grown high-quality SESAMs with a large number of QWs [51] and investigated a novel direct bonding technique resulting in superior SESAM flatness and thermal properties [52]. These newly developed technologies enable SESAM structures fulfilling the requirements for high peak-power, short-pulsed modelocked operation.

5. Conclusion and outlook

We demonstrated the first peak power scaling of a SESAM-modelocked Yb:LuO TDL to more than 10 MW. Our cavity design based on an 8-pass geometry allowed us to operate at comparatively low intracavity powers and scale the peak power by increasing the cavity length. We achieved high peak-power modelocking at output powers up to 90 W. The highest peak-power was obtained at 82 W with 616-fs pulses at a repetition rate of 9.5 MHz. The corresponding pulse energy of 8.6 μJ and peak power of 12.3 MW are the highest demonstrated to date with a TDL based on Yb:LuO. These results were achieved thanks to the high quality of our very thin 110- μm -thick Yb:LuO disk contacted on diamond, which resulted in negligible thermal lensing. This allowed us to increase the length of our laser resonator and operate it in a pressure-controlled environment. Due to the low residual nonlinearity of our cavity, intracavity peak powers up to 185 MW were reached.

The presented peak-power-scaling experiments were limited by the onset of instabilities, similar to the limits observed for many years in high-power SESAM-modelocking of TDLs. Therefore, we discussed the challenges of peak power scaling SESAM-modelocked TDLs towards the 100-W, 10- μJ , 200-fs regime. We identified the two main limiting effects as the SESAM reflectivity rollover and the finite gain bandwidth. These effects can jointly be taken into account by calculating an overall net cavity gain for pulsed operation as a function of the intracavity pulse energy in a given laser configuration. Stable modelocked operation can be achieved at intracavity pulse energies exceeding the maximum of this net cavity gain curve $E_{\text{p},0}^{\text{cav}}$ up to a factor of ≈ 2 . For short pulse durations where the effect of the gain bandwidth is significant, this optimal operation range does not coincide with the maximum of the SESAM reflectivity, thus requiring a trade-off between robustness to modelocking instabilities and thermal load on the SESAM. In the case of Yb:LuO, we illustrated how the SESAM parameters

and the cavity design can be optimized to allow for stable modelocking at high output pulse energies (15 μJ) and short pulse durations (200 fs) by:

- increasing the number of laser passes (≈ 32) through the thin-disk to allow for higher output coupler transmissions and relaxed intracavity conditions
- keeping the saturation fluence moderately high ($\approx 120 \mu\text{J}/\text{cm}^2$) to allow for high pulse energies with enough saturation of the quantum wells
- increasing the SESAM modulation depth to several percent ($\approx 10\%$) to overcome the gain reduction at short pulse durations
- increasing the laser mode radius ($\approx 2.6 \text{ mm}$) on the SESAM to operate on the rising edge of the SESAM reflectivity curve

These last two point can be stated more generally: the rate of change in saturable loss with respect to the energy of the soliton must balance the reduced gain due to the finite bandwidth of the gain medium. We expect that this criterion will be applicable both to SESAM modelocked TDLs but also other laser configurations, e.g. KLM TDLs or those incorporating both a Kerr lens and a SESAM.

The required SESAM parameters can be achieved by growing strain-compensated structures with a large number of quantum wells (>8) and carefully designing dielectric top-coatings to tailor the saturation fluence and modulation depth. The enhanced thermal management required by the high SESAM losses due to operation away from the rollover point and the increased cavity mode sensitivity to thermal lensing due to the large spot size can both be addressed by contacting the SESAM using a novel direct substrate transfer technique providing superior flatness and heat removal capabilities.

The ongoing improvements of the SESAM structures combined to the new insights on optimizing modelocked operation at short pulse durations are opening a route to demonstrating SESAM-modelocked Yb:LuO thin-disk oscillators reaching multi-10-MW output peak powers at pulse durations around 200 fs. Additionally, combining the SESAM with other types of loss modulators and achieving a broad gain profile could be key to further scale the output peak of short pulsed TDLs toward $>100 \text{ MW}$.

Funding

This work was supported by the Swiss National Science Foundation (SNSF) project grant Nr. 200020_172644. The ETH Zurich authors also acknowledge support of the technology and cleanroom facility FIRST of ETH Zurich for advanced micro- and nanotechnology.

This work was supported by the excellence cluster “The Hamburg Centre for Ultrafast Imaging – Structure, Dynamics and Control of Matter at the Atomic Scale” of the Deutsche Forschungsgemeinschaft (EXC 1074) and the German Ministry of Education and Research (BMBF) (13N14192).

2.3 Conclusion

In this chapter, we presented our results in scaling the peak power of TDL oscillators based on the gain material Yb:LuO. We demonstrated a SESAM-modelocked Yb:LuO TDL delivering peak powers in excess of 10 MW at average powers of $\approx 80\text{-}90$ W and pulse durations >530 fs, shorter than typical pulse durations achieved with Yb:YAG at comparable peak powers. The generated peak powers are the highest reported from an Yb:LuO TDL to date.

This result was enabled by a high-quality $110\ \mu\text{m}$ thin-disk used in a cavity including multiple passes of the intracavity beam on the disk in order to operate at larger OC transmissions. Additionally the cavity was extended via telescope extensions in order to increase the pulse energy, and operated in a pressure-controlled environment to mitigate the nonlinearity induced by the high intracavity peak powers >120 MW.

In a second part, we presented an in-depth study of the effect of the limited gain bandwidth and the two-photon absorption (TPA)-induced rollover effect in the SESAM reflectivity on the modelocking performance. We developed a numerical model to evaluate the maximum performance, i.e. the maximum pulse energy and corresponding soliton pulse duration, that can be achieved in a given laser configuration before the onset of modelocking instabilities.

Under the assumption of soliton shaping, i.e. that the pulse duration is determined by equation (1.6) in chapter 1, we evaluate the net cavity gain (defined as the difference of the disk gain and the cavity losses) for the soliton pulse and for a cw wave as a function of the soliton pulse energy (and corresponding pulse duration). We showed how the combined effect of the TPA-induced rollover and the limited gain-bandwidth lead to a rollover point in the net cavity gain for the soliton pulse. As higher peak powers and shorter pulse durations are targeted, the strength of both rollover effects is increased, shifting the rollover point to lower energies and hindering peak-power scaling.

It should be noted that the detrimental effect of the SESAM rollover and the limited gain bandwidth were already known and in some cases

partially included in analytical descriptions of modelocking stability in earlier works [60,67,68,115,116]. However our model combines both aspects in a numerical model that can be directly compared with experimental results. Indeed we used our experimental data gathered during our peak-power scaling experiments with Yb:LuO to compare the maximum performance that was obtained in very diverse laser configurations with the corresponding simulated net cavity gain curve for pulsed operation. Our results showed with reasonable accuracy that the maximum performance of the laser corresponds to a pulse energy twice higher than the pulse energy at the rollover point of the net cavity gain curve. This result is in good agreement with the onset of double-pulsing [67] and provides a criterion for designing a TDL oscillator operating at a high peak power and short pulse duration.

In the next chapter, we will extend the investigation presented at the end of our publication, concerning the SESAM parameters required for high-peak power modelocking at short pulse durations, and apply it to Yb:YAG and Yb:CALGO.

Investigation of the short-pulsed modelocking regime via numerical simulations

3.1 The average power vs. pulse duration trade-off

Modelocking of TDLs was successfully demonstrated in diverse configurations and using a variety of gain materials, allowing for high average powers or short pulse durations. However, the combination of high average power >100 W and short pulse durations <200 fs remains challenging, as can be seen in figure 1.4 in chapter 1.

The significant reduction in generated average power observed at short pulse durations can be attributed in part to the generally lower crystal quality, thermal conductivity and gain cross-section of broadband gain materials (see for example figure 1.4 in chapter 1 for the thermal conductivity) [104, 105, 108, 109]. The presence of defects or impurities in the crystal introduces scattering losses and beam distortions that hinder single-transverse mode (singlemode) operation with large beam sizes on the disk. In order to limit these scattering losses, broadband laser crystals are often grown with lower doping concentrations than for example Yb:YAG. The low doping concentration, in combination with the low gain cross-section, results in an overall low gain of the disk. This can be compensated to some extent by having a thicker disk, however the increased

disk thickness combined with a low reduced thermal conductivity will lead to strong thermal lensing effects. As a result, TDL oscillators based on broadband gain materials often operate with a small pump and laser mode size on the disk, a low OC transmission and at low pump powers, leading to an overall low output power. However, the trade-off between high output power and short pulse durations is observed also for Yb:LuO, although this material seems ideally suited for high-power operation with short pulses (see section 2.1). We therefore investigated the limitations for generating energetic short pulses via numerical simulations.

The minimum achievable pulse duration in a given laser oscillator is a crucial parameter for pushing the performance of modelocked lasers. This topic was investigated early on, both analytically and numerically [60,115, 116]. Analytical descriptions of soliton modelocking stabilized by a fast or slow saturable absorber already highlighted the main contribution of the gain bandwidth and the absorber loss modulation for reaching short pulse durations [60]. For the case of a slow saturable absorber, the minimum achievable pulse duration for a soliton pulse limited by the growth of a cw continuum was estimated in [60]:

$$\tau_{p,\min} \approx \frac{g^{3/8}}{\Delta\Omega_g^{3/4}} \left(\frac{\tau_a}{\Delta R} \right)^{1/4} \frac{1}{\varphi_0^{1/8}} \quad (3.1)$$

where g is the roundtrip power gain, $\Delta\Omega_g$ is the FWHM gain bandwidth, τ_a is the absorber recovery time, ΔR is the absorber maximum loss modulation and φ_0 is the soliton phase shift.

Equation (3.1) highlights that there is a trade-off between the contributions of the roundtrip power gain g and the gain bandwidth $\Delta\Omega_g$ and absorber modulation depth ΔR to the minimum achievable pulse duration. The dominant role of the gain bandwidth and the influence of the saturable absorber parameters for the generation of short pulses motivated the investigation of broadband gain materials and the development of adapted SESAM designs [84,92,100]. Although equation (3.1) provides some useful insights into the relevant parameters for the generation of short pulses, it is based on several assumptions such as a Lorentzian gain profile or a fully saturated absorber, which deviate from experimental con-

ditions. In particular, rollover effects due to ISA are not included, which play a crucial role in limiting the achievable pulse duration. In order to evaluate the modelocking limits of our experimental TDL oscillators, we rely on a numerical model as introduced in the publication presented in section 2.2 of the previous chapter.

3.2 Numerical model

3.2.1 Limitations of the linearized model

In the framework of our peak-power scaling experiments with Yb:LuO described in chapter 2, we developed a numerical model to evaluate the maximum performance, i.e. the maximum pulse energy and corresponding soliton pulse duration, that can be achieved in a given laser configuration before the onset of modelocking instabilities. This model is based on a linearized steady-state condition for the roundtrip cavity gain G_{rt} :

$$\begin{aligned} G_{\text{rt}} = e^{n_{\text{passes,l}} N_{\text{dop}} \sigma_g l_{\text{disk}}} \cdot R_{\text{cav}} &\simeq (1 + G_{\text{lin}}) \cdot (1 - L_{\text{cav}}) = 1 \\ \Rightarrow G_{\text{lin}} - L_{\text{cav}} &= 0 \end{aligned} \quad (3.2)$$

where $G_{\text{lin}} = n_{\text{passes,l}} N_{\text{dop}} \sigma_g l_{\text{disk}}$ is the linearized roundtrip power gain, $n_{\text{passes,l}}$ is the number of laser passes through the disk per roundtrip, N_{dop} is the Yb-doping concentration of the disk, σ_g is the inversion-dependent gain cross-section, l_{disk} is the disk thickness, and $R_{\text{cav}} = 1 - L_{\text{cav}}$ is the roundtrip cavity reflectivity, with L_{cav} the roundtrip cavity losses.

Based on this linearized steady-state condition, we determine the inversion level $\beta_{\text{ss,cw}}$ resulting in a steady-state for cw operation. The inversion $\beta_{\text{ss,cw}}$ is then used to estimate the net roundtrip cavity gain for pulsed operation as a function of the soliton pulse energy. Although this approach simplifies the formalism of the numerical model, it is inaccurate on several points:

- for a modelocked laser oscillator, the steady-state condition is verified for pulsed operation,

- due to the absorber saturation and the reduction of the gain for pulsed operation, the inversion leading to a steady-state is expected to vary as a function of the soliton pulse energy,
- the linearization of the steady-state condition leads to inaccuracies when the roundtrip gain and cavity losses are large, as for example in multipass cavity geometries.

For the study carried out in our publication presented in section 2.2, these points impact the results by $\lesssim 10\%$ due to the low gain and cavity losses, and the small SESAM modulation depth compared to the overall cavity losses. In the following section, we discuss the key aspects our improved and self-consistent numerical model that will be used to evaluate the modulation depth requirements for high-peak power modelocking at short pulse durations.

3.2.2 Self-consistent numerical model

We consider a laser oscillator consisting of four key elements: a thin-disk gain medium, a saturable absorber (here a SESAM), an OC mirror and linear cavity losses encompassing the various sources of losses on the intracavity components. The aim of the model is to find the steady-state for the modelocked state defined by an intracavity power P_{ic} and a pulse duration τ_p , and evaluate the stability of this modelocked state against Q-switching instabilities, double-pulsing or cw breakthrough.

The steady-state condition implies that the roundtrip gain for the soliton pulse $G_{rt,pulse}$ is unity:

$$G_{rt,pulse} = G_{pulse} \cdot R_{cav,pulse} = 1 \quad (3.3)$$

where G_{pulse} is the disk gain for the pulse and $R_{cav,pulse}$ are the total roundtrip cavity losses for the pulse.

In general, the roundtrip cavity gain is a function of the intracavity and pump powers, and of the spectral and temporal intensity profiles of the pulse. In the case of soliton shaping, the spectral and temporal shape of the soliton pulse is directly linked to the intracavity power and the roundtrip gain becomes a function of two variables: the intracavity and

pump powers. For a given modelocking state defined by the intracavity power, we therefore need to find the pump power yielding the steady-state.

Before describing the formalism of the numerical procedure used to find the steady-state, we introduce some general definitions.

3.2.2.1 General definitions

Soliton pulse

We consider a soliton pulse circulating inside the laser oscillator, with a normalized spectrum given by:

$$S_{\text{norm},l}(\nu) = \text{sech}^2\left(\pi^2\tau(\nu - \nu_l)\right) \quad (3.4)$$

where ν_l is the center frequency of the pulse and τ is related to the FWHM pulse duration by:

$$\tau = \frac{\tau_p}{2 \text{sech}^{-1}(1/\sqrt{2})} \quad (3.5)$$

The soliton pulse shaping is defined with respect to a reference intracavity power $P_{\text{IC,ref}}$ and pulse duration $\tau_{p,\text{ref}}$, rather than the intracavity SPM coefficient and GDD. This facilitates the parameterization of the model in terms of targeted laser performance. For a given intracavity power P_{IC} , the soliton pulse duration is given by:

$$\tau_p = \tau_{p,\text{ref}} \times \frac{P_{\text{IC,ref}}}{P_{\text{IC}}} \quad (3.6)$$

Pump spectrum

For the pump beam, we assume a flat-top spectral profile with a narrow bandwidth:

$$S_{\text{norm},p}(\nu) = \text{rect}\left(\frac{\nu - \nu_p}{\Delta\nu_p}\right) \quad (3.7)$$

where ν_p is the center frequency and $\Delta\nu_p$ is the FWHM bandwidth of pump spectrum.

Effective cross-sections and saturation intensities

Here we define effective emission and absorption cross-sections that will be used for the calculation of the photon fluxes and the gain cross-section.

The effective cross-sections for the laser pulse and for the pump are given by:

$$\sigma_{\text{abs},i}^{\text{eff}} = \frac{\int \frac{S_{\text{norm},i}(\nu)}{h\nu} \sigma_{\text{abs}}(\nu) d\nu}{\int \frac{S_{\text{norm},i}(\nu)}{h\nu_i} d\nu} \quad (3.8a)$$

$$\sigma_{\text{em},i}^{\text{eff}} = \frac{\int \frac{S_{\text{norm},i}(\nu)}{h\nu} \sigma_{\text{em}}(\nu) d\nu}{\int \frac{S_{\text{norm},i}(\nu)}{h\nu_i} d\nu} \quad (3.8b)$$

where $i = l$ or p , for the laser pulse or the pump, and h is the Planck constant.

For evaluating the gain for cw light, frequency-dependent cross-sections are used to calculate the gain versus frequency.

The saturation intensities at the laser and pump wavelength are used to evaluate the stability of the modelocked state against Q-switching instabilities, and are defined as:

$$I_{\text{sat},i} = \frac{\gamma_{\text{rad}} h\nu_i}{\sigma_{\text{abs}}(\nu_i) + \sigma_{\text{em}}(\nu_i)} \quad (3.9)$$

where $i = l$ or p , for the laser pulse or the pump, and γ_{rad} is the upper-state decay rate given by the inverse of the upper-state lifetime.

Gaussian beam profiles

We consider the effect of the radial intensity profile for the disk gain and the SESAM saturation. On the disk, we assume a Gaussian profile for the laser beam and a super-Gaussian profile for the pump beam:

$$I_{\text{disk,l}}(r) = e^{-2\left(\frac{r}{w_{\text{disk,l}}}\right)^2} \quad (3.10a)$$

$$I_{\text{disk,p}}(r) = e^{-2\left(\frac{r}{w_{\text{disk,p}}}\right)^{n_{\text{SG}}}} \quad (3.10b)$$

where r is the radial coordinate on the disk, $w_{\text{disk,l}}$ and $w_{\text{disk,p}}$ are the beam waists on the disk for the laser and pump beams respectively, and n_{SG} is the super-Gaussian order of the pump beam profile (typically 8 [117]).

The peak intensity of the pump and laser beams on the disk is defined by:

$$I_{\text{pk,i}} = \frac{P_i}{\int 2\pi r I_{\text{disk,i}}(r) dr} \quad (3.11)$$

where $i = 1$ or p , for the laser pulse or the pump, and $P_i = P_{\text{ic}}$ or P_{pump} .

On the SESAM, we assume a Gaussian profile for the laser beam:

$$I_{\text{SESAM,l}}(r) = e^{-2\left(\frac{r}{w_{\text{SESAM,l}}}\right)^2} \quad (3.12)$$

where r is the radial coordinate on the SESAM and $w_{\text{SESAM,l}}$ is the beam waist of the intracavity laser beam on the SESAM.

3.2.2.2 Determination of the steady-state

In order to find the steady-state of the modelocked laser for a given intracavity power, we calculate the roundtrip gain for the pulse $G_{\text{rt,pulse}}$ as a function of the incident pump power on the disk P_{pump} and then deduce the pump power $P_{\text{pump,ss}}$ yielding the steady-state $G_{\text{rt,pulse}}(P_{\text{pump,ss}}) = 1$. The procedure involves four steps described in this subsection.

Step 1 - Determination of the radial inversion profile

In this first step, we determine the inversion profile in the pumped area of the disk. For the thin-disk geometry, we assume a constant inversion

along the beam propagation direction, i.e. along the disk thickness, and only consider the radial dependence of the inversion profile. This means that spatial hole burning effects are neglected in this calculation [118].

To deduce the inversion profile, we start from the incident photon flux $N_p(r)$, given by the pump intensity profile on the disk. For the laser rate equations, we need the radially-dependent effective photon flux $N_{p,ss}^{\text{eff}}(\beta, r)$, accounting for the multiple passes and re-imaging of the pump beam on the disk. The effective pump flux is constrained by the rate equations given an assumed laser intensity. We can then infer the inversion level $\beta_{ss}(r)$ by finding a value of beta which yields the required photon flux given the incident flux.

For the pump power P_{pump} , the radially-dependent incident pump photon flux is determined by the pump intensity on the disk, using equations (3.10b) and (3.11):

$$N_p(r) = \frac{I_{\text{pk,p}}}{h\nu_p} I_{\text{disk,p}}(r) \quad (3.13)$$

For a quasi-three-level system such as Yb-doped materials, in the absence of excited-state absorption (ESA), upconversion and non-radiative decay processes, the rate equations for the population of the upper laser level N_2 and the ground state N_1 read [119]:

$$\frac{dN_2}{dt} = \left(\sigma_{\text{abs,p}}^{\text{eff}} N_1 - \sigma_{\text{em,p}}^{\text{eff}} N_2 \right) N_p^{\text{eff}} + \left(\sigma_{\text{abs,l}}^{\text{eff}} N_1 - \sigma_{\text{em,l}}^{\text{eff}} N_2 \right) N_1^{\text{eff}} - \gamma_{\text{rad}} N_2 \quad (3.14a)$$

$$\frac{dN_1}{dt} = - \frac{dN_2}{dt} \quad (3.14b)$$

In the steady-state $\frac{dN_2}{dt} = 0$. By introducing the inversion level $\beta = \frac{N_2}{N_{\text{dop}}}$ and noting that the two level populations are linked by the doping concentration $N_{\text{dop}} = N_1 + N_2$, we obtain an expression for the effective pump flux using equation (3.14a):

$$N_{p,ss}^{\text{eff}} = \frac{\beta \gamma_{\text{rad}} + N_1^{\text{eff}} \left(\beta \left(\sigma_{\text{abs,l}}^{\text{eff}} + \sigma_{\text{em,l}}^{\text{eff}} \right) - \sigma_{\text{abs,l}}^{\text{eff}} \right)}{\sigma_{\text{abs,p}}^{\text{eff}} - \beta \left(\sigma_{\text{abs,p}}^{\text{eff}} + \sigma_{\text{em,p}}^{\text{eff}} \right)} \quad (3.15)$$

where N_1^{eff} is the radially-dependent effective laser photon flux, calculated from the Gaussian intensity profile on the disk for the modelocked state with an intracavity power P_{ic} using equations (3.10a) and (3.11):

$$N_1^{\text{eff}}(r) = n_{\text{passes},l} \frac{I_{\text{pk},l}}{h\nu_1} I_{\text{disk},l}(r) \quad (3.16)$$

where $n_{\text{passes},l}$ is the number of passes of the laser beam through the disk per roundtrip. The steady-state effective pump photon flux $N_{\text{p,ss}}^{\text{eff}}$ (equation (3.15)) is therefore a function of both the inversion β and the radial coordinate r .

In the thin-disk geometry, the effective pump intensity, and consequently the effective pump photon flux, is enhanced by the multiple passes of the pump beam through the disk. The steady-state incident pump photon flux is therefore given by:

$$N_{\text{p}}(r) = \frac{N_{\text{p,ss}}^{\text{eff}}(\beta, r)}{\eta_{\text{enh}}(\beta)} \quad (3.17)$$

and the pump enhancement factor $\eta_{\text{enh}}(\beta)$ is given by:

$$\eta_{\text{enh}}(\beta) = -2e^{\alpha_{\text{p}}(\beta)l_{\text{disk}}} \frac{1 - e^{-2n_{\text{passes},p}\alpha_{\text{p}}(\beta)l_{\text{disk}}}}{1 - e^{2\alpha_{\text{p}}(\beta)l_{\text{disk}}}} \quad (3.18)$$

where l_{disk} is the disk thickness, $n_{\text{passes},p}$ is the number of passes of the pump beam through the disk and $\alpha_{\text{p}}(\beta)$ is the pump absorption coefficient defined as:

$$\alpha_{\text{p}}(\beta) = -N_{\text{dop}}\sigma_{\text{pump}}^{\text{eff}}(\beta) \quad (3.19)$$

and the effective pump cross-section $\sigma_{\text{pump}}^{\text{eff}}(\beta)$ is given by:

$$\sigma_{\text{pump}}^{\text{eff}}(\beta) = \beta\sigma_{\text{em},p}^{\text{eff}} - (1 - \beta)\sigma_{\text{abs},p}^{\text{eff}} \quad (3.20)$$

We therefore seek for the radially-dependent inversion profile $\beta_{\text{ss}}(r)$ yielding the condition:

$$N_p(r) \cdot \eta_{\text{enh}}(\beta_{\text{ss}}(r)) = N_{p,\text{ss}}^{\text{eff}}(\beta_{\text{ss}}(r), r) \quad (3.21)$$

where $N_{p,\text{ss}}^{\text{eff}}$ is given by equation (3.15).

For each radial coordinate r , equation (3.21) yields an equation which is a function of the inversion at that radial coordinate, and we seek for the inversion $\beta_{\text{ss}}(r)$ for which the equation is satisfied. Numerically we can evaluate both sides of the equation as a function of beta, then compute their difference and find the crossing point with zero.

Step 2 - Calculation of the pulse gain

In a second step, we calculate the gain for the soliton pulse based on the inversion profile obtained in step 1. The gain cross-section is defined as:

$$\sigma_{g,\text{pulse}}(r) = \beta_{\text{ss}}(r)\sigma_{\text{em},l}^{\text{eff}} - (1 - \beta_{\text{ss}}(r))\sigma_{\text{abs},l}^{\text{eff}} \quad (3.22)$$

and the radial power gain profile is given by:

$$G_{r,\text{pulse}}(r) = e^{n_{\text{passes},l}N_{\text{dop}}\sigma_{g,\text{pulse}}(r)l_{\text{disk}}} \quad (3.23)$$

Finally the gain for the pulse is obtained by integrating over the Gaussian profile of the laser beam on the disk:

$$G_{\text{pulse}} = \frac{\int G_{r,\text{pulse}}(r)I_{\text{disk},l}(r)rdr}{\int I_{\text{disk},l}(r)rdr} \quad (3.24)$$

Step 3 - Calculation of the cavity reflectivity

The cavity reflectivity is generally defined as:

$$R_{\text{cav}} = R_{\text{OC}} \cdot R_{\text{SESAM}} \cdot R_{\text{cav},\text{lin}} \quad (3.25)$$

where R_{OC} is the OC mirror reflectivity, R_{SESAM} is the SESAM reflectivity and $R_{\text{cav},\text{lin}}$ is the linear reflectivity of the cavity, taking into account the various reflectivities and source of loss of the intracavity elements.

For the OC mirror, we consider the general case of a frequency-dependent reflectivity $R_{\text{OC}}(\nu)$. The effective OC reflectivity for the soliton pulse is calculated using:

$$R_{\text{OC,pulse}} = \frac{\int R_{\text{OC}}(\nu) S_{\text{norm,I}}(\nu) d\nu}{\int S_{\text{norm,I}}(\nu) d\nu} \quad (3.26)$$

For the SESAM, we consider the Gaussian profile of the incident laser beam and calculate the radial fluence distribution on the SESAM using equation (3.12):

$$F(r) = F_{\text{pk}} I_{\text{SESAM,I}}(r) \quad (3.27)$$

where the peak fluence of the Gaussian profile is given by:

$$F_{\text{pk}} = \frac{P_{\text{ic}} / f_{\text{rep}}}{\pi/2 \cdot w_{\text{SESAM}}^2} \quad (3.28)$$

where f_{rep} is the repetition rate of the laser oscillator.

The nonlinear reflectivity of the SESAM as a function of the incident fluence is given by [120]:

$$R_{\text{SESAM}}(F) = R_{\text{ns}} \frac{\ln \left(1 + R_{\text{lin}} / R_{\text{ns}} \left(e^{F/F_{\text{sat}}} - 1 \right) \right)}{F/F_{\text{sat}}} e^{-F/F_2(\tau_{\text{p}})} \quad (3.29)$$

where $R_{\text{lin}} = 1 - \Delta R - \Delta R_{\text{ns}}$ is the linear reflectivity of the SESAM, $R_{\text{ns}} = 1 - \Delta R_{\text{ns}}$ is the maximum reflectivity of the SESAM in the absence of rollover, F_{sat} is the saturation fluence, ΔR is the modulation depth, ΔR_{ns} are the nonsaturable losses and $F_2(\tau_{\text{p}})$ is the effective rollover coefficient of the SESAM. This effective rollover coefficient is proportional to the pulse duration [68] and determined in relation to the measured rollover coefficient $F_{2,\text{meas}}$ at a pulse duration $\tau_{\text{p},F_{2,\text{meas}}}$:

$$F_2(\tau_{\text{p}}) = F_{2,\text{meas}} \cdot \frac{\tau_{\text{p}}}{\tau_{\text{p},F_{2,\text{meas}}}} \quad (3.30)$$

The SESAM reflectivity for the soliton pulse is finally obtained by integration of the SESAM reflectivity over the incident Gaussian fluence profile:

$$R_{\text{SESAM,pulse}} = \frac{\int R_{\text{SESAM}}(F(r)) F(r) r dr}{\int F(r) r dr} \quad (3.31)$$

The linear cavity reflectivity $R_{\text{cav,lin}}$ is a fixed parameter given to the model.

Step 4 - Calculation of the roundtrip gain as a function of the pump power

Going through steps 1 to 3, we obtain the roundtrip gain $G_{\text{rt,pulse}} \cdot R_{\text{cav,pulse}}$ for the modelocked state with an intracavity power P_{ic} for a given pump power P_{pump} . By iterating this procedure for several pump powers we obtain the roundtrip gain for the modelocked state as a function of the pump power and can deduce the value $P_{\text{pump,ss}}$ yielding the steady-state $G_{\text{rt,pulse}}(P_{\text{pump,ss}}) = 1$. The full process can then be reiterated for a different modelocking state with a different intracavity power.

3.2.2.3 Stability of the steady-state

Once the steady-state is determined, we evaluate the stability of the modelocked state with respect to Q-switching instabilities, double-pulsing and cw-breakthrough.

Stability against Q-switching

To characterize the stability against QML, we evaluate a stability condition analogous to the one derived in [66].

We use the pump power $P_{\text{pump,ss}}$ to calculate the corresponding inversion profile $\beta_{\text{ss}}(r)$ following the procedure of step 1 (section 3.2.2.2). For a given modelocking state with an intracavity power P_{ic} , we calculate the roundtrip gain variation $dG_{\text{rt,pulse}}$ for a small variation of the intracavity power P_{ic} (at fixed inversion) and evaluate the stability term:

$$\eta_{\text{QML}} = \frac{\partial G_{\text{rt,pulse}}}{\partial P_{\text{ic}}} \Big|_{\beta} - \left(1 + \frac{I_1^{\text{eff}}}{I_{\text{sat},l}} + \frac{I_{\text{p}}^{\text{eff}}}{I_{\text{sat},\text{p}}} \right) \cdot \frac{\gamma_{12}}{f_{\text{rep}}} \quad (3.32)$$

where $I_{\text{sat},l}$ and $I_{\text{sat},\text{p}}$ are defined by equation (3.9), and the effective laser and pump intensities are calculated as:

$$I_1^{\text{eff}} = \frac{I_{\text{pk},l}}{2} \cdot n_{\text{passes},l} \quad (3.33a)$$

$$I_{\text{p}}^{\text{eff}} = I_{\text{pk},\text{p}} \cdot \max[\eta_{\text{enh}}(\beta_{\text{ss}}(r))] \quad (3.33b)$$

Provided that $\eta_{\text{QML}} < 0$, the steady-state is stable against QML [66].

Gain for double-pulsing

We evaluate the roundtrip gain for the case of a splitting of the (single) soliton pulse into two non-interacting pulses, each with half the energy of the single pulse. For this we recalculate the laser effective cross-sections (equation (3.8) in section 3.2.2.1) for a soliton pulse at half the intracavity power $P_{\text{ic}}/2$ (section 3.2.2.1) and then recalculate the pulse gain (step 2, section 3.2.2.2), the cavity reflectivity (step 3, section 3.2.2.2) and the roundtrip gain for this case. Note that spectral interference between these two pulses is neglected when calculating their gain.

If the roundtrip gain for double-pulsing exceeds unity, there is a risk of destabilizing the soliton pulse and switching to the double-pulsing regime.

Gain for a cw wave

We finally evaluate the gain for a cw wave. Using the steady-state radial inversion profile, we calculate the gain cross-section and the power gain as a function of the radial coordinate and the frequency:

$$\sigma_{\text{g,cw}}(r, \nu) = \beta(r) \sigma_{\text{em}}^{\text{cw}}(\nu) - (1 - \beta(r)) \sigma_{\text{abs}}^{\text{cw}}(\nu) \quad (3.34)$$

$$G_{rv,cw}(r, \nu) = e^{n_{\text{passes}} I N_{\text{dop}} \sigma_{g,cw}(r, \nu) I_{\text{disk}}} \quad (3.35)$$

The frequency-dependent cw gain is obtained by integrating over the Gaussian profile of the laser beam on the disk:

$$G_{\nu,cw}(\nu) = \frac{\int G_{rv,cw}(r, \nu) I_{\text{norm},l}(r) dr}{\int I_{\text{norm},l}(r) dr} \quad (3.36)$$

And the gain for a cw wave is taken at the maximum of the cw gain spectrum. We also deduce the cw (single) frequency:

$$G_{\text{cw}} = \max [G_{\nu,cw}(\nu)] \quad (3.37a)$$

$$\nu_{\text{cw}} \text{ such that } G_{\nu,cw}(\nu_{\text{cw}}) = G_{\text{cw}} \quad (3.37b)$$

It is worth noting that our formalism does not include the recovery dynamics of the absorber. We therefore evaluate the modelocking stability for the best case situation in which noise is growing far away from the pulse and not during the recovery time.

3.3 Evaluation of the modulation depth requirements for a 100-W 200-fs TDL

3.3.1 Design considerations

In this section, we use the model presented in section 3.2.2 to evaluate the modulation depth required for stable SESAM-modelocking of a high-peak-power TDL operating at a pulse duration of 200 fs and based on Yb:YAG, Yb:LuO or Yb:CALGO. The targeted performance is an average power of 100 W with a pulse duration of 200 fs at a repetition rate of 10 MHz, corresponding to a pulse energy of 10 μ J and a peak power >40 MW.

We consider disks with a typical thickness and doping concentration for the respective gain material (see table 3.1), and mounted inside a standard 36-pass TDL head with a large pump beam diameter of 4.5 mm and

a laser mode size amounting to 70% of the pump mode size, as typically used in 100-W class TDLs [16,18,76].

Parameter	Material		
	Yb:YAG	Yb:LuO	Yb:CALGO
l_{disk}	100 μm	110 μm	150 μm
$N_{\text{dop,at.\%}}$	10 at.%	3 at.%	5 at.%
λ_{pump}	969 nm	976 nm	979 nm
$n_{\text{passes,p}}$	36	36	36
$n_{\text{passes,l}}$	$4 \times 2 \times 2$	$6 \times 2 \times 2$	$8 \times 2 \times 2$
$w_{\text{disk,p}}$	2.25 mm	2.25 mm	2.25 mm
$w_{\text{disk,l}}$	1.58 mm	1.58 mm	1.58 mm
β_{target}	$\approx 15\%$	$\approx 15\%$	$\approx 10\%$

Table 3.1 – Disk parameters for the numerical simulation of a 100-W 200-fs TDL.

For the cavity losses, we set the OC transmission to 10%, corresponding to an intracavity power of 1 kW and an intracavity peak power >400 MW. These are realistic intracavity conditions, as demonstrated for example in [18], that can be supported with an appropriate resonator design. Together with the choice of the OC transmission, we set a targeted inversion value of $\approx 15\%$ for Yb:YAG and Yb:LuO, and $\approx 10\%$ for Yb:CALGO. This corresponds to typical inversion values at which efficient laser operation is achieved and the effect of the limited gain bandwidth is not too strong. The targeted inversion level and the total cavity losses allow us to define the number of laser passes required on the disk.

It should be noted that operating at a larger OC transmission is possible, and even desirable in order to relax the intracavity conditions, however this will result in an increased inversion and therefore increased gain rollover, or will require an increased number of passes on the disk to keep the inversion low. Here we choose the lowest OC transmission based on realistic intracavity conditions, in order to illustrate the minimum modulation depth requirements for high-power modelocking at 200 fs. The disk parameters used in the numerical simulations are summarized in table 3.1.

3.3.2 Gain reduction at 200 fs

Using the parameters defined in table 3.1, we calculate the gain cross-section σ_g for the different gain materials and compare it to the spectrum of a 200-fs soliton pulse in figure 3.1(a). The FWHM bandwidth of the pulse corresponds to about 67% of the FWHM gain bandwidth for Yb:YAG, 46% for Yb:LuO and only 12% for Yb:CALGO. We further compute the gain spectrum and determine the difference in gain between a soliton pulse and a cw wave as a function of the FWHM soliton pulse duration in figure 3.1(b). As expected from the fraction of the gain bandwidth sampled by the 200-fs pulse, the strongest gain reduction is obtained with Yb:YAG and amounts to 10.7%. The gain reduction obtained with Yb:LuO is significantly lower with 3.8% and for Yb:CALGO, the pulse gain is only 0.16% lower than the cw gain. These values give an indication for the minimum effective loss modulation required from a saturable absorber to create a gain advantage for the pulse and favour mode-locked operation. In the following section we evaluate the actual SESAM parameters required to overcome this gain reduction.

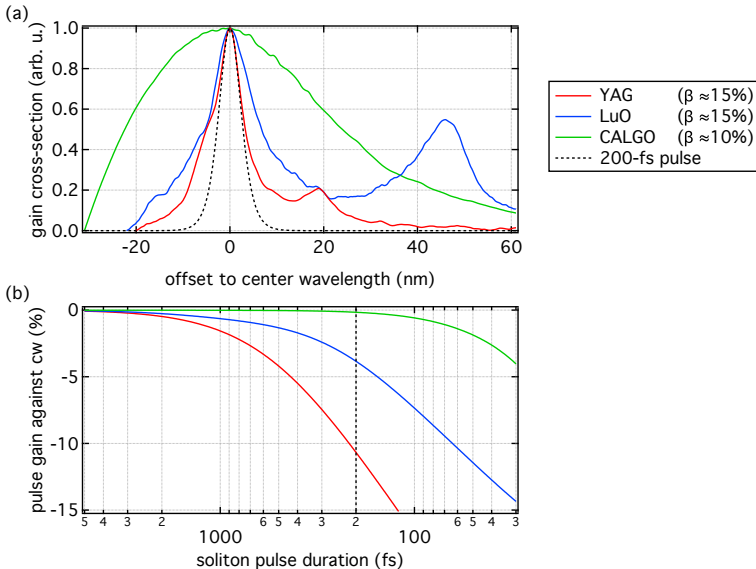


Figure 3.1 – Gain cross-section and gain reduction for Yb-doped YAG, LuO and CALGO. (a) The gain cross-section is calculated for typical inversion levels in the thin-disk geometry. In order to highlight the available gain bandwidth, the data is normalized to the peak gain cross-section and the wavelength axis is referenced to the peak wavelength (1030 nm for Yb:YAG, 1033 nm for Yb:LuO and 1049 nm for Yb:CALGO). The spectrum of a 200-fs sech^2 pulse with a center wavelength of 1030 nm is shown for comparison. We note that the FWHM $\Delta\lambda_{\text{FWHM}}$ of a sech^2 centered at 1030 nm, 1033 nm or 1049 nm differs by less than 4%. (b) The difference between the gain for a pulse and the gain for a cw wave is shown as a function of the FWHM duration of a soliton pulse. Note that the pulse duration axis is reversed.

3.3.3 SESAM modulation depth requirements

In order to investigate the modulation depth requirements for a SESAM used to modelock a TDL at 100 W, 200 fs and 10 MHz, we use our modelocking stability model to calculate the gain for pulsed operation and for cw operation as described section 3.2.2. We use the disk parameters introduced in table 3.1 and first introduce a SESAM with typical parameters for high-power modelocking (table 3.2, initial) [16, 121]. The laser mode radius on the SESAM is set to 1.5 mm.

3. INVESTIGATION OF THE SHORT-PULSED MODELOCKING REGIME VIA NUMERICAL SIMULATIONS

	Initial	Yb:YAG	Yb:LuO	Yb:CALGO
$ \Delta G(\tau_p = 200 \text{ fs}) $		10.7%	3.8%	0.16%
ΔR	1%	30%	15%	2%
ΔR_{ns}	0.1%	3%	1.5%	0.2%
$F_{\text{sat}} (\mu\text{J}/\text{cm}^2)$	120	120	120	120
$F_{2,1 \text{ ps}} (\text{J}/\text{cm}^2)$	5	5	5	5
$w_{\text{SESAM}} (\text{mm})$	1.5	1.5	1.5	1.5

Table 3.2 – SESAM parameters used for the numerical simulation of a 100-W 200-fs TDL. The initial SESAM parameters correspond to typical values for high-power SESAMs. The parameters reported for the different gain materials correspond to the values leading to $1.5 \cdot P_0^{\text{cav}} = 100 \text{ W}$. For reference, the gain reduction at 200 fs is also indicated.

Following the conclusions of our publication presented in section 2.2, we seek to optimize the SESAM parameters to have the targeted power $P_{\text{target}} = 100 \text{ W}$ in the middle of the modelocking stability region $P_{\text{target}} = 1.5 \cdot P_0^{\text{cav}}$, i.e. between the point of maximum gain advantage for the pulse P_0^{cav} and twice this optimal point $2 \cdot P_0^{\text{cav}}$. The roundtrip gain advantage for pulsed operation against cw operation $\Delta G_{\text{rt}} = G_{\text{rt,pulse}} - G_{\text{rt,cw}}$ is calculated and shown in figure 3.2(a)-(c) for the initial SESAM parameters (dashed line) with a modulation depth of 1%. For these SESAM parameters, the targeted operation point is beyond $1.5 \cdot P_0^{\text{cav}}$ for all gain materials. In the next step, we illustrate how an increased modulation depth shifts the roundtrip gain advantage towards the desired operation point. We increased the modulation depth until the operation point matches $1.5 \cdot P_0^{\text{cav}}$ and show the corresponding curve in figure 3.2(a)-(c) (solid line). For this simulation, we kept the saturation fluence, rollover coefficient and beam size on the SESAM constant, and we scaled the nonlinear losses by the same amount as the modulation depth. This scaling is motivated by the fact that the nonsaturable losses are linked to the number of quantum wells (QWs) of the SESAM structure, which also determines the product $F_{\text{sat}} \cdot \Delta R$ [122]. We therefore expect the nonsaturable losses to scale proportionally to the modulation depth at a fixed saturation fluence.

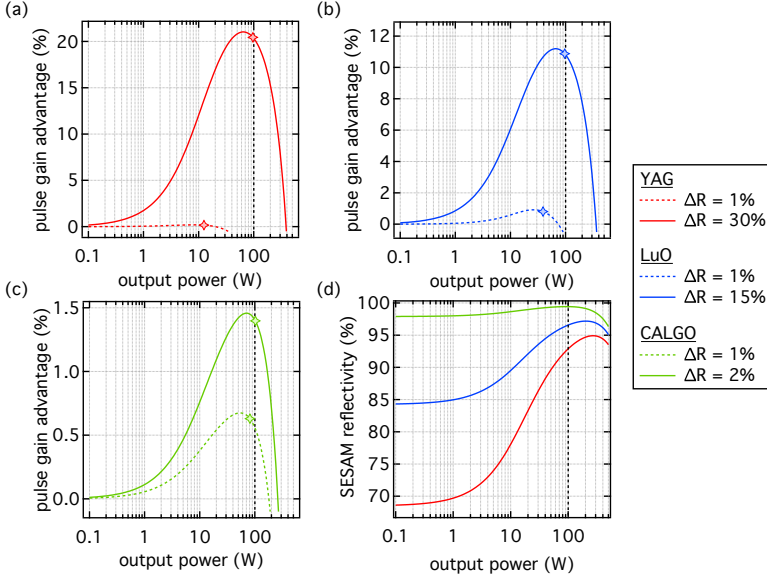


Figure 3.2 – Pulse gain advantage and SESAM reflectivity as a function of the output power for a 100-W 200-fs Yb:YAG TDL based on Yb:YAG, Yb:LuO or Yb:CALGO. (a)-(c) Roundtrip gain advantage for pulsed operation against cw operation for the different gain materials considered in our simulations. For each material, the curve is shown for two different values of the SESAM modulation depth with the parameters defined in table 3.2. The pulse duration follows soliton shaping. The markers indicate the point of the curve corresponding to $1.5 \cdot P_0^{\text{cav}}$. The black line indicates the targeted operation point of 100 W and 200 fs. (d) SESAM reflectivity versus output power for the modulation depth supporting 100 W, 200 fs modelocked operation for each gain material. The operation point is again indicated by the black dashed line.

The modulation depth obtained for each gain material is reported in table 3.2 and compared to the gain reduction calculated in section 3.3.2. Additionally, the corresponding SESAM reflectivity curves are shown in figure 3.2(d). The strong discrepancy between these two quantities can be explained by the combination of the TPA and gain-bandwidth-induced rollovers:

1. the TPA-induced rollover strongly reduces the available modulation depth, shifting the point of maximum loss modulation to lower powers, therefore a large modulation depth is needed to shift this point

back to higher powers,

2. the strongly increasing gain rollover, particularly in the case of Yb:YAG and Yb:LuO, further shifts the cavity rollover point to lower powers, and a large increasing reflectivity of the SESAM is needed to counteract this effect. Therefore the SESAM requires a large modulation depth and has to be operated at powers below the SESAM rollover point (see figure 3.2(d), red and blue curves).

3.4 Conclusion on high-peak-power modelocking at short pulse durations

In this chapter, we investigated high-peak-power modelocking at short pulse durations with our numerical model, and focused in particular on the SESAM parameters required to support this regime of modelocking in a TDL based on the typical gain materials Yb:YAG, Yb:LuO and Yb:CALGO.

Our numerical model, combined with the data acquired during our peak-power scaling experiments with Yb:LuO (chapter 2), allows us to evaluate the maximum performance (average power and pulse duration) of a given laser oscillator, based only on experimental input parameters. We used this model to evaluate the gain reduction for pulsed operation against cw operation for a 200 fs soliton pulse in the chosen gain materials. We further evaluated the required modulation depth to support modelocking at 100 W, 10 MHz with 200 fs pulses, and found values of 30% for Yb:YAG, 15% for Yb:LuO and 2% for Yb:CALGO. These values are significantly larger than the gain reduction in the disk at 200 fs (see table 3.2), which can be explained by the combination of the TPA-induced reflectivity rollover in the SESAM and the gain rollover induced by the limited available gain bandwidth. In particular, in the case of a strong gain rollover, e.g. in Yb:YAG or Yb:LuO, the SESAM has to be operated in the rising part of the nonlinear reflectivity curve in order to compensate for the decreasing gain of the soliton pulse.

Concerning the results of our numerical simulations, a few remarks should be added:

1. Here we increased the modulation depth while keeping all other SESAM parameters (except the nonsaturable losses) constant. The question could be raised, whether a global optimization of all the SESAM parameters could result in a smaller modulation depth supporting the 200-fs pulses. From a SESAM design standpoint, the relevant parameter is the number of QWs in the SESAM structure, which determines the product $F_{\text{sat}} \cdot \Delta R$, as well as the nonsaturable losses and rollover coefficient in typical SESAM designs (see chapter 5). We found that the presented optimization leads to an $F_{\text{sat}} \cdot \Delta R$ product close to minimal, i.e. other combinations result in larger $F_{\text{sat}} \cdot \Delta R$ values, which corresponds to technically more challenging SESAM structures.
2. The rollover coefficient F_2 was kept constant, however an increase of ΔR is achieved by including more QWs in the SESAM structure, which will tend to decrease the rollover coefficient F_2 (see chapter 5), leading to a stronger and earlier SESAM rollover. In the regime of strong gain rollover, the SESAM rollover is not the dominant contribution to the cavity rollover, however the strong TPA in the SESAM will still contribute to shifting the cavity rollover to lower powers and longer pulse durations and additionally lead to a large heat load on the SESAM.
3. The high linear losses of the SESAM would result in a large heat load in cw operation, which would be difficult to evacuate with the current cooling techniques. Additionally, the large modulation depth of the SESAM would increase tendency to operate in the Q-switching regime, particularly since the SESAM needs to be operated still on the rising edge of the nonlinear reflectivity curve (see figure 3.2(d)).

In conclusion, our numerical simulations show that the SESAM parameters required to achieve high-power modelocking at 100 W with 200-fs pulses and sufficient pulse energy to generate high-peak powers >40 MW with Yb:YAG or Yb:LuO pose several technical challenges:

1. the required modulation depth leads to $F_{\text{sat}} \cdot \Delta R$ products of order $\approx 20\text{-}30 \mu\text{J}/\text{cm}^2$, while typical high-power SESAMs currently have an $F_{\text{sat}} \cdot \Delta R$ product of order $1 \mu\text{J}/\text{cm}^2$. The number of QWs necessary to achieve such a high modulation depth would require very careful

strain-compensation of the epitaxial layers and is beyond what has been demonstrated so far in terms of SESAM growth [122],

2. the SESAM would be subject to a significant heat load of a few tens of Watts, which would require an efficient cooling scheme that could involve direct cooling of the SESAM front face.

Therefore, high-peak-power SESAM-modelocking at short pulse durations around 200 fs currently seems difficult to realize with Yb:YAG or Yb:LuO, and Yb:CALGO is the most promising candidate material for this purpose. However, the quality of Yb:CALGO disks remains limited to this day and power-scaling Yb:CALGO TDLs to 100 W has not been demonstrated yet (see chapter 4). In chapters 5 to 7, we present alternative approaches towards the goal of high-peak-power modelocking at short pulse durations with Yb:YAG and Yb:LuO, addressing the main challenges discussed in this chapter: the TPA-induced rollover in the SESAM (chapter 5), the limited gain bandwidth (chapter 6) and the moderate modulation depth of SESAMs (chapter 7).

Thin-disk lasers based on Yb:CALGO

4.1 Properties of Yb:CALGO

The gain material Yb:CALGO is amongst the most promising Yb-doped materials for the generation of ultrashort pulses <100 fs, due to its broad emission bandwidth of ≈ 80 nm (see figure 1.4(a) in chapter 1). Although the spectroscopic properties of the CALGO crystal were investigated for various doping ions (Nd^{3+} , Ti^{3+} , Er^{3+}) in the late 1990s [123–125], the first crystal growth and characterization of Yb-doped CALGO was reported in 2005 [126]. Besides the large emission bandwidth, Yb:CALGO has a comparably high thermal conductivity (see figure 1.4(a) in chapter 1) and favorable thermo-optic properties [126, 127]. Additionally it can be grown by the well-established Czochralski method and is easily polished [126], making it well-suited for use in the thin-disk geometry.

Yb:CALGO is a uniaxial crystal and can be found in two different cuts for laser applications, as illustrated in figure 4.1(a):

- the **c-cut** is obtained by cutting the crystal perpendicular to its optical axis (*c*- or π -axis), such that the laser beam propagates along the *c*-axis and the thermal, optical and mechanical properties of the crystal are isotropic in the transverse plane (along the *a*- or σ -axes);
- the **a-cut** is realized along the optical axis, such that the laser beam propagates along one *a*-axis and experiences anisotropic properties in the transverse plane given by one *a*-axis and the *c*-axis.

The optical, mechanical and thermal properties of Yb:CALGO along the σ - and π -axes are given in table 4.1, and the gain cross-section for both axes is shown in figure 4.1(b).

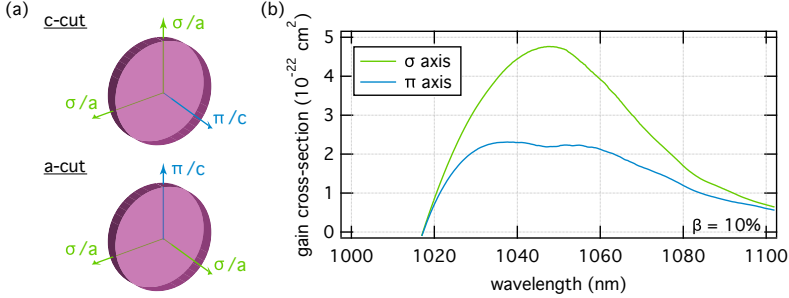


Figure 4.1 – Illustration of the two disk cuts and simulated gain cross-section of Yb:CALGO for the σ and π axes. (a) Illustration of the c- and a-cuts. (b) Simulated gain cross-section for the σ and π axes at a typical inversion level of 10%

	σ axis	π axis
Thermal conductivity (W/(m·K))	≈ 4.0	≈ 3.6
Thermal expansion coefficient (10^{-6} K^{-1})	10	16
Thermo-optic coefficient dn/dT	-7.6	-8.6
Pump absorption cross-section (10^{-20} cm^2)	1.3	3.7
Peak gain cross-section (10^{-22} cm^2), $\beta = 10\%$	4.8	2.3
FWHM gain bandwidth (nm), $\beta = 10\%$	47	59

Table 4.1 – Properties of Yb:CALGO for an Yb-doping concentration of ≈ 5 at.%. References [112,127,128].

In the c-cut, the disk is isotropic in the transverse plane and the thermal lens is expected to be radially symmetric. The unpolarized pump beam and the polarized laser beam experience the crystal properties along the σ -axes of the crystal. Although the σ -axis exhibits a smaller pump absorption cross-section and narrower gain bandwidth than the π -axis, it offers the highest gain (see table 4.1). The c-cut therefore appears as a good candidate for high-power laser applications.

In the a-cut, the disk provides access to both crystal axes for the pump

and laser beams. This results in a high pump absorption cross-section and gives access to the broad and flat gain cross-section along the π -axis (see figure 4.1(b)) [128]. On the downside, the gain is reduced along the π -axis and the disk exhibits anisotropic thermal properties in the transverse plane. Although the thermal lens is somewhat reduced in the a-cut [127], this anisotropy leads to an astigmatic thermal lens that could limit the laser performance at high pump powers [91].

4.2 Modelocked lasers based on Yb:CALGO

The first modelocked laser oscillators using Yb:CALGO as gain materials were based on the bulk, or solid-state, technology. Many of these oscillators operated at an average power around 1 W with short pulses <200 fs, as illustrated in figure 4.2. The highest average power achieved in the bulk geometry was 12.5 W with a pulse duration of 95 fs, reported in 2012 [129], and remained the highest average power demonstrated at sub-100-fs pulse duration until recent KLM experiments with Yb:LuO in the thin-disk geometry [109].

The first thin-disk laser based on Yb:CALGO was reported in 2011

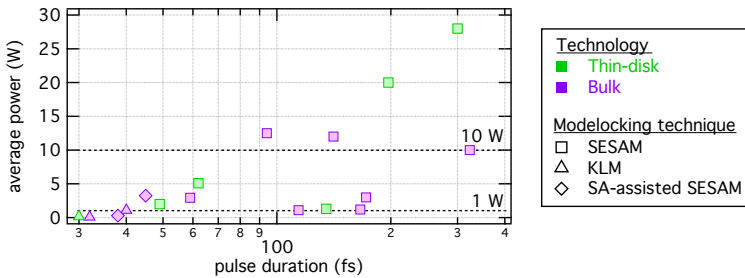


Figure 4.2 – Overview of the performance of modelocked oscillators based on Yb:CALGO. The output average power of modelocked oscillators using Yb:CALGO as gain material is shown against the pulse duration. The marker color indicates the laser technology, bulk (purple) or thin-disk (green) and the marker shape indicates the modelocking technique: SESAM modelocking (square), KLM (triangle) or soft aperture (SA)-assisted SESAM-modelocking. References [91–93, 129–134]

[135], followed by the first modelocking results one year later [91]. Using an a-cut 2 at.%-doped 350- μm Yb:CALGO disk and SESAM modelocking, high average powers up to 28 W with 300-fs pulses and 20 W with 197-fs pulses were demonstrated at a repetition rate of 21 MHz. Following results focused on reducing the pulse duration achievable in TDLs. With SESAM-modelocking, a pulse duration of 62 fs was demonstrated at an average power of 5 W [92], and pulses as short as 49 fs were obtained at 2 W of average power [101]. These are the shortest pulses generated in a SESAM-modelocked TDL oscillator. First KLM operation of an Yb:CALGO TDL was demonstrated in 2018 and yielded 30-fs pulses [109], which are the shortest pulses demonstrated with Yb:CALGO. The average power was however limited to 150 mW.

Thin-disk lasers based on Yb:CALGO have shown promising results in terms of modelocked average power (up to 28 W) and short pulse durations (down to sub-50 fs). During this thesis, we investigated thin-disk laser operation with Yb:CALGO with the goal to scale the average power towards the 100-W regime.

4.3 Investigation of thin-disk laser operation using Yb:CALGO

In the course of this thesis, we tested disks coming from different Yb:CALGO boules produced between June 2012 and October 2017, with different doping concentrations and disk thicknesses. In order to keep isotropic material properties in the transverse plane and maximize the gain of the disk, we were primarily interested in c-cut disks. From a total of ≈ 70 disks, we selected 9 disks to be tested in laser operation by visual inspection, as described in section 4.3.1. The properties and laser performance of the tested disks are given in table 4.2. The disk properties were chosen for high-power TDL operation and in consideration of the availability and quality of the grown material at the time of acquisition:

- high-doping concentration for a high gain,
- reduced disk thickness for efficient heat removal,
- large disk area for power scaling with large beam sizes.

After visual inspection, the selected disks were coated (Layertec GmbH) and contacted onto a diamond heatsink (Dausinger + Giesen GmbH or TRUMPF Scientific Lasers GmbH + Co. KG), then tested in laser operation.

As a remark, we also selected two 6.2 at.-%-doped, 150- μm -thick a-cut disks to be tested, however the contacting of these disks failed due to breaking of the disk or peeling of the coating. Although the exact reason for this failure remains unclear, this could be explained by the different mechanical and adhesion properties of the disk along the two different crystal axes, according to discussions with the involved parties.

Disk	1	2	3	4	5	6	7	8	9
Batch	Jun 12				Sep 14 (UH)		May 15		Oct 17
N_{dop} (at.%)	4.6	4.6	4.6	4.6	5.4	3.4	3.4	6.6	6.2
$\alpha_{\text{p, a}}$ (cm^{-1})	7.8	7.8	7.8	7.8	n.a.	5.7	5.7	11.2	10.5
D_{disk} (mm)	6	6	6	6	6	9.3	9.3	9.3	12
l_{disk} (μm)	135	227	223	430	120	120	150	120	160
Heatsink	Dia.	Dia.	Cu	Dia.	Dia.	Dia.	Dia.	Dia.	Dia.
$P_{\text{max,sm}}$ (W)	21.1	4.5	12.8	18.4	7.9	22.1	7.0 ^(a)	5.2	18.2
$T_{\text{OC,sm}}$	1.0%	1.7%	3.0%	3.0%	0.9%	1.6%	0.8% ^(a)	1.3%	1.8%

Table 4.2 – Properties and cw laser performance in singlemode operation of the Yb:CALGO disks tested during this thesis. All disks presented in this table are c-cut. The disks were produced and polished by FEE GmbH (now a division of Electro-Optics Technology, Inc.), except for the disk 5 produced at the Universität Hamburg by the group of Prof. Dr. Günter Huber. We also note that the disk 3 was contacted on a copper heatsink. ^(a)The disk 7 was used by the group of Prof. Thomas Südmeyer at the Université de Neuchâtel for the first demonstration of a KLM Yb:CALGO TDL. The laser tests in singlemode cw operation were done with a hard aperture inside the cavity as described in [109].

4.3.1 Visual inspection of the disks

In order to determine the most promising disks for laser operation, we inspected the Yb:CALGO disks as received from the manufacturer with a microscope (Nikon Eclipse L200) under different illuminations:

- in bright field (BF) illumination, large absorbing defects are made visible,
- in dark field (DF) illumination, scattering defects and the “graininess” of the disk are made visible,
- in cross-polarized light (XPL) illumination, defects or impurities leading to a depolarization are revealed.

The rather low crystal quality of Yb:CALGO is attributed to the presence of scattering and color centers [136–138]. The scattering centers have a detrimental effect on the optical-to-optical efficiency in laser operation and the color centers introduce additional decay channels that result in an increased heat load and a reduced upper-state lifetime [137]. The color centers lead to a yellow-brown coloration of the crystal. We highlight that the aim of our inspection of the disks was to determine the most suitable disk for laser operation by comparison of the number and size of the observed defects between different disks, and not a careful study of these defects.

In figure 4.3, we show example images obtained with the disks 7-9 (see table 4.2):

- disk 7 is from the most recent batch of low-doping disks tested during this thesis (May 2015), with a Yb-doping concentration of 3.4%,
- disk 8 originates from one of the first boules grown with a high Yb-doping concentration of 6.6% (May 2015),
- disk 9 was prepared from recent material (October 2017) grown with a high doping concentration of 6.2%.

In particular, the disks 7 and 8 are both originating from boules that exhibited the yellow-brown coloration attributed to color centers, while disk 9 originates from a clear, transparent boule.

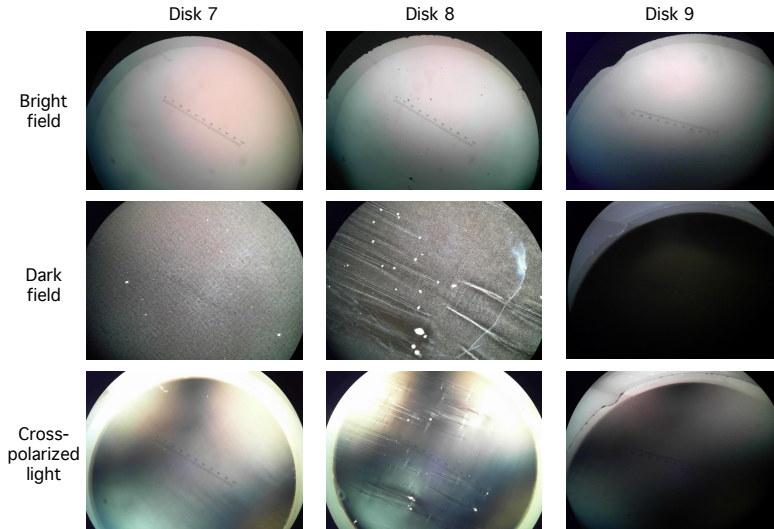


Figure 4.3 – Microscope images of Yb:CALGO disks observed under different illumination conditions.

The low-doping material (disk 7) does not have any visible defects under BF illumination, and few defects under DF illumination. The XPL image shows a slight waviness, which was also observed in other samples. The first batch of high-doping material (disk 8) clearly exhibits many large scale defects or impurities visible both in the BF and DF images. The patterns observed in the DF image are also found in the XPL image, highlighting the strong inhomogeneity of the material. In contrast, the newly produced high-doping material (disk 9) shows close to no defects and very little structure in all three illumination modes. This is the result of significant improvements of the crystal growth. The defects observed in the microscope images are also visible by looking at the disk illuminated at the pump or laser wavelength. However, additional defects only visible when illuminated at the laser wavelength later became apparent, as discussed in section 4.3.2. This suggests that for the most accurate determination of disk quality, illumination at the laser wavelength should also be considered.

4.3.2 Laser operation

After coating and contacting of the selected disks reported in table 4.2, we characterized the temperature rise and thermal lensing of the disks in fluorescence operation, and built a TDL cavity to test the disks in cw operation.

For the thermal measurements, we pump the disk without laser cavity and measure the maximum temperature rise compared to the unpumped disk as a function of the pump power with a thermal camera (FLIR SC640). The results of the thermal measurements are shown in figure 4.4(a). The lower-doped disks generally heat up less than the disks with higher doping concentrations. This additional heat load seems to be mainly related to the worse crystal quality of highly-doped Yb:CALGO material. Indeed it is interesting to compare the disks 8 and 9, with a similarly high doping concentration but very different crystal qualities (see figure 4.3). Disk 9, from the new batch of highly-doped material, is mostly free of defects and heats up significantly less than the disk 8.

For testing the disks in laser operation, we built a cw laser cavity with a single reflection of the intracavity beam on the disk and optimized it to obtain singlemode operation ($M^2 < 1.1$) for each disk. We then tested the performance of the laser for different transmissions of the OC mirror and we show the power slope yielding the highest output power in figure 4.4(b). The maximum output power and the corresponding OC transmission are additionally reported in table 4.2. For these laser experiments, the pump power was increased until the output power began to saturate, or the cavity mode became too unstable. The best results were obtained with the low-doped disks 1, 4 and 6, and with the new high-doped disk 9, all delivering average powers > 18 W. However it should be noted that the cavity mode was flickering significantly with the highly-doped disk 9 and alignment was made difficult by scattering defects (not visible in figure 4.3) that became apparent at the laser wavelength.

Using a cavity with a double reflection on the disk, we obtained slightly higher powers up to 25-30 W with the disks 1, 4 and 9. However, the output power in these experiments is mainly limited by thermal issues:

- likely due to the defects, particularly in the case of highly-doped material, and leading to hot spots that destabilize the cavity mode at high pump powers,
- due to the large thermal lensing of the disk, particularly for the thicker disks at low doping concentrations, which reduces the range of pump powers over which the cavity is stable [139].

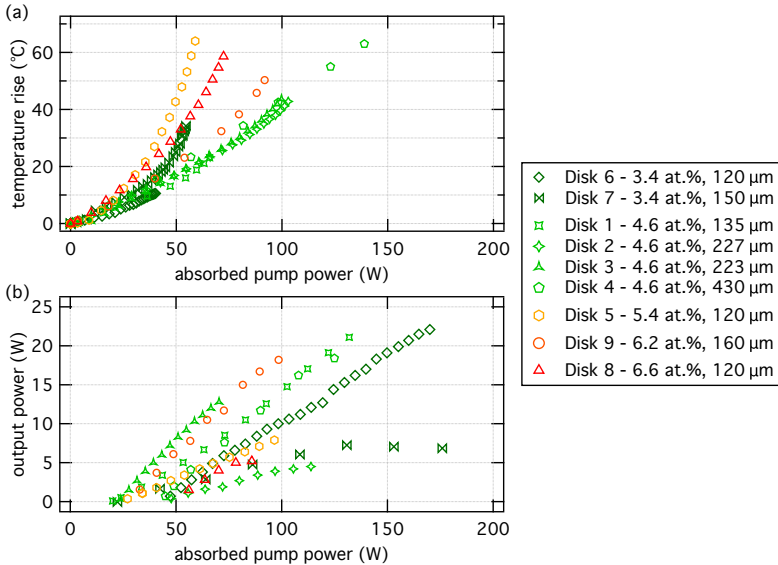


Figure 4.4 – Temperature rise in fluorescence operation and output power in cw operation with the different Yb:CALGO disks. All disks were pumped using a 400-W VBG-stabilized pump diode emitting at 979 nm. The pump spot diameter on the disk was 2.5-2.6 mm. The temperature rise and the output power are plotted against the absorbed pump power in order to account for different number of pump passes depending on the TDL head used with each disk. The marker color corresponds to the doping concentration, from low-doping (green) to high-doping concentrations (red) and the disks are listed by increasing doping concentration in the legend. **(a)** Temperature rise of the pumped disk in fluorescence operation as a function of the absorbed pump power. **(b)** Output power in singlemode cw operation ($M^2 < 1.1$) as a function of the absorbed pump power. The OC transmission is reported in table 4.2

With the limited power available in cw operation, we could obtain mode-locking at reduced average powers ≤ 10 W with the low-doped disks 1, 3

and 4, and with the highly-doped disk 9.

4.4 Conclusion

We inspected and tested several Yb:CALGO disks in TDL operation, originating from different boules grown between June 2012 and October 2017. We observed a net improvement of the crystal quality over this period. The coloration of the crystal, attributed to the presence of color centers, and the density of defects observed in the disks were successfully reduced in the latest batch of disks. The improvement is particularly striking for highly-doped material.

In terms of thermal management and laser operation, low-doped Yb:CALGO disks (≤ 5 at.%) currently provide the best results and we obtained cw operation in a single-pass TDL cavity with average powers >20 W. The low-doping however requires thicker disks in order to operate with cavity losses of order few percents. This results in a larger thermal lensing limiting the laser performance. On the other hand, we obtained promising results with recent 6.2 at.%-doped material, with up to 18.5 W in cw operation. The laser performance was limited in this case by thermal effects induced by defects and destabilizing the cavity mode.

The better high-power suitability of low-doping material is confirmed by the early modelocking results that demonstrated 28 W of modelocked average power [91], for which a 2 at.%-doped, 350- μm -thick a-cut disk was used. We planned on testing 6.2 at.%-doped, 150- μm -thick a-cut disks, however the contacting process failed, likely due to the anisotropic properties of the a-cut.

Scaling Yb:CALGO TDLs to the 100-W regime is currently challenging due to the limited quality of the material over large areas required for high-power TDL operation. With the current limitation in usable pump power due to thermal effects, a possible scheme to scale the output power would be to combine several disks in one cavity, as demonstrated in [101]. On the material side, the progress made over the last few years in the growth of highly-doped material still offers perspectives of high-quality, highly-doped Yb:CALGO disks in the near future.

SESAM with reduced two-photon absorption

One limitation when targeting high-power and short-pulsed modelocked operation is the ISA leading to a decrease of the SESAM nonlinear reflectivity at high pulse energies and short pulse durations. This effect, illustrated in figure 5.1 is called rollover. The rollover leads to a reduction of the effectively available modulation depth and an increase of the effective losses of the SESAM. Furthermore, the optimal operation point is shifted to lower pulse energies. This limits the maximum performance in terms of high average power and short pulse duration, and increases the heat load on the SESAM potentially leading to strong thermal lensing and beam distortions. It is therefore of interest to study this rollover and investigate potential SESAM designs where this effect is mitigated.

In the picosecond regime, the rollover is attributed to a combination of TPA and some additional mechanisms not clearly identified yet, possibly free-carrier absorption, Auger recombination or hot-carrier generation [68]. In the sub-ps regime, the rollover is dominated by TPA and we consequently focus on the reduction of TPA in typical SESAM structures used in high-power TDLs.

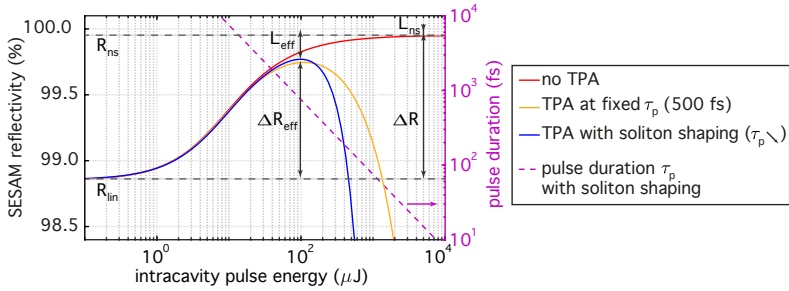


Figure 5.1 – Simulated nonlinear reflectivity curves of a typical high-power SESAM. We simulate the nonlinear reflectivity curve of a typical high-power SESAM as used in our peak-power scaling experiments with Yb:LuO in section 2.2. The Gaussian beam waist on the SESAM is 1.3 mm. We simulate the nonlinear reflectivity in different cases: without TPA effect (orange), for a fixed F_2 value corresponding to a pulse duration of 500 fs (yellow) and finally accounting for soliton shaping, for a given intracavity dispersion and nonlinearity (purple) (see equation (1.2) in chapter 1). The soliton pulse duration is plotted in a pink dashed line and reaches 500 fs for an incident pulse energy of 150 μJ . The reduced effective modulation depth ΔR_{eff} and increased losses L_{eff} compared to the specified modulation depth ΔR and nonsaturable losses ΔR_{ns} are indicated at the rollover point. Adapted from the publication presented in section 2.2

5.1 Two-photon absorption in typical high-power SESAMs

A typical design for a high-power SESAM used in TDL oscillators is depicted in figure 5.2. The SESAM structure is grown on a GaAs wafer by molecular beam epitaxy (MBE) and includes the following layers:

1. A distributed Bragg reflector (DBR) consisting of 30 pairs of AlAs/GaAs quarter-wave ($\lambda/4$) layers providing a high reflectivity $R_{\text{DBR}} > 99.9\%$.
2. An absorber section consisting of InGaAs QWs embedded in AlAs and generally positioned at an antinode of the standing-wave pattern of the electric field in the structure. The number of QWs determines the product $F_{\text{sat}} \cdot \Delta R$ [140].

Additionally, dielectric topcoatings (not shown in figure 5.2) can be deposited on the SESAM structure in order to modify the strength of the electric field in the QW layers and thus change the saturation properties of

the SESAM, i.e. increase of decrease the saturation fluence of the SESAM (note that the modulation depth will be decreased on increased accordingly, such that the product $F_{\text{sat}} \cdot \Delta R$ stays constant).

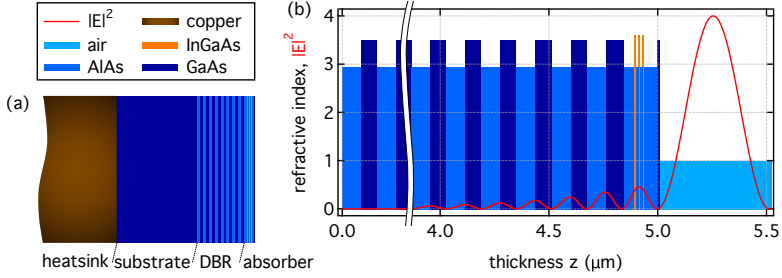


Figure 5.2 – Typical SESAM design for use in high-power TDLs. (a) Illustration of the full SESAM structure as used in a laser oscillator. The thickness of the different layers is not to scale. The SESAM consists of a DBR and an absorber section grown by epitaxy ($\approx 5 \mu\text{m}$ thick) on a GaAs wafer ($\approx 600 \mu\text{m}$ thick). The resulting semiconductor chip is contacted on a copper heatsink ($\approx 3 \text{ mm}$ thick) for heat removal and temperature control. **(b)** Illustration of the epitaxially-grown layers and the standing-wave pattern of the electric field. The electric field squared is normalized to 4 outside of the SESAM structure. The three InGaAs QWs are positioned at an antinode of the standing wave pattern. The illustrated design does not include additional dielectric topcoatings.

In order to investigate the various contributions to the TPA process within the SESAM structure, we use the nonlinear reflectivity model function of the SESAM expressed as a function of incident fluence and peak intensity [87, 120]:

$$R(F_p, I_p) = R_{\text{ns}} \frac{\ln \left(1 + R_{\text{lin}} / R_{\text{ns}} \left(e^{F_p / F_{\text{sat}}} - 1 \right) \right)}{F_p / F_{\text{sat}}} \cdot e^{-I_p / I_2} \quad (5.1)$$

The first term of equation (5.1) describes the saturable absorption of the QWs, and the second term describes the TPA-induced rollover, characterized by the rollover intensity I_2 given by [87]:

$$I_2 = \frac{1}{0.665 \int \beta_{\text{TPA}}(z) n^2(z) |\epsilon(z)|^4 dz} \quad (5.2)$$

where β_{TPA} is the TPA coefficient, n is the refractive index, $|\varepsilon|^4$ is the normalized field intensity and z is the position within the SESAM structure along the growth direction.

To characterize the TPA contribution of the different epitaxial layers, we define an effective TPA coefficient inside the SESAM structure as:

$$\beta_{\text{TPA,eff}}(l) = \frac{1}{l} \int_0^l \beta_{\text{TPA}}(z) n^2(z) |\varepsilon_n(z)|^4 dz \quad (5.3)$$

And the rollover intensity I_2 is therefore given by:

$$I_2 = \frac{1}{0.665 \beta_{\text{TPA,eff}}(l_{\text{SESAM}}) l_{\text{SESAM}}} \quad (5.4)$$

Where l_{SESAM} is the total thickness of the epitaxially grown layers.

Equations (5.1) and (5.2) highlight the fact that for a given incident peak intensity on the SESAM, the TPA-induced losses depend on the TPA coefficients $\beta_{\text{TPA}}(z)$ of the materials used in the SESAM layers, and the strength of the electric field intensity $|\varepsilon(z)|^4$ within the structure. In order to minimize the effect of TPA, it is therefore desirable to use high-bandgap materials (with a low β_{TPA}), particularly in the layers where the field is the highest. In table 5.1 we report the bandgap energy and TPA coefficient of typical semiconductor and dielectric materials used in SESAM structures and topcoating layers. The InGaAs QWs have a high TPA coefficient and are usually located close to an antinode of the standing-wave pattern of the electric field in the structure. A large TPA contribution can therefore be expected from the QWs.

In order to quantify the TPA contribution of the different layers in the SESAM structure, we calculate the effective TPA coefficient defined in equation (5.3) as a function of the epitaxial layers (i.e. the position inside the SESAM structure along the growth direction) and show the result in figure 5.3 for two different SESAM structures:

1. A standard SESAM with 3 QWs embedded in AlAs and positioned at an antinode of the standing-wave pattern of the electric field. This structure will be referred to as 1x3 QWs. This is a typical SESAM

Material	Refractive index	Bandgap energy (eV)	TPA coefficient (cm/GW)
GaAs	3.50	1.4	27
AlAs	2.94	2.2	6
InGaAs	3.61	1.3	30
AlGaAsP	2.92	2.2	5
SiO ₂	1.48	9.1	0
Si ₃ N ₄	1.90	5.0	0
Ta ₂ O ₅	2.15	4.2	0

Table 5.1 – Refractive index, bandgap energy and TPA coefficient of typical semiconductor and dielectric materials used in SESAM structures and topcoating layers. The refractive indices and TPA coefficients are given for a wavelength of 1020 nm. As a reference, the photon energy at 1020 nm is 1.2 eV. For InGaAs, we consider an indium fraction of 25%, and for AlGaAsP, we consider a phosphorus fraction of 11% as used for QWs operating at 1020 nm [122].

design used in high-power TDL oscillators (optionally with the addition of dielectric topcoatings) [16,76,141].

2. A SESAM incorporating 6 QWs, each positioned at an antinode of the electric field, as recently investigated in [122]. The QWs are embedded in a combination of AlAs and AlGaAsP layers. The additional AlGaAsP layers are designed to compensate the strain accumulated in the QW layers due to lattice mismatch [122]. This strain compensation is needed to achieve a good surface quality of the SESAM chip. This structure with the strain compensated (SC) QWs will be referred to as 6x1 SCQWs.

SESAM	Calculated rollover intensity (TW/cm ²)	
	Semiconductor DBR 30x AlAs/GaAs	Dielectric DBR 12x SiO ₂ /Ta ₂ O ₅
1x3 QWs	3.1	6.9
6x1 SCQWs	1.3	1.6

Table 5.2 – Rollover intensity I_2 estimated for a 1x3 QWs and a 6x1 SCQWs SESAM with a standard AlAs/GaAs semiconductor DBR or a SiO₂/Ta₂O₅ dielectric DBR.

It is interesting to compare the TPA contributions in these two struc-

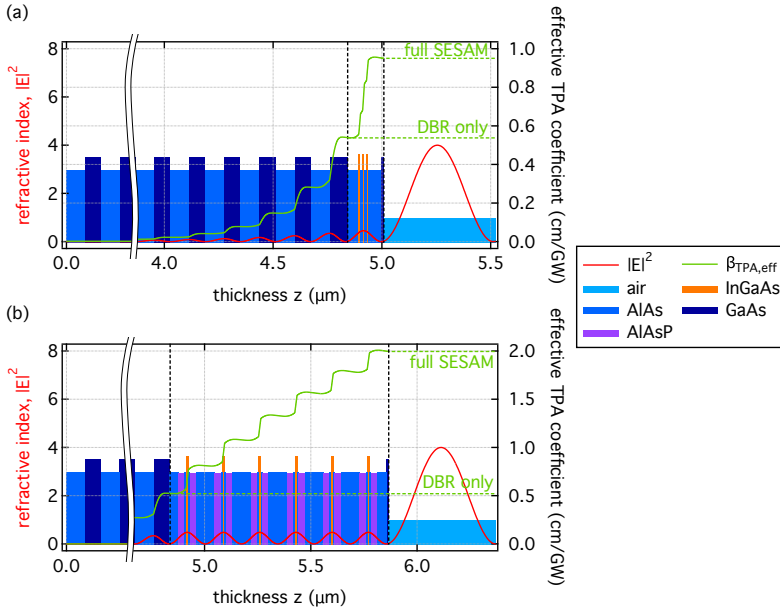


Figure 5.3 – TPA contributions in a standard SESAM with 1x3 QWs and in a SESAM with 6x1 SCQWs. The refractive index and standing-wave pattern of the electric field inside the structure are represented on the left axis. The effective TPA coefficient is represented on the right axis as a function of the epitaxial layers. The contribution of the DBR only is indicated by the dashed line. **(a)** Standard SESAM structure with 3 QWs positioned at one antinode of the electric field (1x3 QWs). **(b)** SESAM structure with 6 QWs, each positioned at a separate antinode of the electric field, and surrounded by strain-compensating layers of AlAsP (6x1 SCQWs).

tures. Both SESAMs have the same DBR with 30 pairs of AlAs/GaAs and the effective TPA coefficient of the DBR is indeed very similar in both structures (≈ 0.5 cm/GW). This amounts to $>50\%$ of the total effective TPA coefficient in the 1x3 QWs structure, but only $\approx 25\%$ in the 6x1 SCQWs SESAM, the remaining contributions originating mainly from the QWs. The combination of a larger effective TPA coefficient and thicker structure in the case of the 1x6 SCQWs leads to a reduced rollover intensity I_2 by more than a factor of 2 compared to the 1x3 QWs SESAM (see table 5.2). This highlights a trade-off between obtaining a large modulation depth by increasing the number of QWs and minimizing TPA.

5.2 SESAM with reduced two-photon absorption

In order to reduce the TPA-induced rollover in the SESAM, we suggest replacing the semiconductor DBR with a TPA-free dielectric DBR, using for example 12 pairs of $\text{SiO}_2/\text{Ta}_2\text{O}_5$ ($R > 99.98\%$ at 1020 nm). The TPA contribution of the semiconductor DBR is then cancelled and we expect an improvement of the rollover intensity as reported in table 5.2. Particularly in the case of the 1x3 QWs structure, we expect an improvement of the rollover intensity by a factor ≈ 2.2 .

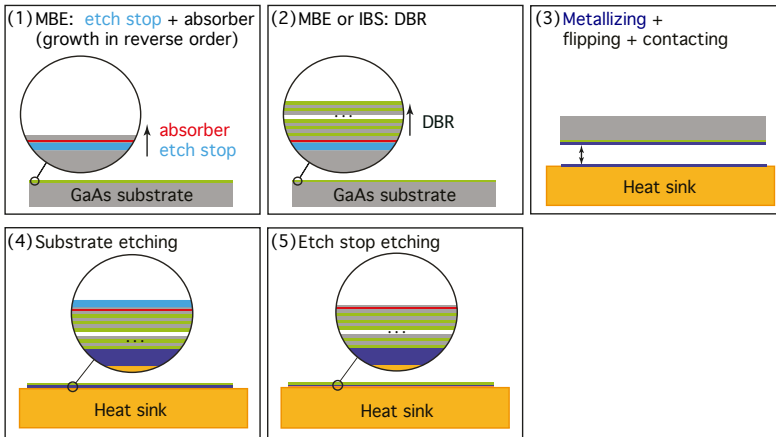


Figure 5.4 – Growth and processing of the SESAM structures used in our TPA reduction study. (1) An etch stop layer and the absorber section of the SESAM are grown on a GaAs substrate by upside-down MBE growth, i.e. the layers are grown in the order of decreasing z . (2) A DBR is grown (still in reverse order) on top of the previous layers, either by MBE for a semiconductor DBR or by ion-beam sputtering (IBS) for a dielectric DBR. (3) The as-grown SESAM structure is metallized and vacuum soldered to a copper heatsink. (4)-(5) Two separate steps of wet etching remove the GaAs wafer and the etch stop layer. Adapted from [62]

Following the procedure illustrated in figure 5.4, we grew and prepared two samples of 1x3 QWs and 6x1 SCQWs SESAMs, one including a semiconductor DBR and the other a dielectric DBR. We then characterized the nonlinear reflectivity of these samples following the procedure presented in [120]. Due to the limited available pulse energy for carrying

out the measurement (of order 10 nJ), we took the following two steps in order to reach sufficiently high fluences to sample the rollover:

1. We used a tight focus with a measured beam radius of 12 μm on the samples.
2. We deposited an extra $\lambda/4$ layer of silicon nitride Si_3N_4 on the SESAMs in order to increase the field strength in the QWs.

The measured nonlinear reflectivity curves of the SESAM samples are shown in figure 5.5(a). Additionally we measured the reflectivity of the semiconductor and dielectric DBRs (without the absorber section) as a function of the incident fluence and show the results in figure 5.5(b). The measured reflectivities are fitted with the SESAM model function (equation (5.1) and with $R_{\text{DBR}}(I_p) = R_{\text{lin}} \cdot e^{-I_p/I_2}$ for the DBRs, and the resulting fit parameters are given in table 5.3.

For the 1x3 QWs and the 6x1 SCQWs structures, the retrieved saturation fluence, modulation depth and nonsaturable losses are comparatively similar for both DBR types, as expected. For the 1x3 QWs SESAM, we obtain an improvement of the rollover intensity I_2 by a factor ≈ 2.8 using the dielectric DBR, comparable to the expected value (≈ 2.2 , see table 5.2). This results in an increase of the optimal pulse fluence F_0 by a factor ≈ 1.7 (at a pulse duration of 170 fs). For the 6x1 SCQWs SESAM, the rollover intensity is close to identical with both DBRs, and the optimal pulse fluence F_0 is slightly higher with the dielectric DBR by a factor ≈ 1.2 . This small change could be due to slightly different field enhancement values in the QWs of both structures. Our results are consistent with the expected smaller reduction of the TPA in this structure. Additionally, we observe a clear suppression of ISA effects in the dielectric DBR, as shown in figure 5.5(b). The lower reflectivity of the dielectric DBR compared to the semiconductor DBR is attributed to some residual dirt on the surface of the samples that could not be removed before deposition of the dielectric layers.

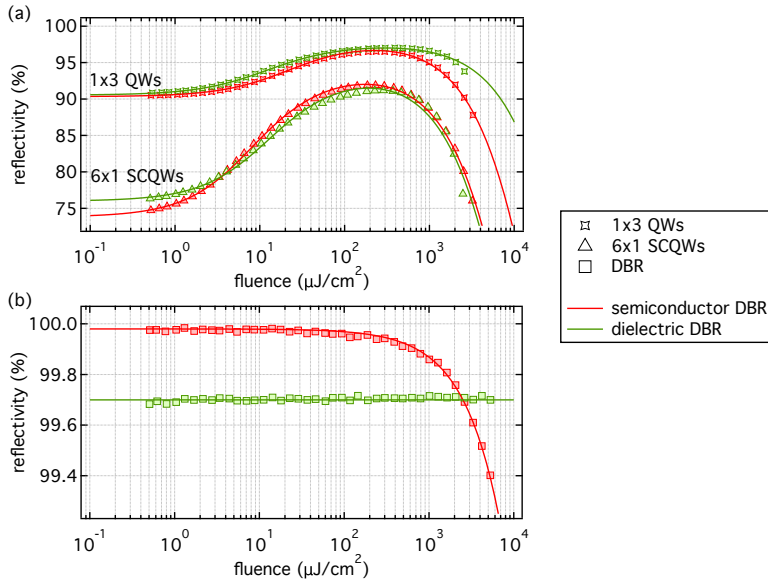


Figure 5.5 – Nonlinear reflectivity measurements and theoretical fits of the SESAM structures and DBRs prepared for the TPA reduction study. The markers indicate the structure for which the curve was measured and the colors indicate the type of DBR. (a) Nonlinear reflectivity of the full SESAM samples 1x3 QWs and 6x1 SCQWs. (b) Nonlinear reflectivity of the DBRs. The data is acquired following the approach presented in [120] and the retrieved fit parameters are summarized in table 5.3. The laser used for the measurement operates at a center wavelength of 1020 nm and delivers 170 fs pulses.

	1x3 QWs		6x1 SCQWs		DBR	
	Semic.	Dielec.	Semic.	Dielec.	Semic.	Dielec.
F_{sat} ($\mu\text{J}/\text{cm}^2$)	13	7	4	7		
ΔR	8.0%	7.3%	20.6%	18.4%		
ΔR_{ns}	1.6%	2.1%	5.6%	5.7%		
R_{lin}	90.4%	90.6%	73.8%	75.9%	99.98%	99.70%
I_2 (GW/cm^2)	155	432	80	74	4660	$> 10^6$
F_0 ($\mu\text{J}/\text{cm}^2$)	235	391	231	287		

Table 5.3 – Least-square fit parameters retrieved from the measured nonlinear reflectivity curves of the 1x3 QWs, 6x1 SCQWs and the DBR samples. The parameter F_0 , corresponding to the fluence yielding the highest reflectivity value, is given for a pulse duration of 170 fs.

5.3 Conclusion

We have presented an analysis of the TPA contributions in SESAM structures. The QW layers, designed to provide saturable absorption, have the largest contribution to TPA compared to the other epitaxial layers. In SESAM designs including a large number of QWs, typically more than three, the TPA process taking place in the QWs is the largest contribution to the total TPA in the SESAM structure. This aspect is of crucial importance when considering SESAM designs for high-power and short-pulsed modelocking, since an increase in the number of QWs, required to achieve larger modulation depths, will inevitably result in an increase of the TPA and consequently an earlier SESAM rollover. For SESAM designs including up to three QWs, the TPA contribution from the semiconductor DBR is about 50% of the overall TPA and significant TPA reduction can therefore be achieved by replacing the semiconductor DBR with a TPA-free dielectric DBR.

To confirm our analysis, we grew, prepared and characterized SESAM samples with 3 QWs in one antinode of the electric field, or 6 QWs each positioned at a separate antinode of the electric field, and either a semiconductor or a dielectric DBR. With the 1x3 QWs design, we obtained an improvement of the rollover intensity I_2 by a factor ≈ 2.8 using a dielectric DBR, resulting in an increase of the optimal fluence F_0 by a factor ≈ 1.7 . With the 6x1 SCQWs design, we obtained very similar SESAM parameters for both types of DBR and no clear reduction of the TPA, as expected.

The structures grown during our studies were unfortunately contaminated between the absorber and the DBR growth, which led to uneven etching results and only small usable areas. As a result, we could not test these structures inside a laser resonator, however we are confident that this technical issue can be addressed in future growth runs.

In conclusion, we demonstrated an efficient approach to mitigate the TPA-induced rollover for SESAM designs with a moderate number of QWs. This could result in improved laser performance in terms of average power by a factor up to ≈ 1.7 , in particular in modelocking experiments with a moderate amount of gain rollover, and contribute to pushing

the performance of SESAM-modelocked TDLs towards higher powers and shorter pulse durations.

Gain-matched mirrors

6.1 Roundtrip gain flattening by intracavity optics

The gain bandwidth of laser materials plays an essential role in determining the shortest pulse duration that can be achieved in a modelocked laser oscillator. A broad gain bandwidth is crucial to efficiently generate ultrashort pulses and considerably relaxes the requirements on the saturable absorber. A striking example in the bulk (or solid-state) geometry is Ti-doped Sa, with a gain bandwidth spanning ≈ 400 nm centered around 800 nm, that allowed for the generation of ultrashort pulses < 10 fs [142–144]. However, Ti:Sa oscillators typically deliver average powers limited to a few Watts. High-power laser oscillators rely on diode-pumped Yb-doped gain materials with narrower gain bandwidths (see figure 1.4 in chapter 1). Amongst Yb-doped materials, those with a broader gain bandwidth (e.g. Yb:CALGO or Yb:CaF) tend to exhibit worse crystal quality than narrowband materials (e.g. Yb:YAG or Yb:LuO), and high-power modelocking > 100 W has so far only been demonstrated with comparatively narrowband gain materials.

Here we investigate a new approach to circumvent the limited gain bandwidth of two laser materials used in state-of-the-art TDLs, Yb:YAG and Yb:LuO, by flattening the roundtrip gain spectrum via intracavity optics with a specifically tailored spectral reflectivity. The idea of exploiting spectral filtering as a means to compensate for gain narrowing

was initially introduced in Ti:Sa regenerative amplifiers, using for example thin etalons or birefringent filters [145, 146]. The concept was later applied in Kerr-lens modelocked Ti:Sa and Cr:LiSAF oscillators using tailored OC coatings, also called gain-matched output couplers (GMOCs) [147–149]. The reduction of the gain filtering via the GMOC allowed for a more efficient and robust KLM operation, and a reduction of the required nonlinearity and self-amplitude modulation (SAM) depth. Here we present our implementation of the gain-matched mirror (GMM) concept for Yb-based gain materials and the results of our first modelocking experiments with Yb:YAG and Yb:LuO.

6.2 Design of gain-matched mirrors

For the design of the GMMs, we are looking for the spectral reflectivity of the laser cavity that will (ideally) result in a spectrally flat roundtrip gain.

$$\forall \lambda, G(\lambda)R_{\text{cav,opt}}(\lambda) = 1 \quad (6.1)$$

Based on this condition, the cavity reflectivity yielding the optimally flat gain profile is given by:

$$R_{\text{cav,opt}}(\lambda) = \begin{cases} \frac{1}{G(\lambda)} & \text{for } G(\lambda) > 1 \\ 1 & \text{otherwise} \end{cases} \quad (6.2)$$

We note that the roundtrip gain will be optimally flat for a specific inversion level.

In practice, the cavity reflectivity might deviate from the profile defined in equation (6.2), mainly for two reasons:

1. Designing a coating reproducing all the features of the gain spectrum might lead to an overly complex and thick coating difficult to produce.
2. A partial flattening of the gain spectrum can be achieved by fitting the main gain peak, for example with a Lorentzian profile, and using this profile to design the GMMs. Additionally the maximum

reflectivity can be set to an arbitrary value <1 in order to increase the overall transmission of the GMMs. This approach would lead to a GMOC.

The cavity reflectivity is determined by the contributions of the various intracavity components:

$$R_{\text{cav}}(\lambda) = R_{\text{OC}}(\lambda) \cdot R_{\text{SESAM}}(\lambda) \cdot R_{\text{cav,lin}}(\lambda) \cdot R_{\text{filter}}^n(\lambda) \quad (6.3)$$

Compared to equation (3.25) in chapter 3, equation (6.3) includes the contribution of n reflections on an intracavity spectral filter $R_{\text{filter}}(\lambda)$. To simplify the notations in the following, we assume that the OC, SESAM and cavity losses from the optics have a flat reflectivity over the considered spectral range.

Given a targeted inversion level, the optimal cavity reflectivity providing the desired gain flattening can be obtained by numerical simulations. By then setting a targeted operation point on the SESAM and estimating the cavity losses, we can deduce the spectral reflectivity of a GMOC or GMMs resulting in the desired gain flattening:

- The GMOC reflectivity is given by:

$$R_{\text{GMOC}}(\lambda) = R_{\text{OC}} \cdot R_{\text{filter}}(\lambda) = \frac{R_{\text{cav,opt}}(\lambda)}{R_{\text{SESAM}} \cdot R_{\text{cav,lin}}} \quad (6.4)$$

The GMOC is a single component used at normal incidence, providing both the spectral filtering and output coupling of the intracavity light. It has the advantage of maximizing the output power and simplifying the cavity layout. On the downside, the GMOC compensates the gain narrowing upon a single reflection and therefore requires a stronger reflectivity dip than several GMMs. This can make the production of such a mirror difficult and additionally results in a large dispersion around the central wavelength of the reflectivity dip.

- The GMM approach relies on several identical filters, or GMMs, with a reflectivity given by:

$$R_{\text{GMM}}(\lambda) = R_{\text{filter}}(\lambda) = \left(\frac{R_{\text{cav,opt}}(\lambda)}{R_{\text{OC}} \cdot R_{\text{SESAM}} \cdot R_{\text{cav,lin}}} \right)^{1/n} \quad (6.5)$$

In this case, a separate standard OC with a flat reflectivity can be used and the OC reflectivity is chosen such that the GMM reflectivity is nominally 1 outside of the gain spectrum (similar to equation (6.2)). The GMM approach requires more components, however it offers more flexibility as the angle of incidence (AOI) on the mirrors can be used as a degree of freedom to carefully adjust the spectral position of the reflectivity dip. Additionally, the spectral filtering is distributed over several components which means that a strong reflectivity change can be achieved by a cumulative effect. The output pulse, coupled out by the standard OC, does not experience any filtering, however the output coupling rate is reduced.

In our experiments we first tested the GMOC approach, initially designed for use with Yb:LuO, and in a second iteration designed some GMMs for Yb:YAG.

6.3 Gain-matched OC experiments

6.3.1 GMOC design

The gain spectrum of Yb:LuO displays a main peak at ≈ 1033 nm and a side peak at ≈ 1079 nm. In our first GMOC experiments, we aimed at flattening the gain profile of Yb:LuO in order to achieve a broad roundtrip gain spectrum potentially spanning from ≈ 1020 nm to ≈ 1090 nm. For these experiments, we used a disk with a doping concentration of 3 at.% and a thickness of 110 μm , in a cavity incorporating 4 reflections of the intracavity beam on the disk per roundtrip. Based on these parameters, we calculated the gain spectrum for an inversion level $\beta \approx 15\%$ and simulated the optimal cavity reflectivity leading to gain flattening. Assuming a SESAM reflectivity of 99% and linear cavity losses of 0.1%, we obtained the GMOC reflectivity shown in figure 6.1(a) (solid line). The simulated flattened roundtrip gain spectrum is shown in figure 6.1(b) (solid line)

and compared to the roundtrip gain spectrum obtained with a standard OC with a flat reflectivity (dashed line). The targeted GMOC reflectivity leads to an efficient flattening of the roundtrip gain profile.

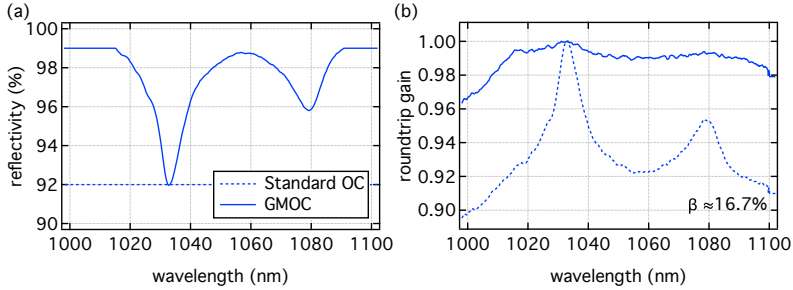


Figure 6.1 – GMOC reflectivity and roundtrip gain flattening in a TDL based on Yb:LuO. (a) Simulated reflectivity of the GMOC designed for Yb:LuO, compared to a flat OC reflectivity with identical peak transmission. (b) Simulated roundtrip gain spectrum with the GMOC and with the standard OC. The inversion level is set to 16.7%, for which the roundtrip gain at 1033 nm is unity for both OCs.

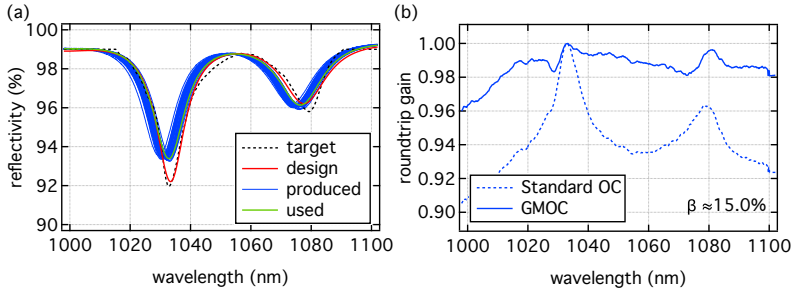


Figure 6.2 – Reflectivity of the produced GMOCs and simulated roundtrip gain flattening for the GMOC used in our modelocking experiments with Yb:LuO. (a) Reflectivity of the produced GMOCs compared to the targeted curve (black dashed line) and the simulated design curve (red). The reflectivity of the GMOC used in modelocking experiments is shown in green. (b) Simulated roundtrip gain spectrum with the GMOC used for the modelocking experiments, compared to the profile obtained with a standard OC with an identical peak transmission of 6.6%. The inversion level is set to 15.0%, for which the roundtrip gain at 1033 nm is unity for both OCs.

For our experiments with Yb:LuO, we obtained the GMOCs commer-

cially. The design of the coating was optimized to achieve a reflectivity close to our simulated GMOC reflectivity curve and for low GDD upon reflection. The design GMOC reflectivity is shown in figure 6.2(a) (red line) and compared to the targeted reflectivity (black dashed line). Due to production tolerances, it was expected that one or two mirrors would have the designed specifications out of a batch of 32 mirrors. We measured the reflectivity of each sample in a spectrophotometer (Varian CARY 5) and show the results in figure 6.2(a) (blue lines). We see that the produced GMOCs have less pronounced spectral dips and generally tend to have the position of these dips shifted to lower wavelengths compared to the design. We simulated the expected roundtrip gain spectrum with each GMOC and chose the sample giving the best result. The reflectivity of this mirror is shown in green in figure 6.2(a) and the corresponding simulated roundtrip gain spectrum is shown in figure 6.2(b). The GMOC still significantly flattens the roundtrip gain profile, although a dip is created at ≈ 1029 nm and the side peak at ≈ 1080 nm is not fully flattened.

6.3.2 Modelocking experiments with Yb:LuO

The TDL oscillator used for testing the GMOC is depicted in figure 6.3. The cavity includes multiple passes of the intracavity beam on the disk in order to increase the roundtrip gain. The cavity was designed to operate at moderate powers and singlemode operation was achieved with powers >40 W with an OC transmission of 6.6%. In order to provide the SPM and GDD balance required for soliton modelocking, the cavity includes a 3-mm thick YAG BP and 3 GTI-type DMs (not depicted in figure 6.3) providing -500 fs² per reflection. In order to initiate and stabilize mode-locked operation, we insert a SESAM at one end of the cavity. For these modelocking experiments, we tested two available SESAMs with the parameters given in table 6.1. Additionally we compared the modelocking performance when using the GMOC or a standard OC with a transmission of 6.6% (peak transmission of the GMOC at 1033 nm).

The results of our modelocking experiments are summarized in table 6.2:

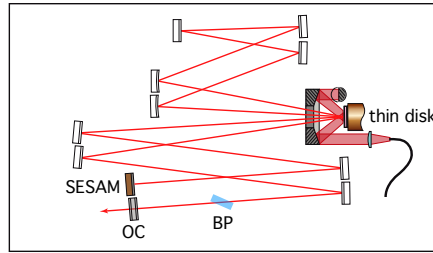


Figure 6.3 – Cavity layout of the TDL oscillator used for the GMOC experiments.

	SESAM 1	SESAM 2
F_{sat}	$35 \mu\text{J}/\text{cm}^2$	$120 \mu\text{J}/\text{cm}^2$
ΔR	2.6%	1.1%
ΔR_{ns}	0.4%	0.1%
$F_{2,1 \text{ ps}}$	$3.1 \text{ J}/\text{cm}^2$	$5.0 \text{ J}/\text{cm}^2$

Table 6.1 – Nonlinear reflectivity parameters of the SESAMs used for the GMOC experiments.

SESAM	standard OC	GMOC
1	12.5 W, 270 fs	QML/instabilities
2	no modelocking	7.1 W, 407 fs

Table 6.2 – Modelocking performance of our 24.4-MHz Yb:LuO TDL oscillator with a standard OC and a GMOC.

1. Using SESAM 1, with the highest modulation depth, we achieved modelocking with up to 12.5 W of average power and a pulse duration of 270 fs with a standard OC. However, no clean modelocked operation could be achieved with the GMOC and QML or modelocking instabilities resulted in damage of the SESAM.
2. Using SESAM 2, with a lower modulation depth, we could not modelock the oscillator with a standard OC, however we achieved modelocking at an average power of 7.1 W and a pulse duration of 407 fs with the GMOC.

In our experiments, we could not find a regime where modelocking

occurred with both types of OC and therefore a direct comparison of the performance obtained with the standard OC and the GMOC is not possible here. Nevertheless, the obtained results are consistent with a roundtrip gain flattening effect by the GMOC. Indeed, the absence of modelocking using SESAM 2 with the standard OC could be explained by a lack of modulation depth to support the short pulse durations. Combining the same SESAM with a GMOC, modelocking could be achieved, which supports the idea of a flatter roundtrip gain profile. However the reason for the onset of QML or modelocking instabilities when using SESAM 1 with the GMOC is not fully clear and further investigations are needed to determine its origin. The strong roundtrip gain flattening introduced by the GMOC could change the dynamics of the pulse formation. When modelocking with SESAM 2 and the GMOC, we observed that the range of powers for which stable modelocking could be achieved was essentially reduced to a single point: decreasing the power led to QML and increasing the power resulted in cw breakthrough or modelocking instabilities.

6.3.3 Modelocking experiments with Yb:YAG

Looking at the reflectivity curves of the produced GMOCs in figure 6.2, we see that a few samples have a reflectivity dip centered at 1030 nm. We therefore considered using these mirrors to flatten the roundtrip gain profile in an Yb:YAG TDL oscillator. In figure 6.4(a), we show the reflectivity profile of a GMOC suited for Yb:YAG and the corresponding simulated roundtrip gain spectrum in figure 6.4(b). Since the GMOC was initially designed for Yb:LuO, we only obtain a partial cancellation of the gain peak at 1030 nm in Yb:YAG. This partial cancellation is however already favorable for generating shorter pulse durations.

We implemented the GMOC in a cavity with a similar layout than the cavity depicted in figure 6.3 for Yb:LuO. We used a 100- μm -thick Yb:YAG disk with a doping concentration of 10 at.%. The nonlinearity in this case was provided only by the intracavity air and we inserted 4 DMs providing -500 fs^2 per reflection and a thin-film polarizer (TFP) for polarization control. For modelocking, we used SESAM 1, with the highest modulation depth (see table 6.1). We first characterized the modelocking

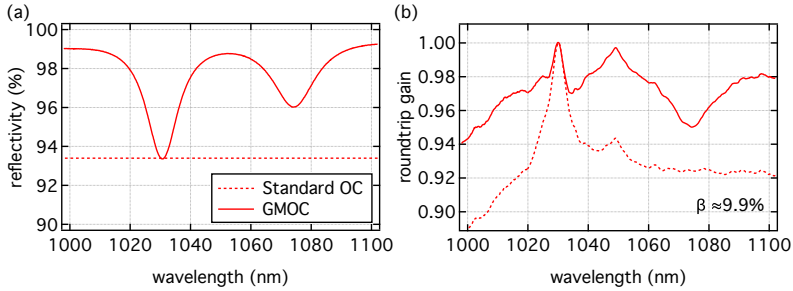


Figure 6.4 – GMOC reflectivity and roundtrip gain flattening in a TDL based on Yb:YAG. (a) Simulated reflectivity of the GMOC used with Yb:YAG, compared to a flat OC reflectivity with identical peak transmission. (b) Simulated roundtrip gain spectrum with the GMOC and with the standard OC. The inversion level is set to 9.9%, for which the roundtrip gain at 1030 nm is unity for both OCs.

performance using a standard OC with a transmission of 6.6%, identical to the peak transmission of the GMOC. Modelocking was initiated at an output power of 17.8 W with a pulse duration of 569 fs, and the output power could be increased up to 23.5 W, with a pulse duration of 419 fs. Replacing the standard OC with the GMOC, we initiated modelocking at an output power of 19.0 W with a pulse duration of 478 fs, and could increase the output power up to 25.0 W, with a pulse duration of 374 fs. The evolution of the pulse duration as a function of the intracavity power is shown in figure 6.5(a) for both types of OC and the optical spectrum and autocorrelation trace of the pulse obtained at the maximum power are shown in figure 6.5(b)-(c). We also report the maximum modelocking performance for both cases in table 6.3.

	Standard OC			GMOC		
	P_{avg}	τ_p	$\Delta\lambda$	P_{avg}	τ_p	$\Delta\lambda$
Output	23.5 W	419 fs	2.8 nm	25.0 W	374 fs	3.3 nm
Intracavity	356 W	419 fs	2.8 nm	396 W	341 fs	3.3 nm

Table 6.3 – Modelocking performance of our 23.9-MHz Yb:YAG TDL oscillator with a standard OC and a GMOC.

From the modelocking results presented in figure 6.5 and table 6.3, we

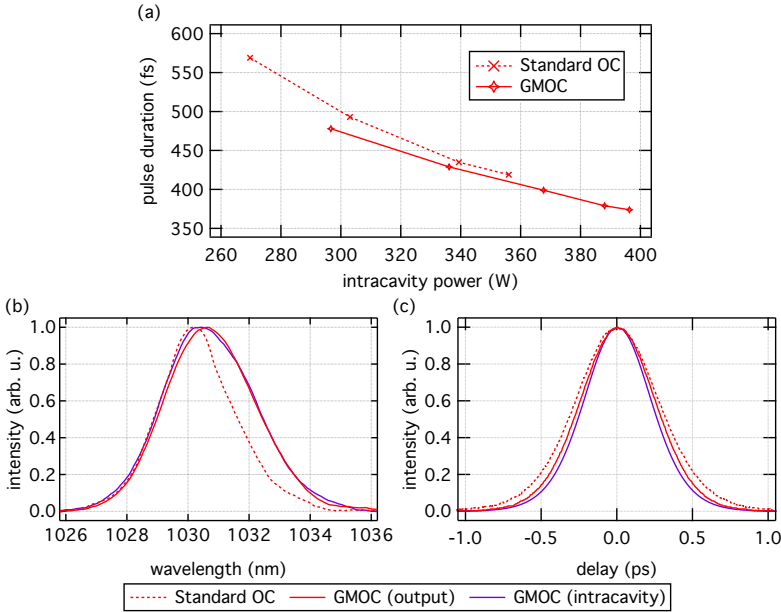


Figure 6.5 – Diagnostics of the modelocking performance obtained with our Yb:YAG TDL oscillator operating with a standard OC and with a GMOC. (a) Output pulse duration as a function of the intracavity power. The markers represent the measured data points and the lines are given as a guide to the eye. **(b)-(c)** Measured spectra and autocorrelation traces at the highest output power of 23.5 W for the standard OC and 25.0 W for the GMOC.

can draw two conclusions:

1. Using the GMOC effectively shifts the stable modelocking range to higher powers and shorter pulse durations. At a given intracavity power, the pulse duration obtained with the GMOC is about 8% shorter than with the standard OC.
2. The intracavity pulse duration is about 10% shorter than the output pulse duration with the GMOC. This effect is expected as a result of the spectral filtering and dispersion experienced by the pulse transmitted through the GMOC.

To summarize these GMOC experiments with Yb:YAG, we could achieve modelocking over a similar range of powers than with a standard OC. However with the GMOC, the maximum achievable intracavity

power was $\approx 10\%$ higher and the intracavity pulse duration was $\approx 20\%$ shorter than with a standard OC. In terms of output performance, the average power was increased by $< 10\%$ due to the lower effective transmission of the GMOC and the output pulse duration was reduced by $\approx 10\%$ due to the spectral filtering and dispersion of the GMOC.

6.3.4 Conclusion of GMOC experiments

Our first GMOC experiments highlighted some important aspects for the design of such intracavity spectral filters:

1. It could be beneficial to design the GMOC accounting for an extra cavity loss, i.e. for a lower inversion level than the simulated optimal inversion. This extra loss could be introduced in the form of a separate OC with a small transmission and could be tuned to higher or smaller values. This would allow for a finer tuning of the total cavity losses and consequently the inversion level in order to achieve the optimal roundtrip gain profile.
2. With the GMOC approach, production errors in the coating layers cannot be compensated for. In particular, an offset in the spectral position of the reflectivity dips could potentially be compensated by tuning the AOI on the mirror. However the GMOC should ideally be used at normal incidence.

Additionally, we achieved some first modelocking results using a GMOC in an Yb-based oscillator.

1. Our GMOC design was optimized to provide optimal gain flattening with Yb:LuO. Achieving stable modelocking with the GMOC has proven difficult and could only be realized using a SESAM with a comparatively small modulation depth and over a very limited parameter range. The results hint towards a flattening of the roundtrip gain profile, however further investigations are needed to confirm this.
2. We could use one GMOC matching the gain peak of Yb:YAG and achieved stable modelocking over a power range similar to what could be obtained with a standard OC. The results obtained with

the GMOC show an increase of the generated pulse bandwidth and consequently a decrease of the pulse duration. Additionally mode-locking could be achieved at slightly higher powers. As a result, at the maximum output power, the pulse duration achieved with the GMOC is 10% shorter extra-cavity and 20% shorter intracavity than with a standard OC.

Following on the promising results obtained with Yb:YAG and taking into account these new design considerations, we designed GMMs optimized for Yb:YAG and present preliminary results obtained with these mirrors in the next section.

6.4 Gain-matched mirrors for Yb:YAG

6.4.1 GMM design

For our second iteration of GMM experiments, we focused on roundtrip gain flattening with Yb:YAG. This material offers several advantages with respect to GMM design:

1. The gain peak at 1030 nm does not shift with varying inversion levels, as is the case in Yb:LuO.
2. Yb:YAG provides a large gain, particularly when combined with multipass cavity geometries. We therefore expect the cavity to be less sensitive to a strong reflectivity dip introduced by spectral filtering elements and to additional sources of losses.
3. Yb:YAG is generally available in excellent crystal quality and by our experience gives the most reproducible results when changing disks.

For the spectral filtering, we decided to split the GMOC into several identical GMMs combined with an OC with a flat spectral reflectivity. This offers the possibility to tune the position of the spectral reflectivity dip by changing the AOI on the mirrors. Additionally, the depth of the reflectivity dip can be reduced, which facilitates the design of the coating. We further designed the GMM reflectivity to have a Lorentzian profile and achieve a partial cancellation of the main gain peak of Yb:YAG at 1030 nm. The definition and parameters used for the Lorentzian profile

are given in equation (6.6) and table 6.4. In figure 6.6(a), we show the reflectivity profile of a single GMM (green line) and the combined effect of 4 reflections on such a mirror (blue line). Together with an 8.15% OC with a flat reflectivity, we obtain the reflectivity profile shown in red, resulting in the simulated roundtrip gain profile shown in figure 6.6(b) (solid line).

$$R_{\text{GMM}}(\lambda) = 1 - \frac{1 - R_{\text{pk}}}{1 + \left(\frac{\lambda - \lambda_{\text{pk}}}{\Delta\lambda_{\text{FWHM}}/2}\right)^2} \quad (6.6)$$

AOI	λ_{pk}	R_{pk}	$\Delta\lambda_{\text{FWHM}}$
5°	1030 nm	95.2%	5 nm

Table 6.4 – Parameters for the lorentzian reflectivity of the GMM for Yb:YAG.

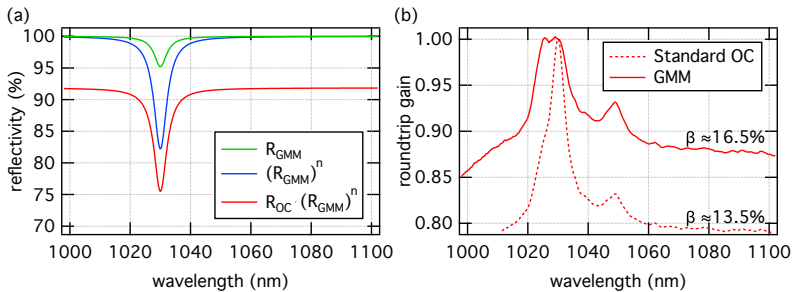


Figure 6.6 – GMM reflectivity and roundtrip gain flattening in a TDL based on Yb:YAG. (a) Simulated reflectivity of a single GMM designed for use with Yb:YAG. The combined effect of 2 GMMs placed inside the laser resonator is shown in blue ($n = 4$ reflections on GMM elements). The combined reflectivity of the GMMs and the 8.15% flat OC is shown in red. (b) Simulated roundtrip gain spectrum with the GMMs and 8.15% OC and with a standard 20% OC as used in preliminary experiments. The inversion level is chosen such that the roundtrip gain at 1030 nm is unity in both cases. We use $R_{\text{SESAM}} = 99\%$ and $R_{\text{cav,lin}} = 99.9\%$

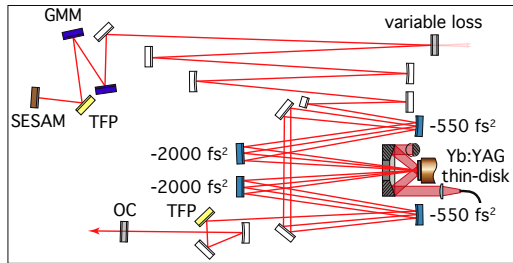


Figure 6.7 – Cavity layout of the Yb:YAG TDL oscillator used for the GMM experiments.

6.4.2 Modelocking experiments

For the modelocking experiments, we built a TDL oscillator based on a multipass cavity arrangement depicted in figure 6.7, similar to the one found in [76]. We used a 100- μm -thick Yb:YAG disk with a doping concentration of 10 at.%. The nonlinearity is provided by the intracavity air and is balanced by dispersive mirrors introduced in the multipass arrangement (see figure 6.7). The GMMs were produced in an IBS machine at the Université de Neuchâtel with real-time monitoring of the layer deposition. We inserted two GMMs at one end of the cavity and used an OC with a flat spectral transmission of 8.15%. Additionally we inserted an OC with a small transmission of 1.6% as an extra loss that can be changed to tune the total losses of the cavity (variable loss in figure 6.7). In this configuration, we expected a roundtrip gain corresponding to the simulated profile shown in figure 6.6(b) (solid line).

In order to carefully optimize the alignment of the GMMs, we plan to implement a spectral gain measurement setup by coupling a tunable cw laser beam, in orthogonal polarization to the intracavity beam, through the TFP at one end of the cavity and extracting it at the other end through the second TFP. By tuning the wavelength of this probe laser and simultaneously measuring its power at the input and output TFPs, we will measure the roundtrip gain spectrum. This work in progress should allow a careful optimization of the gain flattening.

In preliminary modelocking experiments without this spectral gain

measurement, we aligned the GMMs as close as possible to the design AOI of 5° and obtained modelocked operation using SESAM 1 (see table 6.1). We could initiate modelocking at an output power of 8.1 W and increase the power to 14.2 W, with a pulse duration decreasing from 966 fs to 603 fs. We also modelocked the oscillator without the GMMs and additional loss, and used a 20% OC. We obtained modelocking starting from 19.9 W and up to 40.5 W, with a pulse duration decreasing from 1079 fs to 602 fs. We compare the results obtained with and without spectral filtering in figure 6.8. We observe a similar behaviour as in our first GMOC experiments shown in figure 6.5. For a given intracavity power, the configuration of the cavity including the GMMs yields shorter pulses by $\approx 13\%$. However here, the minimum pulse duration is the same in the case with or without spectral filtering. These preliminary results confirm again the positive action of the GMMs for reaching shorter pulses, however further investigations are needed to characterize and optimize the effect of the spectral filtering more accurately.

As a final remark, we highlight that the current setup was not optimized to deliver high average power. The output power of ≈ 10 W with the GMMs might seem excessively low considering the high-gain multi-pass arrangement. However, the GMMs each extract $\approx 9.6\%$ of the intracavity power, and the additional OC also transmits $\approx 3.2\%$, so that the total power extracted from the cavity is ≈ 30 -50 W.

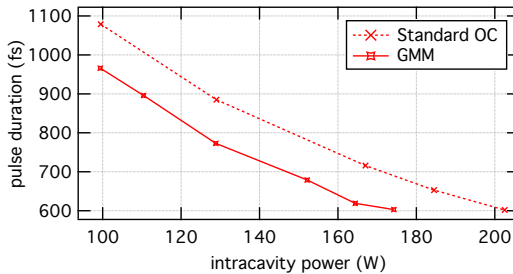


Figure 6.8 – Evolution of the output pulse duration as a function of intracavity power in our Yb:YAG TDL oscillator without spectral filtering and with GMMs. The markers represent the measured data points and the lines are given as a guide to the eye.

6.5 Conclusion

We investigated a new approach to circumvent the limited gain bandwidth of typical gain materials used in high-power TDL oscillators by introducing specially tailored spectral filters in the laser cavity. This approach has proven successful in KLM Ti:Sa oscillators to achieve modelocking at reduced nonlinearity and SAM strength. We presented some design considerations for making a GMOC or GMMs combined with a flat OC for Yb-based materials. Due to the sharp features of the gain spectrum in Yb:YAG or Yb:LuO, the design of a GMOC is rather delicate and sensitive to production errors. We found the GMM approach to be more flexible as the AOI can be used to match the reflectivity dip of the mirror with the peak of the gain spectrum.

Our first modelocking experiments hinted towards a roundtrip gain flattening effect when using a GMOC or GMMs. We found that shorter pulses were generated in the presence of spectral filtering for a given intracavity power and in one case the maximum output power could be increased in the presence of spectral filtering, resulting in a shorter minimum achievable pulse duration. So far the strength of this pulse shortening effect is rather small, about 10%.

We believe that current efforts to measure the spectral roundtrip gain profile *in situ*, combined with numerical models, will help gather new insights and optimize this regime of operation.

Nonlinear-mirror modelocking

7.1 A promising alternative modelocking technique

In the previous two chapters, we investigated new approaches to improve the modelocking performance of TDL oscillators in terms of reaching high powers and short pulse durations using the existing SESAM technology. We first proposed a SESAM with reduced TPA leading to an improved rollover behaviour (chapter 5), and in a second step, we investigated the mitigation of the gain bandwidth limitation by using intracavity spectral filters (chapter 6). In this chapter, we take a different approach by investigating an alternative modelocking technique based on the frequency-doubling nonlinear mirror (NLM).

The concept of the frequency-doubling NLM was introduced by Stankov in 1988 [150] and directly applied to passively modelock a neodymium (Nd)-doped YAG laser [151]. The NLM consists of a $\chi^{(2)}$ crystal cut for type 1 second harmonic generation (SHG), combined to a dichroic OC which partially reflects the fundamental wave (FW) and fully reflects the second harmonic (SH). The incident intracavity FW is partially converted to the SH in the $\chi^{(2)}$ crystal, then partially reflected on the OC, and finally replenished by optical parametric amplification (OPA) on the return pass through the $\chi^{(2)}$ crystal. Since the SHG and OPA processes are intensity dependent, a higher incident intensity results in a higher reflectivity for the FW, as illustrated in figure 7.1. The NLM therefore

provides a saturable reflectivity and can be used as a modelocking device. More details on the operation of the NLM are provided in the publications attached to this chapter.

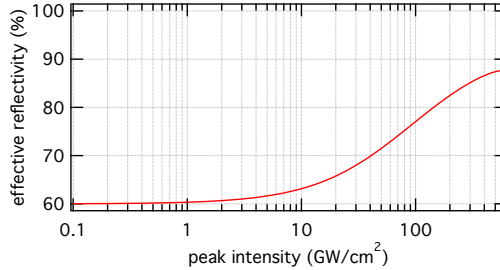


Figure 7.1 – Example nonlinear reflectivity curve of a NLM based on a 1-mm-thick LBO and a 60% dichroic OC. Nonlinear reflectivity of the FW as a function of the incident peak intensity on the $\chi^{(2)}$ crystal. We consider a 1-mm-thick LBO crystal aligned at the phase-matching angle for type 1 SHG at 1030 nm and a dichroic OC with a linear reflectivity of 60% for the FW and 100% for the SH. The incident FW has a beam size of 300 μm on the LBO and the pulse duration is 500 fs. The phase offset between the electric field of the SH and the electric field squared of the FW for the OPA process is set to π for optimal back-conversion.

In section 7.2, we include the publication presenting our first demonstration of NLM modelocking in a TDL oscillator. We implemented the NLM in a TDL based on Yb:YAG, operating at moderate average powers between 20 W and 30 W, and we demonstrated modelocking at 21 W with pulses as short as 323 fs at a repetition rate of 17.8 MHz. This first result highlights the advantages of combining the NLM concept with the TDL technology:

1. The high intracavity peak power available in TDLs allows for the use of thin $\chi^{(2)}$ crystals. This leads to a reduced group-velocity mismatch (GVM) between the FW and SH and enables shorter pulse durations in the femtosecond regime compared to previous demonstrations in bulk lasers ($\tau_p > 5$ ps) [152–154].
2. The NLM provides a large and ultrafast loss modulation favoring short pulse durations. The achieved pulse duration of 323 fs is comparable to values usually obtained with KLM in Yb:YAG TDLs

[18,77], and substantially shorter than values achieved with SESAM modelocking (see figure 1.4 in chapter 1). The NLM modelocking technique therefore represents an interesting alternative to KLM for generating short pulses in TDL oscillators.

The experimental results is complemented by the description of our numerical model used to simulate the NLM and we discuss the bandwidth limitations of the NLM as well as considerations for power scaling.

In section 7.3, we include a second manuscript presenting a first step in power scaling the NLM modelocking technique towards 100 W average power. We implemented the NLM in a high-power Yb:YAG TDL oscillator based on a high-gain cavity design including multiple passes of the intracavity beam through the disk. This allowed us to increase the OC transmission and achieve higher output powers. Additionally we added a SESAM to the cavity in order to obtain reliable initiation of the mode-locked operation and optimize the NLM. Our power scaling experiments highlighted further important aspects of the NLM modelocking regime:

1. Q-switching instabilities are a major challenge in NLM modelocking, intrinsically linked to the capability of the NLM to saturate a large fraction of the cavity losses. These instabilities can however be mitigated to some extent by introducing a rollover in the NLM reflectivity when operating the NLM with a phase mismatch.
2. The NLM introduces a nonlinear phase-shift that strongly depends on the NLM tuning parameters. This contribution can be a significant fraction of the overall SPM contributing to the soliton pulse formation, hence influencing the pulse duration.

Additionally we improved the thermal properties and damage threshold of the NLM by using low-absorption $\chi^{(2)}$ crystals and designing a high-damage-threshold dichroic coating for the OC. With these improvements, we obtained modelocking at a power of 66 W with 426 fs pulses and up to 87 W with 586 fs pulses at repetition rates close to 9 MHz. In particular, this corresponds to output peak powers close to 15 MW, which is difficult to achieve with SESAM modelocking at these pulse durations (see figure 1.4 in chapter 1).

7.2 Publication 1

The design and modelocking performance of our first NLM-modelocked TDL oscillator based on Yb:YAG are presented in the following publication.

Title: "Modelocking of a thin-disk laser with the frequency-doubling nonlinear-mirror technique", [80]

Journal: *Optics Express*

doi: 10.1364/OE.25.023254

URL: <https://doi.org/10.1364/OE.25.023254>

Published: September 13th, 2017

©2017 Optical Society of America. One print or electronic copy may be made for personal use only. Systematic reproduction and distribution, duplication of any material in this paper for a fee or for commercial purposes, or modifications of the content of this paper are prohibited.

Modelocking of a thin-disk laser with the frequency-doubling nonlinear-mirror technique

F. SALTARELLI*, A. DIEBOLD, I. J. GRAUMANN, C. R. PHILLIPS,
AND U. KELLER

Institute for Quantum Electronics, ETH Zurich, 8093 Zurich, Switzerland
*saltarelli@phys.ethz.ch

Abstract: We demonstrate a frequency-doubling nonlinear-mirror (NLM) modelocked thin-disk laser. This modelocking technique, composed of an intracavity second harmonic crystal in combination with a dichroic output coupler, offers robust operation decoupled from cavity stability (as in semiconductor saturable absorber mirror (SESAM) modelocking) combined with an ultrafast saturable loss and high modulation depth (as in Kerr-lens modelocking (KLM)). With our NLM diode-pumped Yb:YAG thin-disk laser we achieve 21 W of average power at 323-fs pulse duration, which is an order of magnitude shorter than the previously obtained duration with the same technique in bulk lasers. Using these first results, we present a theoretical model for the NLM technique, which accurately predicts its loss modulation properties and the shortest achievable pulse duration without relying on any fitting parameters. Based on this simulation, we expect that the NLM technique will enable thin-disk lasers with average power of more than 100 W, with potentially sub-200 fs pulses. This could potentially solve the pulse duration limitations with SESAM modelocked Yb:YAG thin-disk lasers without imposing strong cavity stability constraints such as in KLM.

© 2017 Optical Society of America

OCIS codes: (140.0140) Lasers and laser optics; (140.4050) Mode-locked lasers; (140.7090) Ultrafast lasers; (190.7110) Ultrafast nonlinear optics.

References and links

1. A. Ancona, S. Doring, C. Jauregui, F. Roser, J. Limpert, S. Nolte, and A. Tünnermann, "Femtosecond and picosecond laser drilling of metals at high repetition rates and average powers," *Opt. Lett.* **34**, 3304-3306 (2009).
2. T. Südmeyer, S. V. Marchese, S. Hashimoto, C. R. E. Baer, G. Gingras, B. Witzel, and U. Keller, "Femtosecond laser oscillators for high-field science," *Nat. Photonics* **2**, 599-604 (2008).
3. T. Nubbemeyer, M. Kaumanns, M. Ueffing, M. Gorjan, A. Alismail, H. Fattahi, J. Brons, O. Pronin, H. G. Barros, Z. Major, T. Metzger, D. Sutter, and F. Krausz, "1 kW, 200 mJ picosecond thin-disk laser system," *Opt. Lett.* **42**, 1381-1384 (2017).
4. M. Müller, M. Kienel, A. Klenke, T. Gottschall, E. Shestae, M. Plötner, J. Limpert, and A. Tünnermann, "1 kW 1 mJ eight-channel ultrafast fiber laser," *Opt. Lett.* **41**, 3439-3442 (2016).
5. P. Russbüldt, T. Mans, J. Weitenberg, H. D. Hoffmann, and R. Poprawe, "Compact diode-pumped 1.1 kW Yb:YAG Innoslab femtosecond amplifier," *Opt. Lett.* **34**, 4169-4171 (2010).
6. F. Emaury, A. Diebold, C. J. Saraceno, and U. Keller, "Compact XUV Source at Megahertz Pulse Repetition Rate with a Low-Noise Ultrafast Thin Disk Oscillator," *Optica* **23**, 980-984 (2015).
7. M. Gaponenko, F. Labaye, V. Wittwer, C. Paradis, N. Modsching, L. Merceron, A. Diebold, F. Emaury, I. Graumann, C. Phillips, C. J. Saraceno, C. Kränkel, U. Keller, and T. Südmeyer, "Compact Megahertz Coherent XUV Generation by HHG inside an Ultrafast Thin Disk Laser," in *Nonlinear Optics*, OSA Technical Digest (online) (Optical Society of America, 2017), NTh3A.1.
8. S. Hädrich, M. Krebs, A. Hoffmann, A. Klenke, J. Rothhardt, J. Limpert, and A. Tünnermann, "Exploring new avenues in high repetition rate table-top coherent extreme ultraviolet sources," *Light Sci Appl* **4**(2015).
9. C. J. Saraceno, F. Emaury, O. H. Heckl, C. R. E. Baer, M. Hoffmann, C. Schriber, M. Golling, T. Südmeyer, and U. Keller, "275 W average output power from a femtosecond thin disk oscillator operated in a vacuum environment," *Opt. Express* **20**, 23535-23541 (2012).
10. C. J. Saraceno, F. Emaury, C. Schriber, M. Hoffmann, M. Golling, T. Südmeyer, and U. Keller, "Ultrafast thin-disk laser with 80 μ J pulse energy and 242 W of average power," *Opt. Lett.* **39**, 9-12 (2014).

11. A. Diebold, F. Emaury, C. J. Saraceno, C. Schriber, M. Golling, T. Südmeyer, and U. Keller, "SESAM mode-locked Yb:CaGdAlO₄ thin disk laser with 62 fs pulse generation," *Opt. Lett.* **38**, 3842-3845 (2013).
12. C. Schriber, L. Merceron, A. Diebold, F. Emaury, M. Golling, K. Beil, C. Kränkel, C. J. Saraceno, T. Südmeyer, and U. Keller, "Pushing SESAM mode-locked thin-disk lasers to shortest pulse durations," in *Advanced Solid State Lasers*, OSA Technical Digest (online) (Optical Society of America, 2014), AF1A.4.
13. I. J. Graumann, A. Diebold, C. G. E. Alfieri, F. Emaury, B. Deppe, M. Golling, D. Bauer, D. Sutter, C. Kränkel, C. J. Saraceno, C. R. Phillips, and U. Keller, "Peak-power scaling of femtosecond Yb:Lu₂O₃ thin-disk lasers," *Opt. Express* (submitted) (2017).
14. C. G. E. Alfieri, A. Diebold, F. Emaury, E. Gini, C. J. Saraceno, and U. Keller, "Improved SESAMs for femtosecond pulse generation approaching the kW average power regime," *Opt. Express*. **24**, 27587-27599 (2016).
15. A. Diebold, T. Zengerle, C. G. E. Alfieri, C. Schriber, F. Emaury, M. Mangold, M. Hoffmann, C. J. Saraceno, M. Golling, D. Follman, G. D. Cole, M. Aspelmeyer, T. Südmeyer, and U. Keller, "Optimized SESAMs for kilowatt-level ultrafast lasers" *Opt. Express* **24**, 10512-10526 (2016).
16. J. Brons, V. Pervak, E. Fedulova, D. Bauer, D. Sutter, V. Kalashnikov, A. Apolonskiy, O. Pronin, and F. Krausz, "Energy scaling of Kerr-lens mode-locked thin-disk oscillators," *Opt. Lett.* **39**, 6442-6445 (2014).
17. J. Brons, V. Pervak, D. Bauer, D. Sutter, O. Pronin, and F. Krausz, "Powerful 100-fs-scale Kerr-lens mode-locked thin-disk oscillator," *Opt. Lett.* **41**, 3567-3570 (2016).
18. J. Zhang, J. Brons, M. Seidel, D. Bauer, D. Sutter, V. Pervak, V. Kalashnikov, Z. Wei, A. Apolonski, F. Krausz, and O. Pronin, "Generation of 49-fs pulses directly from distributed Kerr-lens mode-locked Yb:YAG thin-disk oscillator," in *Advanced Solid State Lasers*, OSA Technical Digest (online) (Optical Society of America, 2015), AT4A.7.
19. C. Paradis, N. Modsching, V. J. Wittwer, B. Deppe, C. Kränkel, and T. Südmeyer, "Generation of 35-fs pulses from a Kerr lens mode-locked Yb:Lu₂O₃ thin-disk laser," *Opt. Express*. **25**, 14918-14925 (2017).
20. B. Borchers, C. Schaefer, C. Fries, M. Larionov, and R. Knappe, "Nonlinear Polarization Rotation Mode-locking via Phase-mismatched Type I SHG of a Thin Disk Femtosecond Laser," in *Advanced Solid State Lasers*, OSA Technical Digest (online) (Optical Society of America, 2015), AT4A.9.
21. K. A. Stankov and J. Jethwa, "A new mode-locking technique using a nonlinear mirror," *Opt. Commun.* **66**, 41-46 (1988).
22. G. M. Thomas, T. Omatsu, and M. J. Damzen, "High-power neodymium-doped mixed vanadate bounce geometry laser, mode locked with nonlinear mirror," *Appl. Phys. B* **108**, 125-128 (2012).
23. G. Cerullo, M. B. Danailov, S. D. Silvestri, P. Laporta, V. Magni, D. Segala, and S. Taccheo, "A diode-pumped nonlinear mirror mode-locked Nd:YAG laser," *Appl. Phys. Lett.* **65**, 2392-2394 (1994).
24. K. A. Stankov, "25 ps pulses from a Nd:YAG laser mode locked by a frequency doubling β -BaB₂O₄ crystal," *Appl. Phys. Lett.* **58**, 2203-2204 (1991).
25. G. M. Thomas and M. J. Damzen, "30W Nd:GdVO₄ oscillator mode-locked with nonlinear mirror," in *2011 Conference on Lasers and Electro-Optics Europe and 12th European Quantum Electronics Conference (CLEO EUROPE/EQEC)*, (2011), 1-1.
26. G. Cerullo, V. Magni, and A. Monguzzi, "Group-velocity mismatch compensation in continuous-wave lasers mode locked by second-order nonlinearities," *Opt. Lett.* **20**, 1785-1787 (1995).
27. H. Iliev, D. Chuchumishev, I. Buchvarov, and V. Petrov, "Passive mode-locking of a diode-pumped Nd:YVO₄ laser by intracavity SHG in PPKTP," *Opt. Express*. **18**, 5754-5762 (2010).
28. K. A. Stankov, V. P. Tzolov, and M. G. Mirkov, "Frequency-doubling mode locker: the influence of group-velocity mismatch," *Opt. Lett.* **16**, 1119-1121 (1991).
29. I. Buchvarov, G. Christov, and S. Saltiel, "Transient behaviour of frequency doubling mode-locker. Numerical analysis," *Optics Communications* **107**, 281-286 (1994).
30. O. V. Chekhlov and V. A. Zaporozhchenko, "Mapping of the second-harmonic nonlinear mirror characteristics for laser mode locking and pulse shortening," *J. Opt. Soc. Am. B* **15**, 210-215 (1998).
31. A. A. Mani, D. Lis, Y. Caudano, P. A. Thiry, and A. Peremans, "Optimal performances of a mode-locking technique: Theoretical and experimental investigations of the frequency-doubling nonlinear mirror," *Opt. Commun.* **284**, 398-404 (2011).
32. R. Eckardt and J. Reintjes, "Phase matching limitations of high efficiency second harmonic generation," *IEEE J. Quantum Elect.* **20**, 1178-1187 (1984).
33. F. X. Kärtner, I. D. Jung, and U. Keller, "Soliton Mode-Locking with Saturable Absorbers," *IEEE J. Sel. Top. Quant.* **2**, 540-556 (1996).
34. K. Kato, "Second-harmonic generation to 2048 Å in b-BaB₂O₄," *IEEE J. Quantum Elect.* **22**, 1013-1014 (1986).
35. R. C. Eckardt, H. Masuda, Y. X. Fan, and R. L. Byer, "Absolute and relative nonlinear optical coefficients of KDP, KD*P, BaB₂O₄, LiIO₃, MgO:LiNbO₃, and KTP measured by phase-matched second-harmonic generation," *IEEE J. Quantum Elect.* **26**, 922-933 (1990).
36. D. Bauer, I. Zawischa, D. H. Sutter, A. Killi, and T. Dekorsy, "Mode-locked Yb:YAG thin-disk oscillator with 41 μ J pulse energy at 145 W average infrared power and high power frequency conversion," *Opt. Express* **20**, 9698-9704 (2012).
37. J. Rothhardt, S. Demmler, S. Hadrich, J. Limpert, and A. Tünnermann, "Octave-spanning OPCA system delivering CEP-stable few-cycle pulses and 22 W of average power at 1 MHz repetition rate," *Opt. Express* **20**, 10870-10878 (2012).

38. K. A. Stankov, V. P. Tzolov, and M. G. Mirkov, "Compensation of group-velocity mismatch in the frequency-doubling modelocker," *Appl. Phys. B* **54**, 303-306 (1992).
39. J. Zhang, K. F. Mak, S. Gröbmeyer, D. Bauer, D. Sutter, V. Pervak, F. Krausz, and O. Pronin, "Generation of 220 fs, 20 W pulses at 2 μm from Kerr-lens mode-locked Ho:YAG thin-disk oscillator," in *Conference on Lasers and Electro-Optics*, OSA Technical Digest (online) (Optical Society of America, 2017), SM11.6.

1. Introduction

Femtosecond laser sources with high peak and average power are an indispensable tool for many industrial and scientific applications, including laser precision micromachining and cutting [1], frequency metrology and strong-field physics in attosecond science [2]. Laser amplifiers based on the thin-disk, fiber, or Innoslab technology represent the state of the art of high-power ultrafast lasers. They reach kW-level average power with peak powers exceeding the GW level [3-5]. However, these systems have a substantial level of complexity and, in some cases, non-diffraction-limited beam quality. Modelocked thin-disk laser (TDL) oscillators are an attractive alternative to complicated amplifier systems and combine high output and peak power in a compact table-top MHz oscillator with excellent output beam quality. Moreover, these systems drive experiments at MHz repetition rates [6, 7], leading to reduced measurement times, and increased signal-to-noise ratios and photon fluxes [2, 8].

Thin-disk lasers offer the highest performance in terms of average power and excellent beam quality among all ultrafast oscillators. Based on the gain material Yb:YAG and modelocked with semiconductor saturable absorber mirrors (SESAMs), they currently achieve up to 275-W average power with 583-fs pulse duration [9] and 80- μJ pulse energy with 1.07-ps pulses [10]. Using broadband gain materials such as Yb:CALGO, pulse durations down to sub-50 fs were achieved with SESAM modelocking, however, at the expense of the output power, which stayed below 5 W [11, 12]. Because of the limited gain bandwidth of Yb-doped materials suitable for high-power operation (Yb:YAG, Yb:LuO), combining shorter pulse durations (sub-500 fs) and high average powers (>100 W) with SESAM-modelocking is a challenging task. This is mainly due to the SESAM's non-instantaneous recovery times, moderate modulation depths, and thermal effects from unsaturated losses and two-photon absorption [13]. Ongoing efforts to address these issues include improved strain compensation [14], and different bonding techniques to achieve flatter samples with efficient heat removal [15]. Modelocking TDLs with the Kerr-lens technique (KLM) has allowed for shorter pulse durations while maintaining high average power. With the gain material Yb:YAG, this technique resulted in 270 W of average power with 330 fs pulses [16] and 155 W with 140 fs pulses [17]. However, these results were limited to pulse energies <15 μJ . Shorter pulses down to sub-50 fs with average power of around 5 W were reported with Yb:YAG [18] and Yb:LuO [19]. In general, the KLM technique imposes strict constraints on the cavity design that needs to be operated close to its stability edge. This requirement introduces additional challenges in alignment sensitivity and stability, as it directly couples spatial and temporal effects. Recently, TDLs have also been modelocked with the nonlinear polarization rotation (NPR) technique. Using Yb:YAG as gain material and introducing the required intensity-dependent phase shift for NPR via a long and phase-mismatched intracavity second harmonic generation (SHG) crystal, these oscillators reached up to 44 W with sub-500 fs pulses [20]. In this work, we investigate and demonstrate modelocking of a TDL with an alternative technique, the frequency-doubling nonlinear mirror (NLM) [21]. In this device, whose operating principles are described in section 2, the combination of a phase-matched SHG crystal and a dichroic output coupling mirror results in a lower effective output coupling rate for high intensity light, thereby providing a saturable reflectivity and enabling modelocked operation. This approach offers a route to overcome the trade-offs in both SESAM and KLM modelocking of high power oscillators. It offers robust operation decoupled from the cavity stability (as in SESAM modelocking), together with an

ultrafast saturable loss (as in KLM), while maintaining power scalability. Compared to the NPR technique, a significantly shorter nonlinear crystal can be used, which should be favorable to avoid thermal lensing in future power scaling experiments (for example we use one 0.5-mm-long BBO crystal in the present work, compared with two ~ 20 -mm-long LBO crystals in [20]). Moreover, the NLM technique offers a large and highly flexible modulation depth that scales with the laser output coupling rate.

In Fig. 1(a) we present an overview of the performance of solid-state lasers modelocked with the NLM technique [Fig. 1(a)] [22–26]. Additionally, this technique has also been used to assist the cascaded $\chi^{(2)}$ lens modelocking process in order to stabilize it and provide self-starting operation [27]. Solid-state NLM-modelocked lasers achieved multi-ps pulse durations at comparatively high repetition rates (~ 100 MHz), which results in intracavity peak powers below 50 kW. Consequently, tight focusing is needed in order to reach the required intensities to drive the SHG process. This, in turn, makes spatial walk-off effects significant, which limits the efficiency of the process. Longer SHG crystals can be used, which, however, sets a lower limit for the achievable pulse duration in the few-ps-range due to group velocity mismatch (GVM) between the fundamental and its second harmonic [28].

High-power ultrafast TDLs, on the other hand, are well suited for the NLM process as their high peak powers allow for driving the nonlinear process with short crystals, which results in minimized thermal effects, larger bandwidths, and a corresponding short response time of the saturable reflectivity. Additionally, the NLM method is easily power-scalable by increasing the spot size on the SHG crystal.

Here we present a first demonstration of a TDL modelocked by the NLM technique, using a Yb:YAG thin disk. We obtain 21 W of average power with 323-fs pulses and, in another configuration, 28 W with 570-fs pulses. Our proof-of-principle laser reaches more than $1 \mu\text{J}$ of pulse energy, which results in more than 3 MW of extracavity peak power. Compared to prior results of NLM modelocking in bulk lasers, we decrease the achieved pulse durations by an order of magnitude [Fig. 1(a)]. Compared to state-of-the-art TDLs using Yb:YAG as gain medium [Fig. 1(b)], this first result reaches pulse durations significantly shorter than those obtained by SESAM-modelocking, and which lie in a range previously only accessible with KLM.

In section 2, we present the operating principles of the NLM technique. In section 3, we discuss the laser experiment. In section 4, we describe in detail our numerical model and use it in order to estimate the shortest pulses achievable with our device. We conclude in section 5 by summarizing the obtained results and envisaging the next generation of NLM modelocked thin-disk lasers with average powers in the 100-W level.

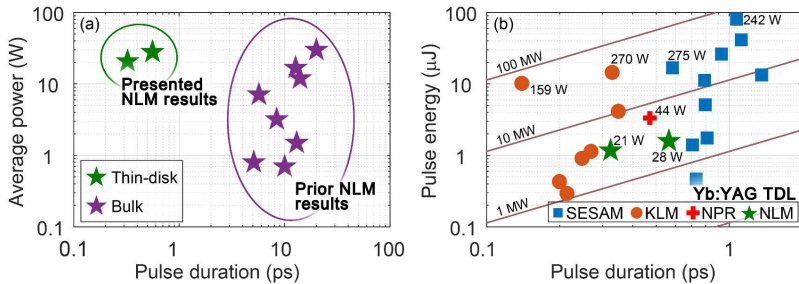


Fig. 1. (a) Pulse duration and average power of NLM modelocked lasers. (b) Pulse duration and pulse energy of modelocked Yb:YAG TDLs. The symbols specify the modelocking technique: square for SESAM, circle for KLM, cross for NPR and star for NLM. In the presented results, we reduce the pulse durations achieved with the NLM modelocking

technique by an order of magnitude, down to sub-350 fs, at output powers approaching 30 W, which is comparable to pulse durations achieved by state-of-the-art thin-disk oscillators.

2. NLM operating principles

We show a general schematic of the frequency-doubling NLM technique in Fig. 2(a), consisting of a second-order nonlinear crystal ($\chi^{(2)}$ crystal) configured for SHG, in combination with a dichroic output coupler (OC). In Fig. 2(b) we present the evolution of the pulse energy for the fundamental wave (FW) and the second harmonic (SH) inside the $\chi^{(2)}$ crystal, based on the simulation discussed in Sec. 4. The NLM device can be described in three stages:

- (i) Intracavity laser light [P_i in Fig. 2(a)] is directed through an intracavity SHG crystal, where some of this FW light is converted to its SH [in Fig. 2(b) solid red and green curves, refer, respectively, to FW and SH]. The SHG crystal is tilted in order to fulfill the phase matching condition ($\Delta k = k_{SH} - 2k_{FW} = 0$) for the SHG process.
- (ii) Both wavelengths travel through a variable length of air [“air space” in Fig. 2(a)] and are reflected from a dichroic OC, which is highly reflective (HR) for the SH and partially reflective for the FW. The transmitted power [P_t in Fig. 2(a)] of the FW defines the transmission of the NLM device.
- (iii) The beams then pass back through the $\chi^{(2)}$ crystal [dashed curves in Fig. 2(b)]. The relative phases of the FW and SH are adjusted via the air space in such a way that the reverse process of SHG (i.e., optical parametric amplification, OPA) occurs optimally ($\Delta\phi = -\pi$), thereby converting the SH light back to the FW.

Essentially, the NLM modelocking device acts as an OC with intensity-dependent reflectivity and transmission. At higher input intensities, more light is converted to the SH in stage (i). This implies a reduced output coupling rate for the FW, and more total power (FW + SH) being reflected by the OC in stage (ii). Then, by converting the reflected SH back to the FW in stage (iii), there is a higher overall reflectivity for the FW.

To quantify the behavior of the device, we consider the average power of the FW at different positions: P_i , P_t , and P_r refer to the initial intracavity power, the transmitted extracavity power, and the final reflected intracavity power, respectively. We also introduce the corresponding FWHM (full-width at half-maximum) pulse durations, denoted τ_i , τ_t , and τ_r . We then define the following parameters [29-31]:

$$R_{nl}(I_{pk}, \tau_i) = P_r / P_i \quad (1)$$

$$T_{nl}(I_{pk}, \tau_i) = P_t / P_i \quad (2)$$

$$\kappa(I_{pk}, \tau_i) = \tau_r / \tau_i. \quad (3)$$

The parameter R_{nl} indicates the nonlinear reflectivity of the device, T_{nl} the ratio between the intracavity power and the output power of the laser, while κ indicates the pulse-shortening factor, which is related to the modulation bandwidth of the device. The variable I_{pk} is the peak intensity of the incoming beam on the $\chi^{(2)}$ crystal, $I_{pk} = \max(I_i(r, t))$.

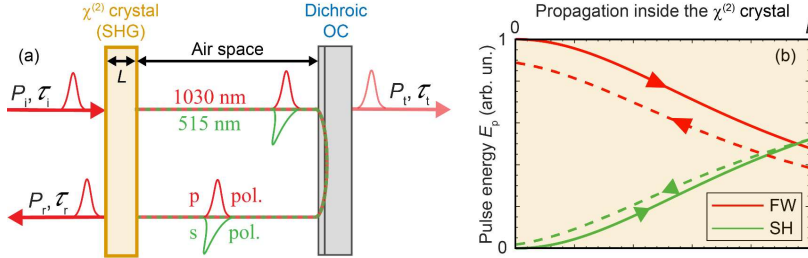


Fig. 2. (a) Schematic representation of the nonlinear-mirror modelocking (NLM) technique. (b) Evolution of the pulse energy inside the $\chi^{(2)}$ crystal. Solid and dashed lines refer, respectively, to the forward and backward pass in the crystal. (OC – output coupler, SHG – second harmonic generation, FW – fundamental wave, SH – second harmonic)

3. Experiment

In this section, we present the laser cavity used in the presented experiment (Sec. 3.1) and the results we obtain with it (Sec. 3.2). Then, we discuss how the output pulse parameters depend on the NLM modelocking device configuration (Sec. 3.3).

3.1 Experimental setup

The laser experiment we present here uses a 230- μm thick, 5-at.% doped Yb:YAG disk, contacted on a CuW heatsink by Dausinger + Giesen GmbH, and mounted in a 24-pass thin-disk pump head with a 2.1-mm diameter pump spot. The disk has a wedge of ~ 0.1 deg between the front and back surface and a non-astigmatic cold radius of curvature of -5.3 m. The disk is diode-pumped up to 160 W at a center wavelength of 936 nm. In Fig. 3(a) we present a schematic of the laser cavity and in Fig. 3(b) the evolution of the $1/e^2$ laser mode radius within the oscillator. We designed our cavity to have a double-reflection on the thin disk in order to increase the available gain per roundtrip. The cavity includes a 2.5-mm undoped YAG Brewster plate (BP), which fixes the polarization in the plane of the optical table and provides $\delta = 6.37$ mrad/MW of self-phase modulation (SPM). In a first step, we operate the cavity without the $\chi^{(2)}$ crystal, but with the dichroic OC, and we achieve up to 30 W of output power with 33% optical-to-optical efficiency in continuous-wave (cw) single-mode operation ($M^2 < 1.1$). The dichroic OC used for the NLM configuration has 19.7% transmission ($R_{\text{FW}} = 80.3\%$) at the FW (1030 nm) and high reflectivity ($R_{\text{SH}} = 99.9\%$) at the SH (515 nm). For modelocking, we insert a 500- μm -thick type-1 BBO crystal close to the cavity focus on the OC mirror (beam waist radius of 185 μm), as shown in the inset [Fig. 3(c)]. The crystal is cut for phase matching at 1030 nm with both faces anti-reflection coated for 1030 nm and 515 nm.

We achieve correct phase matching for the SHG process by optimizing the tilt of the BBO crystal while looking at the small green leakage from the OC. For a correct phase offset $\Delta\phi$ between FW and SH for high-efficiency OPA we tune the spacing between the nonlinear crystal and the OC in a range between 5 mm and 8 mm in order to minimize the non-back-converted SH. The modelocking process is initiated by lightly tapping the mounting post of the focusing mirror before the BBO crystal.

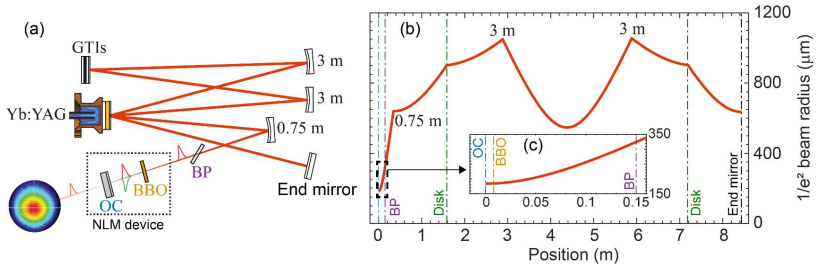


Fig. 3. (a) Schematic representation of the laser cavity. (b) Evolution of the $1/e^2$ mode radius. Vertical dashed lines indicate the position of crystals, OC, and end mirror. Labels indicate the curvature of concave mirrors. Inset (c): zoom of mode radius near the OC. (GTIs – dispersive mirrors, BP – Brewster plate)

Flat dispersion-compensating mirrors providing negative group delay dispersion (GDD) are used in the cavity to balance the SPM accumulated in air, the BBO crystal, the BP, and the disk.

3.2 Modelocking results

In our optimization of the modelocked operation, we focused on the one hand on reaching the shortest pulse duration, and on the other hand on maximizing the output power. We always optimize the distance between BBO crystal and OC in order to have the maximum back-conversion of the SH during the second pass in the BBO crystal. However, by adjusting the SHG phase matching, we adapt the reflectivity saturation and thus obtain the following two configurations:

- Short pulse (SP) configuration: the BBO tilt is tuned such that the green leakage through the OC (in cw operation) is maximized, i.e., $\Delta k = 0$. This maximizes the reflectivity modulation of the NLM device, allowing for the shortest pulses.
- High power (HP) configuration: we slightly phase mismatch the SHG process by reducing the transmitted green light through the OC to $\sim 85\%$ of the maximum value (in cw operation). This reduction of the SHG efficiency corresponds to a phase mismatch $|\Delta k \cdot L| \sim 0.3\pi$ [32]. This results in a higher OC rate and lower FW reflectivity, which, in turn, allows for higher output power.

Using an intracavity GDD from the GTI mirrors of -5900 fs^2 per roundtrip, we obtain 323-fs pulses at 21 W of output power in the SP configuration, at a repetition rate of 17.8 MHz. This corresponds to a pulse energy of $1.2 \mu\text{J}$ and to more than 3 MW of extracavity peak power. The pulses are supported by an optical spectrum with a FWHM of 4.23 nm [see Fig. 4(a)], which corresponds to a transform-limited duration of 263 fs. The chirp in the pulses could be due to the SHG process, and will be investigated in future work.

In the HP configuration, we could increase the output power up to 28 W at 150 W of pump power, however with substantially longer pulses of 570 fs. In this case, the intracavity GDD is increased to -7000 fs^2 per roundtrip.

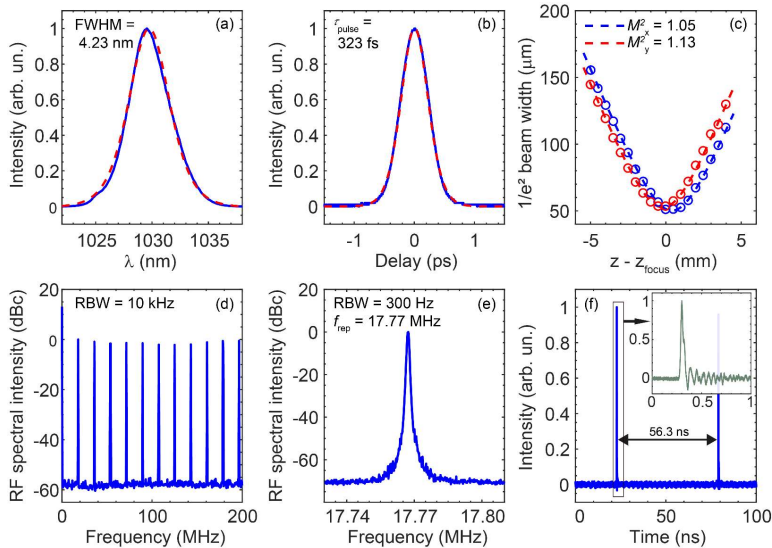


Fig. 4. Diagnostics for the configuration with the highest peak power (SP configuration, total GDD from the mirrors -5900fs^2 yielding 323 fs pulse duration and 21 W average power). We acquire the diagnostics on the output beam of the laser. (a) optical spectrum, (b) autocorrelation trace, (c) M^2 measure, (d) radio frequency (RF) trace showing the RF comb, (e) RF trace showing the peak at the repetition rate (Res BW = resolution bandwidth), (f) sampling scope trace, in the inset a zoom on a single pulse with a different span. The ripple in the sampling oscilloscope trace is due to the detector. The $1/e^2$ beam radius in the M^2 measurement is calculated using the second momentum width ($D^2\sigma$). The autocorrelation trace and the optical spectrum are fitted with a sech^2 function (red dashed line). (RBW – Resolution bandwidth)

We ensured clean modelocking in all configurations by obtaining the optical spectrum, the autocorrelation trace and radio frequency spectra. Moreover, by scanning the autocorrelator delay up to 60 ps and acquiring a sampling oscilloscope trace with a 45 GHz bandwidth photodiode we prove single-pulsed operation. The beam quality is assessed by measuring the M^2 of the output beam using a commercially available scanning-slit automatized beam profiler. In all configurations, we obtain a nearly-diffraction-limited beam with an average $M^2 = [(M^2_x) + (M^2_y)]/2$ below 1.10. In Fig. 4 we present the diagnostics for the 323 fs pulse, corresponding to the highest peak power. Stable modelocking was observed for several hours in daily operation without any breakdown of modelocking.

The maximum achievable output power in this proof-of-principle experiment is currently limited by the comparatively small pump-spot size on our disk. We chose a maximum pump intensity safety limit of $\sim 5 \text{ kW/cm}^2$, which restricted the maximum pump power on our disk to 160 W. Additionally, the non-optimal center wavelength of the pump diodes led to our comparatively low optical-to-optical efficiency of 33 % in continuous wave single-mode operation and ~ 19 % in modelocked operation.

3.3 Experimental investigation of the NLM-modelocking regime

In Fig. 5(a) and 5(b) we show the pulse duration and output power versus pump power for three different experimental conditions: two short pulse (SP) configurations with different values of GDD, and one high-power (HP) configuration. In the NLM modelocking technique, the effective OC rate of the cavity varies with the peak intensity in the $\chi^{(2)}$ crystal. For a given configuration, increasing the pump power results in a decrease of the effective transmission, which yields a non-linear relation between output power and pump power as we can see in Fig. 5(b).

In order to accurately determine the intensity-dependent OC rate T_{nl} , we employed a photodiode to measure a small FW leakage through an intracavity mirror in order to infer the intracavity power in modelocked operation. We calibrated the ratio between photodiode voltage and intracavity power in cw operation, since in this case the OC rate is equal to the linear transmission of the OC at the laser wavelength. Using the beam waist on the BBO crystal calculated from the cavity design [Fig. 3(b)] and the pulse duration retrieved from the autocorrelation trace (assuming a sech² pulse), we can estimate the peak intensity on the BBO crystal. The fluctuations in the effective OC transmission from different measurements are within 10%.

In Fig. 5(a) each data point is labelled with the corresponding OC rate for comparison to Fig. 5(c), where we show the effective OC rate versus the peak intensity on the BBO crystal. The solid points in Fig. 5(c) represent the same data points presented in Fig. 5(a) and 5(b) while the dashed points are additional measurements shown only in Fig. 5(c). For clarity of presentation, these additional points are not shown in Fig. 5(a) and 5(b). The solid purple line in Fig. 5(c) is the prediction of our numerical model, which we describe in section 4. The model accurately predicts the behavior of the device. The configurations optimized for high power generally present an effective OC rate slightly higher than the ones optimized for short pulses, and higher than the model (which assumes $\Delta k=0$). This trend is consistent with the fact that in the high-power configuration, the SHG process efficiency is slightly sub-optimal, leading to a less pronounced effect of the NLM of reducing the effective OC transmission. Additionally, our model does not take into account the reflection losses on the BBO, which are <0.5%. These losses will have the effect of slightly reducing the effective OC transmission.

Next, we also investigate the influence of the NLM device on the pulse shaping. For that we compare in Fig. 5(a) the pulse duration achieved in the short-pulse and high-power configuration with the same amount of intracavity GDD (-5900 fs²). The difference between these two configurations clearly indicate that the phase matching substantially influences the pulse duration. Moreover, we compare the pulse durations achieved in the SP configuration for different values of intracavity GDD [in Fig. 5(b) we show -4800 fs² and -5900 fs²]. The change in GDD only slightly influences the shortest achievable pulse duration. This observation suggests that the leading process in pulse formation is the NLM, rather than the soliton shaping effect. To further test this hypothesis, we fit the experimental data with an exponential function, $\tau = cE_p^{-\alpha}$, where E_p is the intracavity pulse energy. We find for α values between 0.5 and 0.8. A conventional soliton shaping mechanism, arising from GDD and SPM, would have $\alpha \sim 1$ [33]. This deviation from pure soliton shaping suggests that the NLM device dynamics strongly contribute to the pulse formation process.

In the HP configuration, the slightly phase mismatched SHG process leads to a non-negligible SPM, with its sign depending on the sign of the phase mismatch Δk . This could potentially influence the pulse formation mechanism. However, in these experiments we did not observe any significant change in the modelocking behavior for different signs of the phase mismatch.

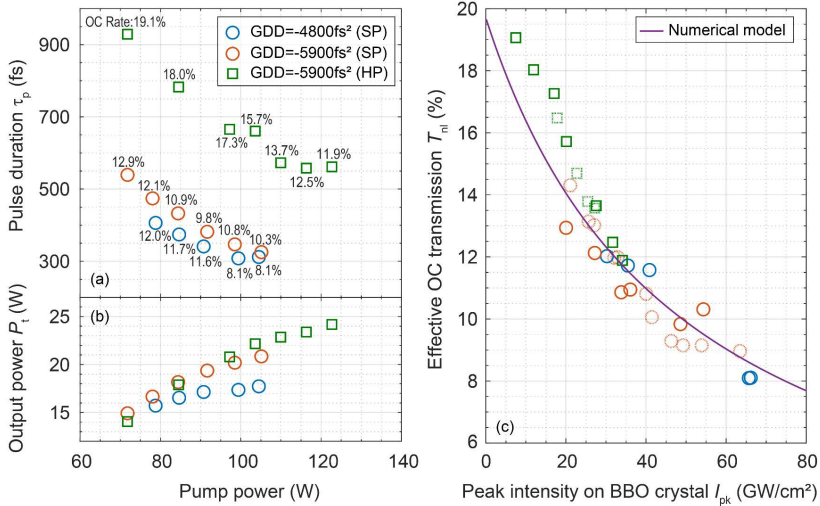


Fig. 5. Characterization of pulse duration (a) and output power (b) versus the pump power. Circles correspond to configurations optimized for short pulses (SP), i.e., $\Delta k = 0$; squares to configurations optimized for high power (HP), i.e., the SHG process is slightly detuned from perfect phase matching. (c) Saturable loss effect of the nonlinear mirror. The solid line is the prediction of our model. Solid points: same data shown in (a) and (b); dashed points: additional data points for the same laser configuration. (GDD – Group delay dispersion)

4. Numerical model of the NLM device

In this section, we present a model for the NLM technique (Sec. 4.1), demonstrate that it stands in excellent agreement with our experimental results presented in section 3 (Sec. 4.2), and predict the next steps needed for scaling the output power and pulse duration of NLM modelocked TDLs.

4.1 Description of the model

We base our model on coupled-wave equations which describe the two-stage process, namely SHG on the first pass through the $\chi^{(2)}$ crystal, followed by the reverse process of OPA on the return pass. Because of the high intracavity pulse energy involved ($>1 \mu\text{J}$), we can use a loose focus (beam waist radius of $185 \mu\text{m}$) on a thin BBO crystal (length $L = 500 \mu\text{m}$), and hence spatial effects such as diffraction and Poynting vector walk-off are negligible. On the other hand, temporal effects (mainly the group velocity mismatch (GVM)) play an important role in limiting the bandwidth of the device [26, 28]. Indeed the GVM delays the SH pulse with respect to the FW, which leads to a reduced back conversion of the SH to the FW during the second pass in the $\chi^{(2)}$ crystal. In our configuration the GVM parameter in the $\chi^{(2)}$ crystal corresponds to $\delta_{1,2} = 1/v_g^{\text{SH}} - 1/v_g^{\text{FW}} = 93 \text{ fs/mm}$ [34]. For two passes in a $500\text{-}\mu\text{m}$ thick BBO crystal, the total delay sums up to $\sim 100 \text{ fs}$ and becomes comparable to the pulse duration, thus it has to be included in our model. By neglecting the spatial effects but including temporal effects to first and second order, we obtain a simplified coupled-wave equations model:

$$\begin{aligned}
\frac{\partial E_{FW}(t, z)}{\partial z} - i \frac{\beta_{FW}}{2} \frac{\partial^2 E_{FW}}{\partial t^2} &= -i \frac{d_{\text{eff}} \omega_{FW}}{c n_{FW}} E_{FW}^*(t, z) E_{SH}(t, z) \exp(-i \Delta k z) \\
\frac{\partial E_{SH}(t, z)}{\partial z} + \left(\frac{1}{v_g(\omega_{SH})} - \frac{1}{v_g(\omega_{FW})} \right) \frac{\partial E_{SH}(t, z)}{\partial t} - i \frac{\beta_{SH}}{2} \frac{\partial^2 E_{SH}}{\partial t^2} &= -i \frac{d_{\text{eff}} \omega_{FW}}{c n_{SH}} E_{FW}^2(t, z) \exp(i \Delta k z)
\end{aligned} \tag{4}$$

We use the following variables: E_j : electric field envelope ($j = FW$ or $j = SH$); n_j refractive index; ω_j : center frequency; v_g : group velocity; d_{eff} : effective nonlinear coefficient of the material [35]; β_j : group velocity dispersion parameter; Δk phase mismatch for wavevectors $k_j = \omega_j n_j / c$; z : longitudinal position in the crystal; t : delay, in the moving coordinate system relative to the group velocity of the FW.

We use Eqs. (4) to model stages (i) and (iii) of the NLM device, as described in section 2. For stage (i), the SHG process, we solve Eqs. (4) using as initial conditions a pulse with a temporal sech profile for $E_{FW}(t, 0)$, and set $E_{SH}(t, 0) = 0$. We assume perfect phase-matching and therefore set Δk to zero. For stage (ii), we take the output envelopes $E_{FW}(t, L)$ and $E_{SH}(t, L)$, where L is the length of the BBO crystal, and apply the linear reflectivity of the OC (i.e., power reflectivities of $R_{FW} = 80.3\%$ for the FW and $R_{SH} = 99.9\%$ for the SH). Additionally, we add a phase shift $\Delta\phi = -\pi$ to the SH. The combination of $\Delta\phi = -\pi$ and $\Delta k = 0$ corresponds to the optimal condition for the back-conversion of the SH to the FW. The resulting envelopes are then used as the input conditions to Eqs. (4) to model the returning pass (iii), i.e., the OPA process. By performing a series of simulations for different peak intensities on the $\chi^{(2)}$ crystal of the incoming pulse (I_{pk}), we retrieve the behavior of the NLM device for a pulse with a Gaussian intensity profile in space. It is worth noting that this model does not rely on any fitting parameters.

4.2 Results of the model: bandwidth considerations

We show the nonlinear reflectivity $R_{\text{nl}}(I_{\text{pk}}, \tau_i)$ as a function of the peak intensity on the BBO crystal I_{pk} for different output pulse durations τ_i in Fig. 6(a). The reflectivity modulation is given by the difference between the $R_{FW} = 80.3\%$ line (i.e., the linear reflectivity of the OC at 1030 nm) and the R_{nl} curve, defined as in Eq. (1).

The nonlinear reflectivity is significantly reduced for shorter pulse durations, because GVM leads to a reduced temporal overlap between the FW and SH in the second pass through the crystal. This effect results in increased losses of the device. The degradation in performance for shorter pulses corresponds to a limited bandwidth for which this device is able to provide optimal performance. We refer to this limit as modulation bandwidth. It is worthwhile to mention that the phase-matching bandwidth of each one of the single $\chi^{(2)}$ processes (namely SHG and OPA) is significantly larger than the bandwidth of the two processes combined together, because the delay between the FW and SH pulses accumulates through the two processes.

In Fig. 5(c), we showed the corresponding transmission of the NLM T_{nl} , as defined in Eq. (2), as a purple solid line. The nonlinear transmission $T_{\text{nl}}(I_{\text{pk}}, \tau_i)$ depends strongly on the pulse peak intensity on the BBO crystal I_{pk} . In contrast to the behavior of R_{nl} , T_{nl} is unaffected by the output pulse duration τ_i in the considered range (i.e., for pulses longer than 200 fs). This independence of T_{nl} from τ_i is due to the fact that it involves only one pass in the $\chi^{(2)}$ crystal and that the bandwidth of the SHG process alone is sufficient for efficient conversion. Thus, in Fig. 5(c) we show only one curve, calculated for a pulse duration of 1 ps, to compare with the experimental values. The good agreement between experiment and theory confirms the validity of our model.

The limitations in the modulation bandwidth of the NLM does not only consist in a reduced nonlinear reflectivity, but translates also into a pulse lengthening effect. Fig. 6(b) shows the pulse-shortening parameter, κ , defined as in Eq. (3), as a function of the pulse

duration transmitted by the NLM. Below a certain pulse duration, the NLM stops acting as a pulse shortener on each round-trip of the cavity. As is clearly visible, this effect is only weakly dependent on the pulse peak intensity on the BBO crystal I_{pk} . Moreover, this threshold point scales with the crystal length. For pulse durations below 300 fs in our experimental configuration, Fig. 6(b) predicts that the NLM causes a pulse lengthening on each round trip. Thus, this transition to $\kappa > 1$ likely explains why 300 fs pulse duration was the shortest we could obtain in this experiment, since the NLM (in the configuration used here) acts to lengthen pulses shorter than this.

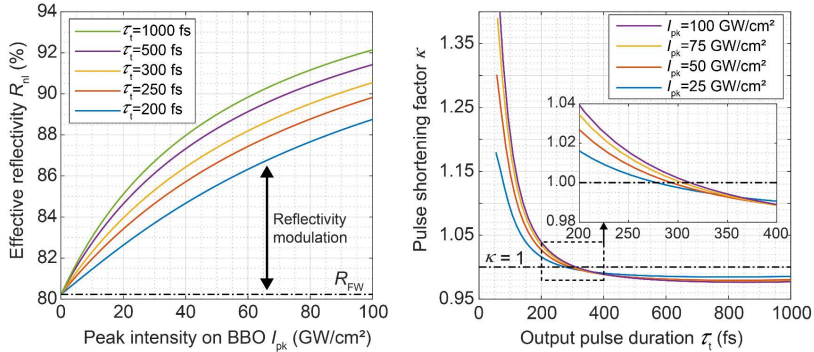


Fig. 6. Analysis of the performance of the NLM as a function of the output pulse duration τ_i and of the peak intensity on the BBO crystal I_{pk} . (a) Saturable reflectivity behaviour: effective reflectivity as a function of I_{pk} for different τ_i , (b) pulse shortening factor $\kappa = \tau_i/\tau_i$ as a function of τ_i for different I_{pk} .

Our model succeeded in predicting both the expected OC rate of the cavity and the shortest achievable pulse duration. Thus, we can use it in the design of the next generation NLM lasers with shorter pulses and higher powers. For example, increasing the nominal transmission of the OC for the FW to 40% instead of 20% would, at the same intensity and BBO crystal length, yield $\kappa = 1$ (i.e. the transition between pulse-shortening and pulse-lengthening) at a pulse duration of ~ 200 fs, together with an effective OC rate of $\sim 25\%$. Yb:YAG thin-disk lasers with a similar or even much higher OC rate have already been demonstrated [10, 36]. Use of a slightly shorter BBO crystal ($\sim 300 \mu\text{m}$ thick) and slightly higher intensity $\sim 90 \text{ GW/cm}^2$ would yield a further reduction in the NLM-limited pulse duration, towards < 150 fs pulses. This intensity is still below the BBO crystal damage threshold, based on other demonstrated systems. For instance in [37] a BBO crystal is used in an optical parametric amplifier with peak intensities up to 300 GW/cm^2 (~ 500 -fs pulses at 515 nm). Additionally, the pulse duration supported by the NLM can be reduced even further by GVM compensation techniques. These techniques have already been proposed [38] and demonstrated [26] to increase the modulation bandwidth of the NLM modelocking technique.

As well as offering more favorable pulse shortening, a higher OC rate also reduces the intracavity power demands for a given output power, which is highly favorable for power scaling. Moreover, with the NLM technique, the available modulation depth is approximately proportional to the nominal transmission of the OC for the FW. Thus, going to higher OC rates also increases the modulation depth accordingly, which is beneficial for obtaining short pulses. By scaling the pump spot size on the disk, and the laser spot size on the disk and BBO crystal, we expect that > 100 W output powers are well within reach. We expect that the BBO

crystal will be able to handle the increased thermal load based on other demonstrated systems, where such crystals are operated with kW-level average power [3].

5. Conclusion and outlook

We demonstrated the first NLM modelocked TDL, achieving 323-fs pulses at 21 W output power, which corresponds to pulses with $>1 \mu\text{J}$ pulse energy and $>3 \text{ MW}$ peak power. A key factor in obtaining this performance was the use of a thin-disk instead of a bulk laser geometry. Indeed the NLM, based on ultrafast nonlinear processes, benefits from high intracavity peak power that is typical of high-power short-pulsed thin disk lasers. Additionally the NLM process is well suited for high-power short-pulsed TDL operation as it provides an easily scalable modulation depth, offers an ultrafast response of the saturable loss (as in KLM), and can be operated in the center of the cavity stability region (as in SESAM modelocking).

We also presented a simple model for the NLM technique that, without any fitting parameters, succeeded in both predicting the effective OC rate and the shortest achievable pulse duration in the presented configuration. Based on our current laser performance and our simulations, we expect this first result to enable a new way towards high-power short-pulsed modelocked thin-disk oscillators in the near future. Increasing the spot size on the disk and simultaneously on the BBO crystal will allow for pumping harder and thus scaling up the average power to the 100-W regime. Employing a shorter crystal and an OC with a higher nominal transmission seems a promising way toward shorter pulses. Additionally, applying broadband gain materials (e.g., Yb:LuO, Yb:CALGO), even shorter pulses could be achieved. By simple adjustment of the $\chi^{(2)}$ crystal parameters or material, the technique also holds great promise for long-wavelength TDLs using new thin-disk gain media such as Ho:YAG [39].

Funding

Swiss National Science Foundation (SNSF) project grant numbers 200020_172644.

Acknowledgements

We would like to thank Prof. Clara J. Saraceno from the Ruhr-Universität Bochum for helpful discussions of thin-disk laser technologies.

7.3 Manuscript 2

Our first power scaling experiments of the NLM modelocking regime, together with our study of the Q-switching instabilities and the effect of the NLM tuning on the pulse formation are presented in the following manuscript.

Title: "Power scaling nonlinear-mirror modelocked thin-disk lasers"

Accepted for publication in Optics Express (2019).

Power-scaling of nonlinear-mirror modelocked thin-disk lasers

I. J. GRAUMANN¹, F. SALTARELLI¹, L. LANG¹, V. J. WITTEW²,
T. SÜDMEYER², C. R. PHILLIPS¹ AND U. KELLER¹

¹*Institute for Quantum Electronics, ETH Zurich, 8093 Zurich, Switzerland*

²*Laboratoire Temps-Fréquence, Université de Neuchâtel 2000 Neuchâtel, Switzerland*
**ivangr@phys.ethz.ch*

Abstract: We present a first power-scaled nonlinear-mirror (NLM) modelocked thin-disk laser based on the gain material Yb:YAG. The laser oscillator delivers average output powers up to 87 W and peak powers up to 14.7 MW with sub-600-femtosecond pulses at ≈ 9 -MHz repetition rate. We demonstrate a threefold improvement in average output power and sixfold improvement in pulse energy compared to previous NLM-modelocking results. We obtain peak powers in excess of 10 MW for the first time from an NLM-modelocked laser oscillator. In our laser, the NLM is assisted by a semiconductor saturable absorber mirror (SESAM) to reliably initiate pulsed operation. We validate the high-power suitability of the NLM modelocking technique using low-absorption $\chi^{(2)}$ crystals and optimized dichroic-mirror coating designs. Furthermore, we discuss stability against Q-switching and study how the tuning of the nonlinear mirror affects the laser performance.

© 2019 Optical Society of America under the terms of the [OSA Open Access Publishing Agreement](#)

1. Introduction

Ultrafast laser sources are key technological devices to a variety of applications both in industry and scientific research. For example, the combination of high peak power and ultrashort pulse duration has enabled industrial micro-machining, nonlinear biomedical imaging, and frequency conversion to extreme wavelengths such as the extreme ultraviolet (XUV) and THz [1–4]. The development of Yb-based systems, with low-cost direct diode-pumping schemes, further facilitated the deployment of these sources and provided the technology for combining high-power and ultrafast laser operation. Today, the leading technologies for high-power ultrafast laser amplifier systems, namely fiber, slab and thin-disk, are based on a geometry that optimizes the surface-to-volume ratio for efficient heat removal, enabling kW-level average powers [5–8]. These benchmark performances are achieved in amplifier systems which consist of a low-power seed oscillator followed by pulse shaping stages, several amplification stages and compression. Besides the overall large footprint of these multiple stages, high-power amplifiers generally have various trade-offs in terms of beam quality, nonlinearity management, repetition rate scaling, spectral bandwidth, pulse quality, and pulse contrast. Alternatively, high-power ultrafast laser operation can be achieved from a single modelocked laser oscillator combining diffraction-limited beam quality, transform-limited pulses, megahertz repetition rates, and low noise [9]. The thin-disk geometry is well-suited for this purpose, with the thin gain medium providing excellent heat removal capabilities, low nonlinearity and power-scalability [10]. Based on the high quality and technological maturity of Yb:YAG as gain material, thin-disk laser (TDL) oscillators have demonstrated continuous-wave (cw) operation up to 10 kW ($M^2 \approx 10$) from a single disk [11] and ultrafast operation up to 350 W [12].

Ultrafast laser operation in TDL oscillators is achieved via passive modelocking and requires an intracavity saturable loss to initiate and stabilize the pulse formation with soliton modelocking [13, 14]. The record performance of 350 W [12] was achieved using a semiconductor saturable absorber mirror (SESAM) [15] (Fig. 1(a)). The SESAM consists of semiconductor layers forming a distributed Bragg-reflector topped by InGaAs quantum wells

acting as saturable absorbers and a top coating for a high damage threshold [15-17]. The epitaxially-grown SESAM structure can be contacted onto a heatsink and directly placed inside the laser resonator to initiate and stabilize soliton modelocking [13]. This flexibility is reflected in the numerous results achieved with very diverse laser configurations and gain materials [9]. However, for targeting shorter pulses, a trade-off between gain bandwidth and average power has been observed for Yb-doped thin-disk gain media when using alternative host materials with broader bandwidths than YAG (see Fig. 3 in [9]). This trade-off is attributed to a combination of less favorable material properties and crystal quality for high-power laser operation, and the slow saturable absorber behavior of the SESAM. Alternatively Kerr-lens modelocked (KLM) thin disk lasers have demonstrated high output powers up to 270 W with 330-fs pulses [18] and 155 W with 140-fs pulses [19] (Fig. 1(a)). Relying on Kerr-lensing combined with soft- and hard-aperture effects, this modelocking scheme provides a fast absorption-free loss modulation. For a given gain material, KLM has enabled shorter pulse durations due to its fast saturable loss mechanism, which enables a larger fraction of the available gain bandwidth to be utilized. However, this comes at the cost of an increased complexity in the resonator design, which couples resonator stability and pulse formation. This reduces the flexibility of KLM and makes initiating pulse formation more challenging.

An attractive alternative providing a fast loss modulation is for example the frequency-doubling nonlinear-mirror (NLM) modelocking technique [20]. In this technique, the output coupler (OC) of the laser cavity is replaced with a new device: an intracavity $\chi^{(2)}$ crystal cut for type-1 second-harmonic generation (SHG), combined with a dichroic output coupler (OC) fully reflecting the second harmonic (SH) but only partially reflecting the fundamental wave (FW) [20]. The incident intracavity FW light is partly converted to the SH in the $\chi^{(2)}$ crystal, experiences losses at the dichroic OC, and is partially replenished by the fully reflected SH in the return pass through the $\chi^{(2)}$ crystal (described in Section 2.1 and Fig. 2). Since SHG is a nonlinear process, higher reflectivities are obtained at higher intensities, yielding a saturable loss mechanism [20]. The resulting NLM promises to combine the advantages of SESAM modelocking and KLM by providing a large, ultrafast, and absorption-free loss modulation that is decoupled from the oscillator geometry. These features make NLM modelocking ideally suited to generate ultrashort pulses at high average powers.

NLM modelocking was mainly investigated with low-power, high repetition rate bulk oscillators. Due to the low available intracavity power, this required the use of few-millimeter-long $\chi^{(2)}$ crystals, which severely limited the lowest achievable pulse duration to >5 ps [21-23] (Fig. 1(b)) due to group-velocity mismatch (GVM) between the FW and SH in the $\chi^{(2)}$ crystal. The higher intracavity peak power available from thin-disk laser oscillators allows for the use of much thinner crystals (≈ 1 mm), thereby enabling significantly shorter pulses. In our recent first demonstration of an NLM-modelocked thin-disk laser, we used a 0.5-mm-thick BBO crystal and obtained pulses as short as 323 fs at an average power of 21 W, reaching 3.2 MW of peak power [24] (Fig. 1(b)). It is worth noting that the achieved pulse duration is comparable to typical pulse durations obtained with KLM (Fig. 1(a)), and is the first sub-picosecond pulse duration reported for NLM-modelocking, to the best of our knowledge (Fig. 1(b)).

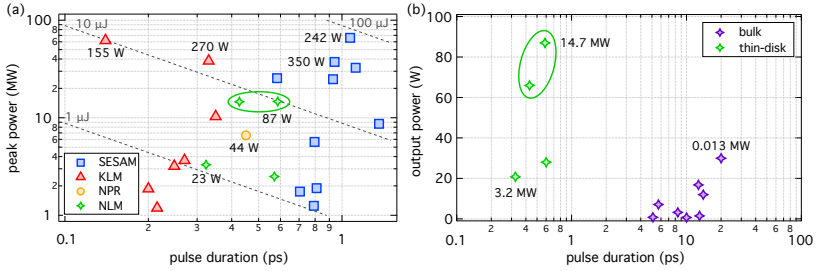


Fig. 1. (a) Overview of passively modelocked thin-disk laser results obtained with the gain material Yb:YAG and different modelocking techniques. Refs. [18, 19, 24-37]. NPR: nonlinear polarization rotation [38]. The dashed lines indicate constant pulse energy values. The average power of state-of-the-art results is indicated on the graph and the presented results are highlighted by the green circle. (b) Average output power and pulse duration of NLM-modelocked oscillators in the thin-disk and bulk geometries. Refs. [21-23, 39-43]. The peak power of state-of-the-art results is indicated on the graph and the presented results are encircled in green.

Here we demonstrate significant improvements in NLM-modelocked thin-disk lasers towards the state-of-the-art demonstrated with other modelocking techniques. We combine the fast loss modulation of the NLM with a SESAM to obtain a reliable initiation of pulsed operation and optimize the NLM-modelocking process in terms of Q-switching instabilities that arise in this new regime of laser operation (femtosecond NLM). We demonstrate an NLM-modelocked Yb:YAG thin-disk laser delivering 66 W in 426-fs pulses at 9.3 MHz in a first configuration, and up to 87 W with 586-fs pulses at 8.8 MHz in a second configuration. The ultrafast oscillator produces pulses with energies up to 9.8 μJ and peak powers up to 14.7 MW (Fig. 1). In particular, we demonstrate peak powers in excess of 10 MW for the first time with an NLM-modelocked oscillator, while the average power is three times higher than previously demonstrated with this modelocking technique, to the best of our knowledge. Moreover, as illustrated in Fig. 1, the pulse duration is significantly shorter than typically achieved by high-power SESAM-modelocked Yb:YAG thin disk lasers.

In the following, we first present our modelocking results (section 2) and comment on our approach to mitigate Q-switching instabilities (section 3). In the final part we present our investigation of the NLM-modelocking regime (section 4) and conclude with prospects for further power scaling.

2. High-power NLM-modelocked oscillator

In this section we present our high-power NLM-modelocked thin-disk laser. We took several key steps compared to our earlier result [24] to enable the improved performance:

- (1) We used a state-of-the-art Yb:YAG thin-disk contacted on a diamond heat spreader.
- (2) We implemented an active-multipass cavity geometry to optimize the oscillator for high-power operation and simultaneously lower the repetition rate compared to previous results.
- (3) We improved the thermal and damage properties of the NLM device by using a low-absorption LBO crystal as the $\chi^{(2)}$ medium, and optimized dichroic output coupler (OC) coatings leading to a higher damage threshold.
- (4) We included an intracavity SESAM to assist the optimization of the NLM device during modelocking and reliably initiate pulsed operation.
- (5) We carefully characterized the NLM operating regime, allowing us to define guidelines to avoid Q-switching instabilities and tune the pulse duration during modelocked operation.

We first present the operating principles of the NLM device and introduce its tuning parameters, then describe the thin-disk oscillator and finally present the modelocking results.

2.1 NLM operating principle

Here we describe the three-stage operating principle of the frequency-doubling NLM and introduce the key parameters used to tune the NLM device, as illustrated in Fig. 2:

- (1) An incident FW with a power P_{FW}^{inc} generates a SH with an efficiency depending on the phase-mismatch $\Delta k = k_{SH} - 2k_{FW}$ (Fig. 2(b), solid lines).
- (2) The FW and SH co-propagate to the OC where a part P_{FW}^{out} of the FW is transmitted. The reflected FW and SH co-propagate back to the $\chi^{(2)}$ crystal. The waves accumulate a relative phase offset due to dispersion in the air gap and different reflection phases in the dichroic OC coating layers.
- (3) The SH is converted back to the FW via optical-parametric amplification (OPA) (Fig. 2(b), dashed lines), resulting in a reflected power P_{FW}^{ref} at the FW and a residual power loss P_{SH}^{loss} in the SH. The efficiency of the back-conversion process is determined by the relative phase offset introduced by the difference in the refractive index of air for the FW and SH, and can be adjusted experimentally via the air gap.

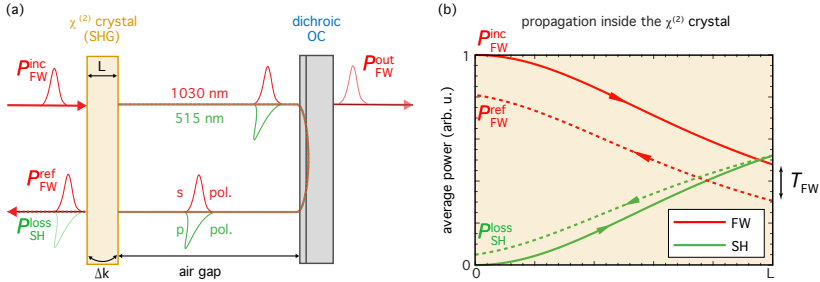


Fig. 2. Nonlinear mirror (NLM): (a) Operating principle of the NLM device: the incident fundamental wave (FW) at 1030 nm is partially converted to the second harmonic (SH) in the $\chi^{(2)}$ crystal, then experiences higher losses than the SH upon reflection on the dichroic output coupler (OC), and is finally replenished by the OPA process during the second propagation through the $\chi^{(2)}$ crystal. The phase-mismatch Δk and the air gap determine the efficiency of the second harmonic generation (SHG) process and the back-conversion, respectively. (b) Evolution of the power in the FW and SH during the first pass through the $\chi^{(2)}$ crystal leading to the generation of the SH (solid lines) and during the second pass through the crystal converting the energy back to the FW (dashed lines). T_{FW} : transmission of the dichroic OC for the FW.

As emerges from this description, for a given beam size on the $\chi^{(2)}$ crystal, the operation of the NLM is mainly determined by two parameters: the phase-mismatch Δk , given by the angle of incidence of the intracavity beam on the $\chi^{(2)}$ crystal, and the air gap between the $\chi^{(2)}$ crystal and the dichroic OC. The operation of the NLM can be characterized experimentally by carefully measuring P_{FW}^{inc} and P_{SH}^{loss} via leakages of intracavity mirrors in addition to P_{FW}^{out} . The effective nonlinear reflectivity, effective nonlinear transmission and SH losses of the NLM are then calculated as follows:

$$R_{\text{eff}} = 1 - \frac{P_{FW}^{out} + P_{SH}^{loss}}{P_{FW}^{inc}} \quad (1)$$

$$T_{\text{eff}} = P_{FW}^{out} / P_{FW}^{inc} \quad (2)$$

$$L_{SH} = P_{SH}^{loss} / P_{FW}^{inc} \quad (3)$$

2.2 Thin-disk laser oscillator

The thin-disk laser oscillator used in our experiments is depicted in Fig. 3(a) and is based on a 100- μm -thick, 10-at.-%-doped Yb:YAG disk with a diameter of 16 mm. The disk is contacted onto a diamond heatsink (TRUMPF Lasers GmbH) and has a concave cold radius of curvature of 2.04 m without any astigmatism. We set up the disk inside a thin-disk head with 36 passes of the 940-nm pump beam through the disk. In our experiments, we used up to 400 W of pump power with a pump beam diameter of 4.4 mm on the disk. Under these conditions, the diopter change due to thermal lensing of the disk is $<0.1\text{ m}^{-1}$ which we measured with an interferometer. In order to optimize the laser resonator for high output power, we increase the available roundtrip-gain by increasing the number of passes of the intracavity laser beam through the disk via a re-imaging scheme [32]. With three reflections on the disk, our cavity supports laser operation with an OC transmission $>40\%$ (Fig. 3(c)). The multipass arrangement also significantly increases the cavity length, leading to repetition rates around 9 MHz. The cavity layout is shown in Fig. 3(a). In addition to the multipass arrangement, it includes a telescope extension at one end of the cavity to adjust the beam size on the NLM device from $\approx 290\text{ }\mu\text{m}$ to $\approx 400\text{ }\mu\text{m}$ (Fig. 3(b)).

We first characterized the performance of the laser in cw operation, i.e. without the $\chi^{(2)}$ crystal and the SESAM inside the cavity. As we expect the overall cavity losses to decrease during modelocked operation, we operated the laser at two different values of the OC transmission. We achieved up to 160 W of average output power with a linear 25% OC, and 99 W with a linear 45% OC, at a pump power of 355 W (Fig. 3(c)). This corresponds to an optical-to-optical efficiency of 45% and 28% respectively. We also characterized the beam quality in both cases and measured an $M^2 < 1.15$, confirming that the beam is close to diffraction-limited. For the modelocking experiments we choose to use a large linear OC transmission around 40% to minimize the intracavity power. The power slope with a 25% OC confirms that the cavity behaves well for lower cavity losses and higher intracavity powers.

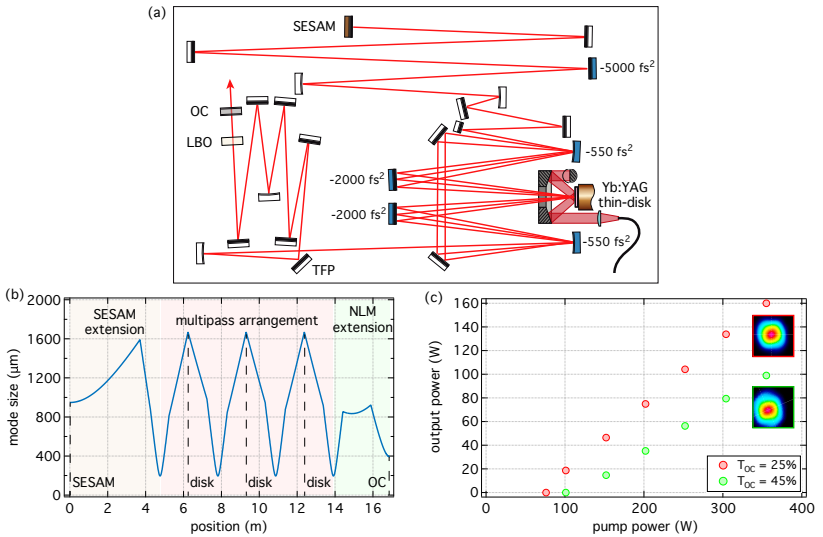


Fig. 3. SESAM-assisted NLM-modelocked thin-disk laser oscillator: (a) Cavity layout. The mirrors indicated with a blue color are Gires-Tournois-Interferometer (GTI)-type mirrors and introduce negative group delay dispersion (GDD). The multipass arrangement is extended on

one end towards the SESAM and on the other end towards the NLM device. A thin-film polarizer (TFP) is introduced for polarization control. The multipass arrangement also includes most of the intracavity dispersion. (b) Evolution of the $1/e^2$ cavity mode radius. The re-imaging scheme on the disk leads to numerous foci. (c) Output power slopes in cw operation for two different OCs. The insets show the corresponding beam profiles at the highest power.

2.3 Modelocking experiments

Femtosecond thin-disk lasers are usually modelocked in the soliton modelocking regime and therefore rely on the balance of intracavity self-phase modulation (SPM) and dispersion for pulse shaping, and a saturable absorber to initiate and stabilize pulsed operation [13]. The re-imaging scheme implemented to increase the number of laser passes on the disk results in numerous intracavity foci (Fig. 3(b)), leading to a large SPM contribution from the intracavity air. We compensate this nonlinear phase with Gires-Tournois-Interferometer (GTI)-type dispersive mirrors inserted in the multipass arrangement (Fig. 3(a)). Accounting for the dispersion of the intracavity thin-film polarizer (TFP) introduced for polarization selection, and the optional addition of a ~ 5000 fs² GTI mirror to the cavity, the total cavity dispersion amounts to either $\sim -31,600$ fs² or $\sim -41,600$ fs² per roundtrip. In order to facilitate the optimization of the NLM device and achieve reliable initiation of the modelocked operation, we introduce a SESAM at one end of the cavity. Using the approach of Ref. [44], we characterized the SESAM nonlinear reflectivity as a function of the incident pulse fluence and retrieved a saturation fluence of $35 \mu\text{J}/\text{cm}^2$, a modulation depth of 2.7%, nonsaturable losses of 0.35% and a rollover parameter of $0.5 \text{ J}/\text{cm}^2$ (for a pulse duration of 170 fs). The $1/e^2$ intracavity beam radius on the SESAM is $\approx 950 \mu\text{m}$.

For our first modelocking experiments, we used a 0.5-mm-thick BBO crystal and a 45% dichroic OC for the NLM device. The $1/e^2$ intracavity beam radius on the BBO crystal was $\approx 290 \mu\text{m}$. We operated the NLM at a non-zero SHG phase-mismatch Δk in order to mitigate Q-switching instabilities (see section 3). With an intracavity dispersion of $\sim -31,600$ fs², we achieved up to 66 W of average output power with pulses as short as 426 fs full-width at half maximum (FWHM), at a repetition rate of 9.3 MHz (Fig. 4(a)-4(c)). This corresponds to a pulse energy of $7.1 \mu\text{J}$ and a peak power of 14.7 MW. Using a leakage through one of the intracavity mirrors, we estimate the intracavity average power to be ≈ 180 W, corresponding to an effective transmission of the NLM device of $\approx 36.7\%$ (Eq. (2)). We also measured the maximum temperature of the BBO crystal with a thermal camera and found that it exceeds 80°C , which would ultimately limit power scaling [45]. The heat load on the crystal is likely due to linear absorption at the laser or second-harmonic wavelength. The linear absorption is specified by the manufacturer (EKSMa) as <1000 ppm/cm at 1030 nm. Additionally, the dichroic OC was very susceptible to damage when initiating modelocking.

To target higher powers, we therefore improved the thermal and damage properties of the NLM device. We replaced the BBO crystal by a low-absorption LBO crystal (<20 ppm/cm at 1030 nm, Cristal Laser) and designed an optimized dichroic coating for the OC mirror with high-damage threshold (see section 3). Furthermore, we increased the beam size on the LBO crystal to $\approx 400 \mu\text{m}$, in order to saturate the NLM device at higher peak powers. Using a 1-mm-thick LBO and a 40% dichroic OC, and with $\sim -41,600$ fs² of intracavity dispersion, we achieved modelocking up to 87 W with a pulse duration of 586 fs and a repetition rate of 8.9 MHz (Fig. 4(d)-4(f)), corresponding to a pulse energy of $9.8 \mu\text{J}$ and a peak power of 14.7 MW. In this configuration, no damage of the dichroic OC occurred and the LBO crystal stayed at a temperature $<25^\circ\text{C}$, for an intracavity power of ≈ 240 W. The effective transmission of the NLM device in that case was $\approx 36.3\%$. For both results, we verified that no double-pulse was present by scanning the autocorrelation delay over a range of ≈ 60 ps. Additionally, we measured the pulse train with a fast (45 GHz) photodiode and a sampling oscilloscope.

The results presented in this section show the power-scalability of the NLM modelocking technique towards the 100-W level. We improved the average power by a factor ≈ 3 over previous results while keeping femtosecond pulse durations and demonstrated peak powers

close to 15 MW. Optimizing our oscillator also provided us with new insights into the mitigation of Q-switching instabilities and the influence of the NLM device on the pulse formation, which we present in the following section.

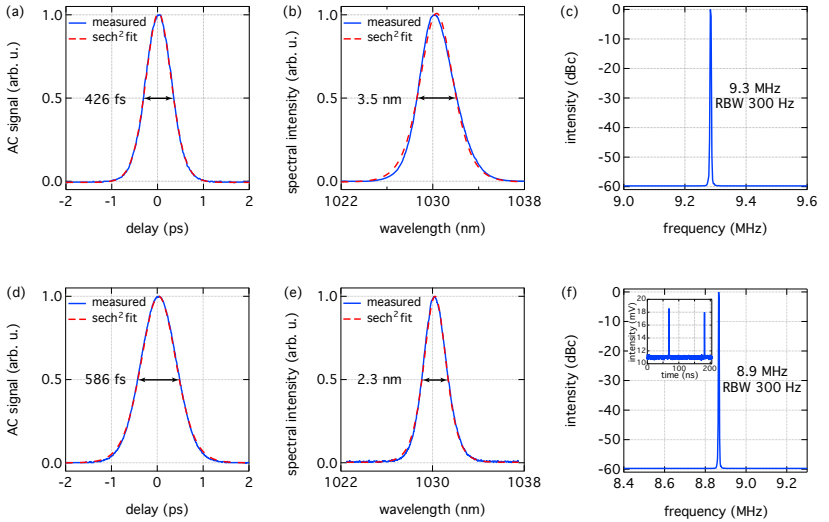


Fig. 4. High-power NLM-modelocked thin-disk laser oscillator: (a) Autocorrelation trace of the 426-fs pulses obtained at 66 W. (b) Optical spectrum of the 426-fs pulses, with a time-bandwidth product (TBP) of 1.34×0.315 (a transform-limited sech²-pulse has 0.315). (c) Microwave spectrum analyzer (MSA) trace showing the repetition rate of 9.3 MHz. (d) Autocorrelation trace of the 586-fs pulses obtained at 87 W. (e) Optical spectrum of the 586-fs pulses, with a TBP of 1.21×0.315 . (f) MSA trace showing the repetition rate of 8.9 MHz. The inset shows a sampling scope measurement with a 45-GHz fast photodiode. No side-pulse is apparent over the roundtrip time of 112.4 ns.

3. Study of the nonlinear-mirror modelocking regime

Here we describe the results of our investigation of the NLM-modelocking regime. In particular, we focus on avoiding Q-switching instabilities, which requires operation of the NLM device with a finite phase-mismatch Δk . We carefully characterize the operation of the NLM in these conditions and show its influence on the shaping of the intracavity pulse.

3.1 Q-switching instabilities

The NLM provides a saturable nonlinear reflectivity for initiating and stabilizing pulsed operation [13]. However, unlike SESAM and KLM modelocking schemes, the NLM effectively saturates the reflectivity of the OC, i.e. the main contribution to the total cavity losses. On one hand, this enables a straightforward scaling of the available modulation depth by changing the OC transmission. On the other hand, however, this implies that the saturation of the NLM device strongly affects the Q-factor of the laser cavity (e.g. by potentially halving the cavity losses). As a result, NLM-modelocked lasers are susceptible to Q-switched modelocking instabilities with a strongly modulated amplitude of the pulse train.

The modulation depth provided by the NLM is maximized when operating the $\chi^{(2)}$ crystal at phase-matching $\Delta k = 0$, and adjusting the phase offset between the electric field of the SH and the electric field squared of the FW on the return pass to $\pi \pmod{2\pi}$ for optimal back-

conversion (Fig. 5(a), blue curve) [24]. For short pulse durations, the group-velocity mismatch (GVM) between the FW and SH in the $\chi^{(2)}$ crystal leads to a reduction of the modulation depth, however this effect is small for the pulse durations considered here (>400 fs). In our experiments, we initially attempted to operate the NLM for optimal efficiency ($\Delta k = 0$ and optimal back-conversion), however we systematically damaged the dichroic OC due to Q-switching instabilities (Fig. 5(b)); the OC in this case was obtained commercially.

In the aftermath of these damage events, we fabricated a custom OC using ion-beam sputtering (IBS), designed to minimize the interaction of the SH with the coating layers. We designed this dichroic mirror to optimize the reflection of the SH within the first layers (see the green line in Fig. 5(c)) and adjusted the underlying layers for a flat 40% transmission of the FW and flat and nearly zero-dispersion for the FW and SH (Fig. 5(d)). We used SiO_2 as low- and Ta_2O_5 as high-index material. Since Ta_2O_5 has a bandgap of ~ 4.2 eV [46], two photon processes of the SH (about 2.4 eV) could ultimately limit further power scaling. Therefore we kept the field intensity of the SH (green line in Fig. 5(c)) low in the Ta_2O_5 layers. This resulted in a significantly improved damage threshold as no damage was observed with this mirror, despite continued Q-switched operation. If nonlinear effects or damage were a limiting factor for further power scaling, we could use HfO_2 (bandgap ~ 5.7 eV [47]) as a high-index material.

In order to mitigate Q-switching instabilities, we introduce a rollover in the nonlinear reflectivity curve of the NLM. The onset of rollover effects generally determine the transition between Q-switched modelocking and cw modelocking [48]. We detune the NLM from its optimal operation regime by rotating the $\chi^{(2)}$ crystal and changing the angle of incidence compared to phase-matching, and therefore operating at a finite phase-mismatch $\Delta k \neq 0$. This induces a rollover in the nonlinear reflectivity of the NLM that can be understood as follows: for a phase-matched cw interaction, the single-pass SHG process of the NLM does not exhibit back-conversion to the FW; however, with a finite phase-mismatch, back-conversion occurs after a certain distance through the SHG crystal, and the maximum SHG efficiency is reduced. Moreover, this distance decreases with input intensity and phase-mismatch [49]. In the context of an NLM device, these effects lead to a reduced maximum reflectivity and a rollover of the reflectivity at high intensities. Hence, the crystal phase mismatch can be used to limit both the available modulation depth and to reduce the intensity at which maximal reflectivity is obtained (Fig. 5(a), yellow and green curves).

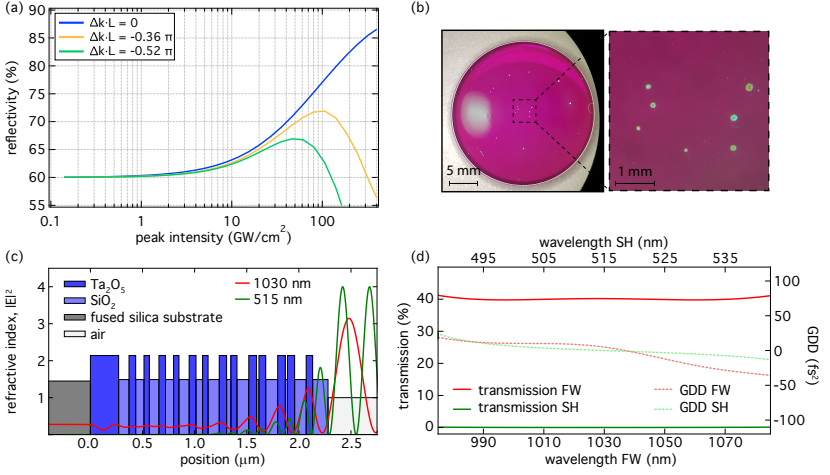


Fig. 5. Optimization of the NLM: (a) Simulated effective nonlinear reflectivity of the NLM device as a function of the incident pulse peak intensity for a 1-mm-long LBO and a 40% dichroic OC. The $1/e^2$ beam radius on the LBO is $300 \mu\text{m}$ and the pulse duration is set to 500 fs; the simulation assumes a Gaussian beam profile and a sech² pulse profile. The nonlinear reflectivity curve is plotted for different values of the phase mismatch Δk . For each case we adjust the phase offset between FW and SH to obtain an optimal back-conversion. (b) Microscope images of the OC mirror used in our first modelocking experiments at phase-matching $\Delta k = 0$, showing several damaged spots. (c) Custom-made dichroic OC using ion-beam sputtering (IBS). Layers and standing-wave pattern of the coating developed for increasing the damage-threshold of the dichroic OC. (d) Transmission and GDD of the produced dichroic mirror, shown for the FW and SH wavelengths.

By operating the NLM with a finite phase mismatch Δk , we suppressed Q-switching instabilities and achieved stable cw modelocking. Both results presented in section 2 were achieved in this regime, with a phase-mismatch $\Delta k < 0$. We further characterized the operation of the NLM in this regime, in particular its influence on pulse shaping.

3.2 Operation at non-zero phase-mismatch

In order to characterize the operation of the NLM, we carefully measure the output power at 1030 nm $P_{\text{FW}}^{\text{out}}$ directly with a power meter, as well as the incident power at 1030 nm $P_{\text{FW}}^{\text{inc}}$ and the SH loss power $P_{\text{SH}}^{\text{loss}}$ from the NLM via leakages of intracavity mirrors. The experimentally deduced effective nonlinear reflectivity and SH losses of the NLM are then calculated using Eq. (1) and Eq. (2). Furthermore, we estimate the nonlinear phase contribution of the NLM under the assumption of soliton modelocking [13].

The total roundtrip nonlinear phase contributing to the soliton pulse formation can be estimated using soliton theory [50]:

$$\varphi_{\text{sol}} = -(1.76/\tau_p)^2 D_{\text{rt}}, \quad (4)$$

where τ_p is the full-width at half-maximum (FWHM) pulse duration and D_{rt} is the total roundtrip dispersion. The two main sources of nonlinear phase-shifts contributing to the roundtrip B-integral B_{rt} are the NLM and the intracavity air. B_{rt} is the accumulated nonlinear phase for the peak of the pulse in space and time, and for free-space propagation the soliton phase φ_{sol} is related to B_{rt} via [51]:

$$\varphi_{\text{sol}} = \frac{3}{4} B_{\text{rt}} = \frac{3}{4} (B_{\text{NLM}} + B_{\text{air}}) = \varphi_{\text{NLM}} + \varphi_{\text{air}}, \quad (5)$$

where φ_{NLM} and φ_{air} are the effective roundtrip nonlinear phase contributions to the soliton pulse formation, accumulated in the NLM and the intracavity air respectively. The effective nonlinear phase contribution from the intracavity air can be calculated using:

$$\varphi_{\text{air}} = \frac{3}{4} B_{\text{air}} = \frac{3}{4} \cdot \frac{2\pi}{\lambda} n_2^{\text{air}} \int \frac{P_{\text{pk}}}{w(z)^2} dz, \quad (6)$$

where λ is the central wavelength of the pulse, n_2^{air} is the nonlinear refractive index of air, $w(z)$ is the $1/e^2$ intracavity beam radius, and P_{pk} is the pulse peak power. We deduce the nonlinear phase contribution from the NLM, under the assumption of soliton modelocking, by calculating: $\varphi_{\text{NLM}} = \varphi_{\text{sol}} - \varphi_{\text{air}}$. We further define the SPM coefficients $\gamma_{\text{NLM}} = \varphi_{\text{NLM}}/P_{\text{pk}}$ and $\gamma_{\text{air}} = \varphi_{\text{air}}/P_{\text{pk}}$.

For our study, we use a 1-mm LBO and a 40% OC for the NLM. In cw operation, we initially align the LBO to obtain phase-matched SHG. The SH power generated in cw is of order 100 nW-1 μ W and can be measured with a calibrated photodiode in order to optimize phase-matching. We then detune the angle of incidence by ≈ 20.7 mrad, corresponding to a phase-mismatch $\Delta kL = -0.61 \pi$, similar to the detuning used in our modelocking experiments ($L = 1$ mm is the length of the LBO). Next, we optimize the air gap in cw operation to obtain optimal back-conversion of the SH to the FW. We then initiate modelocking by gently knocking the OC and tune the air gap in pulsed operation by moving the LBO to study the influence of the phase offset on the laser performance.

In Fig. 6(a), we show the evolution of the output power and the pulse duration as a function of the air gap. The first point of the scan (air gap ≈ 83 mm) corresponds to the optimal air gap for back-conversion in cw, with modelocked operation initiated at this point. We then translate the LBO away from the OC to increase the air gap. As observed on Fig. 6(a), the output power is ≈ 70 W and varies by less than 5% over the scan range. However, the pulse duration varies significantly over the same range, from ≈ 790 fs down to ≈ 490 fs, hinting towards a large change of the roundtrip nonlinear phase as a function of the air gap. Since the intracavity beam size on the LBO (predicted from ray transfer matrix calculations) stays virtually constant ($310 \pm 2 \mu\text{m}$) across the scan range, the change in nonlinear phase can be attributed to the change of the NLM parameters, in this case the phase offset. Under the assumption of soliton shaping, we calculated the SPM coefficients γ_{air} , γ_{NLM} for the intracavity air and for the NLM device and show the results in Fig. 6(c). The intracavity peak power was evaluated using $P_{\text{pk}} = 0.88 (P_{\text{FW}}^{\text{inc}}/f_{\text{rep}})/\tau_{\text{p,FTL}}$, where f_{rep} is the pulse repetition rate and $\tau_{\text{p,FTL}}$ is the transform-limited pulse duration deduced from the measured spectrum of the output beam. As expected, the SPM coefficient for air is almost constant at ≈ 8 mrad/MW, as most of the SPM from air originates from the multipass part of the cavity, which essentially stays unaffected by the changing NLM air gap. The inferred SPM coefficient of the NLM device, however, varies significantly from ≈ 3.2 mrad/MW to ≈ 8.9 mrad/MW, becoming comparable to the SPM coefficient of the intracavity air for large air gaps. We conclude that the nonlinear phase introduced by the NLM is strongly dependent on the phase offset between the FW and SH on the return pass, and that this dependence leads to the tuning of the pulse duration we observe in Fig. 6(a). We have recently demonstrated compensation of positive SPM contributions with an intracavity phase-mismatched second-harmonic-generation crystal in a high-power thin-disk laser [52], which could be implemented to compensate or add to the nonlinear phase from the NLM device when targeting short pulses at higher powers and keep the laser operated in air.

We also calculated the experimental effective reflectivity and SH losses of the NLM device as a function of the air gap and plotted the results in Fig. 6(b). Interestingly, we initiated modelocking in a regime for which the effective reflectivity of the NLM is lower than the linear reflectivity of the OC, clearly indicating that the NLM device is not operating optimally. This indicates that the experimental conditions for optimal back-conversion in cw operation are different than those for pulsed operation, which could be due to a combination of intensity and temperature dependent phase-shifts in the LBO crystal. This difference also justifies the

presence of the SESAM in the cavity for initiating modelocking. We can differentiate two regimes of operation:

- Modelocking initiation: At the optimal air gap found in cw operation, we initiate modelocked operation. The SESAM losses are saturated, providing a modulation depth of $\approx 2\%$, but the NLM losses *increase* ($R_{\text{eff}} < R_{\text{lin}}$) by $\approx 1\%$, resulting in a net $\approx 1\%$ saturable loss in the cavity.

- Modelocking optimization: As we increase the air gap, the SESAM losses stay saturated, but the effective reflectivity of the NLM increases and eventually provides a net positive loss modulation (i.e. when $R_{\text{eff}} > R_{\text{lin}} = 60\%$) of $\approx 2\%$, resulting in a net 4% saturable loss in the cavity.

The fast loss modulation provided by the NLM supports the shorter pulses generated at larger air gaps. This improvement of the NLM operating regime when increasing the air gap is also reflected in the decreasing SH losses. It is worth noting that pulse durations < 700 fs are usually not supported by SESAM-modelocked thin-disk lasers based on Yb:YAG [9, 51], which further confirms the additional pulse reduction due to the fast saturable-absorber effect of the NLM device.

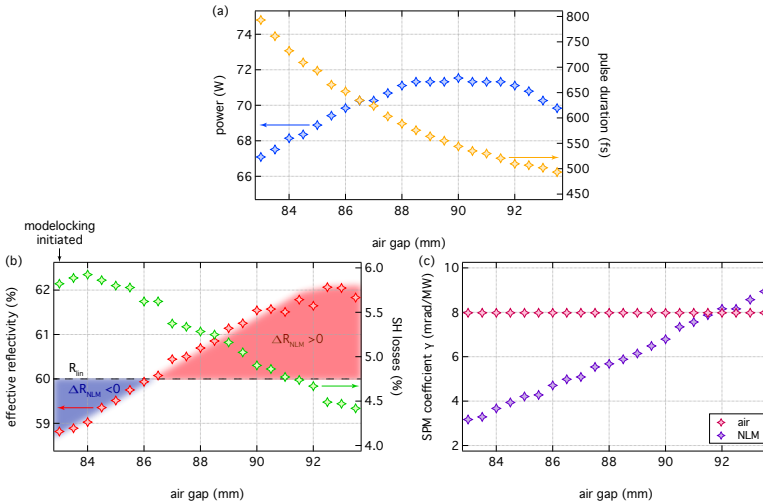


Fig. 6. Experimental characterization of the NLM-modelocking regime at a phase-mismatch $\Delta kL = -0.61 \pi$. The NLM device combines a 1-mm LBO with a 40% dichroic OC. We tune the air gap in pulsed operation by moving the $\chi^{(2)}$ crystal relative to the OC. We show the evolution of: (a) the output power and pulse duration, (b) the experimentally deduced effective reflectivity and SH losses, the dashed line represents the linear reflectivity of 60%, (c) the deduced SPM coefficients for the intracavity air and the NLM device as a function of the air gap.

To summarize: we characterized the operation of the NLM device at a fixed phase-mismatch and variable air gap between the LBO crystal and the OC. By adjusting the air gap, we change the efficiency of the back-conversion process and hence the strength of the NLM. This tuning also yielded shorter pulses at the output of the oscillator. Based on the assumption of soliton pulse shaping, i.e. that the reduced pulse duration corresponds to a change in intracavity nonlinearity, we deduce a strong dependence of the nonlinear phase contribution of the NLM on the phase offset set by the air gap.

3.3 Power scaling prospects

The underlying mechanism of the NLM is readily scalable by the beam size on the device. However, at some power level the thermal load on the crystal due to absorption at the FW or SH will become significant and lead to thermo-optic distortions. While thermal lensing effects are well-known in the context of power scaling, for an NLM there is the additional, related effect of thermal dephasing of the nonlinear interaction. Therefore, in this section we consider the sensitivity of the NLM process to changes in the phase mismatch, as would occur in the presence of excessive absorption in the crystal. We evaluate the case of an NLM consisting of a 1-mm-thick LBO crystal and a 40% dichroic OC, operating at a phase-mismatch $\Delta k \cdot L = -0.36\pi$, for which the optimal peak intensity lies around 100 GW/cm^2 (Fig. 5(a), yellow). For a phase-mismatch $\Delta k \cdot L = -0.52\pi$, the optimal peak intensity is reduced by a factor of two (Fig. 5(a), green). Using the temperature sensitivity of the phase mismatch of $d\Delta k/dT = 0.09 \text{ mm}^{-1}/\text{K}$, calculated from the Sellmeier relations [53], we can evaluate the temperature difference leading to such a dephasing for a 1-mm LBO crystal and find a value of $\approx 5.6^\circ\text{C}$. Power scaling could most readily be achieved by finding a suitable crystal and beam geometry to keep the on-axis temperature increase (arising due to absorption at the FW and SH) below these levels. Given the multi-100-W SHG results achieved in recent years [7, 52, 54], we are optimistic about further power scaling of the NLM approach.

Additionally, shorter pulse durations could be generated by using GVM compensation techniques [22]. This could allow for the generation of sub-200 fs pulses from a multi-100 W NLM-modelocked TDL.

4. Conclusion and outlook

We presented a first power-scaled NLM-modelocked thin-disk laser oscillator delivering close to 15 MW of peak power in 426-fs or 586-fs pulses, representing a promising alternative to KLM for generating peak powers $>10 \text{ MW}$ at sub-500-fs pulse durations. We designed our laser resonator using a re-imaging scheme on the disk allowing us to couple out $>40\%$ of the intracavity power and operate at reduced repetition rates $<10 \text{ MHz}$. We further used a SESAM to facilitate the optimization of the NLM device and enable reliable modelocked operation.

During our first modelocking attempts, we identified Q-switching instabilities as the main obstacle for stable cw modelocking because the NLM can saturate a large fraction of the cavity losses. We designed a new dichroic OC coating with a minimized interaction of the second harmonic wave and the coating layers, which led to significant improvements in terms of damage threshold. Furthermore, we mitigated Q-switching instabilities by operating the NLM device at a finite phase-mismatch, thus introducing a rollover in the nonlinear reflectivity of the device.

Using a BBO crystal, we demonstrated modelocking up to 66 W with 426-fs pulses at a repetition rate of 9.3 MHz. The crystal however suffered from a high absorption leading to a significant temperature increase during laser operation. For our next modelocking experiments, we replaced the BBO with a low-absorption LBO crystal and achieved up to 87 W of average power with a pulse duration of 586 fs and a repetition rate of 8.9 MHz. This is to the best of our knowledge the highest power demonstrated with the NLM-technique (≈ 3 times more than the previous record [23]). The corresponding pulse energy is 9.8 μJ and the peak power is 14.7 MW.

We characterized the operation of the NLM device at a fixed phase-mismatch and in particular the influence of the phase offset on the laser performance. We tuned this parameter by adjusting the air gap between the $\chi^{(2)}$ crystal and the OC, which effectively adjusts the efficiency of the back-conversion process. This is confirmed by our experiments, showing an increase of the NLM reflectivity and a simultaneous decrease of the SH losses when tuning the air gap. However, this tuning also significantly impacts the pulse formation process, likely due to a phase-offset-dependent nonlinear phase-shift provided by the NLM device. In our

experiments, we could tune the pulse duration by a factor of almost two, from 790 fs down to 490 fs at almost constant output power. Based on this change and the other sources of nonlinear phase inside the cavity, we infer a change in the SPM coefficient introduced by the NLM device by one order of magnitude.

Our experiments validate the compatibility of the NLM for high-power modelocking. We expect that modelocking at multi-100s-W is achievable with the combination of low-absorption nonlinear crystals and optimized dichroic OC coating used in this work. Additionally, we identified a strong dependence of the NLM nonlinear phase on the tuning of the air gap, which can be exploited to tune the output pulse duration or calls for a strong intracavity source of SPM to decouple pulse shaping from NLM optimization. Finally, new NLM designs with a reduced loss modulation could allow for high-power NLM-modelocking at phase-matching without Q-switching instabilities.

Funding

Swiss National Science Foundation (SNSF 200020_172644).

Acknowledgments

The authors acknowledge the support of the technology and cleanroom facility FIRST of ETH Zurich for advanced micro- and nanotechnology, Dr. Matthias Golling for the SESAM fabrication and Dr. Olga Razskazovskaya (Université de Neuchâtel, Switzerland) for her contribution in the fabrication and characterization of optical coatings. The University of Neuchâtel group acknowledges the financial support from the Swiss National Science Foundation (R' EQUIP 144970 and 170772) for an ion-beam sputtering (IBS) machine used to produce the optimized dichroic OC.

Disclosures

The authors declare no conflict of interest.

References

1. U. Keller, "Recent developments in compact ultrafast lasers," *Nature* **424**, 831-838 (2003).
2. T. Südmeyer, S. V. Marchese, S. Hashimoto, C. R. E. Baer, G. Gingras, B. Witzel, and U. Keller, "Femtosecond laser oscillators for high-field science," *Nature Photonics* **2**, 599 (2008).
3. W. Sibbett, A. A. Lagatsky, and C. T. A. Brown, "The development and application of femtosecond laser systems," *Opt. Express* **20**, 6989-7001 (2012).
4. C. J. Saraceno, "Mode-locked thin-disk lasers and their potential application for high-power terahertz generation," *Journal of Optics* **20**(2018).
5. P. Russbuehler, T. Mans, J. Weitenberg, H. D. Hoffmann, and R. Poprawe, "Compact diode-pumped 1.1 kW Yb:YAG Innoslab femtosecond amplifier," *Opt. Lett.* **35**, 4169-4171 (2010).
6. M. Müller, A. Klenke, A. Steinkopff, H. Stark, A. Tünnermann, and J. Limpert, "3.5 kW coherently combined ultrafast fiber laser," *Opt. Lett.* **43**, 6037-6040 (2018).
7. J.-P. Negel, A. Loeschner, A. Voss, D. Bauer, D. Sutter, A. Killi, M. A. Ahmed, and T. Graf, "Ultrafast thin-disk multipass laser amplifier delivering 1.4 kW (4.7 mJ, 1030 nm) average power converted to 820 W at 515 nm and 234 W at 343 nm," *Opt. Express* **23**, 21064-21077 (2015).
8. T. Nubbemeyer, M. Kaumanns, M. Ueffing, M. Gorjan, A. Alismail, H. Fattahi, J. Brons, O. Pronin, H. G. Barros, Z. Major, T. Metzger, D. Sutter, and F. Krausz, "1 kW, 200 mJ picosecond thin-disk laser system," *Opt. Lett.* **42**, 1381-1384 (2017).
9. C. J. Saraceno, F. Emaury, C. Schriber, A. Diebold, M. Hoffmann, M. Golling, T. Südmeyer, and U. Keller, "Toward Millijoule-Level High-Power Ultrafast Thin-Disk Oscillators," *IEEE Journal of Selected Topics in Quantum Electronics* **21**, 106-123 (2015).
10. A. Giesen, H. Hügel, A. Voss, K. Wittig, U. Brauch, and H. Opower, "Scalable concept for diode-pumped high-power solid-state lasers," *Applied Physics B* **58**, 365-372 (1994).

11. T. Gottwald, C. Stolzenburg, D. Bauer, J. Kleinbauer, V. Kuhn, T. Metzger, S. Schad, D. Sutter, and A. Killi, *Recent disk laser development at Trumpf*, SPIE Security + Defence (SPIE, 2012), Vol. 8547.
12. F. Saltarelli, I. J. Graumann, L. Lang, D. Bauer, C. R. Phillips, and U. Keller, "Power scaling of ultrafast oscillators: 350-W average-power sub-picosecond thin-disk laser," *Opt. Express* **27**, 31465-31474 (2019).
13. F. X. Kärtner, I. D. Jung, and U. Keller, "Soliton mode-locking with saturable absorbers," *IEEE Journal of Selected Topics in Quantum Electronics* **2**, 540-556 (1996).
14. F. X. Kärtner, J. A. d. Au, and U. Keller, "Mode-locking with slow and fast saturable absorbers-what's the difference?," *IEEE Journal of Selected Topics in Quantum Electronics* **4**, 159-168 (1998).
15. U. Keller, K. J. Weingarten, F. X. Kärtner, D. Kopf, B. Braun, I. D. Jung, R. Fluck, C. Honninger, N. Matuschek, and J. A. d. Au, "Semiconductor saturable absorber mirrors (SESAM's) for femtosecond to nanosecond pulse generation in solid-state lasers," *IEEE Journal of Selected Topics in Quantum Electronics* **2**, 435-453 (1996).
16. C. J. Saraceno, C. Schriber, M. Mangold, M. Hoffmann, O. H. Heckl, C. R. E. Baer, M. Golling, T. Südmeyer, and U. Keller, "SESAMs for High-Power Oscillators: Design Guidelines and Damage Thresholds," *IEEE Journal of Selected Topics in Quantum Electronics* **18**, 29-41 (2012).
17. A. Diebold, T. Zengerle, C. G. E. Alfieri, C. Schriber, F. Emaury, M. Mangold, M. Hoffmann, C. J. Saraceno, M. Golling, D. Follman, G. D. Cole, M. Aspelmeier, T. Südmeyer, and U. Keller, "Optimized SESAMs for kilowatt-level ultrafast lasers," *Opt. Express* **24**, 10512-10526 (2016).
18. J. Brons, V. Pervak, E. Fedulova, D. Bauer, D. Sutter, V. Kalashnikov, A. Apolonskiy, O. Pronin, and F. Krausz, "Energy scaling of Kerr-lens mode-locked thin-disk oscillators," *Opt. Lett.* **39**, 6442-6445 (2014).
19. J. Brons, V. Pervak, D. Bauer, D. Sutter, O. Pronin, and F. Krausz, "Powerful 100-fs-scale Kerr-lens mode-locked thin-disk oscillator," *Opt. Lett.* **41**, 3567-3570 (2016).
20. K. A. Stankov and J. Jethwa, "A new mode-locking technique using a nonlinear mirror," *Optics Communications* **66**, 41-46 (1988).
21. M. B. Danailov, G. Cerullo, V. Magni, D. Segala, and S. De Silvestri, "Nonlinear mirror mode locking of a cw Nd:YLF laser," *Opt. Lett.* **19**, 792-794 (1994).
22. G. Cerullo, V. Magni, and A. Monguzzi, "Group-velocity mismatch compensation in continuous-wave lasers mode locked by second-order nonlinearities," *Opt. Lett.* **20**, 1785-1787 (1995).
23. G. M. Thomas and M. J. Damzen, "30 W Nd:GdVO₄ oscillator modelocked with nonlinear mirror," in *2011 Conference on Lasers and Electro-Optics Europe and 12th European Quantum Electronics Conference (CLEO EUROPE/EQEC)*, (2011), 1-1.
24. F. Saltarelli, A. Diebold, I. J. Graumann, C. R. Phillips, and U. Keller, "Modelocking of a thin-disk laser with the frequency-doubling nonlinear-mirror technique," *Opt. Express* **25**, 23254-23266 (2017).
25. O. Pronin, J. Brons, C. Grasse, V. Pervak, G. Boehm, M. C. Amann, V. L. Kalashnikov, A. Apolonskiy, and F. Krausz, "High-power 200 fs Kerr-lens mode-locked Yb:YAG thin-disk oscillator," *Opt. Lett.* **36**, 4746-4748 (2011).
26. J. Brons, O. Pronin, M. Seidel, V. Pervak, D. Bauer, D. Sutter, V. Kalashnikov, A. Apolonskiy, F. E. D. H. G. Krausz, and P. Moulton, "120 W, 4 μ J from a purely Kerr-lens mode-locked Yb:YAG thin-disk oscillator," in *Advanced Solid-State Lasers Congress*, OSA Technical Digest (online) (Optical Society of America, 2013), AF3A.4.
27. J. Zhang, J. Brons, N. Lilienfein, E. Fedulova, V. Pervak, D. Bauer, D. Sutter, Z. Wei, A. Apolonskiy, O. Pronin, and F. Krausz, "260-megahertz, megawatt-level thin-disk oscillator," *Opt. Lett.* **40**, 1627-1630 (2015).
28. J. Aus der Au, G. J. Spühler, T. Südmeyer, R. Paschotta, R. Hövel, M. Moser, S. Erhard, M. Karszewski, A. Giesen, and U. Keller, "16.2-W average power from a diode-pumped femtosecond Yb:YAG thin disk laser," *Opt. Lett.* **25**, 859-861 (2000).
29. E. Innerhofer, T. Südmeyer, F. Brunner, R. Häring, A. Aschwanden, R. Paschotta, C. Hönninger, M. Kumkar, and U. Keller, "60-W average power in 810-fs pulses from a thin-disk Yb:YAG laser," *Opt. Lett.* **28**, 367-369 (2003).
30. F. Brunner, E. Innerhofer, S. V. Marchese, T. Südmeyer, R. Paschotta, T. Usami, H. Ito, S. Kurimura, K. Kitamura, G. Arisholm, and U. Keller, "Powerful red-green-blue laser source pumped with a mode-locked thin disk laser," *Opt. Lett.* **29**, 1921-1923 (2004).
31. S. V. Marchese, T. Südmeyer, M. Golling, R. Grange, and U. Keller, "Pulse energy scaling to 5 μ J from a femtosecond thin disk laser," *Opt. Lett.* **31**, 2728-2730 (2006).
32. J. Neuhaus, J. Kleinbauer, A. Killi, S. Weiler, D. Sutter, and T. Dekorsy, "Passively mode-locked Yb:YAG thin-disk laser with pulse energies exceeding 13 μ J by use of an active multipass geometry," *Opt. Lett.* **33**, 726-728 (2008).
33. J. Neuhaus, D. Bauer, J. Zhang, A. Killi, J. Kleinbauer, M. Kumkar, S. Weiler, M. Guina, D. H. Sutter, and T. Dekorsy, "Subpicosecond thin-disk laser oscillator with pulse energies of up to 25.9 microjoules by use of an active multipass geometry," *Opt. Express* **16**, 20530-20539 (2008).
34. D. Bauer, I. Zawischa, D. H. Sutter, A. Killi, and T. Dekorsy, "Mode-locked Yb:YAG thin-disk oscillator with 41 μ J pulse energy at 145 W average infrared power and high power frequency conversion," *Opt. Express* **20**, 9698-9704 (2012).

35. C. J. Saraceno, F. Emaury, O. H. Heckl, C. R. E. Baer, M. Hoffmann, C. Schriber, M. Golling, T. Südmeyer, and U. Keller, "275 W average output power from a femtosecond thin disk oscillator operated in a vacuum environment," *Opt. Express* **20**, 23535-23541 (2012).
36. C. J. Saraceno, F. Emaury, C. Schriber, M. Hoffmann, M. Golling, T. Südmeyer, and U. Keller, "Ultrafast thin-disk laser with 80 μ J pulse energy and 242 W of average power," *Opt. Lett.* **39**, 9-12 (2014).
37. F. Saltarelli, I. J. Graumann, L. Lang, D. Bauer, C. R. Phillips, and U. Keller, "Power Scaling of Ultrafast Laser Oscillators: 350-W Output Power Sub-Ps SESAM-Modelocked Thin-Disk Laser," in *2019 Conference on Lasers and Electro-Optics (CLEO)*, (2019), 1-2.
38. B. Borchers, C. Schäfer, C. Fries, M. Larionov, and R. Knappe, "Nonlinear polarization rotation mode-locking via phase-mismatched type I SHG of a thin disk femtosecond laser," in *Advanced Solid State Lasers*, OSA Technical Digest (online) (Optical Society of America, 2015), ATTh4A.9.
39. G. Cerullo, M. B. Danailov, S. De Silvestri, P. Laporta, V. Magni, D. Segala, and S. Taccheo, "A diode-pumped nonlinear mirror mode-locked Nd:YAG laser," *Applied Physics Letters* **65**, 2392-2394 (1994).
40. P. K. Datta, Shivanand, S. Mukhopadhyay, A. Agnesi, and A. Lucca, "Picosecond pulse generation and its simulation in a nonlinear optical mirror mode-locked laser," *Appl. Opt.* **43**, 2347-2352 (2004).
41. G. M. Thomas, A. Bäuerle, D. J. Farrell, and M. J. Damzen, "Nonlinear mirror modelocking of a bounce geometry laser," *Opt. Express* **18**, 12663-12668 (2010).
42. G. M. Thomas, S. P. Chard, and M. J. Damzen, "High power modelocking of a stigmatic bounce geometry laser using a nonlinear mirror," *Applied Physics B* **101**, 553-557 (2010).
43. G. M. Thomas, T. Omatsu, and M. J. Damzen, "High-power neodymium-doped mixed vanadate bounce geometry laser, mode locked with nonlinear mirror," *Applied Physics B* **108**, 125-128 (2012).
44. D. J. H. C. Maas, B. Rudin, A. R. Bellancourt, D. Iwaniuk, S. V. Marchese, T. Südmeyer, and U. Keller, "High precision optical characterization of semiconductor saturable absorber mirrors," *Opt. Express* **16**, 7571-7579 (2008).
45. J. Rothhardt, S. Demmler, S. Hädrich, T. Peschel, J. Limpert, and A. Tünnermann, "Thermal effects in high average power optical parametric amplifiers," *Opt. Lett.* **38**, 763-765 (2013).
46. V. A. Shvets, V. S. Aliev, D. V. Gritsenko, S. S. Shaimееv, E. V. Fedosenko, S. V. Rykhlitski, V. V. Atuchin, V. A. Gritsenko, V. M. Tapilin, and H. Wong, "Electronic structure and charge transport properties of amorphous Ta₂O₅ films," *Journal of Non-Crystalline Solids* **354**, 3025-3033 (2008).
47. T. V. Perevalov, V. A. Gritsenko, S. B. Erenburg, A. M. Badalyan, H. Wong, and C. W. Kim, "Atomic and electronic structure of amorphous and crystalline hafnium oxide: X-ray photoelectron spectroscopy and density functional calculations," *Journal of Applied Physics* **101**, 053704 (2007).
48. T. R. Schibli, E. R. Thoen, F. X. Kärtner, and E. P. Ippen, "Suppression of Q-switched mode locking and break-up into multiple pulses by inverse saturable absorption," *Applied Physics B* **70**, S41-S49 (2000).
49. R. Eckardt and J. Reintjes, "Phase matching limitations of high efficiency second harmonic generation," *IEEE Journal of Quantum Electronics* **20**, 1178-1187 (1984).
50. G. P. Agrawal, "Chapter 5 - Optical Solitons," in *Nonlinear Fiber Optics (Fifth Edition)* (Academic, 2013), pp. 129-191.
51. J. Herrmann, "Theory of Kerr-lens mode locking: role of self-focusing and radially varying gain," *J. Opt. Soc. Am. B* **11**, 498-512 (1994).
52. F. Saltarelli, A. Diebold, I. J. Graumann, C. R. Phillips, and U. Keller, "Self-phase modulation cancellation in a high-power ultrafast thin-disk laser oscillator," *Optica* **5**, 1603-1606 (2018).
53. K. Kato, "Temperature-tuned 90 deg phase-matching properties of LiB₃O₅," *IEEE Journal of Quantum Electronics* **30**, 2950-2952 (1994).
54. T. Dietrich, S. Piehler, M. Rumpel, P. Villeval, D. Lupinski, M. Abdou-Ahmed, and T. Graf, "Highly-efficient continuous-wave intra-cavity frequency-doubled Yb:LuAG thin-disk laser with 1 kW of output power," *Opt. Express* **25**, 4917-4925 (2017).

7.4 Conclusion

We successfully implemented the frequency-doubling NLM modelocking technique for the first time in a TDL oscillator. The NLM combines a $\chi^{(2)}$ crystal with a dichroic OC, resulting in an intensity-dependent reflectivity. Passive modelocking using the NLM is as an attractive alternative to SESAM and KLM modelocking, and appears as a “best-of-both-worlds” solution by offering a large and fast saturable loss (similar to KLM) combined to operation at the center of the cavity stability (similar to SESAM modelocking).

In our first demonstration of NLM modelocking in a Yb:YAG TDL oscillator, we achieved pulse durations down to 323 fs at a moderate average power of 21 W. The short pulse durations obtained in this experiment are comparable to typical pulse durations achieved by KLM TDL oscillators. This first result demonstrates the advantage of combining the NLM with the TDL technology: the high intracavity peak power available in TDL oscillators allows for the use of thin $\chi^{(2)}$ crystals, reducing the GVM between the FW and the SH and allowing for a fast and large loss modulation supporting femtosecond pulse durations.

We followed this first demonstration by power scaling experiments using a multipass cavity design and inserting a SESAM in the cavity to facilitate the initiation of modelocked operation and the optimization of the NLM. We identified the Q-switching instabilities as a main challenge due to the potential of the NLM to saturate a large fraction of the cavity losses. This effect can be mitigated by operating the NLM with a phase mismatch, thus introducing a rollover in the nonlinear reflectivity of the device. Additionally we designed a high-damage threshold dichroic coating for the OC. With these improvements, we demonstrated modelocking at average powers >66 W and pulse durations >426 fs, resulting in peak powers close to 15 MW. We further highlighted the strong dependence of the nonlinear phase introduced by the NLM on the phase mismatch and phase offset. This nonlinear phase can significantly impact the soliton pulse formation, as was the case in our experiments.

The NLM provides an attractive alternative to the two established

modelocking techniques used in TDLs (SESAM modelocking and KLM) and is an accessible technology using standard nonlinear crystals. Our experiments show the potential of this modelocking technique for generating high-peak powers at comparatively short pulse durations. We believe that the additional knowledge gained during our power scaling experiments can be exploited to demonstrate a 100-W class, 300-fs NLM-modelocked TDL.

Conclusion

In this thesis, we investigated novel approaches to power scale ultrafast TDLs while keeping the pulse duration short. Over the last 20 years of TDL development, a clear trade-off between high average powers and short pulse durations was observed, with exception for a few recent results [19, 109]. We investigated the origins of this average power-pulse duration trade-off and presented alternative approaches to overcome this trend.

We first presented our peak-power scaling experiments using the gain material Yb:LuO. This material exhibits excellent thermal properties and a broader emission bandwidth than the state-of-the-art material for high-power TDL operation Yb:YAG. Yb:LuO therefore seems well suited for high-power modelocked operation at short pulse durations. We demonstrated a peak power >10 MW for the first time using this material, corresponding to an improvement by a factor 4 over previous results. Our SESAM-modelocked Yb:LuO TDL oscillator delivered average powers up to 90 W with pulse durations >530 fs, shorter than typical pulse durations achieved with Yb:YAG. The high-quality of the disk used for these experiments was a key factor for the achieved result, as well as the extended cavity design with a double-pass on the disk and the pressure-controlled housing of the oscillator.

We developed a numerical model with the aim to investigate the modelocking limitations when targeting high-average powers and short pulses.

In particular we used this model to highlight the effect of the limited gain bandwidth and the SESAM rollover on the laser performance. We calculate a net roundtrip cavity gain for pulsed operation against cw operation in a TDL cavity assuming soliton pulse shaping. This net roundtrip gain for pulsed operation, calculated as a function of the intracavity power, or pulse energy, gives an indication of the robustness of the soliton pulse against perturbations such as QML, double-pulsing and cw breakthrough. We showed that the net roundtrip gain for pulsed operation exhibits a rollover point as the soliton energy increases and the pulse duration correspondingly decreases. This rollover results from the combination of the TPA-induced rollover of the SESAM reflectivity and a gain rollover due to the limited gain bandwidth. The relative strength of both effects depends on the SESAM properties and the targeted pulse duration. The intracavity power corresponding to the rollover point in the net roundtrip gain for pulsed operation is shifted to lower powers as higher powers and shorter pulse durations are targeted. Additionally, by comparison with our experimental data, we found that the maximum achievable power is around twice the power at the rollover point, limited by the onset of double-pulsing.

Using our numerical model and the criterion for the maximum achievable power in a given TDL oscillator, we investigated the requirements in terms of SESAM parameters required to support modelocking at 100 W with 200 fs pulses for a TDL based on Yb:YAG, Yb:LuO or Yb:CALGO. Starting from typical parameters for SESAM structures used in high-power TDLs, we simulated the net roundtrip gain for pulsed operation against cw operation and scaled the SESAM modulation depth in order to shift the optimum of the net roundtrip cavity gain for pulsed operation towards the desired operation point at 100 W, 200 fs. We obtain a required SESAM modulation depth of 30% for Yb:YAG, 15% for Yb:LuO and 2% for Yb:CALGO. The SESAM modulation depth required for Yb:YAG and Yb:LuO is overly challenging with the current SESAM technology, as this would require a structure with >10 QWs, which is difficult to achieve with a good surface quality. Additionally, the large number of QWs would lead to a strongly enhanced TPA making operation at high powers difficult. On the other hand, the modulation depth required to modelock an

Yb:CALGO TDL at 100 W and 200 fs are readily obtained with standard SESAM structures. Yb:CALGO therefore appears as the most promising candidate for high-power SESAM-modelocking at short pulse durations.

We investigated Yb:CALGO in TDL operation with the aim of pushing the output power towards 100 W. We characterized and tested several cut Yb:CALGO disks coming from different boules grown between June 2012 and October 2017. In particular we tested different doping concentrations and disk thicknesses. Our results show that low-doping material currently gives the best results both in terms of thermal management and laser performance. This is attributed to the generally better quality of low-doping material. However the low-doping concentration should be balanced by a thicker disk or a multipass cavity geometry in order to operate at a reasonably high OC transmissions. We nevertheless observed a significant improvement of the quality of the high-doping material and a strong reduction of the observed defects in the disks over the course of this thesis, with promising prospects for further improvements in the near future. In the best cw tests, we obtained up to 20-30 W of output power. For high-power modelocking experiments, we therefore turned to alternative approaches based on the high-power compatible gain materials Yb:YAG and Yb:LuO.

We first focused on the reduction of the TPA in SESAM structures. We showed that the TPA contribution is the largest in the QW layers of the SESAM structure. Therefore SESAMs with a large number of QWs will also have a strong rollover effect. For SESAM structures including up to 3 QWs, the contribution of the semiconductor DBR to the overall TPA of the SESAM is about 50%. This contribution can be suppressed efficiently by replacing the semiconductor DBR with a dielectric DBR. We prepared and characterized SESAM samples with the same absorber section, but differing by the type of DBR. For a 1x3 QWs SESAM, we found that the TPA was reduced by more than a factor of 2 using the dielectric DBR. For a 6x1 SCQWs SESAM, we verified that the TPA was essentially unchanged with the dielectric DBR. Due to an uneven etching process, the samples could not be used in a laser and a second generation of SESAMs with dielectric DBR is needed to test the performance of these samples in a TDL.

We also addressed the limitation due to the limited gain bandwidth of Yb:YAG and Yb:LuO. We mitigated the gain narrowing effect of the disk by introducing a spectral filter in the cavity with a reflectivity mirroring the spectral gain profile, thus achieving a flattening of the roundtrip gain profile. We discussed the design considerations for such a filter and showed some preliminary results obtained in SESAM-modelocking with Yb:YAG. So far we obtained a small reduction of the pulse duration by $\approx 10\%$ for a given intracavity power compared to the case without spectral filtering. Ongoing experiments with the goal to measure the actual gain spectrum *in situ* will provide crucial information for further optimization of this operation regime.

Finally, we turned to a different approach and investigated an alternative modelocking technique based on the frequency-doubling NLM. This modelocking technique combines a $\chi^{(2)}$ -crystal and a dichroic OC mirror and exhibits an intensity-dependent reflectivity. The combination of the NLM-modelocking technique with the TDL technology is particularly promising for the generation of short pulse durations, as thin $\chi^{(2)}$ -crystals can be used, leading to an ultrafast and large modulation depth, and favorable thermal properties. We demonstrated the first implementation of this modelocking technique in a TDL oscillator based on Yb:YAG and obtained pulses as short as 323 fs at an average power of 21 W. This pulse duration is comparable to typical pulse durations obtained with KLM Yb:YAG TDLs and about twice shorter than typical pulse durations obtained with SESAM modelocking. In our first power scaling experiments using NLM modelocking, we further investigated the mitigation of Q-switching instabilities in the femtosecond NLM-modelocking regime and showed how operation with a phase-mismatch introduces a rollover in the nonlinear reflectivity of the NLM. Using low-absorption $\chi^{(2)}$ -crystals and an optimized coating of the dichroic OC, we demonstrated average powers >66 W with pulse durations down to 426 fs, and peak powers close to 15 MW. This result further establishes the NLM as an attractive alternative to SESAM-modelocking and KLM for modelocking high-power TDLs, in particular when targeting short pulse durations.

In conclusion of this thesis, we have investigated the challenges faced when targeting high-power SESAM-modelocking at short pulse duration

in the thin-disk geometry. We showed that with the existing SESAM technology, the most promising material for reaching this goal is Yb:CALGO. However high-power laser operation with Yb:CALGO remains limited by the low crystal quality. We therefore proposed alternative approaches exploiting the high-power compatible laser materials Yb:YAG and Yb:LuO. The reduction of the TPA in SESAMs is of interest for high-power modelocking in the regime of moderate gain rollover, where moderate modulation depths up to 2-3% are required. For targeting short pulses with Yb:YAG or Yb:LuO, this could be combined with spectral filtering in order to flatten the roundtrip gain profile. However this regime of operation needs further investigation. The NLM-modelocking technique therefore appears as the most promising approach presented in this thesis for reaching high average powers at short pulse durations. The NLM-modelocking technique gives access to short pulse durations similar to KLM but without the complexity of the KLM cavity design. In combination with state-of-the-art Yb:YAG disks, we believe that NLM-modelocking has the potential to demonstrate modelocking at average powers >100 W and pulse durations as short as 200-300 fs.

Bibliography

- [1] “May 16, 1960: Maiman Builds First Working Laser,” *APS News* **19** (2010).
- [2] T. H. Maiman, “Stimulated Optical Radiation in Ruby,” *Nature* **187**, 493–494 (1960).
- [3] D. H. Auston, K. P. Cheung, J. A. Valdmanis, and D. A. Kleinman, “Cherenkov Radiation from Femtosecond Optical Pulses in Electro-Optic Media,” *Phys. Rev. Lett.* **53**, 1555–1558 (1984).
- [4] A. McPherson, G. Gibson, H. Jara, U. Johann, T. S. Luk, I. A. McIntyre, K. Boyer, and C. K. Rhodes, “Studies of multiphoton production of vacuum-ultraviolet radiation in the rare gases,” *J. Opt. Soc. Am. B* **4**, 595–601 (1987).
- [5] M. Ferray, A. L’Huillier, X. F. Li, L. A. Lompre, G. Mainfray, and C. Manus, “Multiple-harmonic conversion of 1064 nm radiation in rare gases,” *J. Phys. B: At. Mol. Opt.* **21**, L31–L35 (1988).
- [6] T. Südmeyer, S. V. Marchese, S. Hashimoto, C. R. E. Baer, G. Gingras, B. Witzel, and U. Keller, “Femtosecond laser oscillators for high-field science,” *Nat. Photonics* **2**, 599 (2008).
- [7] C. J. Saraceno, “Mode-locked thin-disk lasers and their potential application for high-power terahertz generation,” *J. Opt.* **20**, 044010 (2018).
- [8] S. Backus, C. G. Durfee, M. M. Murnane, and H. C. Kapteyn, “High power ultrafast lasers,” *Rev. Sci. Instrum.* **69**, 1207–1223 (1998).
- [9] I. Matsushima, H. Yashiro, and T. Tomie, “10 kHz 40 W Ti:sapphire regenerative ring amplifier,” *Opt. Lett.* **31**, 2066–2068 (2006).
- [10] J.-P. Negel, A. Loescher, A. Voss, D. Bauer, D. Sutter, A. Killi, M. A. Ahmed, and T. Graf, “Ultrafast thin-disk multipass laser amplifier delivering 1.4 kW (4.7 mJ, 1030 nm) average power converted to 820 W at 515 nm and 234 W at 343 nm,” *Opt. Express* **23**, 21064–21077 (2015).

- [11] T. Nubbemeyer, M. Kaumanns, M. Ueffing, M. Gorjan, A. Alismail, H. Fattahi, J. Brons, O. Pronin, H. G. Barros, Z. Major, T. Metzger, D. Sutter, and F. Krausz, "1 kW, 200 mJ picosecond thin-disk laser system," *Opt. Lett.* **42**, 1381–1384 (2017).
- [12] T. Eidam, S. Hanf, E. Seise, T. V. Andersen, T. Gabler, C. Wirth, T. Schreiber, J. Limpert, and A. Tünnermann, "Femtosecond fiber CPA system emitting 830 W average output power," *Opt. Lett.* **35**, 94–96 (2010).
- [13] M. Mueller, A. Klenke, H. Stark, J. Buldt, T. Gottschall, J. Limpert, and A. Tünnermann, "16 Channel Coherently-Combined Ultrafast Fiber Laser," in "Laser Congress 2017 (ASSL, LAC)," (Optical Society of America, 2017), AW4A.3.
- [14] P. Russbuedt, T. Mans, J. Weitenberg, H. D. Hoffmann, and R. Poprawe, "Compact diode-pumped 1.1 kW Yb:YAG Innoslab femtosecond amplifier," *Opt. Lett.* **35**, 4169–4171 (2010).
- [15] D. Bauer, I. Zawischa, D. H. Sutter, A. Killi, and T. Dekorsy, "Mode-locked Yb:YAG thin-disk oscillator with 41 μ J pulse energy at 145 W average infrared power and high power frequency conversion," *Opt. Express* **20**, 9698–9704 (2012).
- [16] C. J. Saraceno, F. Emaury, O. H. Heckl, C. R. E. Baer, M. Hoffmann, C. Schriber, M. Golling, T. Südmeyer, and U. Keller, "275 W average output power from a femtosecond thin disk oscillator operated in a vacuum environment," *Opt. Express* **20**, 23535–23541 (2012).
- [17] C. J. Saraceno, F. Emaury, C. Schriber, M. Hoffmann, M. Golling, T. Südmeyer, and U. Keller, "Ultrafast thin-disk laser with 80 μ J pulse energy and 242 W of average power," *Opt. Lett.* **39**, 9–12 (2014).
- [18] J. Brons, V. Pervak, E. Fedulova, D. Bauer, D. Sutter, V. Kalashnikov, A. Apolonskiy, O. Pronin, and F. Krausz, "Energy scaling of Kerr-lens mode-locked thin-disk oscillators," *Opt. Lett.* **39**, 6442–6445 (2014).
- [19] J. Brons, V. Pervak, D. Bauer, D. Sutter, O. Pronin, and F. Krausz, "Powerful 100-fs-scale Kerr-lens mode-locked thin-disk oscillator," *Opt. Lett.* **41**, 3567–3570 (2016).
- [20] F. Saltarelli, I. J. Graumann, L. Lang, D. Bauer, C. R. Phillips, and U. Keller, "Power scaling of ultrafast oscillators: 350-W average-power sub-picosecond thin-disk laser," *Opt. Express* **27**, 31465–31474 (2019).
- [21] R. Graf, T. Metzger, M. Chyla, D. H. Sutter, Z. Major, A. Apolonskiy, and F. Krausz, "High average power Yb:YAG thin disk regenerative amplifier at up to 1 MHz repetition rate," in "5th EPS-QEOD EUROPHOTON Conference," (European Physical Society, 2012).

- [22] M. Chyla, T. Miura, M. Smrz, P. Severova, O. Novak, A. Endo, and T. Mocek, "Zero-phonon-line pumped 1 kHz Yb:YAG thin-disk regenerative amplifier," in "Solid State Lasers XXII: Technology and Devices," (Proc. SPIE 8599, 2013), 366 – 373.
- [23] C. Y. Teisset, M. Schultze, R. Bessing, M. Häfner, S. Prinz, D. Sutter, and T. Metzger, "300 W Picosecond Thin-Disk Regenerative Amplifier at 10 kHz Repetition Rate," in "Advanced Solid-State Lasers Congress Postdeadline," (Optical Society of America, 2013), JTh5A.1.
- [24] R. Fleischhaker, R. Gebbs, A. Budnicki, M. Wolf, J. Kleinbauer, and D. H. Sutter, "Compact gigawatt-class sub-picosecond Yb:YAG thin-disk regenerative chirped-pulse amplifier with high average power at up to 800 kHz," in "2013 Conference on Lasers Electro-Optics Europe International Quantum Electronics Conference CLEO EUROPE/IQEC," (Optical Society of America, 2013), CFIE.4.1.
- [25] M. Ueffing, R. Lange, T. Pleyer, V. Pervak, T. Metzger, D. Sutter, Z. Major, T. Nubbemeyer, and F. Krausz, "Direct regenerative amplification of femtosecond pulses to the multimillijoule level," *Opt. Lett.* **41**, 3840–3843 (2016).
- [26] M. Smrž, O. Novák, J. Mužík, H. Turčičová, M. Chyla, S. S. Nagisetty, M. Vyvlečka, L. Roškot, T. Miura, J. Černohorská, P. Sikocinski, L. Chen, J. Huynh, P. Severová, A. Pranovich, A. Endo, and T. Mocek, "Advances in High-Power, Ultrashort Pulse DPSSL Technologies at HiLASE," *Appl. Sci.* **7** (2017).
- [27] J.-P. Negel, A. Voss, M. A. Ahmed, D. Bauer, D. Sutter, A. Killi, and T. Graf, "1.1 kW average output power from a thin-disk multipass amplifier for ultrashort laser pulses," *Opt. Lett.* **38**, 5442–5445 (2013).
- [28] A. Loeschner, J.-P. Negel, T. Graf, and M. A. Ahmed, "Radially polarized emission with 635 W of average power and 2.1 mJ of pulse energy generated by an ultrafast thin-disk multipass amplifier," *Opt. Lett.* **40**, 5758–5761 (2015).
- [29] F. Röser, T. Eidam, J. Rothhardt, O. Schmidt, D. N. Schimpf, J. Limpert, and A. Tünnermann, "Millijoule pulse energy high repetition rate femtosecond fiber chirped-pulse amplification system," *Opt. Lett.* **32**, 3495–3497 (2007).
- [30] Y. Zaouter, J. Bouillet, E. Mottay, and E. Cormier, "Transform-limited 100 μ J, 340 MW pulses from a nonlinear-fiber chirped-pulse amplifier using a mismatched grating stretcher-compressor," *Opt. Lett.* **33**, 1527–1529 (2008).
- [31] T. Eidam, S. Hadrich, F. Roser, E. Seise, T. Gottschall, J. Rothhardt, T. Schreiber, J. Limpert, and A. Tünnermann, "A 325-W-Average-Power Fiber CPA System Delivering Sub-400 fs Pulses," *IEEE J. Sel. Top. Quant.* **15**, 187–190 (2009).

- [32] A. Ruehl, A. Marcinkevicius, M. E. Fermann, and I. Hartl, "80 W, 120 fs Yb-fiber frequency comb," *Opt. Lett.* **35**, 3015–3017 (2010).
- [33] T. Eidam, J. Rothhardt, F. Stutzki, F. Jansen, S. Hädrich, H. Carstens, C. Jauregui, J. Limpert, and A. Tünnermann, "Fiber chirped-pulse amplification system emitting 3.8 GW peak power," *Opt. Express* **19**, 255–260 (2011).
- [34] M. Baumgartl, F. Jansen, F. Stutzki, C. Jauregui, B. Ortaç, J. Limpert, and A. Tünnermann, "High average and peak power femtosecond large-pitch photonic-crystal-fiber laser," *Opt. Lett.* **36**, 244–246 (2011).
- [35] M. Baumgartl, C. Lecaplain, A. Hideur, J. Limpert, and A. Tünnermann, "66 W average power from a microjoule-class sub-100 fs fiber oscillator," *Opt. Lett.* **37**, 1640–1642 (2012).
- [36] Y. Kobayashi, N. Hirayama, A. Ozawa, T. Sukegawa, T. Seki, Y. Kuramoto, and S. Watanabe, "10-MHz, Yb-fiber chirped-pulse amplifier system with large-scale transmission gratings," *Opt. Express* **21**, 12865–12873 (2013).
- [37] L. Daniault, M. Hanna, D. N. Papadopoulos, Y. Zaouter, E. Mottay, F. Druon, and P. Georges, "High peak-power stretcher-free femtosecond fiber amplifier using passive spatio-temporal coherent combining," *Opt. Express* **20**, 21627–21634 (2012).
- [38] Y. Zaouter, L. Daniault, M. Hanna, D. N. Papadopoulos, F. Morin, C. Hönniger, F. Druon, E. Mottay, and P. Georges, "Passive coherent combination of two ultrafast rod type fiber chirped pulse amplifiers," *Opt. Lett.* **37**, 1460–1462 (2012).
- [39] A. Klenke, S. Breitkopf, M. Kienel, T. Gottschall, T. Eidam, S. Hädrich, J. Rothhardt, J. Limpert, and A. Tünnermann, "530 W, 1.3 mJ, four-channel coherently combined femtosecond fiber chirped-pulse amplification system," *Opt. Lett.* **38**, 2283–2285 (2013).
- [40] F. Guichard, Y. Zaouter, M. Hanna, F. Morin, C. Hönniger, E. Mottay, F. Druon, and P. Georges, "Energy scaling of a nonlinear compression setup using passive coherent combining," *Opt. Lett.* **38**, 4437–4440 (2013).
- [41] A. Klenke, S. Hädrich, T. Eidam, J. Rothhardt, M. Kienel, S. Demmler, T. Gottschall, J. Limpert, and A. Tünnermann, "22 GW peak-power fiber chirped-pulse-amplification system," *Opt. Lett.* **39**, 6875–6878 (2014).
- [42] F. Guichard, Y. Zaouter, M. Hanna, K.-L. Mai, F. Morin, C. Hönniger, E. Mottay, and P. Georges, "High-energy chirped-and divided-pulse Sagnac femtosecond fiber amplifier," *Opt. Lett.* **40**, 89–92 (2015).
- [43] M. Kienel, M. Müller, A. Klenke, J. Limpert, and A. Tünnermann, "12 mJ kW-class ultrafast fiber laser system using multidimensional coherent pulse addition," *Opt. Lett.* **41**, 3343–3346 (2016).

-
- [44] M. Müller, M. Kienel, A. Klenke, T. Gottschall, E. ShestaeV, M. Plötner, J. Limpert, and A. Tünnermann, "1 kW 1 mJ eight-channel ultrafast fiber laser," *Opt. Lett.* **41**, 3439–3442 (2016).
- [45] M. Müller, A. Klenke, A. Steinkopff, H. Stark, A. Tünnermann, and J. Limpert, "3.5 kW coherently combined ultrafast fiber laser," *Opt. Lett.* **43**, 6037–6040 (2018).
- [46] P. Russbueldt, T. Mans, G. Rotarius, J. Weitenberg, H. Hoffmann, and R. Poprawe, "400 W Yb:YAG Innoslab fs-amplifier," *Opt. Express* **17**, 12230–12245 (2009).
- [47] P. Rußbüldt, J. Weitenberg, T. Sartorius, G. Rotarius, H. D. Hoffmann, and R. Poprawe, "Ytterbium Innoslab amplifiers - The high average power approach of ultrafast lasers," *AIP Conference Proceedings* **1462**, 120–123 (2012).
- [48] P. Russbueldt, D. Hoffmann, M. Höfer, J. Löhring, J. Luttmann, A. Meissner, J. Weitenberg, M. Traub, T. Sartorius, D. Esser, R. Wester, P. Loosen, and R. Poprawe, "Innoslab Amplifiers," *IEEE J. Sel. Top. Quant.* **21**, 447–463 (2015).
- [49] F. Emaury, A. Diebold, C. J. Saraceno, and U. Keller, "Compact extreme ultraviolet source at megahertz pulse repetition rate with a low-noise ultrafast thin-disk laser oscillator," *Optica* **2**, 980–984 (2015).
- [50] A. Giesen, H. Hügel, A. Voss, K. Wittig, U. Brauch, and H. Opower, "Scalable concept for diode-pumped high-power solid-state lasers," *Appl. Phys. B* **58**, 365–372 (1994).
- [51] C. J. Saraceno, "Cutting-edge high-power ultrafast oscillators. Pushing the limits of SESAM modelocked thin-disk lasers," Ph.D. thesis, ETH Zurich, Zürich, Switzerland (2012). Diss. No. 20917.
- [52] O. E. Martinez, R. L. Fork, and J. P. Gordon, "Theory of passively mode-locked lasers including self-phase modulation and group-velocity dispersion," *Opt. Lett.* **9**, 156–158 (1984).
- [53] T. Brabec, C. Spielmann, and F. Krausz, "Mode locking in solitary lasers," *Opt. Lett.* **16**, 1961–1963 (1991).
- [54] G. P. Agrawal, *Chapter 5 - Optical Solitons* (Academic Press, Boston, 2013), 129–191.
- [55] J. Herrmann, "Theory of Kerr-lens mode locking: role of self-focusing and radially varying gain," *J. Opt. Soc. Am. B* **11**, 498–512 (1994).
- [56] H. Haus, "Theory of mode locking with a slow saturable absorber," *IEEE J. Quant. Elect.* **11**, 736–746 (1975).
- [57] H. A. Haus, "Theory of mode locking with a fast saturable absorber," *J. Appl. Phys.* **46**, 3049–3058 (1975).

- [58] U. Keller, D. A. B. Miller, G. D. Boyd, T. H. Chiu, J. F. Ferguson, and M. T. Asom, "Solid-state low-loss intracavity saturable absorber for Nd:YLF lasers: an antiresonant semiconductor Fabry-Perot saturable absorber," *Opt. Lett.* **17**, 505–507 (1992).
- [59] U. Keller, K. J. Weingarten, F. X. Kärtner, D. Kopf, B. Braun, I. D. Jung, R. Fluck, C. Honninger, N. Matuschek, and J. A. d. Au, "Semiconductor saturable absorber mirrors (SESAM's) for femtosecond to nanosecond pulse generation in solid-state lasers," *IEEE J. Sel. Top. Quant.* **2**, 435–453 (1996).
- [60] F. X. Kärtner and U. Keller, "Stabilization of solitonlike pulses with a slow saturable absorber," *Opt. Lett.* **20**, 16–18 (1995).
- [61] F. X. Kärtner, J. A. d. Au, and U. Keller, "Mode-locking with slow and fast saturable absorbers-what's the difference?" *IEEE J. Sel. Top. Quant.* **4**, 159–168 (1998).
- [62] A. Diebold, T. Zengerle, C. G. E. Alfieri, C. Schriber, F. Emaury, M. Mangold, M. Hoffmann, C. J. Saraceno, M. Golling, D. Follman, G. D. Cole, M. Aspelmeyer, T. Südmeyer, and U. Keller, "Optimized SESAMs for kilowatt-level ultrafast lasers," *Opt. Express* **24**, 10512–10526 (2016).
- [63] D. E. Spence, P. N. Kean, and W. Sibbett, "60-fsec pulse generation from a self-mode-locked Ti:sapphire laser," *Opt. Lett.* **16**, 42–44 (1991).
- [64] T. Brabec, C. Spielmann, P. F. Curley, and F. Krausz, "Kerr lens mode locking," *Opt. Lett.* **17**, 1292–1294 (1992).
- [65] F. X. Kärtner, I. D. Jung, and U. Keller, "Soliton mode-locking with saturable absorbers," *IEEE J. Sel. Top. Quant.* **2**, 540–556 (1996).
- [66] C. Hönniger, R. Paschotta, F. Morier-Genoud, M. Moser, and U. Keller, "Q-switching stability limits of continuous-wave passive mode locking," *J. Opt. Soc. Am. B* **16**, 46–56 (1999).
- [67] T. R. Schibli, E. R. Thoen, F. X. Kärtner, and E. P. Ippen, "Suppression of Q-switched mode locking and break-up into multiple pulses by inverse saturable absorption," *Appl. Phys. B* **70**, S41–S49 (2000).
- [68] R. Grange, M. Haiml, R. Paschotta, G. Spühler, L. Krainer, M. Golling, O. Ostinelli, and U. Keller, "New regime of inverse saturable absorption for self-stabilizing passively mode-locked lasers," *Appl. Phys. B* **80**, 151–158 (2005).
- [69] J. Aus der Au, G. J. Spühler, T. Südmeyer, R. Paschotta, R. Hövel, M. Moser, S. Erhard, M. Karszewski, A. Giesen, and U. Keller, "16.2-W average power from a diode-pumped femtosecond Yb:YAG thin disk laser," *Opt. Lett.* **25**, 859–861 (2000).

- [70] E. Innerhofer, T. Südmeyer, F. Brunner, R. Häring, A. Aschwanden, R. Paschotta, C. Hönninger, M. Kumkar, and U. Keller, "60-W average power in 810-fs pulses from a thin-disk Yb:YAG laser," *Opt. Lett.* **28**, 367–369 (2003).
- [71] F. Brunner, E. Innerhofer, S. V. Marchese, T. Südmeyer, R. Paschotta, T. Usami, H. Ito, S. Kurimura, K. Kitamura, G. Arisholm, and U. Keller, "Powerful red-green-blue laser source pumped with a mode-locked thin disk laser," *Opt. Lett.* **29**, 1921–1923 (2004).
- [72] S. V. Marchese, T. Südmeyer, M. Golling, R. Grange, and U. Keller, "Pulse energy scaling to 5 μ J from a femtosecond thin disk laser," *Opt. Lett.* **31**, 2728–2730 (2006).
- [73] J. Neuhaus, J. Kleinbauer, A. Killi, S. Weiler, D. Sutter, and T. Dekorsy, "Passively mode-locked Yb:YAG thin-disk laser with pulse energies exceeding 13 μ J by use of an active multipass geometry," *Opt. Lett.* **33**, 726–728 (2008).
- [74] J. Neuhaus, D. Bauer, J. Zhang, A. Killi, J. Kleinbauer, M. Kumkar, S. Weiler, M. Guina, D. H. Sutter, and T. Dekorsy, "Subpicosecond thin-disk laser oscillator with pulse energies of up to 25.9 microjoules by use of an active multipass geometry," *Opt. Express* **16**, 20530–20539 (2008).
- [75] S. V. Marchese, C. R. E. Baer, A. G. Engqvist, S. Hashimoto, D. J. H. C. Maas, M. Golling, T. Südmeyer, and U. Keller, "Femtosecond thin disk laser oscillator with pulse energy beyond the 10-microjoule level," *Opt. Express* **16**, 6397–6407 (2008).
- [76] F. Saltarelli, A. Diebold, I. J. Graumann, C. R. Phillips, and U. Keller, "Self-phase modulation cancellation in a high-power ultrafast thin-disk laser oscillator," *Optica* **5**, 1603–1606 (2018).
- [77] O. Pronin, J. Brons, C. Grasse, V. Pervak, G. Boehm, M. C. Amann, V. L. Kalashnikov, A. Apolonski, and F. Krausz, "High-power 200 fs Kerr-lens mode-locked Yb:YAG thin-disk oscillator," *Opt. Lett.* **36**, 4746–4748 (2011).
- [78] J. Brons, O. Pronin, M. Seidel, V. Pervak, D. Bauer, D. Sutter, V. Kalashnikov, A. Apolonskiy, and F. Krausz, "120 W, 4 μ J from a purely Kerr-lens mode-locked Yb:YAG thin-disk oscillator," in "Advanced Solid-State Lasers Congress," (Optical Society of America, 2013), AF3A.4.
- [79] J. Zhang, J. Brons, N. Lilienfein, E. Fedulova, V. Pervak, D. Bauer, D. Sutter, Z. Wei, A. Apolonski, O. Pronin, and F. Krausz, "260-megahertz, megawatt-level thin-disk oscillator," *Opt. Lett.* **40**, 1627–1630 (2015).
- [80] F. Saltarelli, A. Diebold, I. J. Graumann, C. R. Phillips, and U. Keller, "Modelocking of a thin-disk laser with the frequency-doubling nonlinear-mirror technique," *Opt. Express* **25**, 23254–23266 (2017).

- [81] S. V. Marchese, C. R. E. Baer, R. Peters, C. Kränkel, A. G. Engqvist, M. Golling, D. J. H. C. Maas, K. Petermann, T. Südmeyer, G. Huber, and U. Keller, "Efficient femtosecond high power Yb:Lu₂O₃ thin disk laser," *Opt. Express* **15**, 16966–16971 (2007).
- [82] C. R. E. Baer, C. Kränkel, C. J. Saraceno, O. H. Heckl, M. Golling, T. Südmeyer, R. Peters, K. Petermann, G. Huber, and U. Keller, "Femtosecond Yb:Lu₂O₃ thin disk laser with 63 W of average power," *Opt. Lett.* **34**, 2823–2825 (2009).
- [83] C. R. E. Baer, C. Kränkel, C. J. Saraceno, O. H. Heckl, M. Golling, R. Peters, K. Petermann, T. Südmeyer, G. Huber, and U. Keller, "Femtosecond thin-disk laser with 141 W of average power," *Opt. Lett.* **35**, 2302–2304 (2010).
- [84] C. J. Saraceno, S. Pekarek, O. H. Heckl, C. R. E. Baer, C. Schriber, M. Golling, K. Beil, C. Kränkel, G. Huber, U. Keller, and T. Südmeyer, "Self-referenceable frequency comb from an ultrafast thin disk laser," *Opt. Express* **20**, 9650–9656 (2012).
- [85] C. J. Saraceno, C. Schriber, O. Heckl, C. Baer, M. Golling, K. Beil, C. Kränkel, T. Südmeyer, G. Huber, and U. Keller, "25 W, 185 fs pulses from an Yb:Lu₂O₃ modelocked thin disk laser," in "5th EPS-QEOD EUROPHOTON Conference," (European Physical Society, 2012), 41.
- [86] I. J. Graumann, A. Diebold, F. Emaury, B. Deppe, C. Kränkel, C. J. Saraceno, and U. Keller, "High-Power Modelocked Yb:Lu₂O₃ Thin-Disk Laser with 10-MW sub-500 fs Pulses," in "Lasers Congress 2016 (ASSL, LSC, LAC)," (Optical Society of America, 2016), ATu1A.3.
- [87] I. J. Graumann, A. Diebold, C. G. E. Alfieri, F. Emaury, B. Deppe, M. Golling, D. Bauer, D. Sutter, C. Kränkel, C. J. Saraceno, C. R. Phillips, and U. Keller, "Peak-power scaling of femtosecond Yb:Lu₂O₃ thin-disk lasers," *Opt. Express* **25**, 22519–22536 (2017).
- [88] B. Kreipe, J. R. C. de Andrade, C. Kränkel, and U. Morgner, "Kerr-lens mode-locked Yb³⁺:Lu₂O₃ thin-disk laser," in "Conference on Lasers and Electro-Optics," (Optical Society of America, 2016), SM11.4.
- [89] C. Paradis, N. Modsching, V. J. Wittwer, B. Deppe, C. Kränkel, and T. Südmeyer, "Generation of 35-fs pulses from a Kerr lens mode-locked Yb:Lu₂O₃ thin-disk laser," *Opt. Express* **25**, 14918–14925 (2017).
- [90] N. Modsching, J. Drs, J. Fischer, C. Paradis, F. Labaye, M. Gaponenko, C. Kränkel, V. J. Wittwer, and T. Südmeyer, "Sub-100-fs Kerr lens mode-locked Yb:Lu₂O₃ thin-disk laser oscillator operating at 21 W average power," *Opt. Express* **27**, 16111–16120 (2019).
- [91] S. Ricaud, A. Jaffres, K. Wentsch, A. Suganuma, B. Viana, P. Loiseau, B. Weichelt, M. Abdou-Ahmed, A. Voss, T. Graf, D. Rytz,

- C. Hönninger, E. Mottay, P. Georges, and F. Druon, "Femtosecond Yb:CaGdAlO₄ thin-disk oscillator," *Opt. Lett.* **37**, 3984–3986 (2012).
- [92] A. Diebold, F. Emaury, C. Schriber, M. Golling, C. J. Saraceno, T. Südmeyer, and U. Keller, "SESAM mode-locked Yb:CaGdAlO₄ thin disk laser with 62 fs pulse generation," *Opt. Lett.* **38**, 3842–3845 (2013).
- [93] C. Schriber, L. Merceron, A. Diebold, F. Emaury, M. Golling, K. Beil, C. Kränkel, C. J. Saraceno, T. Südmeyer, and U. Keller, "Pushing SESAM modelocked thin-disk lasers to shortest pulse durations," in "Advanced Solid State Lasers," (Optical Society of America, 2014), AF1A.4.
- [94] B. Dannecker, X. Délen, K. S. Wentsch, B. Weichelt, C. Hönninger, A. Voss, M. A. Ahmed, and T. Graf, "Passively mode-locked Yb:CaF₂ thin-disk laser," *Opt. Express* **22**, 22278–22284 (2014).
- [95] B. Dannecker, M. A. Ahmed, and T. Graf, "SESAM-modelocked Yb:CaF₂ thin-disk-laser generating 285 fs pulses with 1.78 μJ of pulse energy," *Laser Phys. Lett.* **13**, 055801 (2016).
- [96] G. Palmer, M. Schultze, M. Siegel, M. Emons, U. Bünting, and U. Morgner, "Passively mode-locked Yb:KLu(WO₄)₂ thin-disk oscillator operated in the positive and negative dispersion regime," *Opt. Lett.* **33**, 1608–1610 (2008).
- [97] F. Brunner, T. Südmeyer, E. Innerhofer, F. Morier-Genoud, R. Paschotta, V. E. Kisel, V. G. Shcherbitsky, N. V. Kuleshov, J. Gao, K. Contag, A. Giesen, and U. Keller, "240-fs pulses with 22-W average power from a mode-locked thin-disk Yb:KY(WO₄)₂ laser," *Opt. Lett.* **27**, 1162–1164 (2002).
- [98] C. R. E. Baer, C. Kränkel, O. H. Heckl, M. Golling, T. Südmeyer, R. Peters, K. Petermann, G. Huber, and U. Keller, "227-fs pulses from a mode-locked Yb:LuScO₃ thin disk laser," *Opt. Express* **17**, 10725–10730 (2009).
- [99] C. J. Saraceno, O. H. Heckl, C. R. E. Baer, M. Golling, T. Südmeyer, K. Beil, C. Kränkel, K. Petermann, G. Huber, and U. Keller, "SESAMs for high-power femtosecond modelocking: power scaling of an Yb:LuScO₃ thin disk laser to 23 W and 235 fs," *Opt. Express* **19**, 20288–20300 (2011).
- [100] C. J. Saraceno, O. H. Heckl, C. R. E. Baer, C. Schriber, M. Golling, K. Beil, C. Kränkel, T. Südmeyer, G. Huber, and U. Keller, "Sub-100 femtosecond pulses from a SESAM modelocked thin disk laser," *Appl. Phys. B* **106**, 559–562 (2012).
- [101] C. Schriber, F. Emaury, A. Diebold, S. Link, M. Golling, K. Beil, C. Kränkel, C. J. Saraceno, T. Südmeyer, and U. Keller, "Dual-gain SESAM modelocked thin disk laser based on Yb:Lu₂O₃ and Yb:Sc₂O₃," *Opt. Express* **22**, 18979–18986 (2014).

- [102] C. J. Saraceno, O. Heckl, C. Baer, M. Golling, T. Südmeyer, K. Beil, C. Kränkel, K. Petermann, G. Huber, and U. Keller, "CW and mode-locked operation of an Yb:(ScYLu)₂O₃ thin-disk laser," in "Conference on Lasers and Electro-Optics (CLEO)," (IEEE, 2011), 1 – 2.
- [103] C. Schriber, "Towards high average power SESAM-mode-locked thin-disk lasers with short pulse durations," Ph.D. thesis, ETH Zurich, Zürich, Switzerland (2015). Diss. No. 22635.
- [104] K. S. Wentsch, L. Zheng, J. Xu, M. A. Ahmed, and T. Graf, "Passively mode-locked Yb³⁺:Sc₂SiO₅ thin-disk laser," *Opt. Lett.* **37**, 4750–4752 (2012).
- [105] O. H. Heckl, C. Kränkel, C. R. E. Baer, C. J. Saraceno, T. Südmeyer, K. Petermann, G. Huber, and U. Keller, "Continuous-wave and mode-locked Yb:YCOB thin disk laser: first demonstration and future prospects," *Opt. Express* **18**, 19201–19208 (2010).
- [106] M. Tokurakawa, A. Shirakawa, K. ichi Ueda, H. Yagi, T. Yanagitani, A. A. Kaminskii, K. Beil, C. Kränkel, and G. Huber, "Continuous wave and mode-locked Yb³⁺:Y₂O₃ ceramic thin disk laser," *Opt. Express* **20**, 10847–10853 (2012).
- [107] C. Kränkel, C. R. E. Baer, O. H. Heckl, M. Golling, T. Südmeyer, U. Keller, R. Peters, K. Petermann, and G. Huber, "Shortest pulse duration of mode-locked thin disk lasers: Ultrafast Yb:LuScO₃ laser generates 227-fs pulses," in "2009 Conference on Lasers and Electro-Optics and 2009 Conference on Quantum electronics and Laser Science Conference," (2009), 1–2.
- [108] K. S. Wentsch, B. Weichelt, S. Günster, F. Druon, P. Georges, M. A. Ahmed, and T. Graf, "Yb:CaF₂ thin-disk laser," *Opt. Express* **22**, 1524–1532 (2014).
- [109] N. Modsching, C. Paradis, F. Labaye, M. Gaponenko, I. J. Graumann, A. Diebold, F. Emaury, V. J. Wittwer, and T. Südmeyer, "Kerr lens mode-locked Yb:CALGO thin-disk laser," *Opt. Lett.* **43**, 879–882 (2018).
- [110] V. Peters, A. Bolz, K. Petermann, and G. Huber, "Growth of high-melting sesquioxides by the heat exchanger method," *Journal of Crystal Growth* **237-239**, 879 – 883 (2002).
- [111] R. Peters, C. Kränkel, S. T. Fredrich-Thornton, K. Beil, K. Petermann, G. Huber, O. H. Heckl, C. R. E. Baer, C. J. Saraceno, T. Südmeyer, and U. Keller, "Thermal analysis and efficient high power continuous-wave and mode-locked thin disk laser operation of Yb-doped sesquioxides," *Appl. Phys. B* **102**, 509–514 (2011).
- [112] A. Jaffrès, S. Ricaud, A. Suganuma, B. Viana, P. Loiseau, P. Georges, and F. Druon, "Thermal conductivity versus Yb³⁺ concentration in Yb:CALGO: A material for high power ultrafast laser," in "2013 Conference on Lasers Electro-Optics Europe International Quantum Electronics Conference CLEO EUROPE/IQEC," (IEEE, 2013), 1–1.

- [113] C. R. E. Baer, O. H. Heckl, C. J. Saraceno, C. Schriber, C. Kränkel, T. Südmeyer, and U. Keller, "Frontiers in passively mode-locked high-power thin disk laser oscillators," *Opt. Express* **20**, 7054–7065 (2012).
- [114] I. J. Graumann, A. Diebold, F. Emaury, B. Deppe, C. Kränkel, C. J. Saraceno, and U. Keller, "10-MW sub-500-fs high-power SESAM-modelocked Yb:Lu₂O₃ thin disk laser," in "7th EPS-QEOD Europhoton Conference," (European Physical Society, 2016), 46 – 46.
- [115] T. Brabec, C. Spielmann, and F. Krausz, "Limits of pulse shortening in solitary lasers," *Opt. Lett.* **17**, 748–750 (1992).
- [116] R. Paschotta and U. Keller, "Passive mode locking with slow saturable absorbers," *Appl. Phys. B* **73**, 653–662 (2001).
- [117] A. Diebold, F. Saltarelli, I. J. Graumann, C. J. Saraceno, C. R. Phillips, and U. Keller, "Gas-lens effect in kW-class thin-disk lasers," *Opt. Express* **26**, 12648–12659 (2018).
- [118] R. Paschotta, J. Aus der Au, G. J. Spühler, S. Erhard, A. Giesen, and U. Keller, "Passive mode locking of thin-disk lasers: effects of spatial hole burning," *Appl. Phys. B* **72**, 267–278 (2001).
- [119] S. T. Fredrich-Thornton, "Nonlinear Losses in Single Crystalline and Ceramic Yb:YAG Thin-Disk Lasers," Ph.D. thesis, Universität Hamburg, Hamburg, Germany (2010).
- [120] D. J. H. C. Maas, B. Rudin, A. R. Bellancourt, D. Iwaniuk, S. V. Marchese, T. Südmeyer, and U. Keller, "High precision optical characterization of semiconductor saturable absorber mirrors," *Opt. Express* **16**, 7571–7579 (2008).
- [121] C. J. Saraceno, C. Schriber, M. Mangold, M. Hoffmann, O. H. Heckl, C. R. E. Baer, M. Golling, T. Südmeyer, and U. Keller, "SESAMs for High-Power Oscillators: Design Guidelines and Damage Thresholds," *IEEE J. Sel. Top. Quant.* **18**, 29–41 (2012).
- [122] C. G. E. Alfieri, A. Diebold, F. Emaury, E. Gini, C. J. Saraceno, and U. Keller, "Improved SESAMs for femtosecond pulse generation approaching the kW average power regime," *Opt. Express* **24**, 27587–27599 (2016).
- [123] A. A. Lagatskii, N. V. Kuleshov, V. G. Shcherbitskii, V. F. Kleptsyn, V. P. Mikhailov, V. G. Ostroumov, and G. Huber, "Lasing characteristics of a diode-pumped Nd³⁺:CaGdAlO₄ crystal," *Quantum Electron.* **27**, 15–17 (1997).
- [124] N. Kodama and M. Yamaga, "Crystal characterization and optical spectroscopy of Ti³⁺-doped CaGdAlO₄ crystals," *Phys. Rev. B* **57**, 811–817 (1998).
- [125] L. Vasylechko, N. Kodama, A. Matkovskii, and Y. Zhydashchevskii, "Crystal structure and optical spectroscopy of CaGdAlO₄:Er single crystal," *J. Alloy. Compd.* **300-301**, 475 – 478 (2000).

- [126] J. Petit, P. Goldner, and B. Viana, "Laser emission with low quantum defect in Yb:CaGdAlO₄," *Opt. Lett.* **30**, 1345–1347 (2005).
- [127] P. Loiko, F. Druon, P. Georges, B. Viana, and K. Yumashev, "Thermo-optic characterization of Yb:CaGdAlO₄ laser crystal," *Opt. Mater. Express* **4**, 2241–2249 (2014).
- [128] K. Beil, B. Deppe, and C. Kränkel, "Yb:CaGdAlO₄ thin-disk laser with 70% slope efficiency and 90 nm wavelength tuning range," *Opt. Lett.* **38**, 1966–1968 (2013).
- [129] A. Greborio, A. Guandalini, and J. A. der Au, "Sub-100 fs pulses with 12.5-W from Yb:CALGO based oscillators," in "Solid State Lasers XXI: Technology and Devices," (Proc. SPIE 8235, 2012), 200 – 205.
- [130] P. Sévillano, P. Georges, F. Druon, D. Descamps, and E. Cormier, "32-fs Kerr-lens mode-locked Yb:CaGdAlO₄ oscillator optically pumped by a bright fiber laser," *Opt. Lett.* **39**, 6001–6004 (2014).
- [131] C. R. Phillips, A. S. Mayer, A. Klenner, and U. Keller, "SESAM modulated Yb:CaGdAlO₄ laser in the soliton modelocking regime with positive intracavity dispersion," *Opt. Express* **22**, 6060–6077 (2014).
- [132] A. Klenner, M. Golling, and U. Keller, "High peak power gigahertz Yb:CALGO laser," *Opt. Express* **22**, 11884–11891 (2014).
- [133] A. S. Mayer, C. R. Phillips, and U. Keller, "Watt-level 10-gigahertz solid-state laser enabled by self-defocusing nonlinearities in an aperiodically poled crystal," *Nat. Commun.* **8**, 1673 (2017).
- [134] S. Manjoran and A. Major, "Diode-pumped 45 fs Yb:CALGO laser oscillator with 1.7 MW of peak power," *Opt. Lett.* **43**, 2324–2327 (2018).
- [135] S. Ricaud, A. Jaffres, P. Loiseau, B. Viana, B. Weichelt, M. Abdou-Ahmed, A. Voss, T. Graf, D. Rytz, M. Delaigue, E. Mottay, P. Georges, and F. Druon, "Yb:CaGdAlO₄ thin-disk laser," *Opt. Lett.* **36**, 4134–4136 (2011).
- [136] P.-O. Petit, "Optimisation de matériaux dopés par les ions ytterbium pour applications laser de fortes puissances," Ph.D. thesis, Université Pierre et Marie Curie - Paris VI, Paris, France (2010).
- [137] A. Jaffres, "Matériaux laser dopés terres rares impulsions dans la gamme spectrale 1 µm et 1,5 µm : efforts sur la montée en puissance et en cadence," Ph.D. thesis, Université Pierre et Marie Curie - Paris VI, Paris, France (2013).
- [138] Q. Hu, Z. Jia, C. Tang, N. Lin, J. Zhang, N. Jia, S. Wang, X. Zhao, and X. Tao, "The origin of coloration of CaGdAlO₄ crystals and its effect on their physical properties," *CrystEngComm* **19**, 537–545 (2017).
- [139] V. Magni, "Multielement stable resonators containing a variable lens," *J. Opt. Soc. Am. A* **4**, 1962–1969 (1987).

- [140] D. Maas, "A new class of ultrafast semiconductor lasers," Ph.D. thesis, ETH Zurich, Zürich, Switzerland (2009).
- [141] F. Saltarelli, I. J. Graumann, L. Lang, D. Bauer, C. R. Phillips, and U. Keller, "Power Scaling of Ultrafast Laser Oscillators: 350-W Output Power Sub-Ps SESAM-Modelocked Thin-Disk Laser," in "2019 Conference on Lasers and Electro-Optics (CLEO)," (Optical Society of America, 2019), SF3E.3.
- [142] A. Stingl, M. Lenzner, C. Spielmann, F. Krausz, and R. Szipöcs, "Sub-10-fs mirror-dispersion-controlled Ti:sapphire laser," *Opt. Lett.* **20**, 602–604 (1995).
- [143] U. Morgner, F. X. Kärtner, S. H. Cho, Y. Chen, H. A. Haus, J. G. Fujimoto, E. P. Ippen, V. Scheuer, G. Angelow, and T. Tschudi, "Sub-two-cycle pulses from a Kerr-lens mode-locked Ti:sapphire laser," *Opt. Lett.* **24**, 411–413 (1999).
- [144] D. H. Sutter, G. Steinmeyer, L. Gallmann, N. Matuschek, F. Morier-Genoud, U. Keller, V. Scheuer, G. Angelow, and T. Tschudi, "Semiconductor saturable-absorber mirror-assisted Kerr-lens mode-locked Ti:sapphire laser producing pulses in the two-cycle regime," *Opt. Lett.* **24**, 631–633 (1999).
- [145] C. P. J. Barty, G. Korn, F. Raksi, C. Rose-Petruck, J. Squier, A.-C. Tien, K. R. Wilson, V. V. Yakovlev, and K. Yamakawa, "Regenerative pulse shaping and amplification of ultrabroadband optical pulses," *Opt. Lett.* **21**, 219–221 (1996).
- [146] C. P. J. Barty, T. Guo, C. L. Blanc, F. Raksi, C. Rose-Petruck, J. Squier, K. R. Wilson, V. V. Yakovlev, and K. Yamakawa, "Generation of 18-fs, multiterawatt pulses by regenerative pulse shaping and chirped-pulse amplification," *Opt. Lett.* **21**, 668–670 (1996).
- [147] L.-J. Chen, M. Y. Sander, and F. X. Kärtner, "Kerr-lens mode locking with minimum nonlinearity using gain-matched output couplers," *Opt. Lett.* **35**, 2916–2918 (2010).
- [148] F. Canbaz, E. Beyatli, L.-J. Chen, A. Sennaroglu, F. X. Kärtner, and U. Demirbas, "Highly efficient and robust operation of Kerr-lens mode-locked Cr:LiSAF lasers using gain-matched output couplers," *Opt. Lett.* **39**, 327–330 (2014).
- [149] C. Cihan, E. Beyatli, F. Canbaz, L. Chen, B. Sumpf, G. Erbert, A. Leitnerstorfer, F. X. Kärtner, A. Sennaroglu, and U. Demirbas, "Gain-Matched Output Couplers for Efficient Kerr-Lens Mode-Locking of Low-Cost and High-Peak Power Cr:LiSAF Lasers," *IEEE J. Sel. Top. Quant.* **21**, 94–105 (2015).
- [150] K. A. Stankov, "A mirror with an intensity-dependent reflection coefficient," *Appl. Phys. B* **45**, 191–195 (1988).
- [151] K. A. Stankov and J. Jethwa, "A new mode-locking technique using a nonlinear mirror," *Opt. Commun.* **66**, 41–46 (1988).

- [152] M. B. Danailov, G. Cerullo, V. Magni, D. Segala, and S. De Silvestri, "Nonlinear mirror mode locking of a cw Nd:YLF laser," *Opt. Lett.* **19**, 792–794 (1994).
- [153] G. Cerullo, M. B. Danailov, S. De Silvestri, P. Laporta, V. Magni, D. Segala, and S. Taccheo, "A diode-pumped nonlinear mirror mode-locked Nd:YAG laser," *Appl. Phys. Lett.* **65**, 2392–2394 (1994).
- [154] G. M. Thomas and M. J. Damzen, "30 W Nd:GdVO₄ oscillator modelocked with nonlinear mirror," in "2011 Conference on Lasers and Electro-Optics Europe and 12th European Quantum Electronics Conference (CLEO EUROPE/EQEC)," (IEEE, 2011), 1–1.

Acknowledgements

In the last pages of this thesis, I would like to thank the people that contributed, directly or indirectly, to the work I have carried out during my four years spent at ETH Zurich.

I would like to thank Prof. Ursula Keller for the opportunity of joining her group and conducting research in one of the world-leading laser labs. I believe it is a privilege to be able to work on a topic one likes and have all the necessary resources at hand to explore different alternatives, and I am thankful to Ursi for providing this fertile working environment.

Many thanks to Prof. Jens Limpert for accepting to be my co-examiner and for all his interesting questions during the doctoral examination, which I enjoyed very much!

A large part of this thesis relies on exotic, high-quality dielectric coatings and would not be possible without the Ion Beam Sputtering machine of the Université de Neuchâtel. I am very grateful to Prof. Thomas Südmeyer for the opportunity to collaborate with his group and benefit from the IBS. Many thanks to Valentin for all the design, production and characterization of the coatings, as well as many interesting discussions. Your work was a precious help to bring my projects forward and I guess that I will miss the flexibility of getting tailor-made coatings in the future. And thanks to Olga for her contribution to these successful coatings.

I would like to thank other members of Thomas' group: François for many discussions on CALGO, LuO and thin-disk lasers, Norbert and Clément for discussions on KLM and for showing that CALGO could be Kerr-lens modelocked in a TDL (but is a 150 mW TDL really a TDL? =P). Thanks Norbert for passing by ETH for a second CALGO KLM attempt!

Many thanks to Dr. Christian Kränkel for providing the LuO disks that I used for my results. Thank you for section 3.2.1 ("Das nulldimensionale Modell") of your PhD thesis, which I referred to numerous times during my thesis to quickly calculate the pump absorption of the disk! And

thanks for many interesting discussions at conferences. We still need to find a way to use the TDL head for the laser beam!

I also would like to thank Dr. Dirk Sutter, Dr. Dominik Bauer, Dr. Tom Metzger and Dr. Catherine Teisset from TRUMPF for their help and advice on TDL heads and TDL technology in general. Many thanks to Dr. Sebastian Riese from Layertec for the design of the first GMOCs I used. And also many thanks to Dr. Christoph Liebald and Dr. Daniel Rytz from FEE for fruitful discussions on CALGO. I hope that the crystal quality will keep getting better!

Of course I would like to thank the different people that shared with me the passion for the thin-disk lasers, the awesome team constantly re-defining the benchmark for high-power oscillators! Many thanks to the former team members: Clara, it was a pleasure to work with you for the first few months of my PhD and I was inspired by your enthusiasm for crazy projects. Florian, an endless source of motivation, optimism and funny moments, I liked how you lightened up the mood in the team ("it's could be worse"). And Andreas, we had some fun in the lab (Christmas R&B/rap playlist), on CATIA or in the workshop (water-cooled post and beam dump for few kW), in the office (the TDL hotline haha) and at tea-time and cake-time. Also thanks to Clara, Florian and Andreas for the crazy deadline mode ("the deadline is never dead" or "after the deadline is the next deadline").

I also would like to thank the current team members: Francesco, thanks for upgrading part of the equipment in E14, pushing for the best diagnostics and, of course, always the highest power. And thank you for the very nice doctor hat! Lukas, I hope that the gain-flattening will soon be successful and thank you for some useful scripts and datasets for my thesis. And finally Chris, thank you for the numerous discussions, ideas, MatLab scripts you shared with me. It was very stimulating to work with you and I am thankful that I could benefit from your broad laser knowledge. I also appreciated your efforts to find an interesting project for every member of the team, which was not always an easy task.

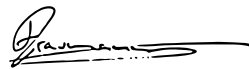
I would like to thank Justas, a temporary member of E14 (RIP XPW project), for building a KLM modelocked oscillator in E14! It was a pleasure to work with you in the lab for a while. And thank you for suggesting the Annapurna trek and introducing me to the awesome Werdinsel WG!

Special thanks go to my office mates, Fabian and Leo. Thank you for turning our office into a planning room for exciting mountaineering, climbing or biking tours. I very much enjoyed the time we spent together on the bike or in the mountains. Sometimes it was a bit hard to keep the work-climbing balance ;-).

And I also thank Stefan for numerous discussions about work, life, academia, food, politics, "proper" clothing etc... and Science in Context, and for organizing work outings to the pub quiz, cinema or just for dinner.

I would like to thank all the other ULP members for the good work atmosphere and the fun we had at various group events: Ajantha, thank you for your nice feedback on the thesis, Arthur, keep pushing in the mountains, Benni the beast, for the meters of shots, Cesare, for your “flowery” language and some good hikes, Dominik, for joining the Xletix, Fabschla, for gluten-free drinks during the ski weekends, Jaco, for taking care of me on a certain Christmas dinner, Jacob, for a spot-on secret santa present, Jochen, for sharing a taste for good wine, Jonas, where is Leo? I don’t know but thanks for taking over the PECVD responsibility, Laura, thank you for the pictures of the defence, Luca, for the salad shots, Lukas Gallmann, for useful discussions and being a “loose bottleneck”, Marco, all the best with the ONEMix project, Matthias, thank you for the SESAM growth and your infinite kindness, Nadja, for the PhD apero, Nico, “ainsi périrent les ennemis de la République”, Özgür, good luck with the 2- μ m growth, Pierre(-Alexis), ça fait toujours plaisir de pouvoir parler français un peu, bon courage pour la suite, Sandra, thank you for your patience when handling all the FedEx/customs invoices, Sergej, all the best with the surface project, and Zeno, for SOLA Basel.

Finally, I would like to thank the members of the Werdinsel WG (Chris B., Chris H., Flavia, Leonie, Marion, and also Noémi and Stéphane) for the good atmosphere in our shared house and for epic parties (still one to come!). I thank my family for their support throughout the PhD time and for all joining on my defence day. And I thank Leonie for the love, energy and inspiration she put in my life over the last few months.

A handwritten signature in black ink, appearing to be 'D. Gallmann', with a long horizontal flourish extending to the right.

Zurich, December 2019